The Influence Of Microstructure On The Corrosion And Wear Mechanisms Of High Chromium White Irons In Highly Caustic Solutions

G. D. Nelson

School of Mechanical Engineering
The University of Adelaide
South Australia

December 2010

Chapter 6

Corrosion Tests

6.1 Introduction

There has been very limited work reported in the literature on the corrosion of white irons in highly alkaline sodium hydroxide solutions. In addition the role of aluminate ions in sodium aluminate solutions or synthetic Bayer liquor has not been investigated. The purpose of these sets of corrosion tests was to investigate the influence of microstructure on the corrosion response of various alloys. Heat treated white irons were also investigated to elucidate the role of matrix chromium content, the role of secondary carbides and the presence of martensite and retained austenite. Corrosion tests on a low carbon steel (AS1163: C350LO) and AISI 420 martensitic stainless steel were also included in the test regime for comparative purposes.

6.2 Anodic Polarization and Tafel Tests

6.2.1 Experimental Methodology

Corrosion tests involved potentiodynamic anodic polarization to investigate the response of the materials over a large range of potentials. The tests were done using a conventional three electrode test cell with an external reference compartment connected to the test cell via a salt bridge of the test solution. The test cell was immersed in a constant temperature water bath which maintained the test solution at a temperature of 90 ± 1°C. The test solution was deaerated for a minimum of 1 hour while warming to the test temperature. The reference electrode used for the corrosion tests was a Red Rod reference electrode (Radiometer Analytical: REF 201) that had a reference potential of 0.194 V versus the standard hydrogen electrode which was used to convert recorded potential values to the SHE scale. The test material or working electrode was freshly wet ground to a 1200 grit finish, degreased in acetone and finally

rinsed with deionized water and hot air dried prior to testing. Prior to a polarization test, the working electrode was conditioned at a cathodic potential of -1.30 $V_{Red\ Rod}$ to reduce any surface oxides. Polarization scans were started at a potential of -0.050 V versus the corrosion potential and finished at a potential of 0 $V_{Red\ Rod}$ for the high chromium white iron alloys and 0.5 $V_{Red\ Rod}$ for the steel and martensitic stainless steel. The scan rate used was 1 mV/s which is similar to many other investigations in caustic solutions. A more detailed account of the corrosion test equipment, sample preparation and experimental methodology can be found in Section 2.4: Corrosion Tests.

Tafel tests were used to determine the corrosion current density and were done using the same equipment, test sample preparation and sample conditioning as for the polarization tests. However, the scan rate was reduced to 0.5 mV/s and were started and finished at -0.25 V and 0.25 V versus the corrosion potential respectively. The corrosion current was determined using the DC105 software supplied with the Gamry potentiostat.

6.2.2 Effect of Environment

Sodium hydroxide is the basis for the solutions used in the Bayer alumina refining process for the separation of the aluminium rich component from bauxite to form sodium aluminate solutions or Bayer liquor. The concentrations of the caustic solutions are a pH of 14 or greater and are commonly at elevated temperatures. The materials that are commonly used for the construction of pipelines and slurry pumps for the transfer of these caustic solutions is low carbon steel and high chromium white irons respectively. In sections susceptible to high levels of wear, such as the inlet and outlets adjacent to slurry pumps, the steel pipelines are commonly weld overlayed with high chromium white irons or pipelines are cast from high chromium white iron to reduce wear and increase pipe longevity. The transfer of the highly caustic slurries causes the erosion-corrosion of the slurry pumps and pipeline sections susceptible to high levels of wear. A better understanding of the corrosion behaviour of the materials used for the transfer of caustic slurries in the alumina industry can allow better material selection to reduce the rate of corrosion which may also lead to improvements in the overall erosion-corrosion wear resistance and increased plant life.

This section reports on the corrosion behaviour of three different high chromium white irons in a sodium aluminate solution and sodium hydroxide solutions of 2.5M and 5.0M concentrations at 90^{o}C. The significance of the standard 2.5M and 5.0M sodium hydroxide solutions is that they approximately correspond to the free and total caustic of sodium aluminate solution, which is 2.7M and 4.9M respectively. The difference between the total caustic and free caustic is due to the alumina combining with the caustic to form sodium aluminate ions. For comparative purposes, a low carbon steel is investigated in the same solutions. A 420 martensitic stainless steel in the quenched condition is also included to compare with the corrosion behaviour of the high chromium white irons. The significance of the 420 martensitic

stainless steel is that the chemical composition and microstructure is very similar to what can be expected for the matrix of heat treated high chromium white irons but without the large carbides.

6.2.2.1 Materials Investigated

The corrosion behaviour of three different high chromium white iron castings, a AS1163: C350LO low carbon steel and a AISI 420 martensitic stainless steel are investigated in a sodium aluminate solution, 2.5M and 5.0M sodium hydroxide solutions at 90°C under deaerated conditions. Two of the white iron alloys, HypoA and HyperA, were sectioned from ex-service alumina plant slurry pump castings. The third high chromium white iron alloy, HyperEXP, is an experimental high chromium white iron castings that has improved toughness and a high nickel content. A summary of the bulk chemical compositions, and where applicable, the chromium to carbon ratio and CVF are given in Table 6.1. Details of sample preparation methods, and sample size for corrosion tests can be found in Chapter 5.

Table 6.1: Bulk chemical compositions, chromium to carbon ratio, CVF and bulk hardness of the investigated materials.

Material	Bulk Chemical Composition wt%							Cr/C ratio	CVF*	Bulk Hardness (HV_{30})
	C	Si	Cr	Mn	Fe	Ni	Mo			
Steel (AS1163: C350LO)	0.135	0.12	0.018	0.66	98.9	0.017	0.003	-	-	147 ± 1.5
AISI 420 (UNS No. S42000)	0.19	0.49	13.1	0.38	87.3	0.45	0.08	68.9	-	615 ± 4
HypoA Casting	2.4	0.97	26.6	0.69	68.9	0.06	0.02	11.1	25.8 ± 1.1	623 ± 4
HyperA Casting	4.5	0.49	34.0	1.9	57.7	0.12	0.95	7.6	51.9 ± 2.5	682 ± 20
HyperEXP Casting	4.51	0.45	25.0	4.6	60.2	4.8	0.33	5.5	49.9 ± 4.3	494 ± 5
*Carbide volume fraction of primary and or eutectic M_7C_3 carbides only										

The three high chromium white iron castings investigated all have distinctly different microstructures, Figure 6.1. HypoA is a hypoeutectic high chromium white iron that has been heat treated to give a matrix microstructure of martensite containing precipitated $M_{23}C_6$ carbides, Figure 6.1(a). HyperA is in the as-cast condition and has a hypereutectic microstructure consisting of large primary M_7C_3 carbides. The majority of the matrix is austenitic but also contains regions of fine precipitated secondary carbides and a band of martensite that surrounds the primary M_7C_3 carbides, Figure 6.1(b). The experimental alloy, HyperEXP, is in the as-cast condition and has a hypereutectic microstructure consisting of primary and eutectic M_7C_3 carbides in an austenitic matrix. The austenitic matrix also contains limited secondary carbide precipitation, Figure 6.1(c). A more detailed account of the microstructures for the three alloys is given in Section 2.2.

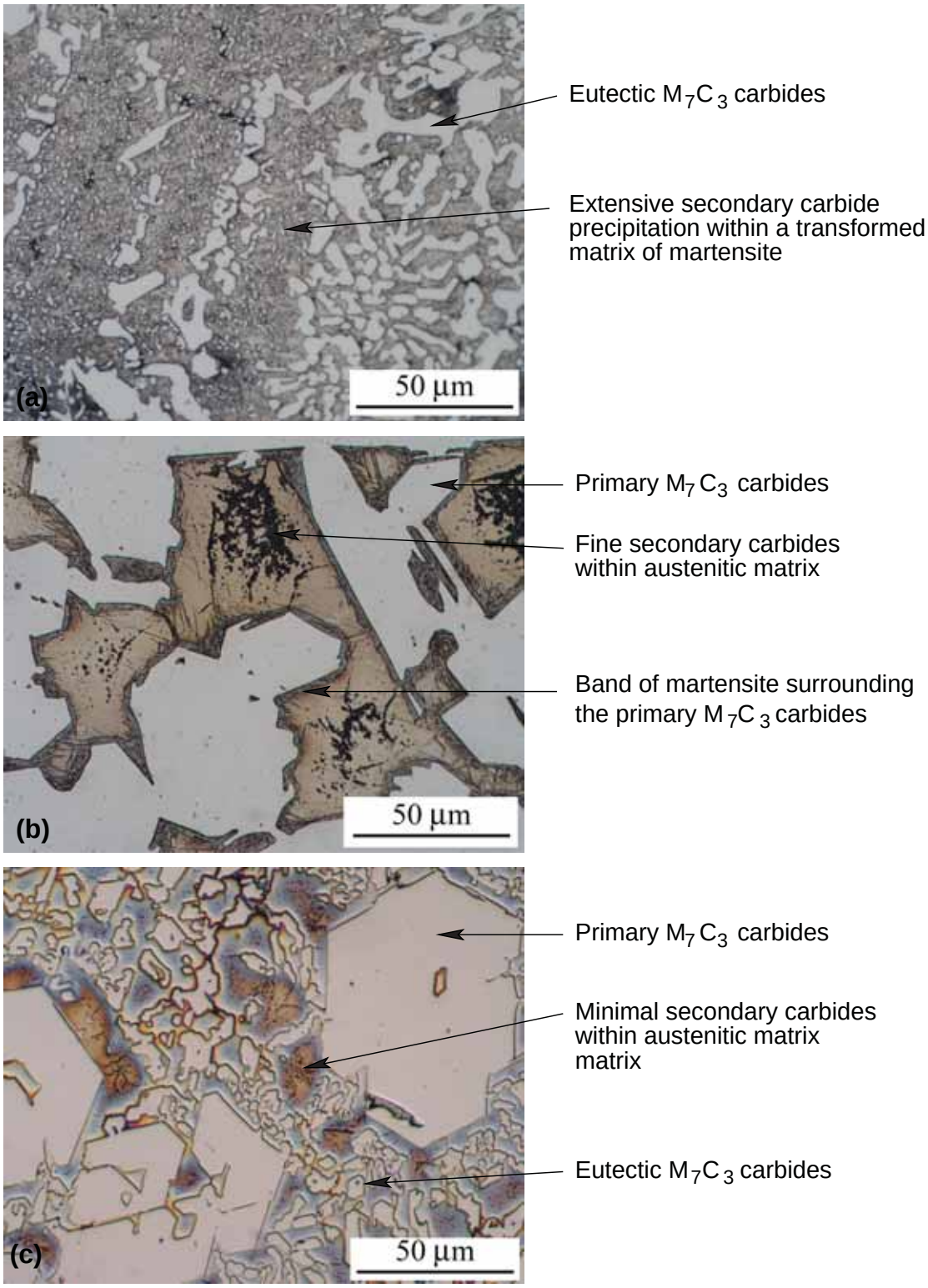

Figure 6.1: Micrographs of the high chromium white iron castings investigated. (a) HypoA, (b) HyperA and (c) HyperEXP. All micrographs are at 500x magnification and etched in acid ferric chloride.

The low carbon steel used in this corrosion investigation was sectioned from a 273.1 x 6.4 mm diameter pipe conforming to AS1163: C350LO (ASTM A53: GradeB). The microstructure of the steel consists of ferrite with a small proportion of pearlite, Figure 6.2(a).

The AISI 420 (UNS No. S42000) martensitic stainless steel was heat treated to transform the wrought form of the alloy to a martensitic microstructure. The heat treatment involved preheating the samples at 750°C, holding for 1 hour before increasing the temperature to 1000°C, holding for 1 hour followed by a nitrogen gas quench. The resulting microstructure is composed of precipitated carbides, martensite and retained austenite, Figure 6.2(b).

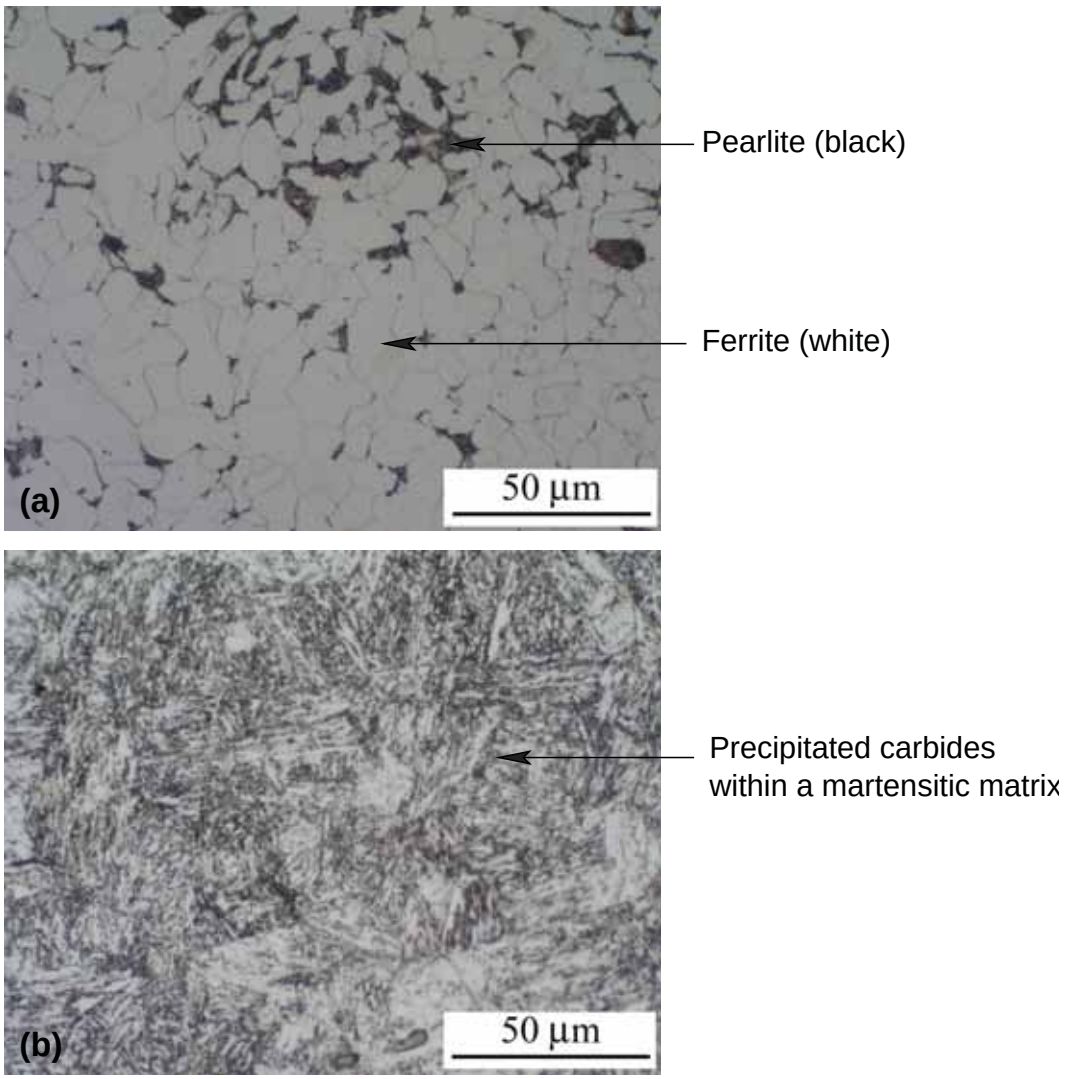

Figure 6.2: (a) Micrograph of the steel (AS1163: C350LO), 500x magnification, etched in Nital. (b) Micrograph of AISI 420 martensitic stainless in the as-quenched condition, 500x magnification, etched in acid ferric chloride.

6.2.2.2 Polarization and Tafel Test Results

Low Carbon Steel

The potentiodynamic anodic polarization curves for low carbon steel tested at 90°C under deaerated conditions in, 2.5M, 5.0M sodium hydroxide solution and the sodium aluminate solution are shown in Figure 6.3. Potential and current densities for significant features of the polarization curves along with the corrosion current density obtained from Tafel tests are summarized in Table 6.2.

The anodic polarization curves for 2.5M and 5.0M NaOH solutions showed similar characteristics. There was an active dissolution regime between -0.9 V_{SHE} and -0.75 V_{SHE} with an approximately linear potential-current behaviour and well defined Tafel slope. At potentials between -0.8 V_{SHE} and -0.75 V_{SHE} the current peaked which signified the transition from the active state to the passive state and the critical potential ($E_{critical}$) and current ($I_{critical}$). Between -0.75 V_{SHE} and -0.6 V_{SHE} the polarization curves had a small secondary current peak. At potentials between -0.5 V_{SHE} and 0.4 V_{SHE} the material demonstrated passive like behaviour or a humped potential regime where the current density did not vary significantly with increasing potential. Above 0.4 V_{SHE} the material experienced a transpassive regime with the current sharply increasing with further increase in potential and oxygen evolution.

Increasing the sodium hydroxide concentration from 2.5M to 5.0M NaOH caused the rest potential to shift in the negative (active) direction by 35 mV. The critical potential for the active to passive transition was also shifted in the negative direction by 30 mV. The current density at the active to passive transition increased from 610 $\mu A/cm^2$ to 825 $\mu A/cm^2$ for the 2.5M and 5.0M NaOH solutions respectively. The size of the small current peak in the active to passive transition zone also decreased in size with increasing NaOH concentration. The current density of the humped potential regime between -0.5 V_{SHE} and 0.4 V_{SHE} for the 5.0M NaOH was 20 $\mu A/cm^2$ greater at -0.3 V_{SHE} than for the 2.5M NaOH solution. The transpassive potential was also found to slightly decreased with an increase in potential.

The polarization curve for low carbon steel tested in sodium aluminate solution showed many similar characteristics to the polarization curves for steel in NaOH solutions. Between -0.89 V_{SHE} and -0.8 V_{SHE} is an active dissolution regime, followed by a distinct current peak corresponding to the critical potential and active to passive transition at -0.8 V_{SHE}. Similarly there is also a small secondary current peak at -0.72 V_{SHE}. However, an additional current peak at -0.4 V_{SHE} was noticed on the polarization curves for steel in the sodium aluminate solution. Between -0.35 V_{SHE} and 0.4 V_{SHE} the polarization curve followed a hump potential regime where the current density did not vary significantly with increasing potential. At potentials greater than 0.4 V_{SHE}, the material experienced a transpassive regime with the current sharply increasing with further increase in potential and oxygen evolution.

A significant difference between the polarization curves for steel in NaOH solutions and the sodium aluminate solution is the critical current density. The critical current density in the sodium aluminate solution was approximately 30 and 60 $\mu A/cm^2$ less than the critical current density for the 2.5M and 5.0M NaOH solutions respectively. The current density in the hump potential regime was very similar for the sodium aluminate and 2.5M NaOH solutions. The rest potential in the sodium aluminate solution was between that of the 2.5M and 5.0M NaOH solutions but the critical potential was similar to the 5.0M NaOH solution.

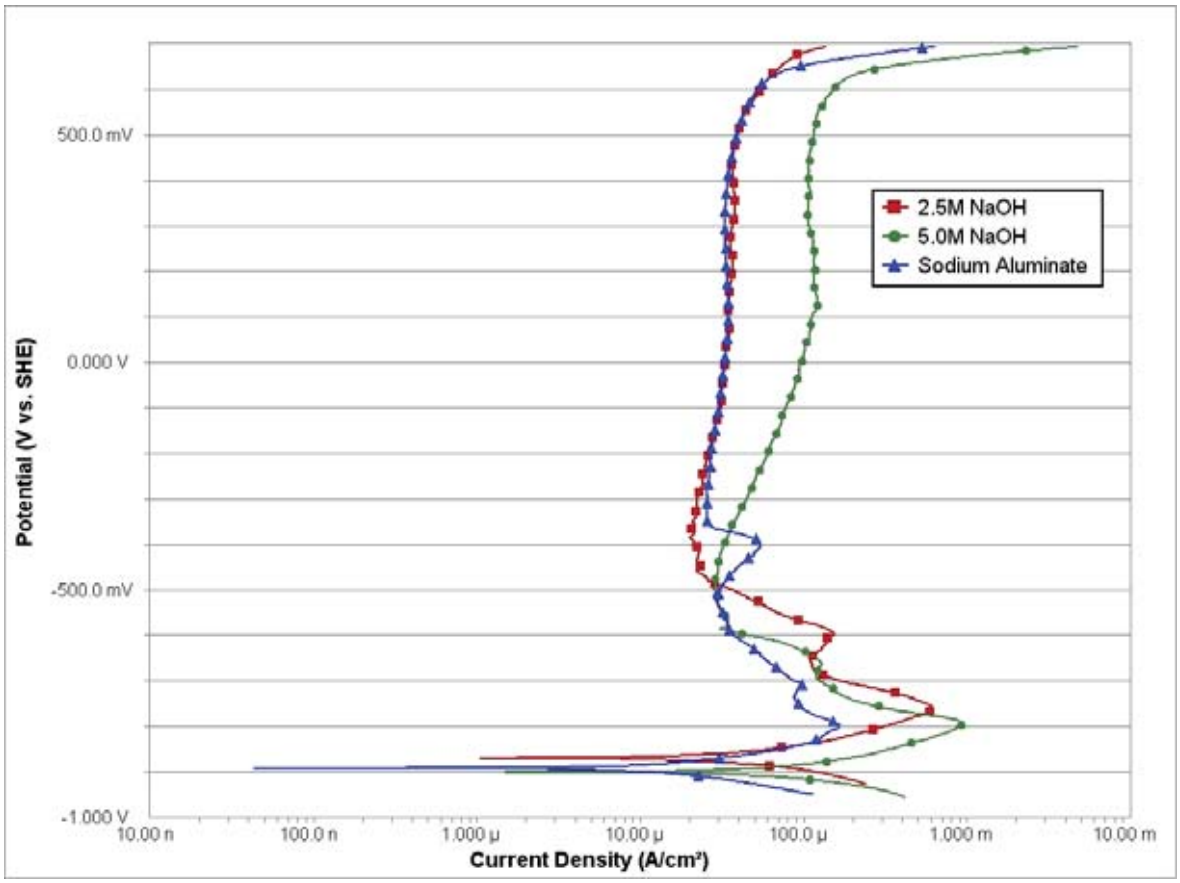

Figure 6.3: Typical anodic polarization curves for AS1163: C350LO low carbon steel in deaerated 2.5M, 5.0M NaOH and sodium aluminate solution at 90°C and a potential scan rate of 1 mV/s.

Table 6.2: Potential and corrosion values for AS1163: C350LO low carbon steel in NaOH and sodium aluminate solutions. Results are averages of multiple polarization tests. Corrosion current results are averages of multiple Tafel tests.

Steel	E_{corr} (V_{SHE})	I_{corr} ($\mu A/cm^2$)	$E_{critical}$ (V_{SHE})	$I_{critical}$ ($\mu A/cm^2$)	$I_{passive}$* ($\mu A/cm^2$)
2.5M NaOH	-0.864 ± 0.004	41.2 ± 2.2	-0.767 ± 0.013	608.8 ± 153.5	21.5 ± 4.4
5.0M NaOH	-0.901 ± 0.001	72.1 ± 7.1	-0.796 ± 0.005	825.6 ± 143.3	40.1 ± 5.6
Sodium Aluminate	-0.886 ± 0.004	10.7 ± 0.9	-0.798 ± 0.003	154.1 ± 15.3	24.6 ± 2.7
*I_{pass} at a potential of -0.306 V_{SHE} (-0.5 $V_{Red\ Rod}$)					

420 Martensitic Stainless Steel

The potentiodynamic anodic polarization curves for AISI 420 martensitic stainless steel in the quenched conditions tested in, 2.5M, 5.0M sodium hydroxide solutions and sodium aluminate solution at 90°C under deaerated conditions are shown in Figure 6.4. Potential and current densities for significant features of the polarization curves along with the corrosion current density obtained from Tafel tests are summarized in Table 6.3.

The anodic polarization curves done in 2.5M and 5.0M NaOH solutions shows a small active dissolution regime between -0.9 V_{SHE} and -0.75 V_{SHE} before a current peak between -0.8 V_{SHE} and -0.75 V_{SHE} signifying the active to passive transition at the critical potential. Between potentials of -0.65 V_{SHE} and -0.1 V_{SHE}, the material demonstrated passive like behaviour with very little change in current density for large increases in potential. At potentials of -0.1 V_{SHE} to 0.15 V_{SHE} for the 5.0M NaOH solution and -0.1 V_{SHE} to 0.3 V_{SHE} for the 2.5M NaOH solution, the polarization curves showed transpassive behaviour. A secondary passivity regime followed between 0.15 V_{SHE} and 0.6 V_{SHE} for the 5.0M NaOH solution and 0.3 V_{SHE} and 0.6 V_{SHE} for the 2.5M NaOH solution. At potentials greater than 0.6 V_{SHE} the material experienced transpassive behaviour and the evolution of oxygen.

The increase in NaOH concentration from 2.5M to 5.0M shifted the rest potential and the critical potential in the negative direction by 30 mV and 20 mV respectively. The critical current density increased with an increase in NaOH solution concentration by 47 $\mu A/cm^2$ to 187 $\mu A/cm^2$. The current density in the passive zone was very similar for both the 2.5M and 5.0M NaOH solution concentrations, only differing by 4 $\mu A/cm^2$. The transpassive potential, secondary passivity potential and second transpassive potential were also found to decrease with increasing solution concentration.

The polarization curve in sodium aluminate solution was characteristically similar to the sodium hydroxide solutions. The rest potential fell between the rest potential in 2.5M and 5.0M sodium hydroxide solutions. From -0.9 V_{SHE} to -0.8V_{SHE}, there is an active dissolution regime before the current peaked at the active to passive transition at -0.8 V_{SHE}. The peak current, or critical current density, was between the critical current densities for the 2.5M and 5.0M NaOH solutions being 47 $\mu A/cm^2$ greater and 10 $\mu A/cm^2$ less than the 2.5M and 5.0M NaOH solutions respectively. At -0.7 V_{SHE} there was a small secondary current hump/peak which was not on the polarization curves in the NaOH solutions. Additionally there was a third current peak at -0.4 V_{SHE} which was not on the polarization curves in the NaOH solutions. From -0.4 V_{SHE} to 0 V_{SHE}, the material showed a passive regime, followed by a transpassive regime between 0.0 V_{SHE} and 0.1 V_{SHE}. The current density in the passive regime was 34 $\mu A/cm^2$ at -0.3 V_{SHE} which was approximately 14 $\mu A/cm^2$ and 10 $\mu A/cm^2$ greater than the 2.5M and 5.0M NaOH solutions respectively. The current density in the second transpassive region was also significantly less than current densities in the NaOH solutions.

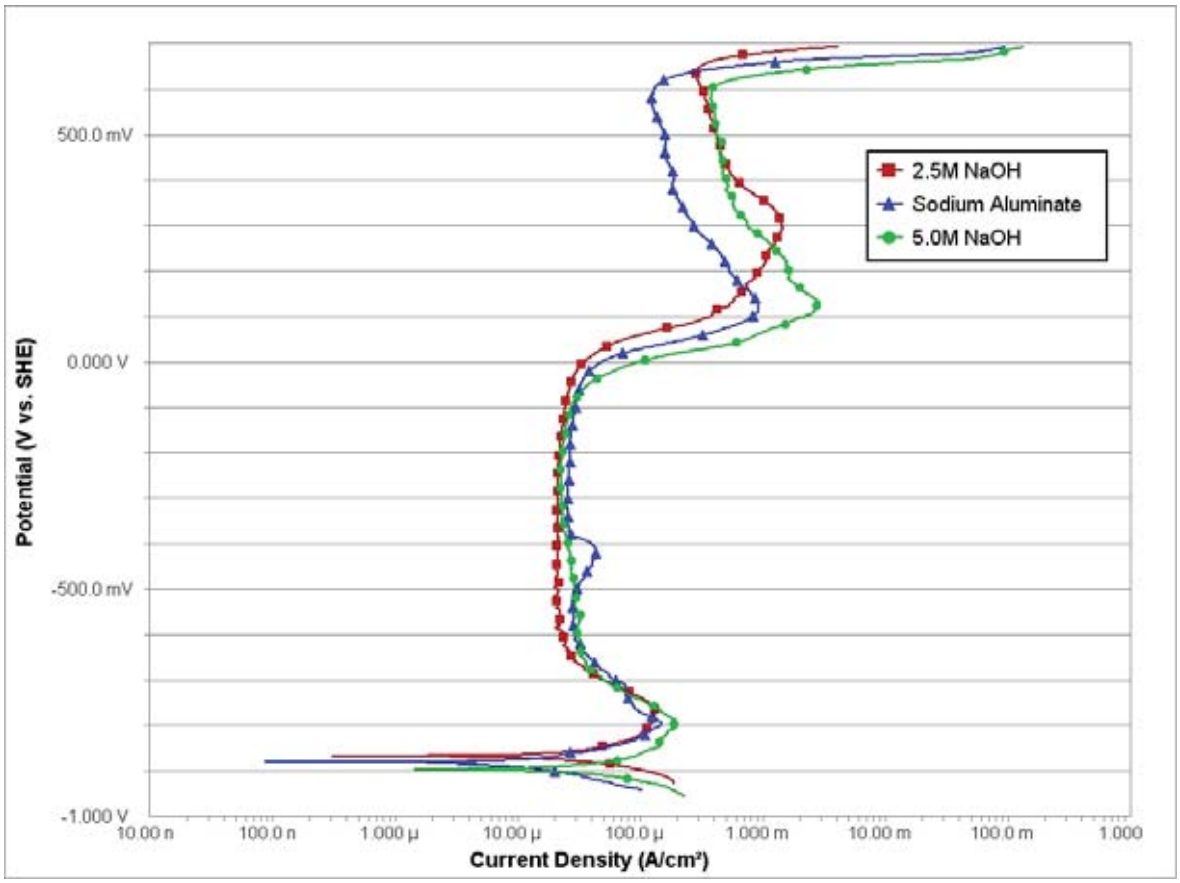

Figure 6.4: Typical anodic polarization curves for AISI 420 martensitic stainless steel in the quenched condition in deaerated 2.5M, 5.0M NaOH and sodium aluminate solution at 90°C and a potential scan rate of 1 mV/s.

Table 6.3: Potential and corrosion test results for AISI 420 martensitic stainless steel in sodium hydroxide and sodium aluminate solutions.

420 Stainless Steel	E_{corr} (V_{SHE})	I_{corr} ($\mu A/cm^2$)	$E_{critical}$ (V_{SHE})	$I_{critical}$ ($\mu A/cm^2$)	$I_{passive}$* ($\mu A/cm^2$)
2.5M NaOH	-0.867 ± 0.000	60.8 ± 5.9	-0.773 ± 0.004	139.8 ± 9.5	20.2 ± 1.6
5.0M NaOH	-0.898 ± 0.001	71.0 ± 8.1	-0.790 ± 0.001	187.2 ± 11.0	24.3 ± 2.3
Sodium Aluminate	-0.888 ± 0.001	8.1 ± 0.7	-0.799 ± 0.003	197.7 ± 37.2	33.6 ± 1.0
*I_{pass} at a potential of -0.306 V_{SHE} (-0.5 $V_{Red\ Rod}$)					

HypoA

The potentiodynamic anodic polarization curves for HypoA tested in 2.5M, 5.0M sodium hydroxide and sodium aluminate solutions at 90°C under deaerated conditions are shown in Figure 6.5. HypoA is a heat treated hypoeutectic high chromium white iron casting having a carbon and chromium content of 2.4 and 27 wt% respectively and a microstructure composed of eutectic M_7C_3 carbides and a transformed matrix of martensite and secondary $M_{23}C_6$ carbides. Potential and current densities for significant features of the polarization curves

along with the corrosion current density obtained from Tafel tests are summarized in Table 6.4.

The anodic polarization curves done in 2.5M and 5.0M NaOH solutions shows a small active dissolution regime between -0.92 V_{SHE} and -0.8 V_{SHE} with approximately linear Tafel regimes. Following the active dissolution region is a current peak at the critical potential of -0.8 V_{SHE} and -0.82 V_{SHE} for the 2.5M and 5.0M solutions respectively. Between potentials of -0.7 V_{SHE} and -0.2 V_{SHE} the material showed quasi passive like behaviour. In the quasi passive region there was a slight current peak for both the 2.5M and 5.0M curves at -0.6 V_{SHE} and -0.625 V_{SHE} respectively. Following the quasi passive region there was a current peak at -0.2 V_{SHE} which is somewhat analogous to a small transpassive like region. This was followed by a reduction in current density before transpassive behaviour at potentials greater than 0 V_{SHE}. The transpassive behaviour represented the onset of severe carbide corrosion.

The increase in NaOH solution concentration from 2.5M to 5.0M resulted in a shift in rest potential and critical potential in the negative direction by 40 mV and 25 mV respectively. The critical current density increased by 100 $\mu A/cm^2$ to 210 $\mu A/cm^2$ for the 2.5M and 5.0M NaOH solutions respectively. The increase in NaOH solution concentration also increased the current densities in the passive region by 20 to 25 $\mu A/cm^2$ for the 5.0M NaOH solution. The potential of the small transpassive like region and transpassive region were also found to decrease with increasing solution concentration.

The anodic polarization curve in sodium aluminate solution showed a larger active dissolution regime from the rest potential of -0.9 V_{SHE} to the critical potential at -0.8 V_{SHE} with linear Tafel behaviour. In the active to passive transition regime, between -0.8 V_{SHE} and -0.7 V_{SHE}, there was a small current peak that was not seen on any of the tests in NaOH solutions. The material exhibited passive behaviour from -0.7 V_{SHE} to -0.2 V_{SHE} but with a small current peak at -0.45 V_{SHE} which was also not seen on any of the polarization curves done in NaOH solutions. Above -0.2 V_{SHE}, the polarization curve characteristics were very similar to those for the sodium hydroxide solution. This involved a small current hump between -0.2 V_{SHE} and -0.5 V_{SHE} before transpassive behaviour and the onset of severe carbide corrosion.

Comparing the differences between the polarization curves done in sodium aluminate and NaOH solutions, it is seen that the rest potential in the sodium aluminate solution is in between the rest potentials for the 2.5M and 5.0M NaOH solutions. The corrosion current density in the sodium aluminate solution is only slightly greater than the 2.5M NaOH solution by approximately 1.5 $\mu A/cm^2$ but lower than the 5.0M NaOH solution by approximately 2 $\mu A/cm^2$. Like the rest potential, the critical potential falls between the critical potential for the 2.5M and 5.0M NaOH solutions. However, the critical dissolution current density in the sodium aluminate solution is significantly greater than the NaOH solution with a large increase of 750 $\mu A/cm^2$ compared with the 5.0M NaOH solution. The passive current densities in sodium aluminate solutions are very similar to the passive current densities in the

2.5M NaOH solution, with a increase of 14 μA/cm^2 at -0.3 V_{SHE} and less in other passive potential regions for the sodium aluminate solution.

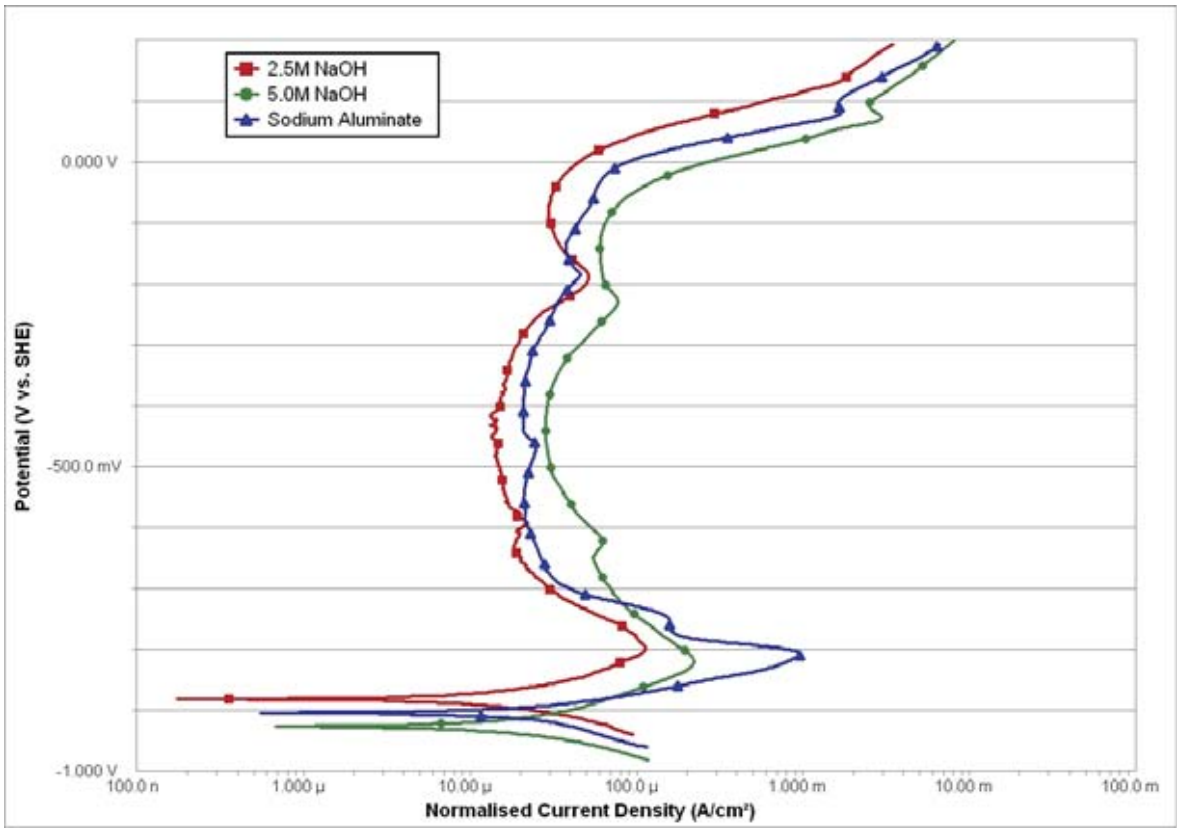

Figure 6.5: Typical anodic polarization curves for the HypoA casting in deaerated 2.5M, 5.0M NaOH and sodium aluminate solution at 90°C and a potential scan rate of 1 mV/s.

Table 6.4: Potential and corrosion test results for the HypoA casting in sodium hydroxide and sodium aluminate solutions. Results are averages of multiple polarization tests. Corrosion current results are averages of multiple Tafel tests.

HypoA	E_{corr} (V_{SHE})	I_{corr} ($\mu A/cm^2$)	$E_{critical}$ (V_{SHE})	$I_{critical}$ ($\mu A/cm^2$)	$I_{passive}^*$ ($\mu A/cm^2$)
2.5M NaOH	-0.882 ± 0.001	18.2 ± 0.5	-0.796 ± 0.005	110.6 ± 5.8	18.3 ± 0.5
5.0M NaOH	-0.924 ± 0.004	22.3 ± 1.4	-0.820 ± 0.001	211.9 ± 12.8	42.5 ± 1.3
Sodium Aluminate	-0.900 ± 0.005	19.9 ± 1.1	-0.804 ± 0.002	980.9 ± 42.0	25.1 ± 2.0
*I_{pass} at a potential of -0.306 V_{SHE} (-0.5 $V_{Red\ Rod}$)					

HyperA

The potentiodynamic anodic polarization curves for HyperA tested in 2.5M, 5.0M sodium hydroxide and sodium aluminate solutions at 90°C under deaerated conditions are shown in Figure 6.6. HyperA is a hypereutectic high chromium white iron castings having a carbon and chromium content of 4.5 and 34 wt% respectively. The microstructure of Hyper A consists of large primary M_7C_3 carbides in a matrix of mainly austenite, martensite and

some secondary carbide precipitation but is denuded of eutectic M_7C_3 carbides. Potential and current densities for significant features of the polarization curves along with the corrosion current density obtained from Tafel tests are summarized in Table 6.5.

The anodic polarization curves in 2.5M and 5.M NaOH shared many of the same characteristics. There was is a small active dissolution regime between -0.93 V_{SHE} and -0.75 V_{SHE} with approximately linear Tafel regimes. Following the active dissolution regime there is a current peak at the critical potential of -0.8 V_{SHE} and -0.75 V_{SHE} for the 2.5M and 5.0M NaOH solution respectively. This was followed by a region demonstrating quasi passive behaviour between -0.7 V_{SHE} and -0.3 V_{SHE} with a reasonable increase in potential before the minimum current density was reached. Above -0.3 V_{SHE} the curve showed transpassive behaviour, or a current peak, at -0.2 V_{SHE} and -0.25 V_{SHE} for the 2.5M and 5.0M NaOH solutions respectively. The transpassive like behaviour was closely followed by a region of secondary passivity before becoming completely transpassive at potentials greater than 0 V_{SHE} where severe carbide corrosion would occur.

The effect of increasing the NaOH concentration from 2.5M to 5.0M resulted in a shift in the corrosion potential and the critical potential in the negative direction by 30 mV. The corrosion current density was also found to have increased by 3 $\mu A/cm^2$ with an increase in NaOH concentration. The critical current density increased by 170 $\mu A/cm^2$ with an increase in solution concentration from 145 $\mu A/cm^2$ to 320 $\mu A/cm^2$ for the 2.5M and 5.0M NaOH solutions respectively. The increase in solution concentration increased the current densities in the quasi passive region by 100 $\mu A/cm^2$. The potential of the transpassive region, both primary and secondary, was found to more negative for the 5.0M solution.

The anodic polarization curve in sodium aluminate solution showed a large active dissolution regime with linear Tafel behaviour between -0.9 V_{SHE} and the critical potential at -0.87 V_{SHE}. In the active to passive transition, between about -0.87 V_{SHE} and -0.7 V_{SHE}, there was a small current peak that was not see on any of the polarization curves done in NaOH solutions. The material exhibited passive behaviour form -0.7 V_{SHE} and -0.3 V_{SHE} with a small current peak at -0.45 V_{SHE} which was also not detected in NaOH solutions. The behaviour above -0.3 V_{SHE} was transpassive like, with the onset of full transpassive behaviour above -0.1 V_{SHE} and the onset of carbide corrosion.

Comparing the differences in polarization curve behaviour between the NaOH solution and sodium aluminate solution, it is found that the rest potential and critical potential of the material in the sodium aluminate solution lies between that in 2.5M and 5.0M NaOH solutions. The corrosion current density was found to be less than in 5.0M NaOH but very similar to the corrosion current density in 2.5M NaOH being 12 $\mu A/cm^2$. However, the most significant difference is the increase in the active dissolution region and significant increase in critical current density in the sodium aluminate solution. The critical current density increased a further 550 $\mu A/cm^2$ compared with the 5.0M NaOH solution. The passive current densities are very similar to the passive current densities in the 2.5M NaOH solution.

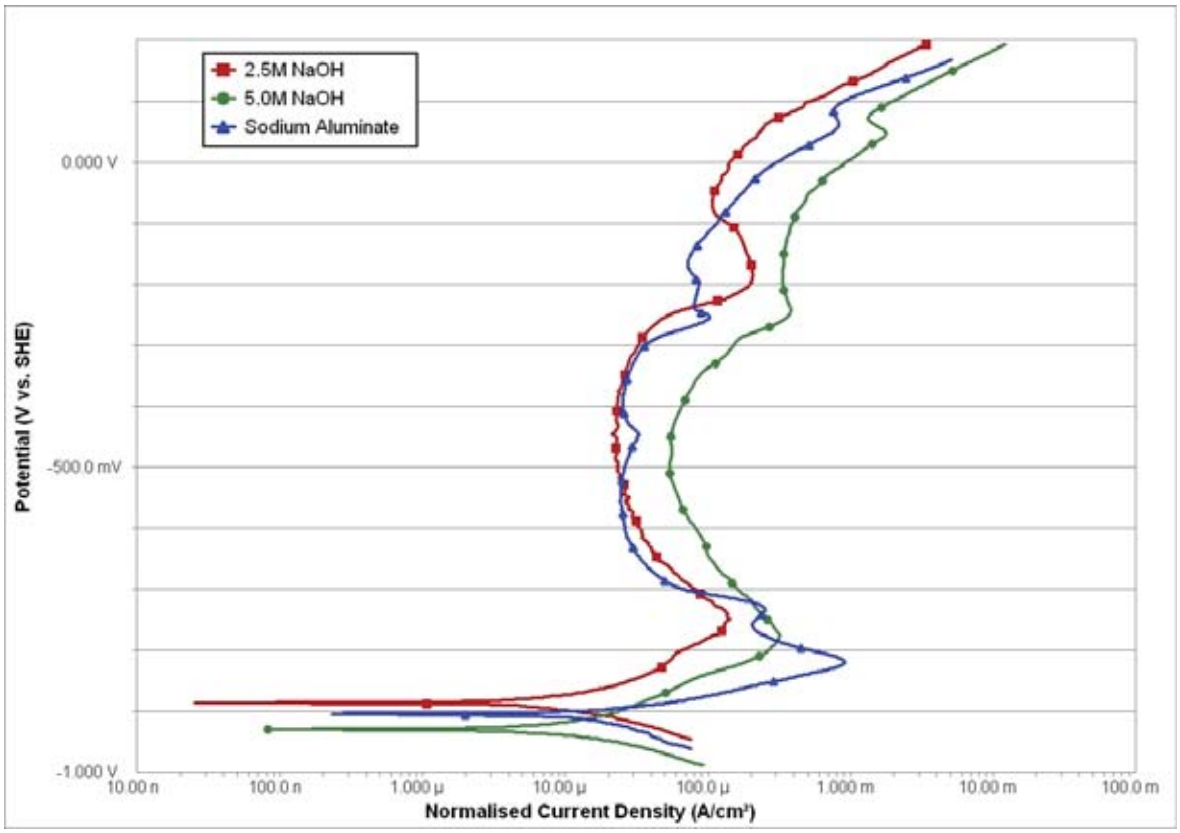

Figure 6.6: Typical anodic polarization curves for the HyperA casting in deaerated 2.5M, 5.0M NaOH and sodium aluminate solution at 90°C and a potential scan rate of 1 mV/s.

Table 6.5: Potential and corrosion values for the HyperA casting in NaOH and sodium aluminate solution. Results are averages of multiple polarization tests. Corrosion current results are averages of multiple Tafel tests.

HyperA	E_{corr} (V_{SHE})	I_{corr} ($\mu A/cm^2$)	$E_{critical}$ (V_{SHE})	$I_{critical}$ ($\mu A/cm^2$)	$I_{passive}^*$ ($\mu A/cm^2$)
2.5M NaOH	-0.889 ± 0.001	11.5 ± 0.4	-0.747 ± 0.008	144.5 ± 3.4	33.4 ± 4.6
5.0M NaOH	-0.931 ± 0.001	14.6 ± 1.2	-0.773 ± 0.006	319.2 ± 3.0	132.8 ± 15.8
Sodium Aluminate	-0.906 ± 0.003	12.0 ± 1.6	-0.819 ± 0.004	872.2 ± 70.5	36.9 ± 2.4
*I_{pass} at a potential of -0.306 V_{SHE} (-0.5 $V_{Red\ Rod}$)					

HyperEXP

The potentiodynamic anodic polarization curves for HyperEXP tested in 2.5M, 5.0M sodium hydroxide and sodium aluminate solution at 90°C under deaerated conditions are shown in Figure 6.7. HyperEXP is a hypereutectic high chromium white iron castings having a carbon and chromium content of 4.5 and 25 wt% respectively. The microstructure of HyperEXP consists of large primary and eutectic M_7C_3 carbides in a matrix of austenite with limited secondary carbide precipitation. Potential and current densities for significant features of the polarization curves along with the corrosion current density obtained from Tafel

tests are summarized in Table 6.6.

The anodic polarization curves in 2.5M and 5.0M NaOH solutions shared many of the same characteristics. There is a very small active dissolution region between -0.91 V_{SHE} and -0.8 V_{SHE}. Following active dissolution is a broad current peak between -0.85 V_{SHE} and -0.8 V_{SHE} which is characteristic of the active to passive transition at the critical potential. Following the critical potential is a reduction in current density before an approximately linear increase in current density and a significant second current peak between -0.65 V_{SHE} and -0.6 V_{SHE}. Following the second current peak is a reduction in current density between -0.6 V_{SHE} and 0 V_{SHE} which remains approximately linear with increasing potential with the exception of a current peak at -0.22 V_{SHE} for the 2.5M NaOH case. At potentials greater than 0 V_{SHE} the material experience transpassive behaviour and severe dissolution of the carbides.

Increasing the sodium hydroxide concentration form 2.5M to 5.0M caused the rest potential and the critical potential to shift in the negative direction by 40 mV. The corrosion current was found to increase by 3 $\mu A/cm^2$ from 21 $\mu A/cm^2$ to 24 $\mu A/cm^2$ for the 2.5M and 5.0M NaOH solutions respectively. The critical current density was also found to increase by 24 $\mu A/cm^2$ with increasing NaOH solution concentration. The potential of the second current peak was shifted in the negative direction but had a higher current density compared with the 2.5M NaOH solution. The transpassive potential was also found to slightly decrease with an increase in potential.

The anodic polarization curve for HyperEXP in sodium aluminate solution showed a large active dissolution regime with linear Tafel behaviour between -0.9 V_{SHE} and the critical potential at -0.79 V_{SHE}. Following the critical potential was active to passive behaviour between -0.79 V_{SHE} and about -0.75 V_{SHE}. At about -0.75 V_{SHE} there were some small current peaks which was followed by a gradual increase in current density and a large secondary current peak at about -0.62 V_{SHE}. This secondary current peak was followed by a reduction in current density between -0.5 V_{SHE} and 0 V_{SHE}. In this region, the polarization behaviour did not demonstrate ideal passive behaviour but consisted of a number of regions that varied slightly in current density over the potential range. At potentials greater than 0 V_{SHE} the material demonstrated transpassive behaviour and the dissolution of the carbides.

Comparing the differences in polarization curve behaviour in the NaOH and sodium aluminate solutions, it is found that the rest potential in sodium aluminate solution lies between the rest potential in 2.5M and 5.0M NaOH. The corrosion current density is reduced in the sodium aluminate solution by 7 $\mu A/cm^2$ compared with the 2.5M NaOH condition. However, the most significant difference is the increase in the active dissolution regime and critical current density in the sodium aluminate solution. The critical current density increased to 790 $\mu A/cm^2$which is an increase of over 750 $\mu A/cm^2$compared with the 5.0M NaOH. Following the active to passive transition in the sodium aluminate solution, the polarization curve characteristics were very similar for the three different solutions. All the polarization curves showed the secondary current peak between -0.62 V_{SHE} and -0.6 V_{SHE} followed by

what can be described as passive like behaviour up to 0 V_{SHE}. The current densities in the passive like regime and transpassive regime above 0 V_{SHE}in sodium aluminate solution were generally between the current densities in the 2.5M and 5.0M NaOH solutions.

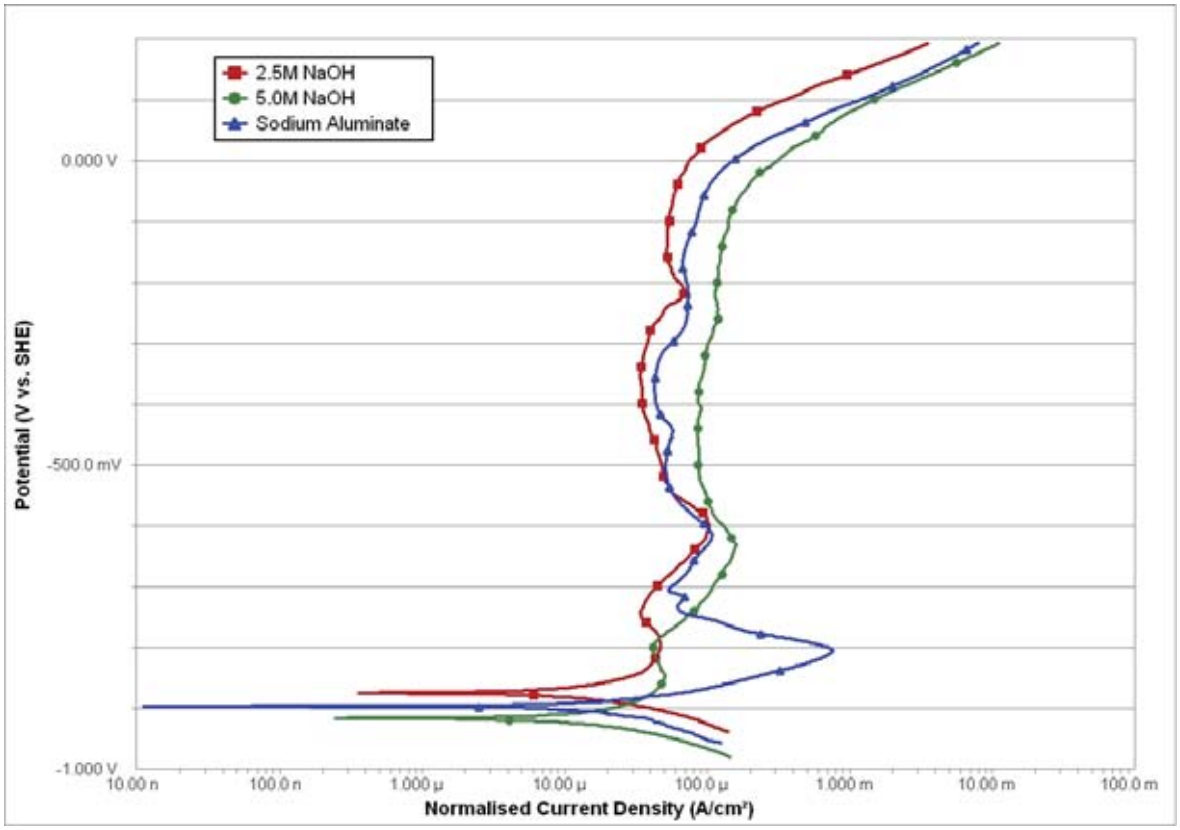

Figure 6.7: Typical anodic polarization curves for the HyperEXP casting in deaerated NaOH and sodium aluminate solution at 90°C and a potential scan rate of 1 mV/s.

Table 6.6: Potential and corrosion current values for the HyperEXP casting in NaOH and sodium aluminate solution. Results are averages of multiple polarization tests. Corrosion current results are averages of multiple Tafel tests.

HyperEXP	E_{corr} (V_{SHE})	I_{corr} ($\mu A/cm^2$)	$E_{critical}$ (V_{SHE})	$I_{critical}$ ($\mu A/cm^2$)	$I_{passive}$* ($\mu A/cm^2$)
2.5M NaOH	-0.876 ± 7E-04	21.0 ± 1.3	-0.797 ± 0.004	52.4 ± 7.7	37.7 ± 0.8
5.0M NaOH	-0.913 ± 0.008	24.0 ± 4.5	-0.840 ± 0.018	106.6 ± 78.9	101.5 ± 2.0
Sodium Aluminate	-0.896 ± 0.001	13.4 ± 0.8	-0.805 ± 0.001	787.8 ± 39.2	51.1 ± 2.2
*I_{pass} at a potential of -0.306 V_{SHE} (-0.5 $V_{Red\ Rod}$)					

6.2.2.3 Summary

Corrosion tests involved potentiodynamic polarization tests in 2.5M, 5.0M NaOH solutions and a sodium aluminate solution. The sodium aluminate solution had a similar free and total caustic to the sodium hydroxide solutions. The materials tested included three high

chromium white iron castings of varying chemical compositions and microstructures. These were a hypoeutectic heat treated alloy (HypoA), a hypereutectic alloy as-cast (HyperA) and a hypereutectic alloy having higher than normal nickel and manganese alloying additions (Hyper EXP). A plain low carbon steel (AS1163: C350LO) and a AISI 420 martensitic stainless in the hardened condition were also corrosion tested for comparison with the high chromium white irons.

The polarization results for all the materials investigated in 2.5M, 5.0M NaOH solutions and the sodium aluminate solution exhibited active passive behaviour when polarized in the anodic direction. An increase in solution concentration from 2.5M to 5.0M NaOH shifted the corrosion potential, the critical potential and the transpassive potential in the negative direction for all materials. As a result of the increased solution concentration, the corrosion current density, the critical current density and the passive current density increased for all materials. At transpassive potentials greater than 0.0 V_{SHE} the carbide began to corrode.

Corrosion polarization results in sodium aluminate solution resulted in active-passive behaviour for all the materials investigated. The corrosion potential for all materials in the sodium aluminate solution was between the corrosion potential in the 2.5 and 5.0M NaOH solutions. For the low carbon steel and the AISI 420 martensitic stainless steel, the corrosion current density was found to significantly decrease compared with the NaOH solutions, while for the high chromium white irons the corrosion current density was only found to decrease slightly compared with the 5.0M NaOH solution. The critical current density in sodium aluminate solution was found to significantly decrease for the low carbon steel, but for the AISI 420 stainless steel was comparable with the 5.0M NaOH solution. However, in the 5.0M NaOH solution, the critical current density was found to increase by an order of magnitude compared with the 2.5M NaOH solution for the three high chromium white iron castings investigated. The passive current densities for the high chromium white irons in sodium aluminate solution were similar to the 2.5M NaOH solution.

6.2.3 The Effect of Microstructure

This section focuses on gaining a better understanding of how microstructural features, in particular, the matrix microstructure effects the corrosion behaviour of high chromium white iron alloys in sodium aluminate solutions.

6.2.3.1 Materials Investigated

The materials investigated included the three high chromium white irons, HypoA, HyperA and HyperEXP, previously covered in Section 6.2.2. An additional high chromium white iron, EutecticA, was also included that has a lower chromium content compared with the other alloys investigated. Two heat treatments were done on each of the high chromium white irons to provide distinct microstructural variations. A destabilization heat treatment was done at 950°C for 6 hours followed by air cooling, which caused the precipitation of secondary carbides and possible transformation to martensite. The other heat treatment used was a normalizing heat treatments at 1150°C for 6 hours followed by air cooling, which generally resulted in the matrix to being composed entirely of austenite. HyperA and HyperEXP were also tested in the as-cast condition, as these alloys were suitable for use in a service environment in the as-cast condition. The details of the heat treatments and detailed metallurgical analysis can be found in Section 5. However, a brief summary of the microstructures for the materials investigated is given in the respective section discussing the results. A summary of the bulk chemical compositions, chromium to carbon ratio and carbide volume fraction (CVF) is given in Table 6.7.

Table 6.7: Bulk chemical compositions, chromium to carbon ratio and carbide volume fraction (CVF) for the investigated high chromium white iron alloys.

Material	Bulk Chemical Composition wt%							Cr/C ratio	CVF*
	C	Si	Cr	Mn	Fe	Ni	Mo		
EutecticA Casting	3.6	0.53	17.8	0.65	75.9	0.10	1.35	4.9	38.6 ± 3.1
HypoA Casting	2.4	0.97	26.6	0.69	68.9	0.06	0.02	11.1	25.8 ± 1.1
HyperA Casting	4.5	0.49	34.0	1.9	57.7	0.12	0.95	7.6	51.9 ± 2.5
HyperEXP Casting	4.51	0.45	25.0	4.6	60.2	4.8	0.33	5.5	49.9 ± 4.3

*Carbide volume fraction of primary and or eutectic M_7C_3 carbides only

6.2.3.2 Polarization and Tafel Test Results

EutecticA

Material EutecticA is a high chromium white iron conforming to AS 2027/CrMo 15 3 (ASTM A532 IIB 15% Cr-Mo). In the as-cast condition, the microstructure of EutecticA consists of the eutectic composition of eutectic M_7C_3 carbides in a matrix of austenite and

pearlite. This particular material would not be used in the as-cast condition due to the presence of pearlite and is heat treated to increase the hardness and improve wear resistance.

Two heat treatments, which were done on the as-cast alloy, consisted of a destabilization heat treatment at 950°C for 6 hours followed by air cooling and a normalizing heat treatment at 1150°C for 6 hours followed by air cooling. The resulting microstructure after the destabilization heat treatment, Figure 6.8(a), consists of eutectic M_7C_3 carbides in a matrix containing secondary $M_{23}C_6$ carbides, martensite and retained austenite. The resulting hardness after the destabilization heat treatment was 870 HV.

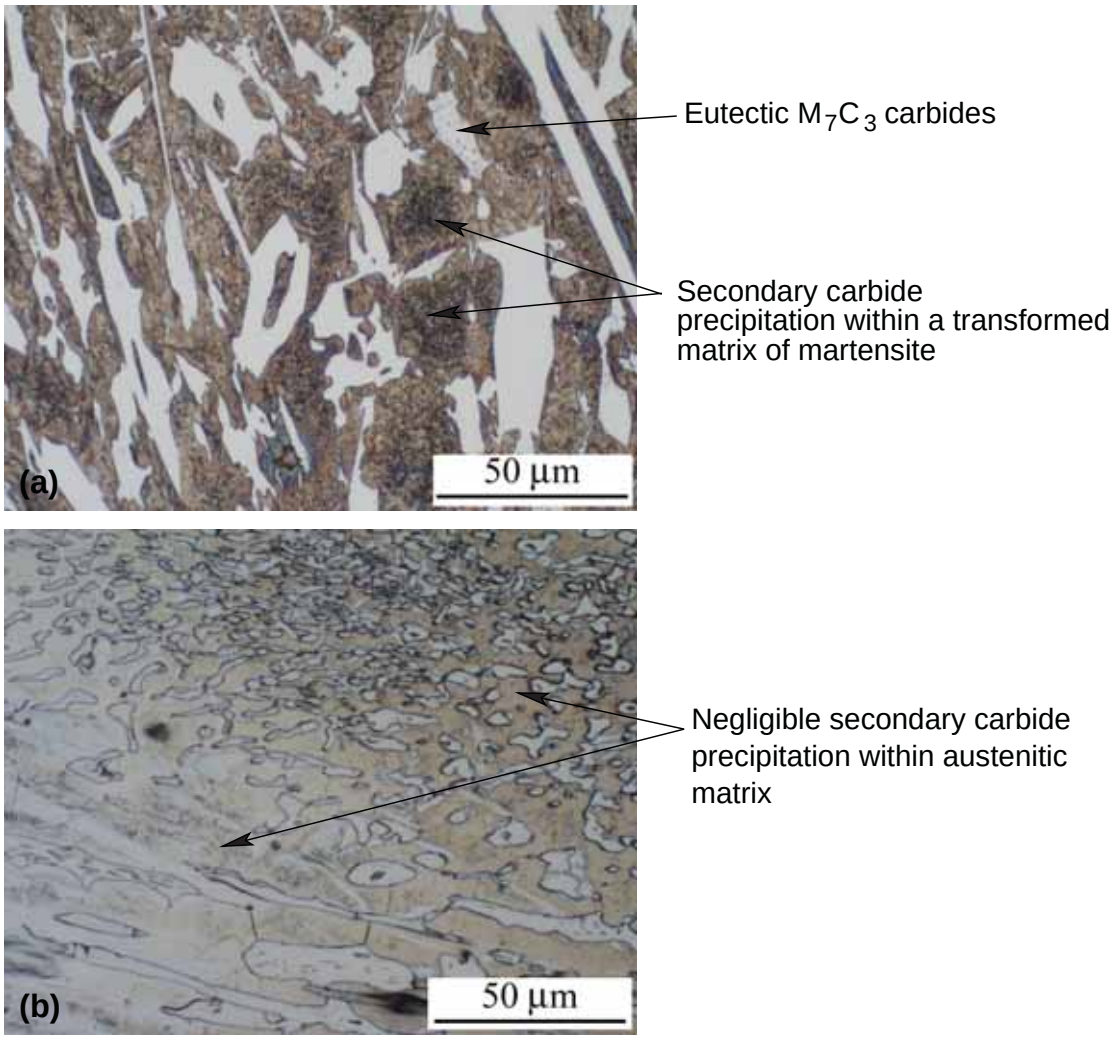

Figure 6.8: Optical light micrographs of the EutecticA casting after heat treatments. (a) Microstructure after destabilization heat treatment at 950°C for 6 hours and air cooling. (b) Microstructure after normalizing heat treatment at 1150°C for 6 hours and air cooling.

The normalizing heat treatment done at 1150°C for 6 hours followed by air cooling resulted in a microstructure of eutectic M_7C_3 carbides in a matrix consisting primarily of austenite, 6.8(b). There was a limited amount of secondary carbide precipitation and some martensite laths were also detected. The hardness after the normalizing heat treatment was 500 HV. The carbon and chromium content of the matrix in the normalized condition is sightly greater

than the matrix in the destabilized condition.

The anodic polarization curves in deaerated sodium aluminate solution at 90°C at a potential scan rate of 1 mV/s for the destabilized and normalized microstructures are shown in Figure 6.9. Both of the polarization curves are similar, having a large active dissolution regime with linear Tafel behaviour between -0.9 V_{SHE} and -0.8 V_{SHE}. The current peaked at the critical potential of -0.8 V_{SHE} which was followed by the active to passive transition with further increase in potential. The materials showed passive like behaviour between -0.7 V_{SHE} and 0 V_{SHE} for the destabilized microstructure and between -0.7 V_{SHE} and -0.3 V_{SHE} for the normalized microstructure. Both materials have a small current peak within the passive region at -0.45 V_{SHE}. For the destabilized microstructure, transpassive behavior did not occur until a potential greater than 0 V_{SHE}. However, for the normalized microstructure, the transition to transpassive behaviour was not as abrupt and appeared as a gradual increase in current density from -0.3 V_{SHE}. In both cases, transpassive behaviour resulted in the corrosion of the eutectic M_7C_3 carbides.

The quantitative differences in the anodic polarization behaviour of the destabilized and normalized microstructures are summarized in Table 6.8. The differences include a shift in potential in the negative direction by approximately 14 mV for the destabilized microstructure compared with the normalized microstructure. The corrosion current density of the destabilized microstructure was also 2 $\mu A/cm^2$ greater than the normalized condition. The critical current density of the destabilized microstructure was also found to be greater by approximately 220 $\mu A/cm^2$ than the normalized condition. In the passive potential regime between -0.7 V_{SHE} and -0.55 V_{SHE}, the passive current density of the destabilized microstructure was slightly less than the passive current density of the normalized microstructure. Between -0.55 V_{SHE} and -0.2 V_{SHE}, the passive current density of the destabilized microstructure was greater than the passive current density of the normalized microstructure.

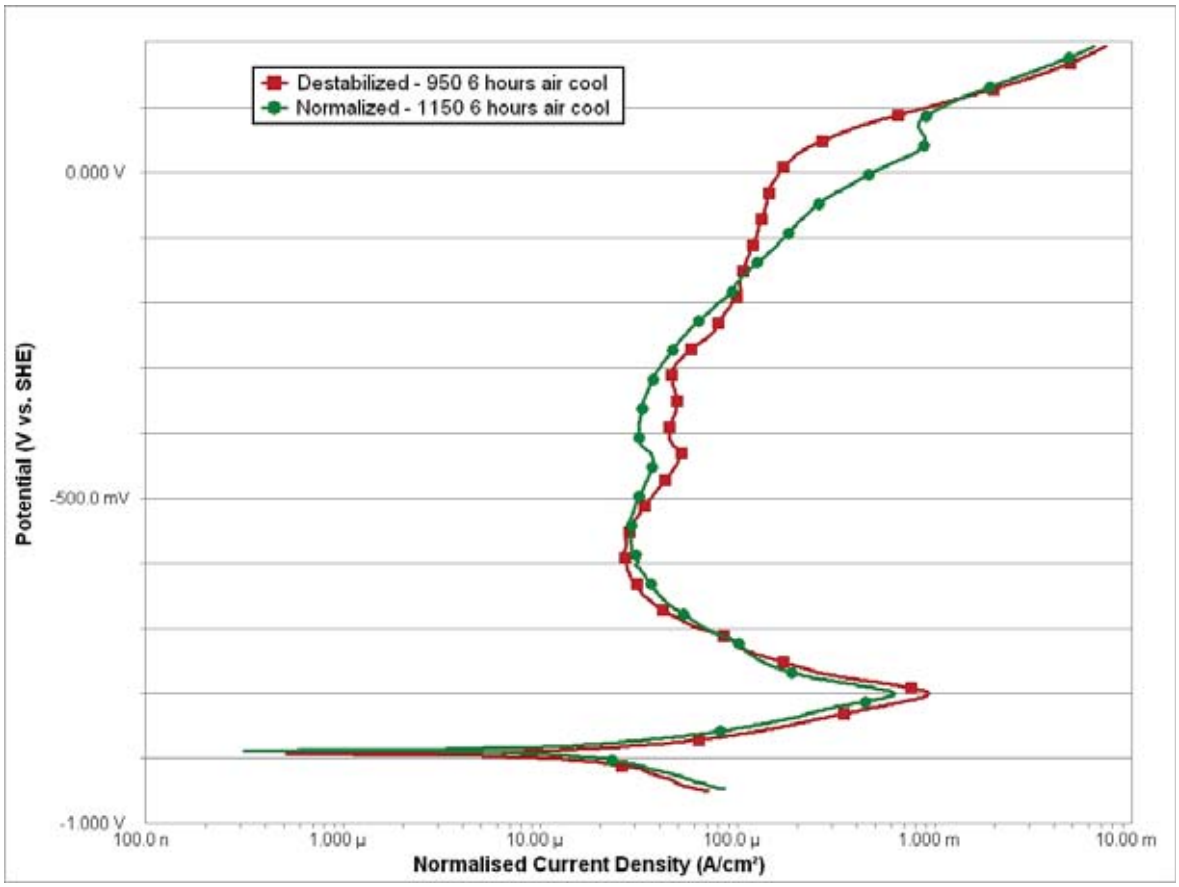

Figure 6.9: Typical anodic polarization curves for the EutecticA casting in deaerated sodium aluminate solution at 90°C and a potential scan rate of 1 mV/s for the destabilized and normalized heat treated condition.

Table 6.8: Potential and corrosion values for EutecticA casting in the destabilized and normalized condition tested in sodium aluminate solution.

EutecticA	E_{corr} (V_{SHE})	I_{corr} ($\mu A/cm^2$)	$E_{critical}$ (V_{SHE})	$I_{critical}$ ($\mu A/cm^2$)	$I_{passive}$* ($\mu A/cm^2$)
950°C for 6 hours "Destabilized"	-0.895 ± 0.002	10.6 ± 0.5	-0.797 ± 0.002	808.8 ± 107.7	46.9 ± 0.9
1150°C for 6 hours "Normalized"	-0.887 ± 0.008	8.6 ± 0.6	-0.799 ± 0.004	514.0 ± 139.2	35.2 ± 3.3

*I_{pass} at a potential of -0.306 V_{SHE} (-0.5 $V_{Red\ Rod}$)

HypoA

Material HypoA is a high chromium white iron casting conforming to AS 2027/Cr 27 LC (ASTM A532 IIIA 25% Cr) that was removed from an ex-service alumina slurry pump impeller. This material was received in the heat treated condition and is of the hypoeutectic composition. The microstructure in the as-received condition, Figure 6.10(a), consists of transformed primary dendrites of austenite and a eutectic of M_7C_3carbides. The material has undergone a destabilization heat treatment to transform the primary austenite dendrites and eutectic matrix to a mixture of secondary carbides, martensite and retained austenite. The destabilized material may also have undergone a temper heat treatment. The hardness of the as-received alloy having the microstructure shown in Figure6.10(a) was 620 HV.

The as-received alloy was given a normalizing heat treatment at 1150°C for 6 hours followed by air cooling. The resulting microstructure after the normalizing heat treatment, shown in Figure 6.10(b), is a matrix consisting almost entirely of austenite. There was only a limited amount of secondary carbide detected. The matrix of the normalized sample, Figure 6.10(b), is higher in carbon and chromium than the matrix of the as-received-destabilized condition shown in Figure 6.10(a).

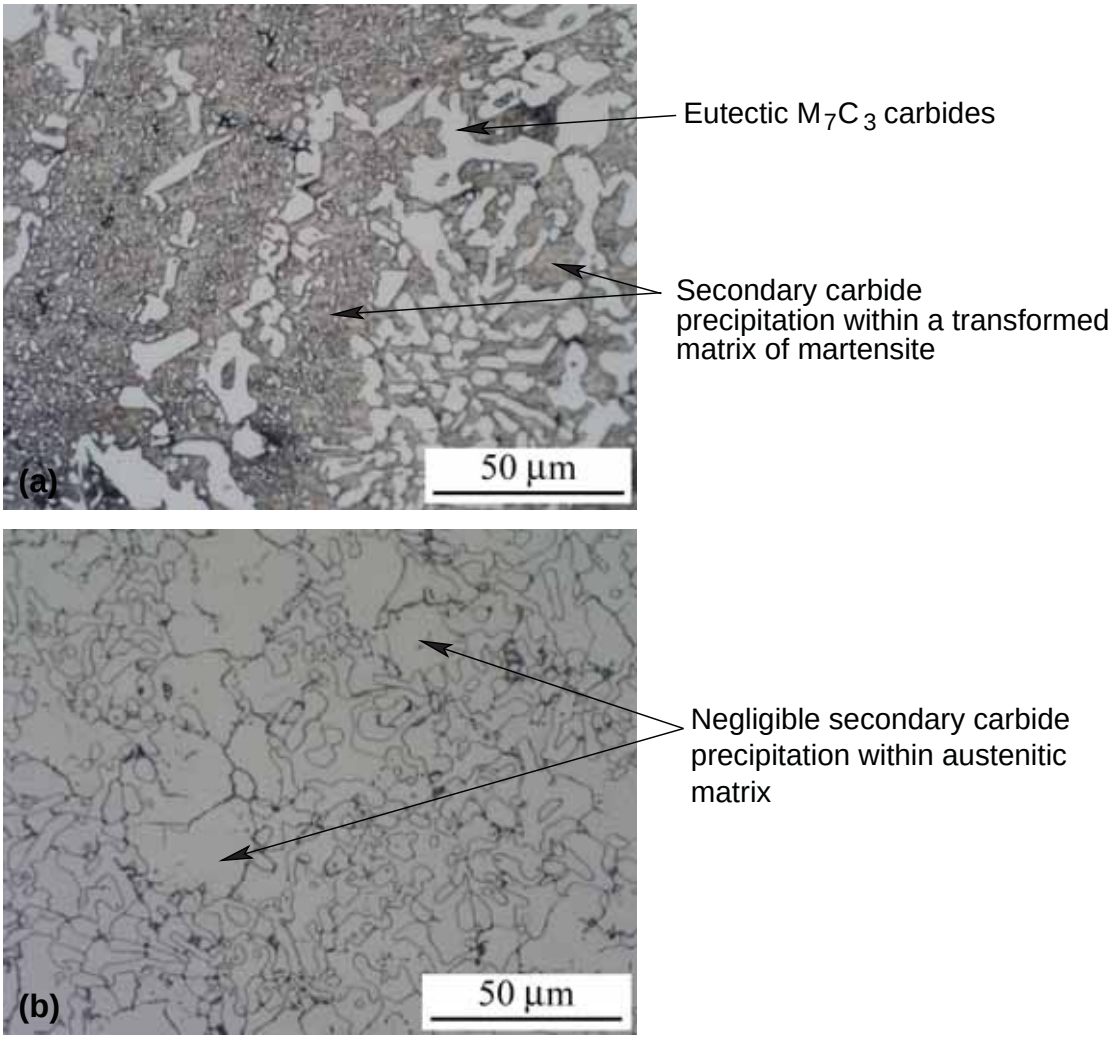

Figure 6.10: Optical light micrographs of the HypoA casting in the as-received and after heat treatment. (a) Microstructure as-received which has already undergone a destabilization heat treatment. (b) Microstructure after normalizing heat treatment at 1150°C for 6 hours and air cooling .

The anodic polarization curves in deaerated sodium aluminate solution at 90°C at a scan rate of 1 mV/s for HypoA in the destabilized and normalized condition are shown in Figure 6.11. Both of the anodic polarization curves for the destabilized and normalized condition were very similar. The polarization curves showed an active dissolution region between -0.9 V_{SHE} and the critical potential where the current peaked at -0.8 V_{SHE}. Both the materials underwent active to passive behaviour between potentials of -0.8 V_{SHE} and -0.7 V_{SHE} before passive behaviour in the potential range between -0.7 V_{SHE} and 0 V_{SHE}. Both the materials

showed a similar current peak in the passive region at approximately -0.45 V_{SHE} and an additional small current peak at -0.2 V_{SHE} for the destabilized HypoA. Above 0 $V_{SHE}$the materials showed transpassive behaviour and the corrosion of the eutectic M_7C_3 carbide network.

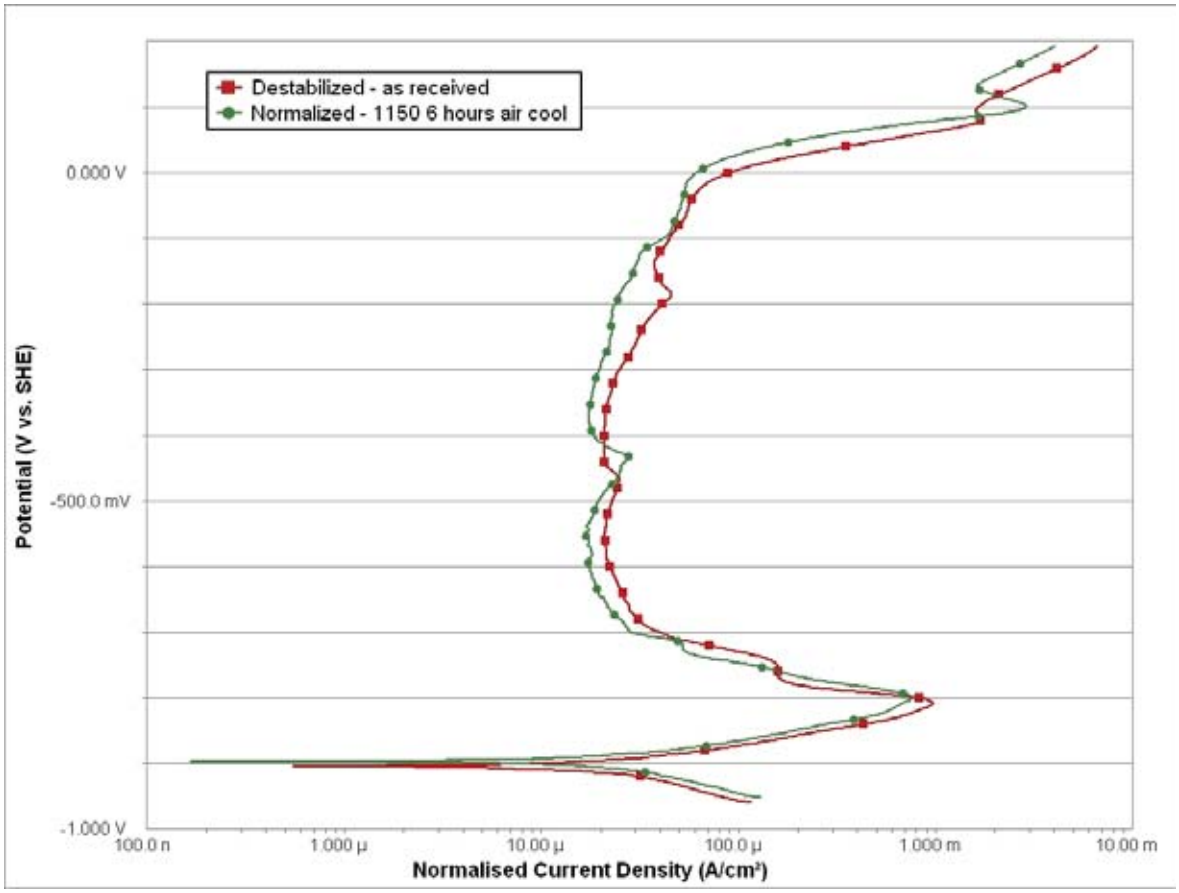

Figure 6.11: Typical anodic polarization curves for HypoA casting in deaerated sodium aluminate solution at 90°C and at a potential scan rate of 1 mV/s for the destabilized and normalized condition.

The quantitative differences in the anodic polarization behaviour of the destabilized and normalized microstructures are summarized in Table 6.9. The destabilized microstructure had a rest potential 13 mV more negative than the normalized microstructure. The corrosion current densities for both of the microstructures were very similar with the averaged current density being approximately 1 μA/cm^2 greater for the destabilized microstructure. Similarly to the rest potential, the critical potential of the destabilized microstructure was less than the normalized microstructure by 8 mV. The critical current density for the destabilized microstructure was 120 μA/cm^2 greater than the normalized microstructure. The passive current densities for the destabilized microstructure, except for a cross over region at -0.45 V_{SHE}, were always greater than the passive current densities for the normalized microstructure by 3 to 6 μA/cm^2.

Table 6.9: Potential and corrosion values for HypoA in the destabilized and normalized condition tested in sodium aluminate solution.

HypoA	E_{corr} (V_{SHE})	I_{corr} ($\mu A/cm^2$)	$E_{critical}$ (V_{SHE})	$I_{critical}$ ($\mu A/cm^2$)	$I_{passive}$* ($\mu A/cm^2$)
As Received	-0.900 ± 0.005	19.9 ± 1.1	-0.804 ± 0.002	980.9 ± 42.0	25.1 ± 2.0
1150°C for 6 hours "Normalized"	-0.895 ± 0.003	18.8 ± 2.5	-0.796 ± 0.004	651.0 ± 166.7	20.3 ± 1.4
*I_{pass} at a potential of -0.306 V_{SHE} (-0.5 $V_{Red\ Rod}$)					

HyperA

HyperA is a hypereutectic high chromium white iron conforming to AS 2027/Cr 35. The material was sectioned from a ex-service alumina slurry pump impeller and was reportedly in the as-cast condition. The as-cast microstructure of the alloy, Figure 6.12(a), consists of large primary M_7C_3 carbides within a matrix that is composed largely of austenite. The as-cast matrix also contains fine secondary carbide precipitation and a band of martensite surrounding the primary carbides.

The microstructure after the destabilization heat treatment of the as-cast alloy at 950°C for 6 hours followed by air cooling is shown in Figure 6.12(b). The destabilized matrix microstructure consists of a large proportion of precipitated secondary carbide in a transformed matrix of martensite and some retained austenite. When the as-cast alloy was heat treated at 1150°C for 6 hours and air cooled, the matrix microstructure consisted almost entirely of austenite with negligible secondary carbide precipitation, Figure 6.12(c). The matrix microstructure of the normalized condition is slightly higher in chromium and carbon than the as-cast and destabilized condition.

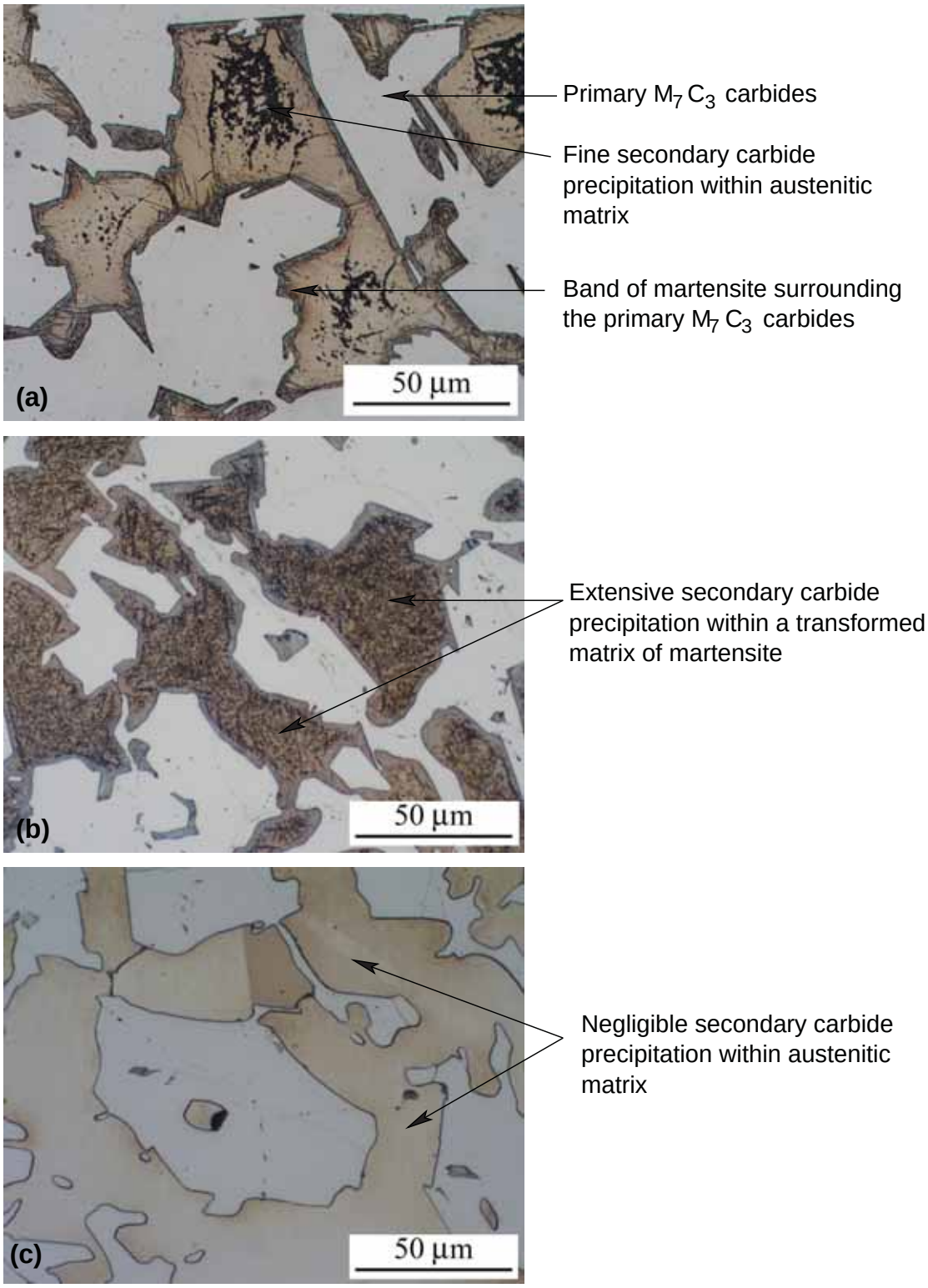

Figure 6.12: Optical light micrographs of the HyperA casting. (a) Microstructure in the as-cast condition. (b) Microstructure after a destabilization heat treatment at 950°C for 6 hours and air cooling. (c) Microstructure after a normalizing heat treatment at 1150°C for 6 hours and air cooling.

The anodic polarization curves in deaerated sodium aluminate solution at 90°C at a scan rate of 1 mV/s for HyperA in the as-cast, destabilized, and normalized condition is shown in Figure 6.13. All the microstructural variations tested showed an active dissolution regime with

approximately linear Tafel behavior between -0.9 V_{SHE} and the critical potential at -0.8 V_{SHE}. Following the critical potential, the materials demonstrated active to passive behaviour between -0.8 V_{SHE} and -0.7 V_{SHE}. However, the as-cast and destabilized microstructures also showed a small current peak in the active to passive transition at -0.75 V_{SHE} which was not a significant feature on the polarization curve for the normalized microstructure. Between -0.7 V_{SHE} and -0.3 V_{SHE}, all the microstructural variations demonstrated passive behaviour with a consistent current peak at -0.45 V_{SHE}. Above -0.3 V_{SHE}, the current density started to gradually increase for all of the variations investigated before transpassive behaviour above 0 V_{SHE}.

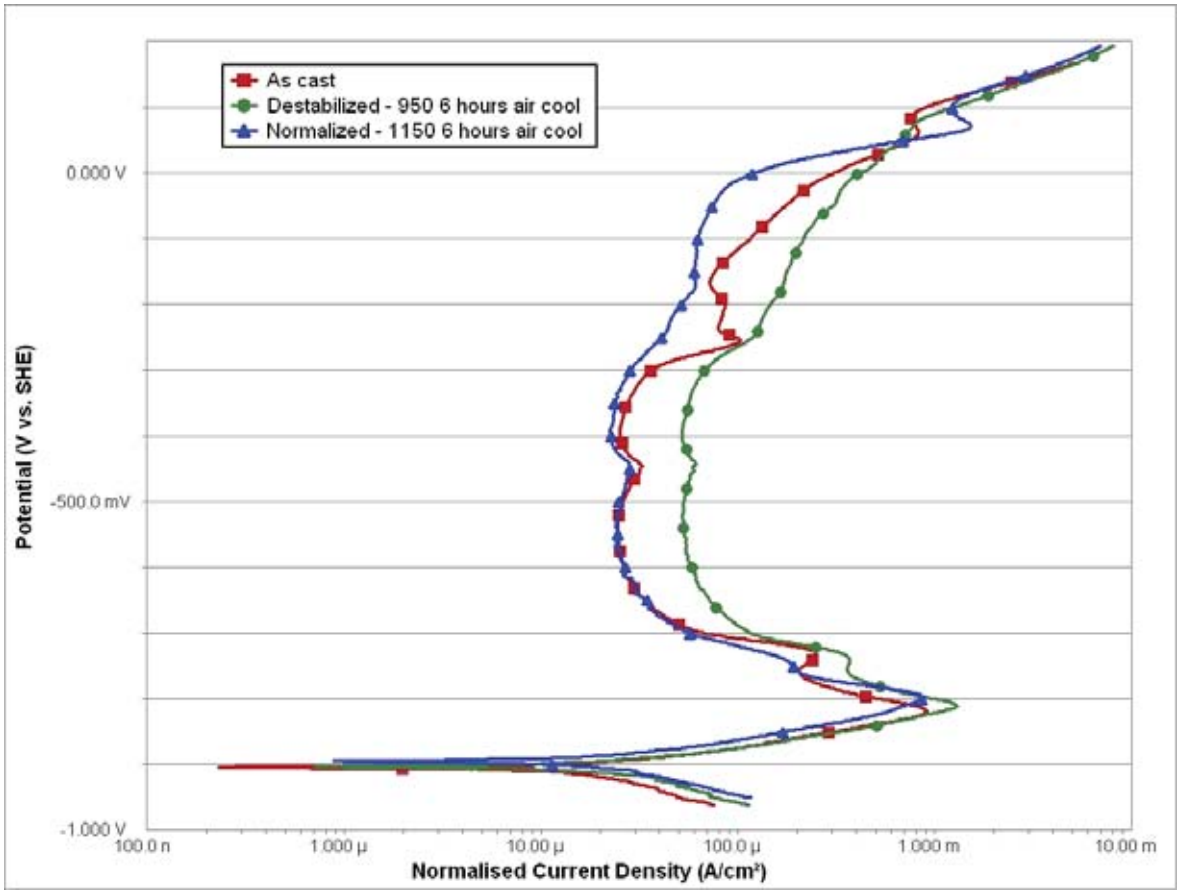

Figure 6.13: Typical anodic polarization curves for the HyperA casting in deaerated sodium aluminate solution at 90°C and a potential scan rate of 1 mV/s for the as-cast, destabilized and normalized heat treated condition.

The quantitative differences in the anodic polarization behaviour of the destabilized and normalized microstructures are summarized in Table 6.10. The variation in corrosion potentials for the as-cast and destabilized microstructures did not vary significantly with the difference being less than 1 mV. However, the corrosion potential of the normalized microstructure increased by 10 mV. The corrosion current densities varied for the three different microstructures investigated. The as-cast microstructure had the lowest corrosion current density followed closely by the normalized microstructure which had a corrosion current density of 3.8 μA/cm^2 greater. The corrosion current of the destabilized microstructure was double that

of the as-cast microstructure and 7.8 μA/cm^2 greater than the normalized microstructure. The variation in the critical potential was 14 mV with the as-cast microstructure having the lowest potential and the normalized microstructure having the higher potential. The critical current densities were found to vary depending on the microstructure. The normalized microstructure had the lowest critical current density of 380 μA/cm^2 which was 110 μA/cm^2 and 210 μA/cm^2 less than the as-cast and destabilized microstructures respectively. The variation in passive current densities for the as-cast and normalized microstructures was not significant in the potential range of -0.7 V_{SHE} to about -0.4 V_{SHE}. Above -0.4 V_{SHE}, the current density was greater for the as-cast microstructure than the normalized microstructure. The passive current densities for the destabilized microstructure was always greater than the as-cast and normalized microstructures.

Table 6.10: Potential and corrosion values for HyperA casting in the as-cast, destabilized and normalized condition in sodium aluminate solution.

HyperA	E_{corr} (V_{SHE})	I_{corr} ($\mu A/cm^2$)	$E_{critical}$ (V_{SHE})	$I_{critical}$ ($\mu A/cm^2$)	$I_{passive}$* ($\mu A/cm^2$)
As Received	-0.906 ± 0.003	12.0 ± 1.6	-0.819 ± 0.004	872.2 ± 70.5	36.9 ± 2.4
950°C for 6 hours "Destabilized"	-0.903 ± 0.001	22.0 ± 2.0	-0.809 ± 0.000	1212.5 ± 105.4	66.0 ± 1.4
1150°C for 6 hours "Normalized"	-0.896 ± 0.002	14.8 ± 1.0	-0.803 ± 0.004	904.2 ± 63.2	25.8 ± 2.7
*I_{pass} at a potential of -0.306 V_{SHE} (-0.5 $V_{Red\ Rod}$)					

HyperEXP

HyperEXP is an experimental hypereutectic high chromium white iron casting that has improved toughness characteristics. The experimental alloy does not conform to any standards due to the unique alloying additions of manganese and nickel. The three microstructural variations investigated were the as-cast, the destabilized and normalized heat treated conditions. The as-cast microstructure consists of large primary M_7C_3 carbides and eutectic M_7C_3 carbides in a matrix containing a very fine dispersion of secondary carbides and austenitic, Figure 6.14(a). The destabilized microstructure consists of primary M_7C_3 carbides and eutectic M_7C_3 carbides in a matrix that contains a considerable number of secondary carbides and austenite, 6.14(b). The normalized microstructure consists of primary M_7C_3 carbides and eutectic M_7C_3 carbides in a matrix that contains some secondary carbides and austenite, 6.14(c). This material is unique such that it can not be hardened by conventional destabilization heat treatments and the matrix always remains austenitic. Thus the differences between the as-cast, destabilized and normalized condition is the proportion and size of the secondary carbides, which would also slightly vary the chromium and carbon composition of the matrix austenite.

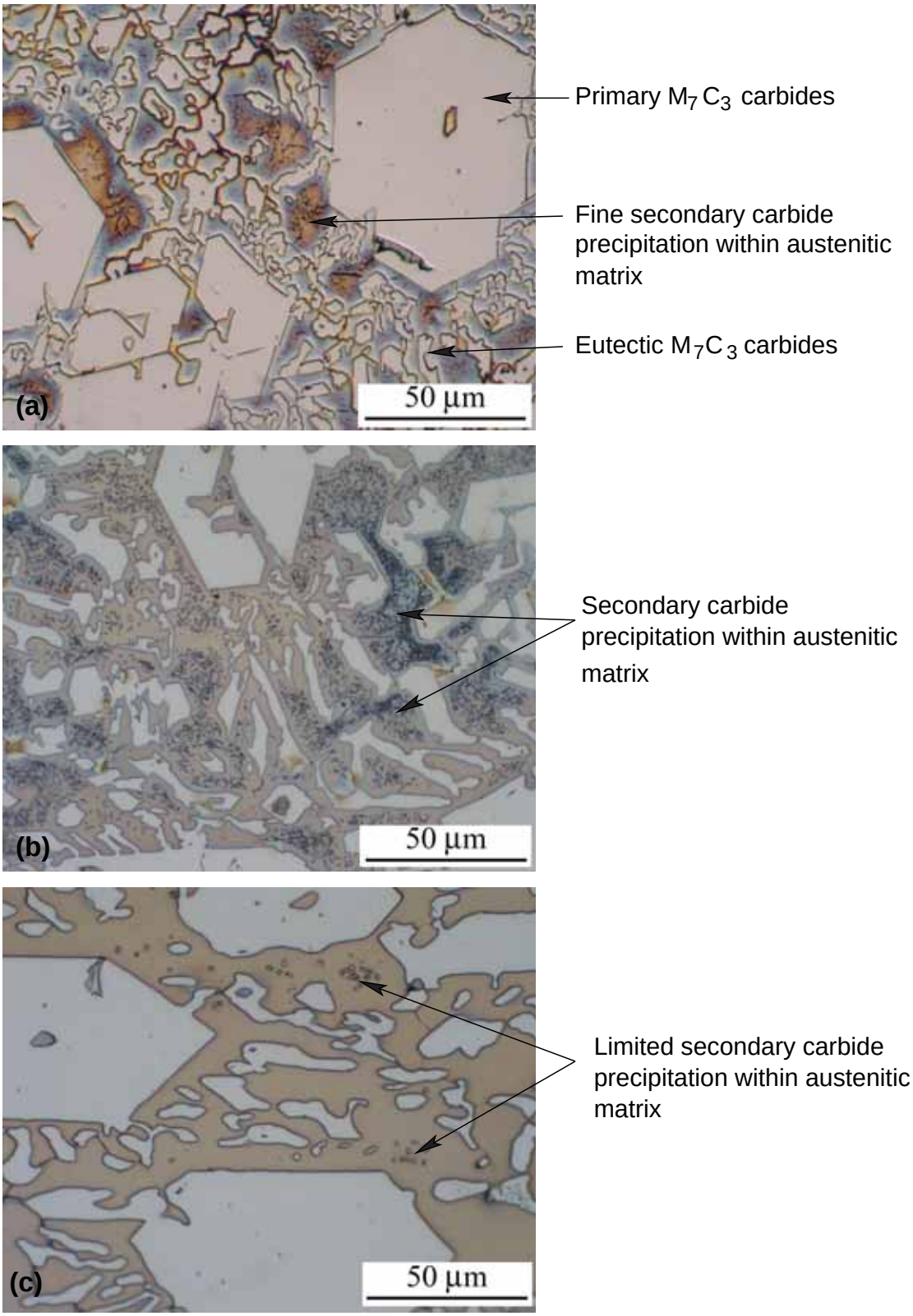

Figure 6.14: Optical light micrographs of the HyperEXP casting. (a) Microstructure in the as-cast condition. (b) Microstructure after a destabilization heat treatment at 950°C for 6 hours and air cooling. (c) Microstructure after a normalizing heat treatment at 1150°C for 6 hours and air cooling.

The anodic polarization curves in deaerated sodium aluminate solution at 90°C at a scan rate

of 1 mV/s for HyperEXP in the as-cast, destabilized and normalized condition are shown in Figure 6.15. The anodic polarization curves of the three microstructural variations investigated showed an active dissolution regime with approximately linear Tafel behaviour between -0.9 V_{SHE} and the critical potential at -0.8 V_{SHE}. The current peak at the critical potential was followed by active to passive behaviour and passive behaviour from -0.75 V_{SHE} to 0 V_{SHE}. Within the passive region there were a number of current peaks that were consistent for all of the three materials. Above 0 V_{SHE}, all the materials demonstrated transpassive polarization behaviour and the corrosion of the carbides.

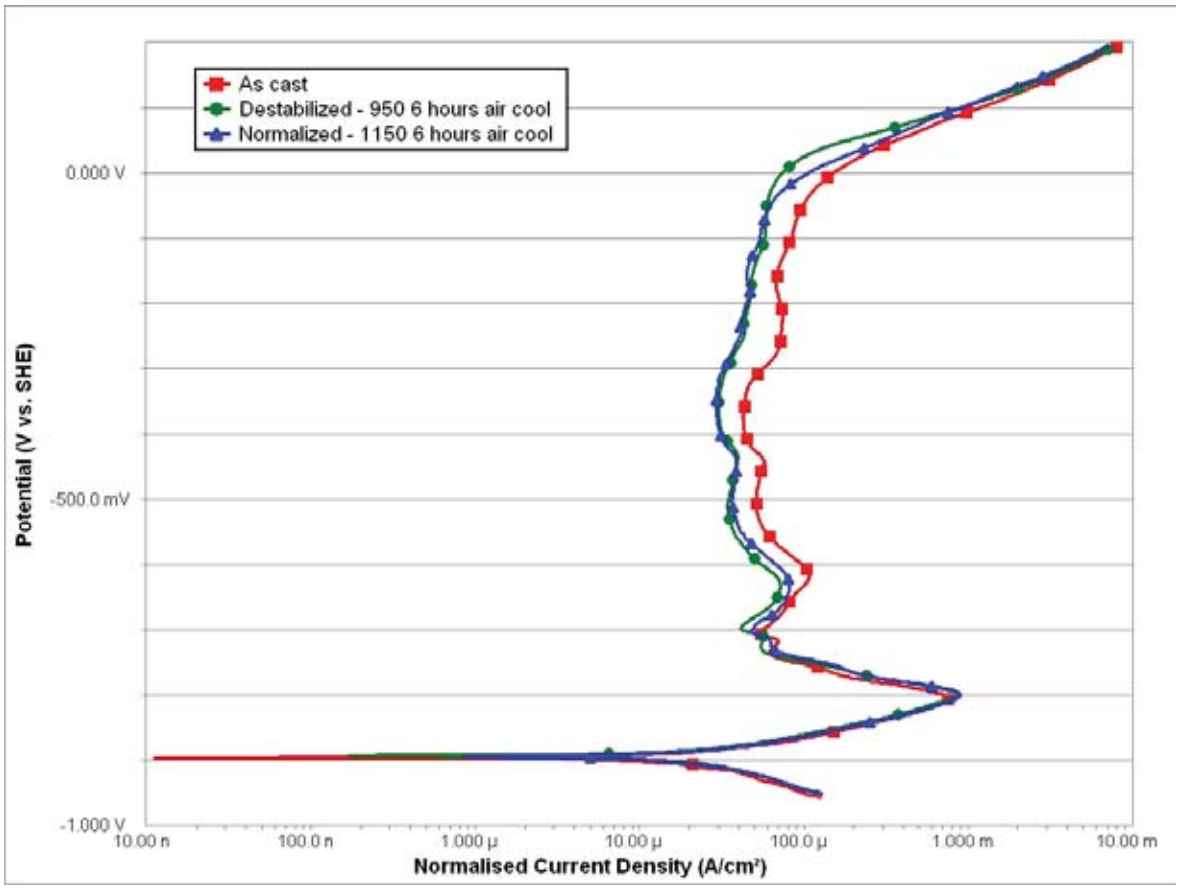

Figure 6.15: Typical anodic polarization curves for HyperA in deaerated sodium aluminate solution at 90°C and a potential scan rate of 1 mV/s for the as-cast, destabilized and normalized heat treated condition.

The difference in the rest potential of the three different microstructures tested was negligible, being less than 0.5 mV, Table 6.11. The difference in the corrosion current density of the three different microstructures was also minimal with the as-cast condition having the lowest corrosion current density of 13.5 μA/cm^2, followed by the destabilized condition being 0.5 μA/cm^2 greater and finally the normalized condition being just under 2 μA/cm^2 greater than the as-cast condition. The critical potentials for the three variations were also similar. The critical current densities of the destabilized and normalized condition were also very similar, however, the as-cast condition had a critical current density 28 μA/cm^2 less that the heat treated variations.

Above -0.7 mV the polarization curves for the destabilized and normalized condition showed similar passive current densities and polarization curve characteristics. The passive current density for the as-cast polarization curve is 10 to 25 μA/cm^2 greater than the passive current densities for the two heat treated samples, Figure 6.15. However, the features of the as-cast polarization curve are similar with the 950 and 1150HT curves.

Table 6.11: Potential and corrosion values for HyperEXP casting in the as-cast, destabilized and normalized condition in sodium aluminate solution.

HyperEXP	E_{corr} (V_{SHE})	I_{corr} ($\mu A/cm^2$)	$E_{critical}$ (V_{SHE})	$I_{critical}$ ($\mu A/cm^2$)	$I_{passive}$* ($\mu A/cm^2$)
As Received	-0.896 ± 0.001	13.4 ± 0.8	-0.805 ± 0.001	787.8 ± 39.2	51.1 ± 2.2
950°C for 6 hours "Destabilized"	-0.896 ± 0.002	14.1 ± 1.4	-0.801 ± 0.002	923.3 ± 137.3	41.2 ± 9.7
1150°C for 6 hours "Normalized"	-0.897 ± 0.003	15.1 ± 1.4	-0.804 ± 0.004	916.9 ± 106.9	33.8 ± 6.9
*I_{pass} at a potential of -0.306 V_{SHE} (-0.5 $V_{Red\ Rod}$)					

6.2.3.3 Summary

Four different high chromium white iron castings that had undergone a destabilization and normalizing heat treatment were subject to polarization corrosion tests in sodium aluminate solution at 90°C. The materials ranged in composition from hypoeutectic (HypoA), eutectic (EutecticA), and hypereutectic (HyperA and HyperEXP). With the exception of the HyperEXP material, all the other materials subjected to a destabilization heat treatment had a transformed matrix of secondary carbides and martensite. The HyperEXP material remained fully austenitic but had considerable secondary carbide precipitation. After a normalizing heat treatment, the materials generally had a homogeneous matrix of austenite. The carbides did not undergo any phase transformation due to heat treatment.

The purpose of these tests was to investigate the influence that the matrix microstructure has on the corrosion behaviour of high chromium white irons in sodium aluminate environments. Generally, it was found that the corrosion current density over the potential range investigated was higher for all the castings with the exception of the HyperEXP casting which did not undergo any matrix transformation to martensite. Rest potential values were not significantly altered by heat treatments with variation being less than 0.015 V for all materials. The corrosion current density in the normalized condition was less than the destabilized condition, with the exception of the HyperEXP sample that was slightly greater. The as-cast condition for the two hypereutectic alloys (HyperA and HyperEXP) gave the lowest corrosion current density. A similar trend was to the corrosion current density was found for the critical potential results. The passive current densities were greater for the destabilized condition than for the normalized condition for the alloys that had a martensitic matrix.

6.2.4 Corrosion of Weld Overlay

6.2.4.1 Materials Investigated

The corrosion behaviour of two commercially deposited high chromium white iron weld overlays were investigated in sodium aluminate solution. The weld overlays were deposited on low carbon steel pipes using a mechanized open arc flux cored arc welding (FCAW) process. The samples for the corrosion investigation were section from ex-service alumina plant samples.

The bulk chemical compositions of the two weld overlays investigated, the chromium to carbon ratio and the carbide volume fraction (CVF) is given in Table 6.12.

Table 6.12: Bulk chemical compositions, chromium to carbon ratio, CVF and bulk hardness of the investigated weld overlay.

Material	Bulk Chemical Composition wt%							Cr/C ratio	CVF*	Bulk Hardness (HV_{30})
	C	Si	Cr	Mn	Fe	Ni	Mo			
WeldoverlayA	5.5	1.6	24.5	1.1	67.0	0.11	0.03	4.5	58.8 ± 2.4	850 ± 30
WeldoverlayB	4.9	0.94	27.3	1.2	65.5	0.06	0.02	5.6	51.2 ± 3.4	741 ± 17

*Carbide volume fraction of primary and eutectic M_7C_3 carbides

The microstructure of WeldoverlayA and WeldoverlayB are shown in Figure 6.16 and Figure 6.17 respectively. Both samples, WeldoverlayA and WeldoverlayB, are of the hypereutectic composition consisting of primary M_7C_3 carbides in a matrix of eutectic M_7C_3 carbides and austenite. However, the microstructures of both the samples showed a number of microstructural variations and the microstructures were not consistent throughout the sample. The microstructural variations are inherent in the FCAW deposition process due to variations in the level of dilution with the steel substrate and previously deposited weld bead. However, many of the microstructural variations are caused by undercooling of the deposited weld. Undercooling refers to the temperature difference between the liquidus temperature and the temperature that solidification first takes place. The undercooling in the cases of the weld overlay samples examined is due to water cooling commonly being used on the underside of the mild steel substrate to prevent burn through. Depending on the extent of undercooling, different non equilibrium, microstructural variations develop that are discussed in more detail in Section 5.2 and summarized below.

At small undercooling the microstructure consists of primary M_7C_3 carbides and eutectic M_7C_3 carbides having a much smaller size than what would be expected under equilibrium cooling conditions. It is common at small undercooling that a halo surrounding the primary M_7C_3 carbides, as seen in Figure 6.16(a) and Figure 6.17(a) will develop. At larger undercooling, the branched primary M_7C_3 carbides and the complex regular M_7C_3 carbides microstructure can form. The branched primary M_7C_3 carbides consist of a number of carbides

that are interconnected to form a monocrystalline array. The complex regular M_7C_3 carbide microstructure occurs at even larger undercooling than for the branched primary M_7C_3 carbide microstructure. The complex regular microstructure consists of a large number of M_7C_3 carbide rods, larger in diameter than the eutectic M_7C_3 carbide rods, that are joined together to form a monocrystalline array exhibiting the shape of equilateral triangle, Figure 6.16(b) and Figure 6.17(b).

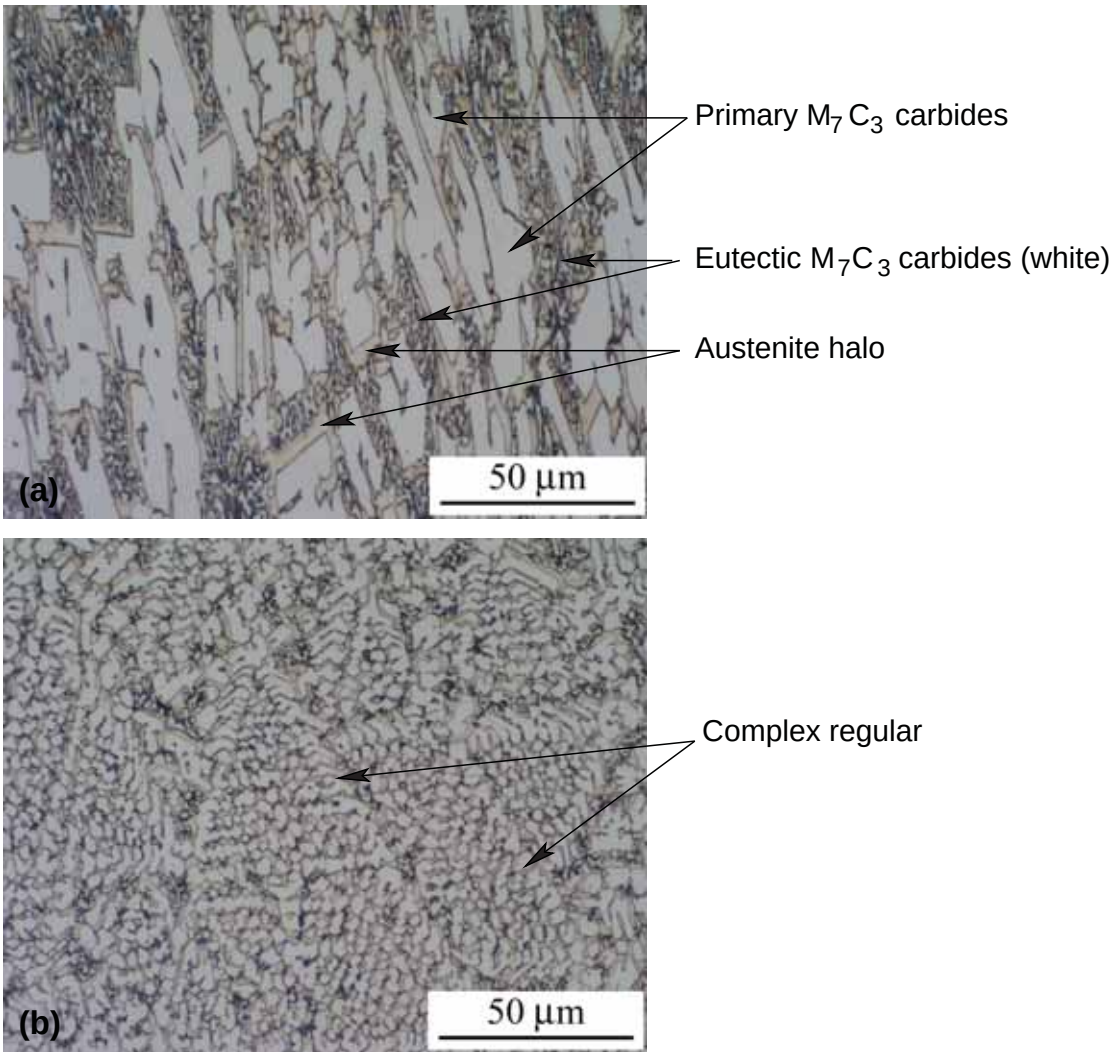

Figure 6.16: Optical micrographs of the hypereutectic high chromium white iron weld overlay, WeldoverlayA. (a) Microstructure showing primary M_7C_3 carbides in a matrix of austenite and eutectic M_7C_3 carbides. The micrograph also shows the austenite halos surrounding the primary M_7C_3 carbides. (b) Microstructure showing the complex regular carbide microstructure caused by undercooling.

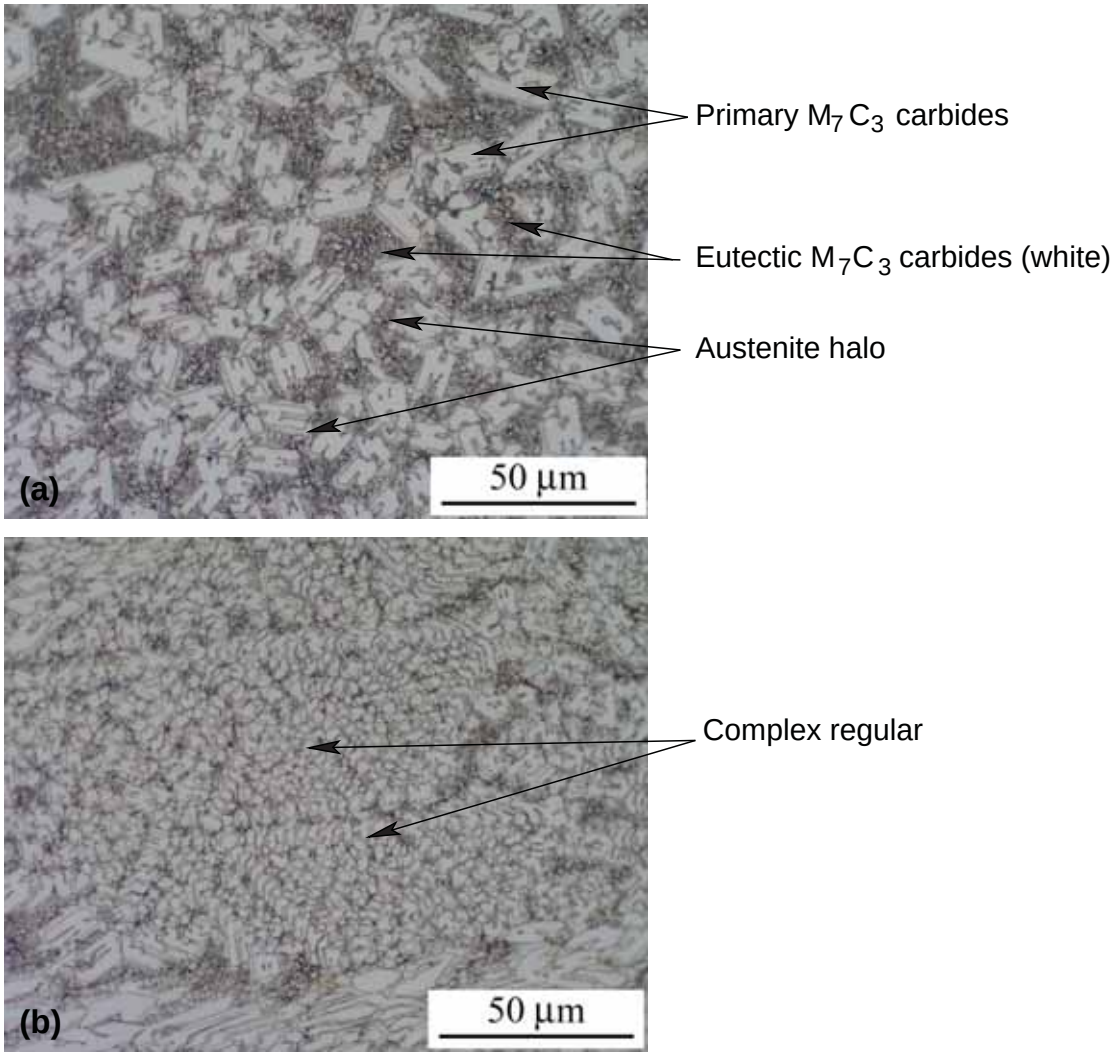

Figure 6.17: Optical micrographs of the hypereutectic high chromium white iron weld overlay, WeldoverlayB. (a) Microstructure showing primary M_7C_3 carbides in a matrix of austenite and eutectic M_7C_3 carbides. The micrograph also shows the austenite halos surrounding the primary M_7C_3 carbides. (b) Microstructure showing the complex regular carbide microstructure caused by undercooling.

A common feature (or problem) with hypereutectic high chromium white iron weld overlays is the presence of check cracking. Check cracking of high chromium white iron weld overlays is caused by tensile residual stresses caused by the varying amounts of thermal contraction of the deposited material and the substrate. The low toughness and ductility of high chromium white iron weld overlays and the tensile residual stresses cause a mesh like check crack pattern to form on the surface of the overlays. The check cracking patterns on the corrosion test samples for WeldoverlayA and WeldoverlayB are shown in Figure 6.18 and Figure 6.19 respectively. The samples also contained a significant amount of subsurface porosity that was revealed when the samples were prepared for metallographic examination.

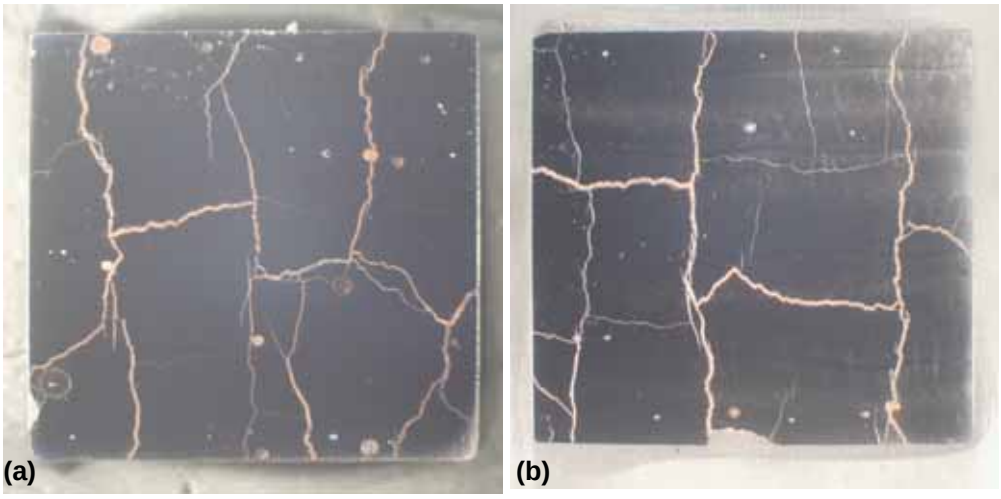

Figure 6.18: Photographs of two WeldoverlayA test samples used for corrosion testing. Note the differences in the check cracking. The dimensions of the samples are 15mm x 15mm.

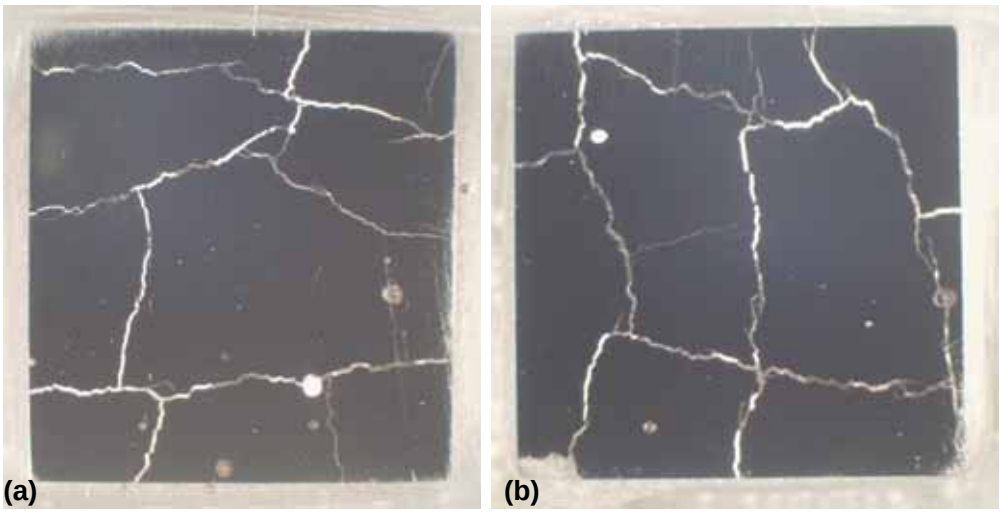

Figure 6.19: Photographs of two WeldoverlayB test samples used for corrosion testing. Note the differences in the check cracking. The dimensions of the samples are 15mm x 15mm.

6.2.4.2 A Note on The Corrosion Test Sample Preparation

The weld overlay samples contained different degrees of check cracking with variations between the test samples taken from the same weld overlay, Figure 6.18 and Figure 6.19. The width of the check cracks varied and often extended to the substrate and contained remnants of alumina plant residue.

It was hypothesized that the check cracks may have a negative effect on the corrosion behaviour of the weld overlays. Therefore, attempts were made to fill the check cracks with epoxy resin using vacuum impregnation techniques during the mounting of the samples . However, although traces of the epoxy resin were found within the check cracks, Figure 6.20, the integrity and effectiveness of the epoxy resin in the caustic test environment at

90°C could not be established. It is therefore possible that during testing the corrosion behaviour of the high chromium white iron weld overlays was influenced to some degree by the check cracking. The influence on the corrosion behaviour is likely to be due to crevice corrosion effects or possibly a coupling with the steel substrate.

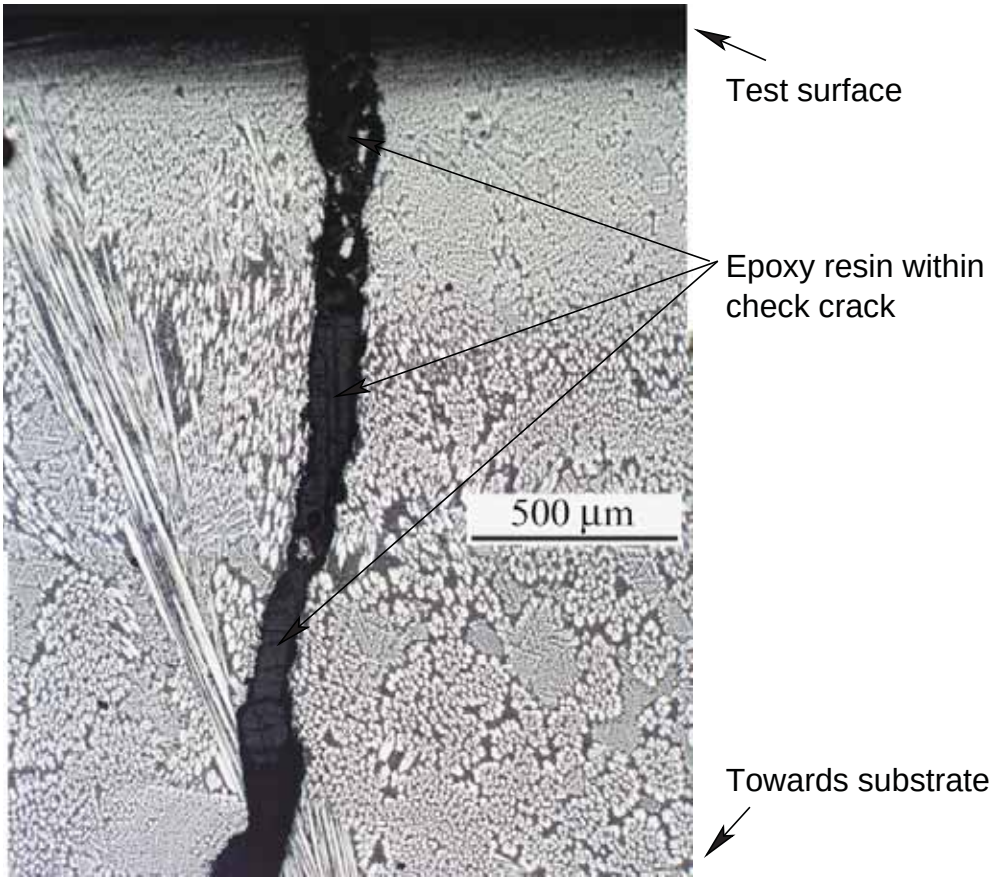

Figure 6.20: Cross sectional micrographs of the WeldoverlayA tests sample used for corrosion testing showing the penetration of epoxy resin in the check crack.

6.2.4.3 Anodic Polarization in Sodium Aluminate Solutions

The potentiodynamic anodic polarization curves for WeldoverlayA and WeldoverlayB in deaerated sodium aluminate solution at 90°C and at a scan rate of 1 mV/s are shown in Figure 6.21. An additional polarization curve for WeldoverlayA has also been included to show the variability in polarization curve results for different corrosion tests samples.

The polarization curves show a small active dissolution regime with approximately linear Tafel behaviour between -0.9 V_{SHE} and -0.8 V_{SHE}. The current peaked at the critical potential at -0.87 to -0.8 V_{SHE} and was followed by a reduction in current density. At -0.75 V_{SHE} the polarization curve had a hump region and low current densities. The hump region was followed by an increase in current and passive like behaviour between -0.7 V_{SHE} and 0 V_{SHE}. Above 0 V_{SHE}, the polarization curves showed transpassive behaviour and the onset of carbide corrosion.

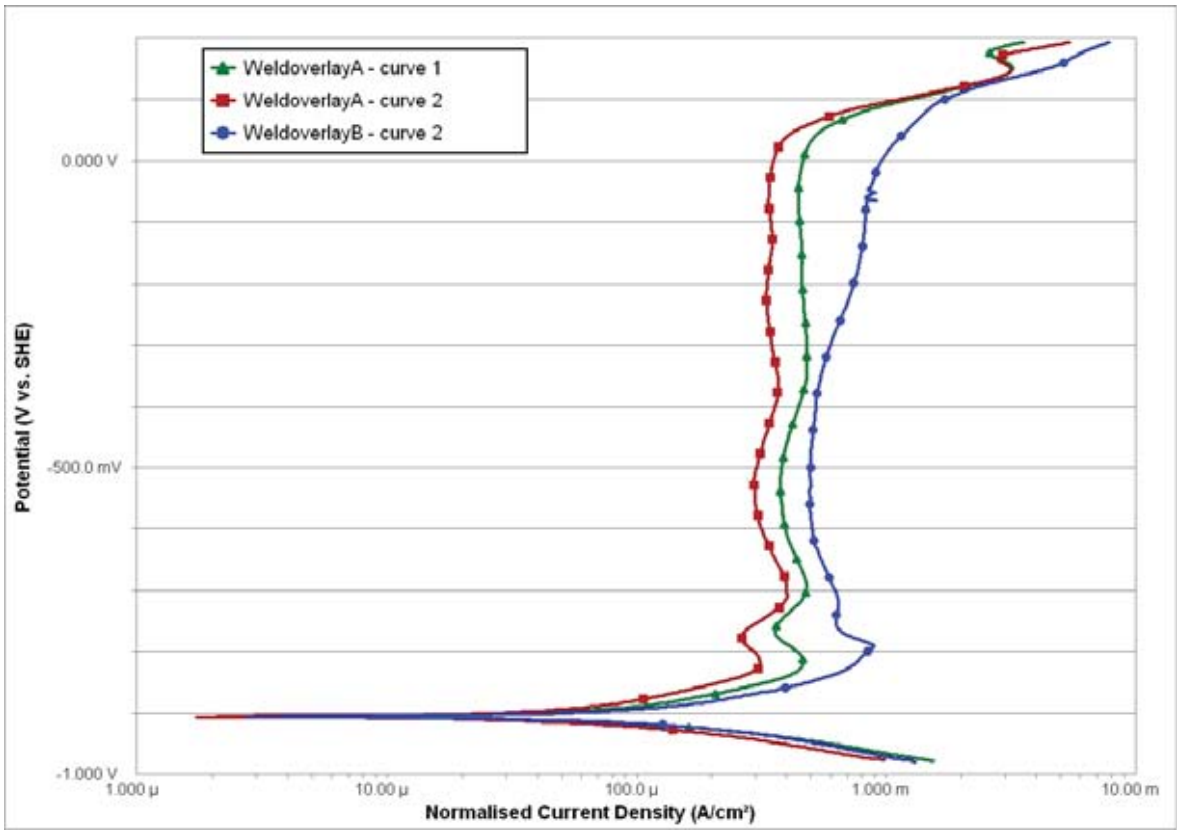

Figure 6.21: Typical anodic polarization curves for WeldoverlayA and WeldoverlayB in deaerated sodium aluminate solution at 90°C and a potential scan rate of 1 mV/s.

Table 6.13: Potential and corrosion values for WeldoverlayA and WeldoverlayB samples in sodium aluminate solution. Results are averages of multiple polarization tests and corrosion current values are averages of multiple Tafel tests.

	E_{corr} (V_{SHE})	I_{corr} ($\mu A/cm^2$)	$E_{critical}$ (V_{SHE})	$I_{critical}$ ($\mu A/cm^2$)	$I_{passive}$* ($\mu A/cm^2$)
WeldoverlayA	-0.908 ± 0.003	142.4 ± 28.5	-0.814 ± 0.009	426.0 ± 156.8	437.0 ± 77.4
WeldoverlayB	-0.907	146.6 ± 36.6	-0.789	874.0	589.0
*I_{pass} at a potential of -0.306 V_{SHE} (-0.5 $V_{Red\ Rod}$)					

6.2.4.4 Summary

Two hypereutectic high chromium white iron weld overlays, sectioned from ex-service alumina plant spools, were subject to polarization corrosion tests in sodium aluminate solution at 90°C. Both the weld overlays had variable microstructures with the branched primary and complex regular microstructure resulting from undercooling seen throughout the weld overlay. In addition, both samples had varying degrees of check cracking that extended to the substrate.

The polarization behaviour was similar for both materials which showed active to passive behaviour. The corrosion current densities were also similar for both materials. However,

there was considerable variation in the critical current densities and passive current densities for the same test material and between the two different test materials.

6.3 Immersion Tests

The anodic polarization test results gave an indication how the material interacts with its operating environment. However, due to the nature of the testing process, the sample is only held at a particular potential for a short interval of time. This does not allow the extent and nature of the corrosion to be determined microscopically. To get a better indication as to the extent of corrosion at a particular potential, constant potential immersion tests were done. This involved subjecting a test sample, prepared identically to the corrosion test samples, to a constant potential over a period of 4 hours in an unstirred sodium aluminate environment identical to that used in the previously reported corrosion tests. In all cases the test sample surface was conditioned by applying a cathodic potential to remove any oxide layers due to atmospheric contamination before the start of the immersion test.

6.3.1 Experimental Methodology and Materials Investigated

Three immersion tests at varying potentials were investigated for different high chromium white iron compositions. The first set of immersion tests was done at the rest potential of the material, i.e. the sample was immersed in the deaerated sodium aluminate solution and the potential was recorded for 4 hours. The second test potential was at -0.825 V_{SHE} which corresponds to a region of active dissolution just below the active to passive transition potential (see Figure 8.14). The third potential investigated was at -0.406 V_{SHE} which corresponds to the passive zone or the zone where the current density is approximately constant for a large variation in potential. After an immersion test the sample was removed from the test cell and cleaned. The upper section of the test sample was cleaned by rubbing with a red rubber stopper to remove loosely adherent corrosion product and to allow a better examination of the surface. The sample was rinsed in acetone and then hot air dried. Examination of the immersion test samples was done using optical light microscopy and electron microscopy in a field emission scanning electron microscope (FESEM).

6.3.2 Immersion Test Results

6.3.2.1 HypoA Casting

Rest Potential

The hypoeutectic high chromium white iron casting sample, HypoA, after the immersion test is shown in Figure 6.22. After the test the sample was covered by a grey/black corrosion product that was easily removed by gently rubbing with a red rubber stopper. The 1200 grit polishing marks were more clearly visible after cleaning.

Further examination in a FESEM indicated that the sample had undergone corrosive attack via the removal of the matrix, Figure 6.23. It was also found that certain areas, suspected to be inclusions of some form, were susceptible to accelerated corrosive attack. Figure 6.23(b) is a higher magnification secondary electron image adjacent to an inclusion, which illustrated the region of accelerated attack and the corrosive attack of the surrounding matrix. The attack of the matrix appears to be in the form of preferential attack of either austenite or martensite, Figure 6.23(b) and (c). EDAX analysis of the inclusions shown in Figure 6.23(b) and (c) was found to contain high levels of sulfur and manganese and are therefore likely to be manganese sulphide inclusions.

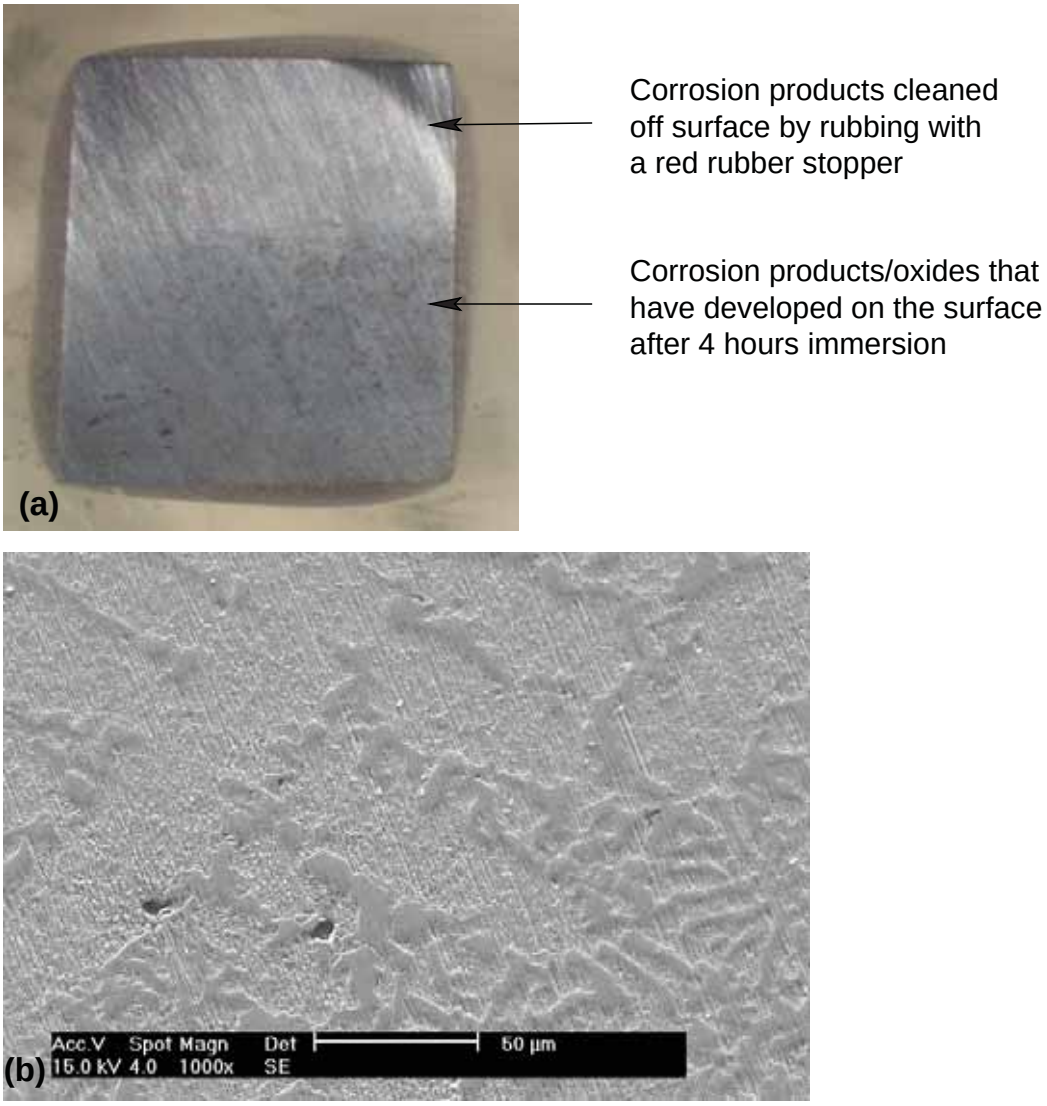

Figure 6.22: HypoA casting after immersion at OCP for 4 hours. (a) General overview of sample with top section having the corrosion product/oxides removed by rubbing with a red rubber stopper. (b) Secondary electron micrograph of the top cleaned section of the immersion test sample, 500x magnification.

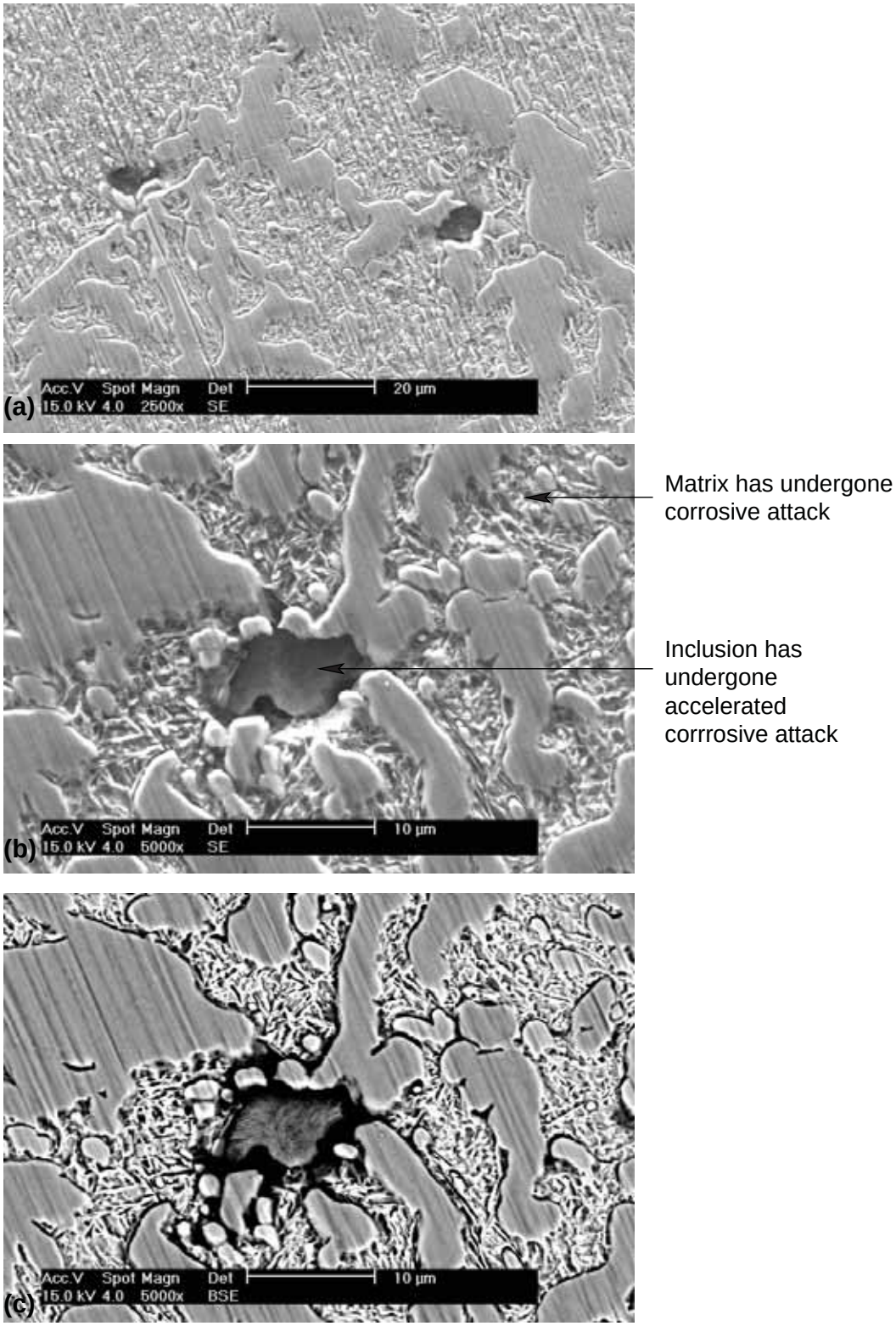

Figure 6.23: HypoA casting after immersion at OCP for 4 hours. (a) General secondary electron image of the area that has been cleaned showing the extent of corrosion and inclusions. (b) Higher magnification secondary electron image of an area containing an inclusion. The matrix has undergone corrosive attack. (c) Corresponding back scattered electron image to the secondary electron image shown in (b).

Active Dissolution

The hypoeutectic casting sample, HypoA, after the constant potential immersion at the active dissolution potential of -0.825V_{SHE} is shown in Figure 6.24. The test sample was covered with a grey/black corrosion product layer that was easily removed by gently rubbing with a red rubber stopper. After cleaning the 1200 grit polish marks were difficult to distinguish.

Figure 6.24(b) shows a optical light micrograph of the cleaned area. The cleaned test surface appears as if in the etched condition. Significant corrosion of the matrix is not evident from the light micrographs.

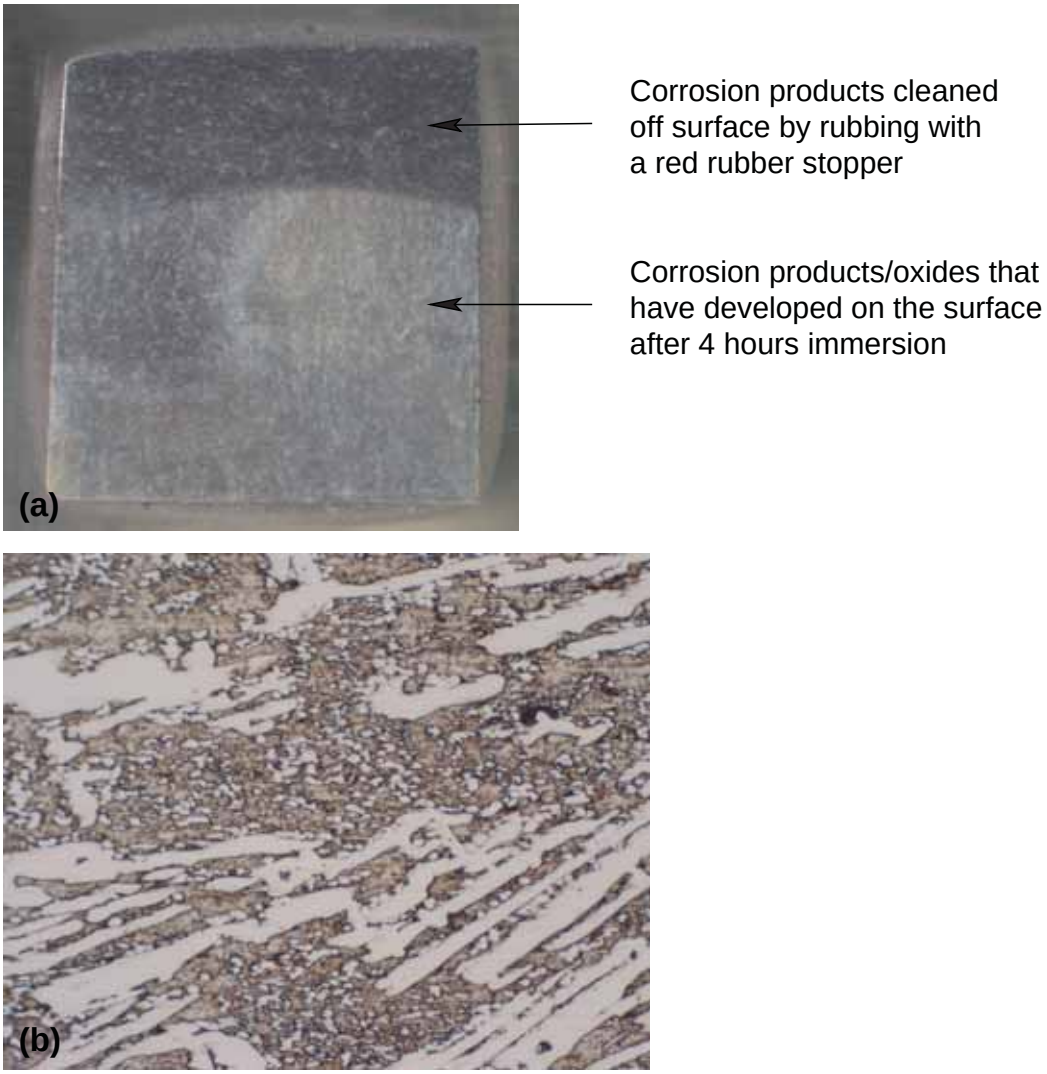

Figure 6.24: HypoA casting after immersion at the active dissolution potential of -0.825V_{SHE} for 4 hours. (a) General overview of sample with top section having the corrosion product/oxides removed by rubbing with a red rubber stopper. (b) Light micrograph of the top cleaned section of the immersion test sample, 500x magnification.

Further examination in a FESEM showed that the matrix had undergone corrosion, Figure 6.25. As occurred in the previous test case at the rest potential of the alloy, inclusions suffered accelerated corrosive attack. EDAX analysis found the inclusions to be high in sulfur and

manganese. At higher magnification, Figure 6.25(b) and (c) it appears that one of the matrix phases, austenite or martensite, has undergone preferential corrosive attack. The carbides, eutectic M_7C_3 and precipitated $M_{23}C_6$ secondary carbides, have undergone no corrosion or at most a minimal amount of corrosive attack. Figure 6.25(b) and (c) show that there is flaring at the edge of the carbide. This flaring is attributed to the polishing of the sample as only one side of the carbide exhibits this flaring and that it is aligned with the polishing marks.

The area that has not been cleaned had a fine dispersion of an unidentified corrosion product covering the entire surface, Figure 6.26.

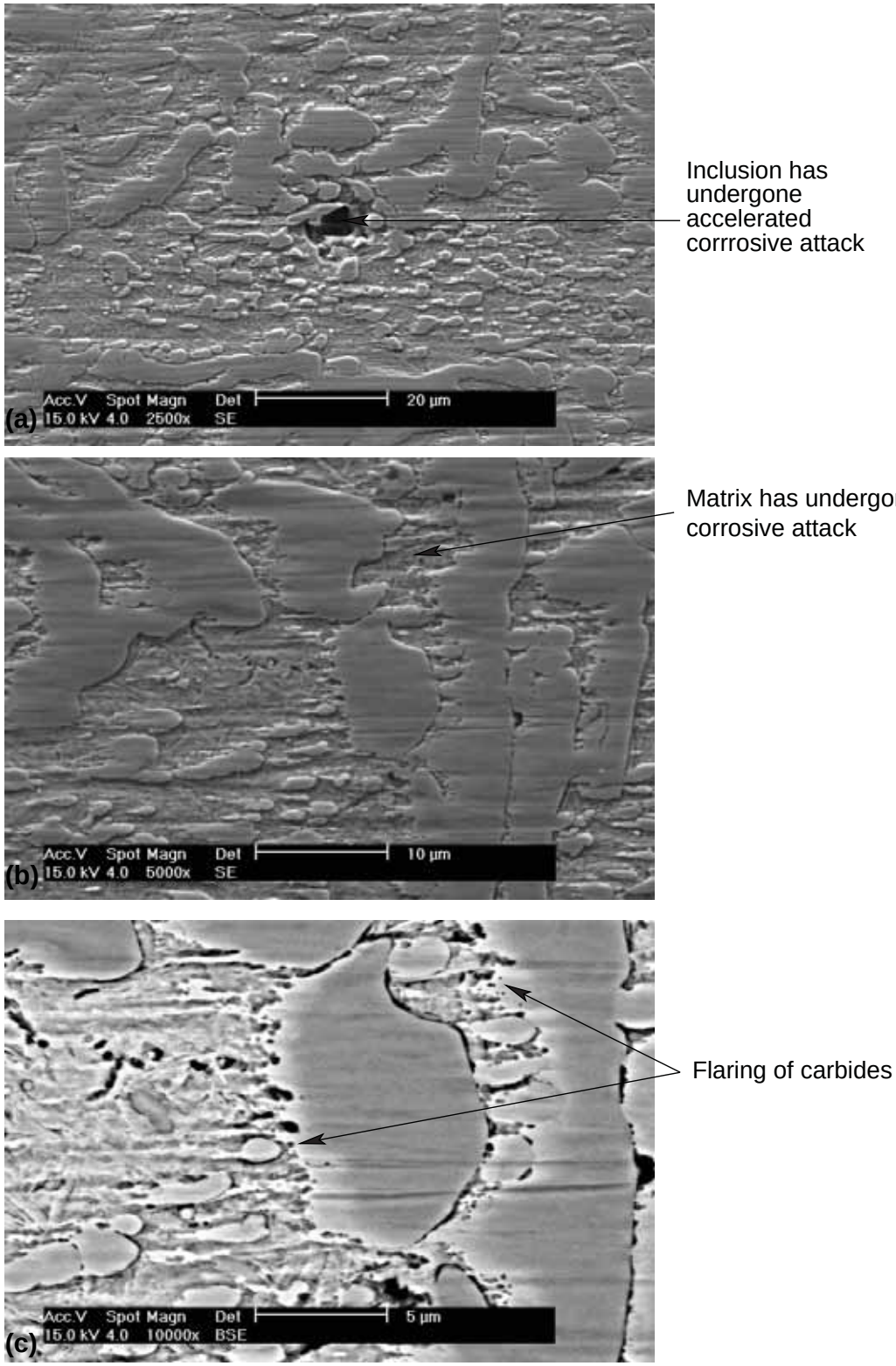

Figure 6.25: HypoA casting after immersion at the active dissolution potential of -0.825V_{SHE} for 4 hours.(a) General secondary electron image of the area that has been cleaned showing the extent of corrosion and an inclusion. (b) Higher magnification secondary electron image further detailing the extent of corrosion. (c) Higher magnification back scattered electron image of (b).

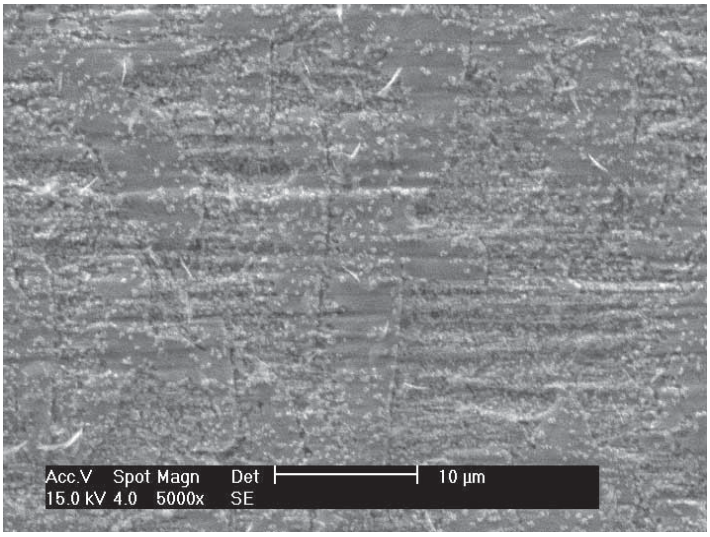

Figure 6.26: HypoA casting after immersion at the active dissolution potential of -0.825V_{SHE} for 4 hours showing the corrosion products that have covered the surface.

Passive Potential

The hypoeutectic casting, HypoA, after the constant potential immersion test in the passive potential regime at -0.406 V_{SHE} is shown in Figure 6.27. After the test the sample was covered with grey/black corrosion product. The corrosion product was easily removed from the sample surface by gently rubbing with a red rubber stopper. After cleaning the 1200 grit marks were readily visible. Figure 6.27(b) is a light micrograph of the cleaned area and shows that the sample has undergone minimal corrosion.

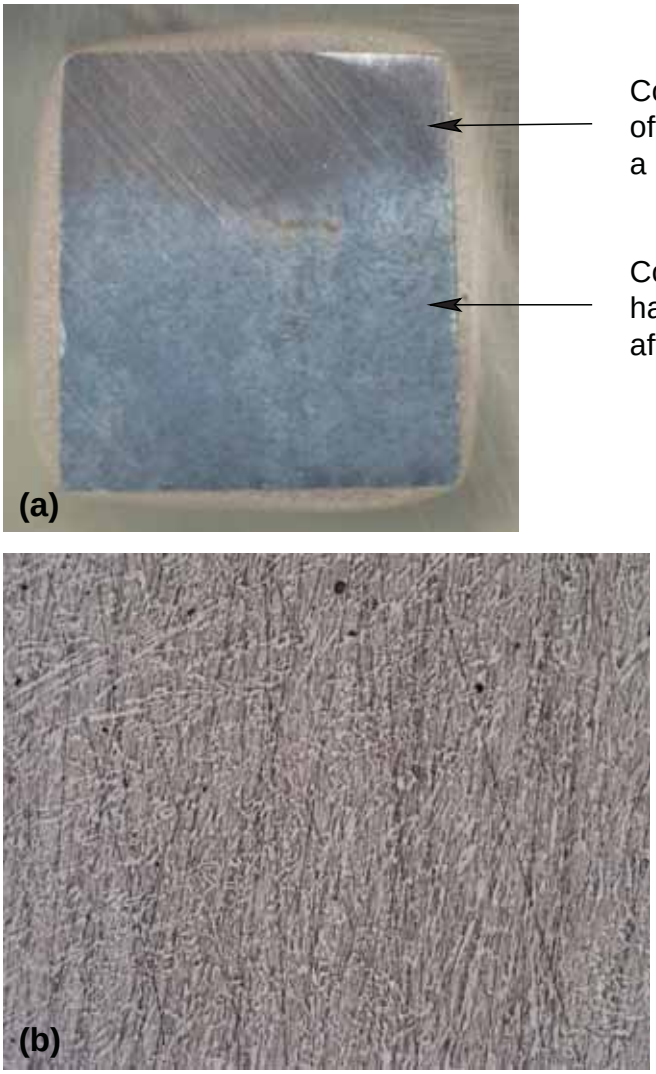

Figure 6.27: HypoA sample after immersion in the passive potential regime at -0.406 V_{SHE} for 4 hours. (a) General overview of sample with top section having the corrosion product/oxides removed by rubbing with a red rubber stopper. (b) Light micrograph of the top cleaned section of the immersion test sample, 100x magnification.

Examination in a FESEM found that the sample did not suffer significant corrosive attack, Figure 6.28. The carbides standing proud of the matrix in the secondary electron micrograph, Figure 6.28(a), would largely be due to the relief polishing of the sample. The higher magnification back scattered electron micrographs Figure 6.28(b) and (c) are further evidence that the test sample did not undergo significant corrosive attack. The 1200 grit polish marks were readily seen through both the carbides and matrix.

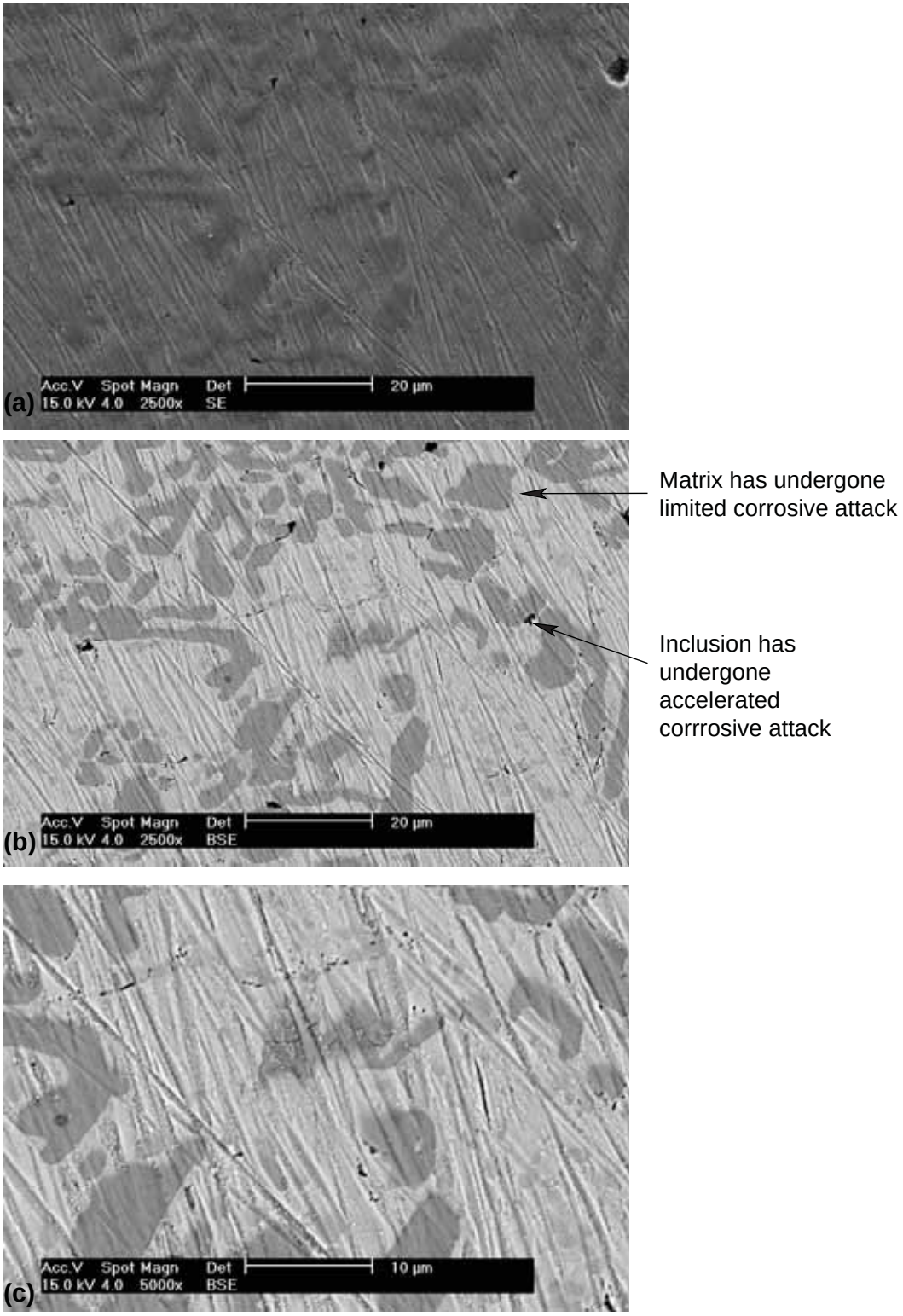

Figure 6.28: HypoA casting after immersion in the passive potential regime at -0.406 V_{SHE} for 4 hours. (a) General secondary electron image of the area that has been cleaned. (b) Corresponding back scattered electron micrograph to (a). (c) Higher magnification back scattered electron micrograph of (b).

6.3.2.2 HyperA Casting

Rest Potential (OCP)

The hypereutectic high chromium white iron casting sample, HyperA, after the immersion test is shown in Figure 6.29. After the test the sample was covered by a grey/black corrosion product that was easily removed by gently rubbing with a red rubber stopper. The 1200 grit polishing marks were more clearly visible after cleaning but could be distinguished with the corrosion product intact. The light micrograph, Figure 6.29(b), showed that the matrix was covered with a brown/black oxide layer that was not removed during the cleaning process.

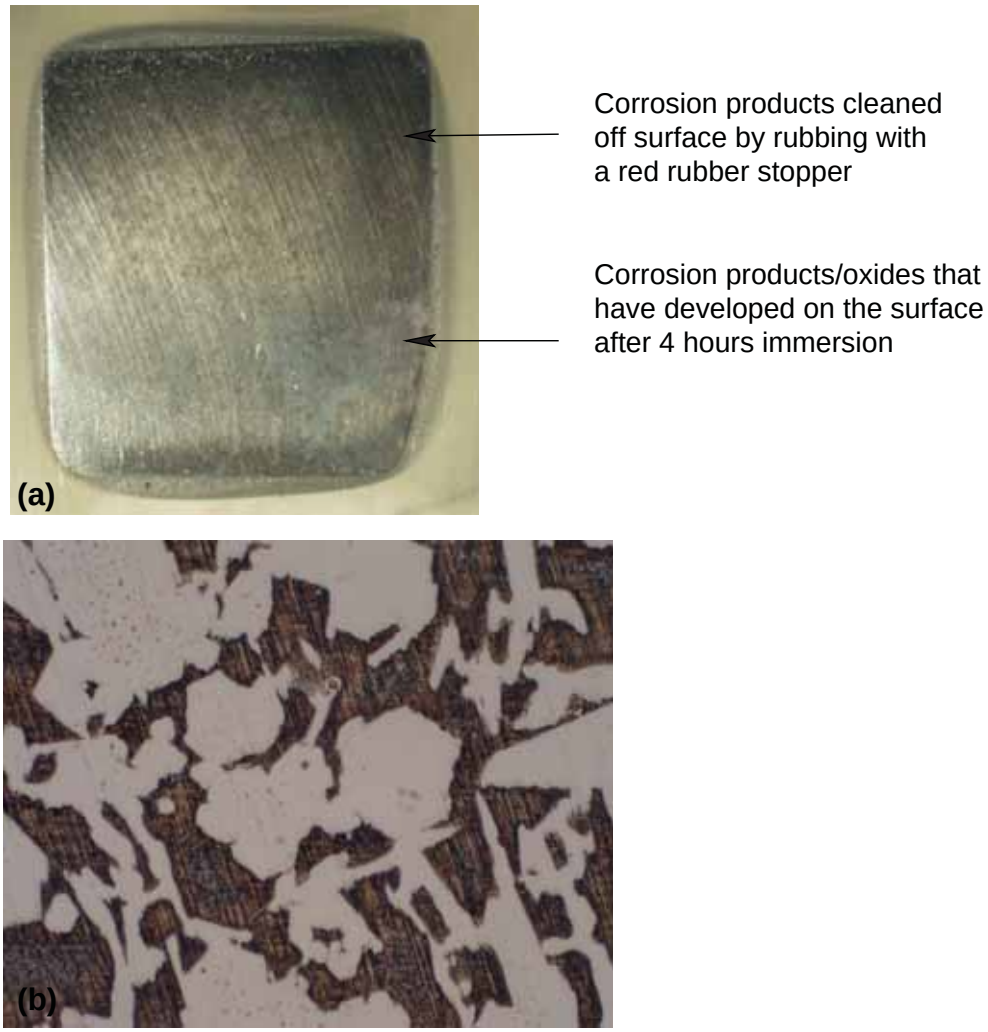

Figure 6.29: HyperA casting after immersion at OCP for 4 hours. (a) General overview of sample with top section having the corrosion product/oxides removed by rubbing with a red rubber stopper. (b) Light micrograph of the top cleaned section of the immersion test sample, 500x magnification.

Further examination in a FESEM found that the sample had undergone corrosive attack via the removal of the matrix, Figure 6.30. Figure 6.30(a) is a secondary electron image that shows the matrix is recessed with respect to the carbides. The polishing marks are still

clearly visible going through the carbides indicating that the corrosion of the carbides did not occur or is negligible. The higher magnification back scattered electron and secondary electron micrographs 6.30(b) and (c) respectively, more clearly show the extent of matrix corrosion. It is seen that in particular matrix regions more localized corrosion has taken place and is commonly found in matrix regions that had precipitated carbides.

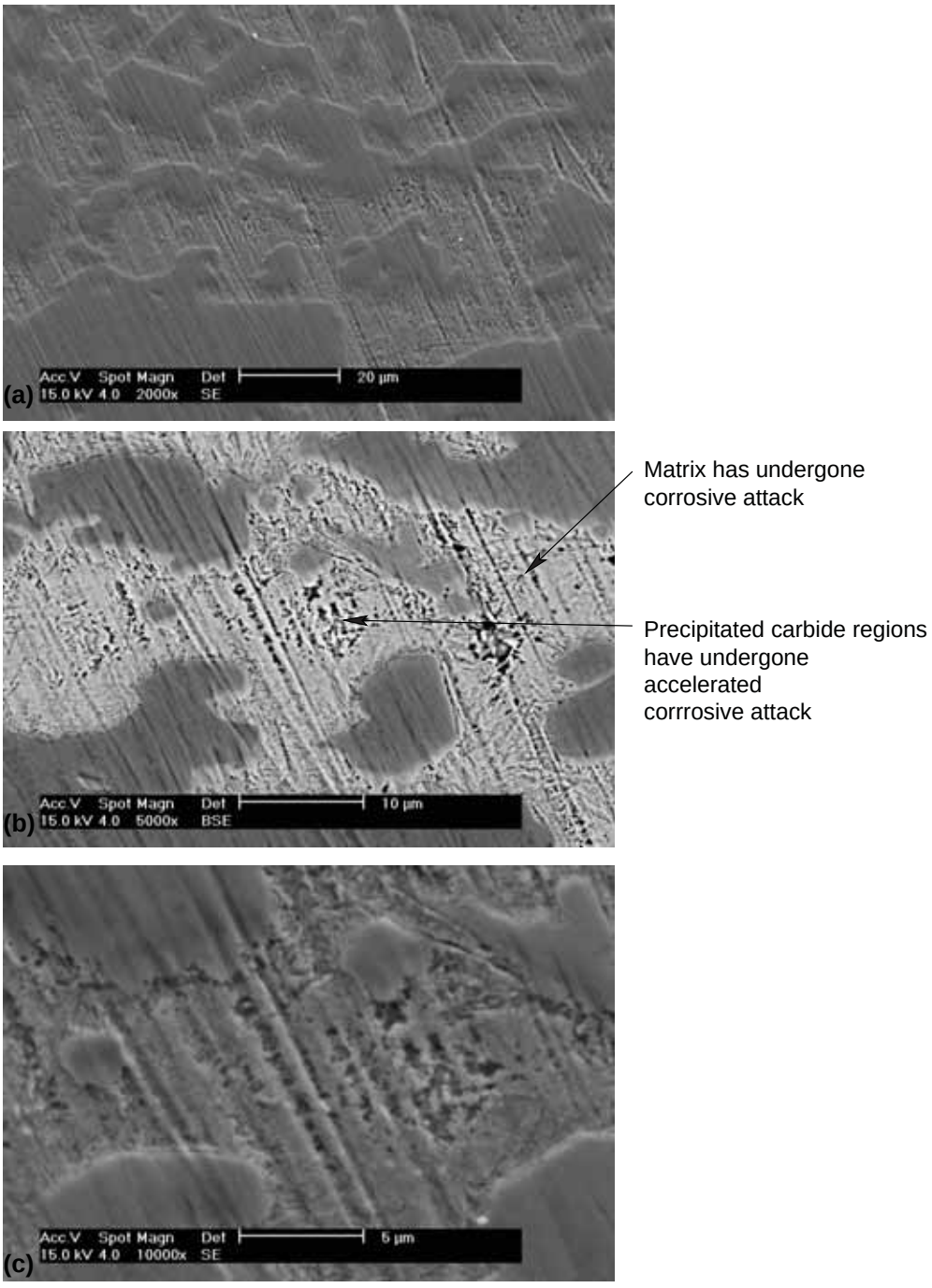

Figure 6.30: HyperA casting after immersion at OCP for 4 hours. (a) General secondary electron micrograph of the area that has been cleaned. (b) Higher magnification back scattered electron micrograph of (a). (c) Higher magnification secondary electron micrograph showing matrix corrosion.

Active Dissolution

The hypereutectic casting sample, HyperA, after the constant potential immersion at the active dissolution potential of -0.825V_{SHE} is shown in Figure 6.31. The test sample was covered with a grey/black corrosion product layer that was easily removed by gently rubbing with a red rubber stopper. After cleaning the 1200 grit polish marks were difficult to distinguish. Figure 6.29(b) shows a optical light micrograph of the cleaned area. The matrix was covered with a brown/black oxide layer that was not removed during the cleaning process. Significant corrosion of the matrix is not evident from the light micrographs.

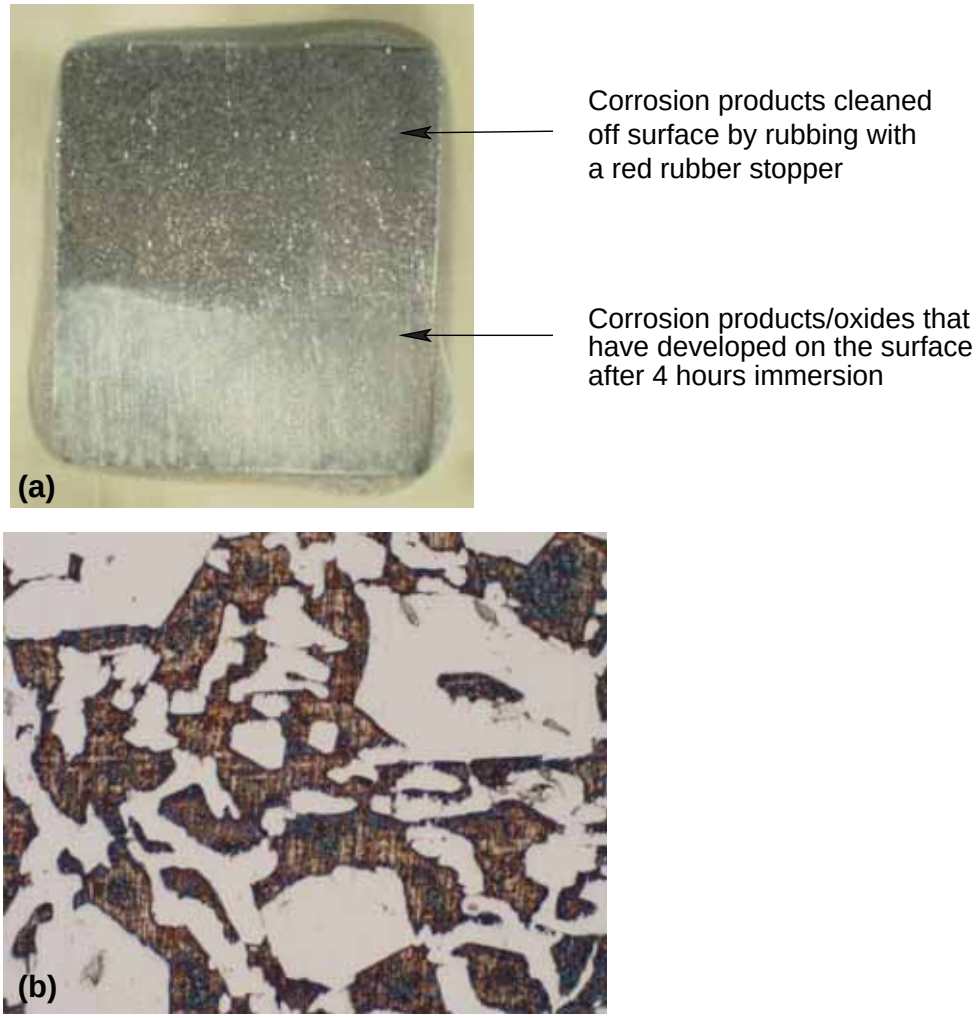

Figure 6.31: HyperA casting after immersion at the active dissolution potential of -0.825V_{SHE} for 4 hours. (a) General overview of sample with top section having the corrosion product/oxides removed by rubbing with a red rubber stopper. (b) Light micrograph of the top cleaned section of the immersion test sample, 500x magnification.

Further examination in a FESEM showed that the matrix had undergone corrosion, Figure 6.32. As seen in the previous samples, inclusions suffered accelerated corrosive attack. EDAX analysis found the inclusions to be high in sulfur and manganese. The area that has not been cleaned had numerous plate like crystals covering the surface, Figure 6.30(c).

EDAX analysis of a clump of these plate like crystals found them to contain significant proportions of oxygen and aluminium and to be free of sodium. This would imply the crystals are are hydrated alumina, $Al_2O_3.3H_2O$.

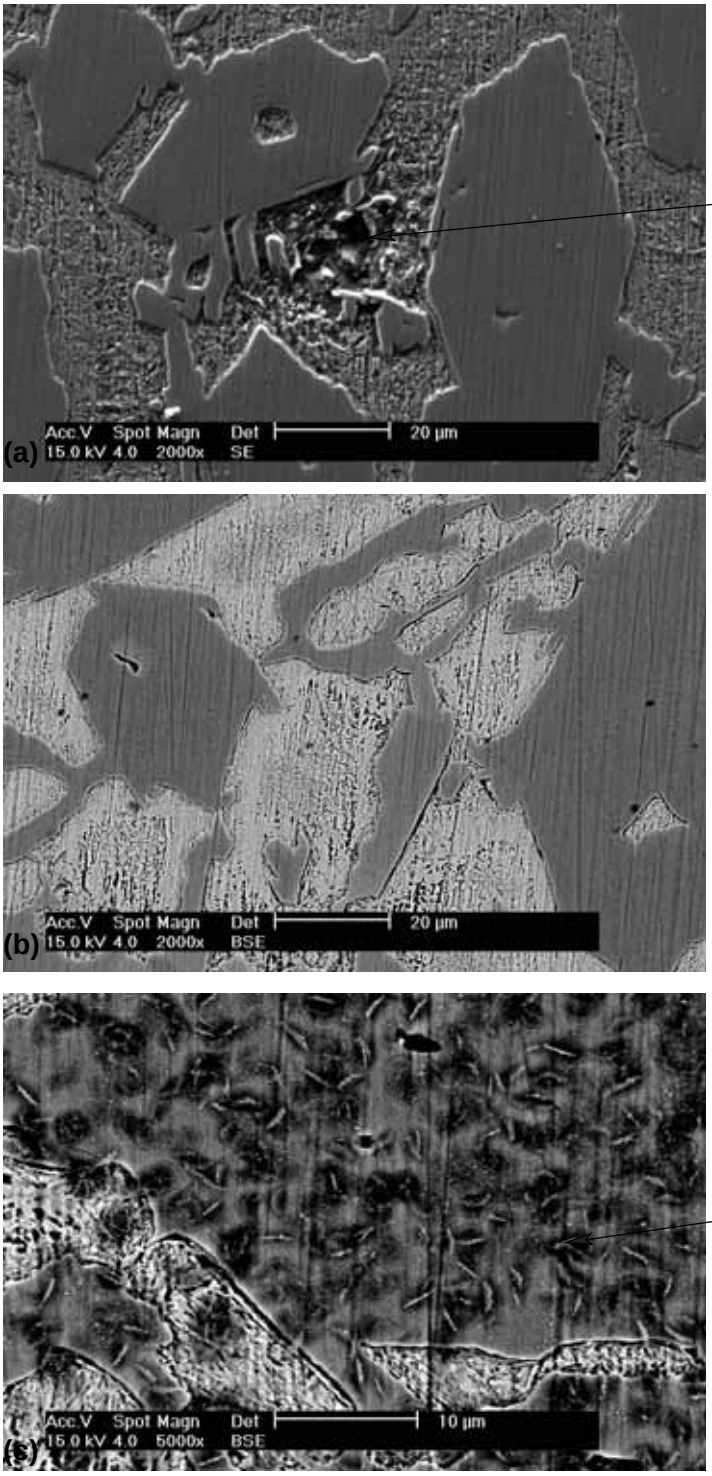

Figure 6.32: HyperA casting after immersion at the active dissolution potential of -0.825V_{SHE} for 4 hours. (a) General secondary electron micrograph of the area that has been cleaned showing accelerated corrosion around an inclusion. (b) General back scattered electron micrograph showing matrix corrosion. (c) back scattered electron micrograph of as tested area showing plate like crystals that are easily removed by rubbing with a red rubber stopper.

Passive Potential

The hypereutectic casting, HyperA, after the constant potential immersion test in the passive potential regime at -0.406 V_{SHE} is shown in Figure 6.33. After the test the sample was covered with a red/black corrosion product. The corrosion product was easily removed from the sample surface by gently rubbing with a red rubber stopper. After cleaning the 1200 grit marks were only slightly visible. Figure 6.33(b) is a light micrograph of the cleaned area and shows that the sample is relatively intact and has undergone minimal corrosion and that the matrix is covered with a red corrosion product layer.

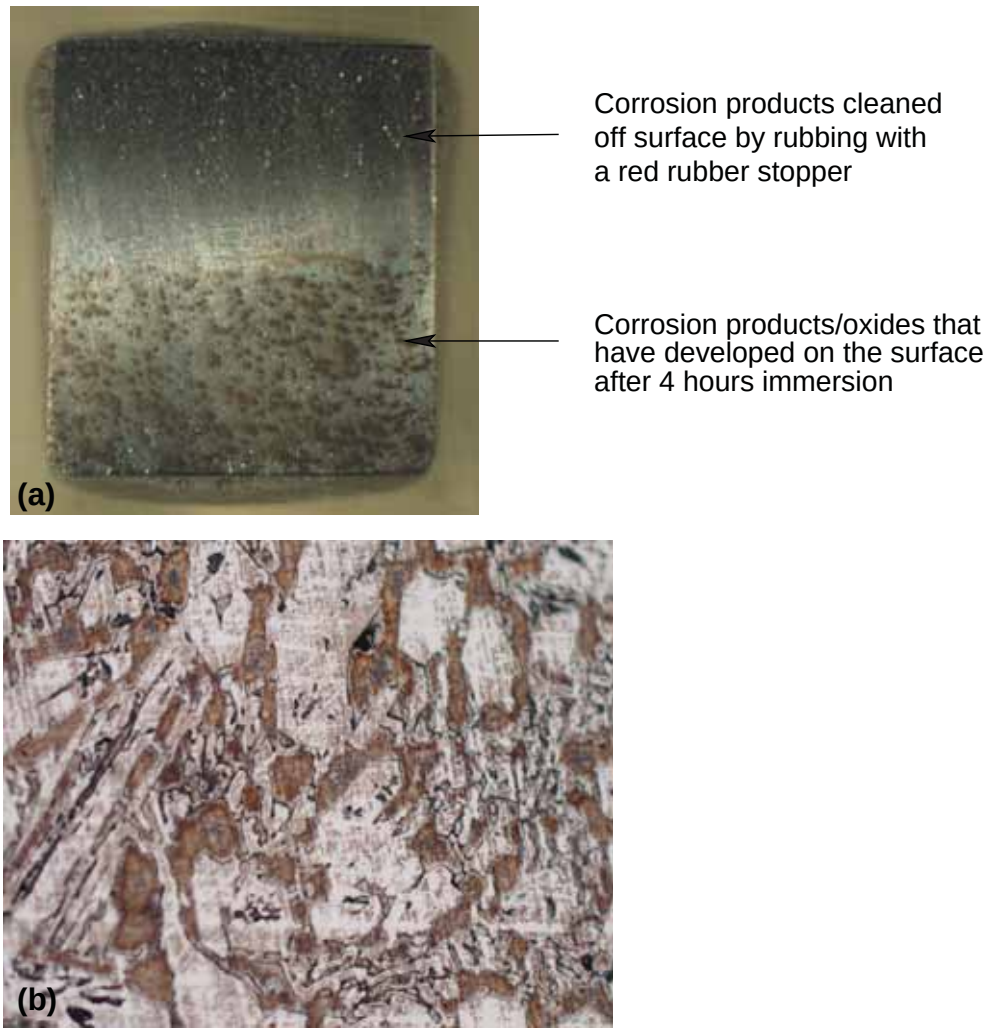

Figure 6.33: HyperA casting after immersion in the passive potential regime at -0.406 V_{SHE} for 4 hours. (a) General overview of sample with top section having the corrosion product/oxides removed by rubbing with a red rubber stopper. (b) Light micrograph of the top cleaned section of the immersion test sample, 200x magnification.

Examination in a FESEM found that the sample did not suffer significant corrosive attack, Figure 6.34. The carbides did still show signs of the 1200 grit polish marks but were, however, not as pronounced as previously seen in the other samples. This could indicate that the carbides do suffer very slight corrosive attack under this set of test conditions. The corro-

sion of the matrix appeared to be uniform with accelerated corrosion around the precipitated carbides and adjacent to the carbide matrix interface, Figure 6.34(c).

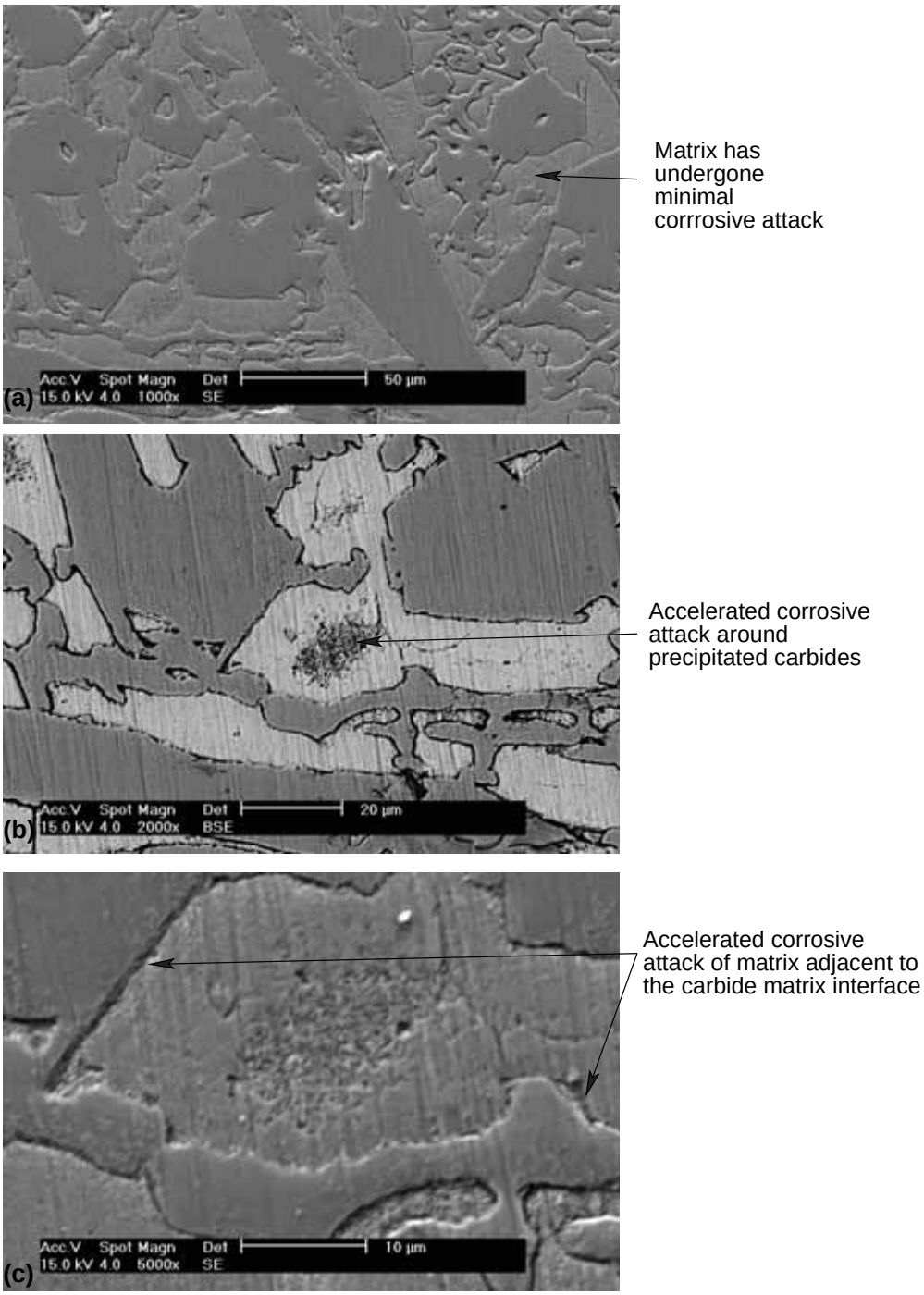

Figure 6.34: HyperA casting after immersion in the passive potential regime at -0.406 V_{SHE} for 4 hours.(a) General secondary electron micrograph of area that has been cleaned. (b) Higher magnification back scattered electron micrograph of (a). (c) High magnification secondary electron micrograph of (b) showing corrosive attack at the M_7C_3 carbide matrix interface.

6.3.2.3 Weld Overlay - WeldoverlayA

Rest Potential (OCP)

The hypereutectic high chromium white iron weld overlay, WeldoverlayA, sample after the immersion test at the open circuit potential is shown in Figure 6.35. After the test, the sample was covered with a grey/black corrosion product that was easily removed by gently rubbing the upper section of the sample with a red rubber stopper. After cleaning the 1200 grit polish marks were visible. Figure 6.35(b) shows a light micrograph of the test surface after the immersion test. The matrix surrounding the primary and eutectic M_7C_3 carbides has been completely removed and is not distinguishable in the light microscope, Figure 6.35(b).

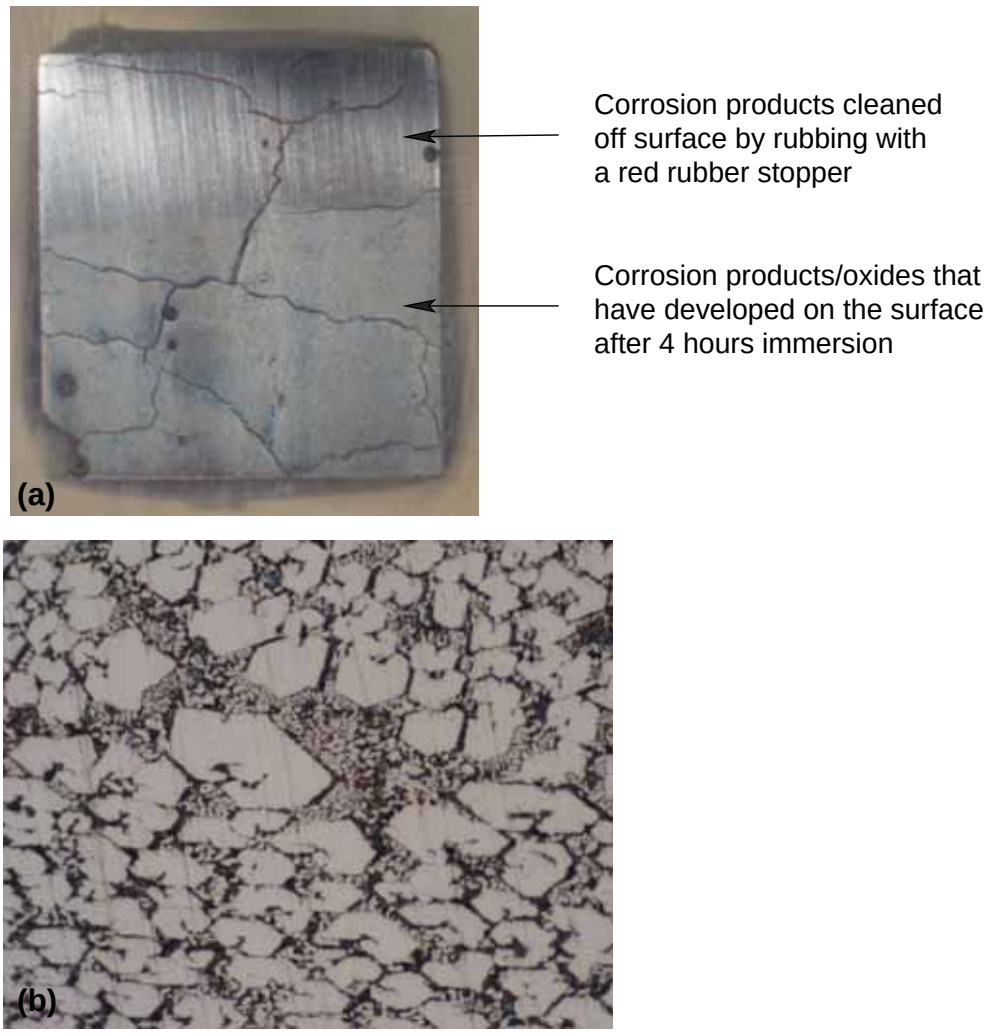

Figure 6.35: WeldoverlayA after immersion at open circuit potential for 4 hours. (a) General overview of sample with top section having the corrosion product/oxides removed by rubbing with a red rubber stopper. (b) Light micrograph of the top cleaned section of the immersion test sample, 500x magnification.

Further examination in a FESEM revealed that the matrix surrounding the primary and eutectic M_7C_3 carbides had been removed, Figure 6.36. Figure 6.36(a) is a secondary electron

image that gives a topographical view of the topography of the sample, in this case the primary and eutectic carbides are on a plane above the matrix. The back scattered electron image, Figure 6.36(b), which is at a higher magnification than Figure 6.36(a), better shows the effects of immersion in sodium aluminate solution for 4 hours at the rest potential. It can be seen that large portions of the austenite halos, which surround the primary M_7C_3 carbides still remain but have undergone corrosive attack. The extent of the corrosive attack on the austenite halos appears to be more localized at the interfaces between the austenite and carbides compared with the central region of the halo. The eutectic austenite, which would have surrounded the fine closely spaced eutectic M_7C_3 carbides, could not be seen in the examination of the wear surface. This indicates that the matrix surrounding the closely spaced eutectic M_7C_3 carbides has been removed by the immersion in sodium aluminate solution at 90°C for 4 hours. In all of the examined areas, the 1200 grit polish marks were still evident on the primary and eutectic carbides, indicating the carbides have suffered little or no corrosion.

The area which had not been cleaned and still has the corrosion product intact was also examined, Figure 6.36(c). The back scattered electron image shows the formation of plate like crystals that grow or are attached to regions between the primary and eutectic carbides where the austenitic matrix once resided. EDAX analysis of a clump of these plate like crystals found them to contain significant proportions of oxygen and aluminium and to be free of sodium. This would imply the crystals are are hydrated alumina, $Al_2O_3.3H_2O$.

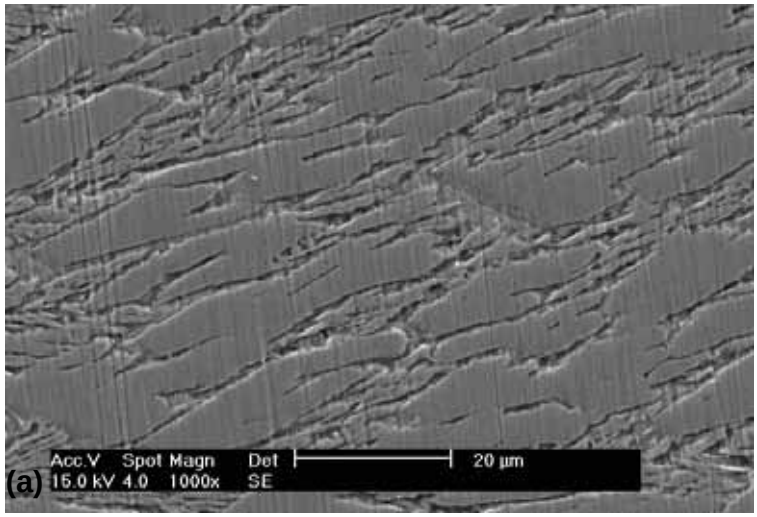

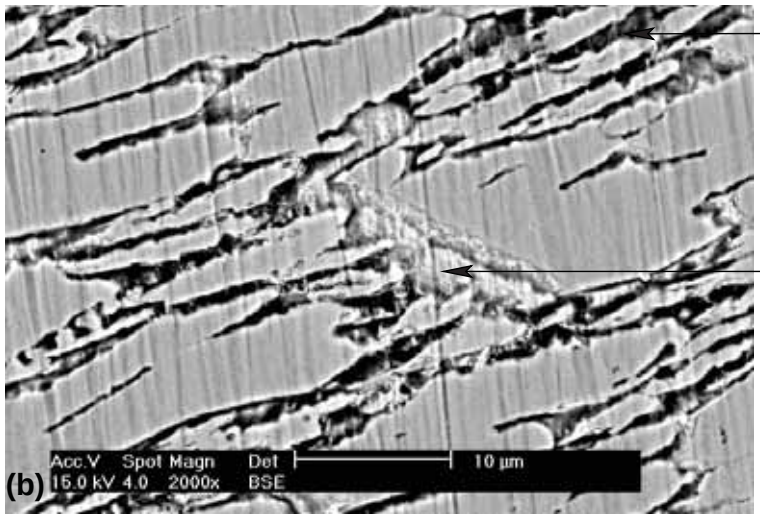

Austenitic matrix not visible in closely spaced eutectic carbide regions

Halo has undergone corrosive attack

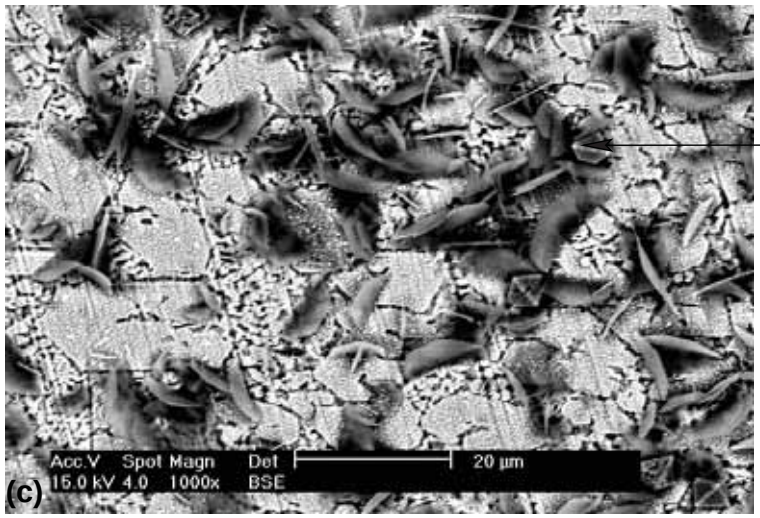

Plate like crystals on the surface that were found to be rich in Al and O by EDAX

Figure 6.36: WeldoverlayA after immersion at open circuit potential for 4 hours. (a) General secondary electron micrograph of area that has been cleaned. (b) Higher magnification back scattered electron micrograph of (a). (c) back scattered electron micrograph of the as tested area showing the plate like crystals that are removed by cleaning with a red rubber stopper.

Active Dissolution

The WeldoverlayA test sample after the constant potential immersion test in the active dissolution regime at a potential of -0.825V_{SHE} for 4 hours is shown in Figure 6.37. As in the previous test, the sample was covered with a grey/black layer that was easily removed by gently rubbing with a red rubber stopper. Figure 6.37(b) shows a light micrograph of the cleaned area that shows the matrix originally surrounding the primary and eutectic carbides has been removed by holding the sample at -0.825 V_{SHE} in 90°C sodium aluminate solution for 4 hours.

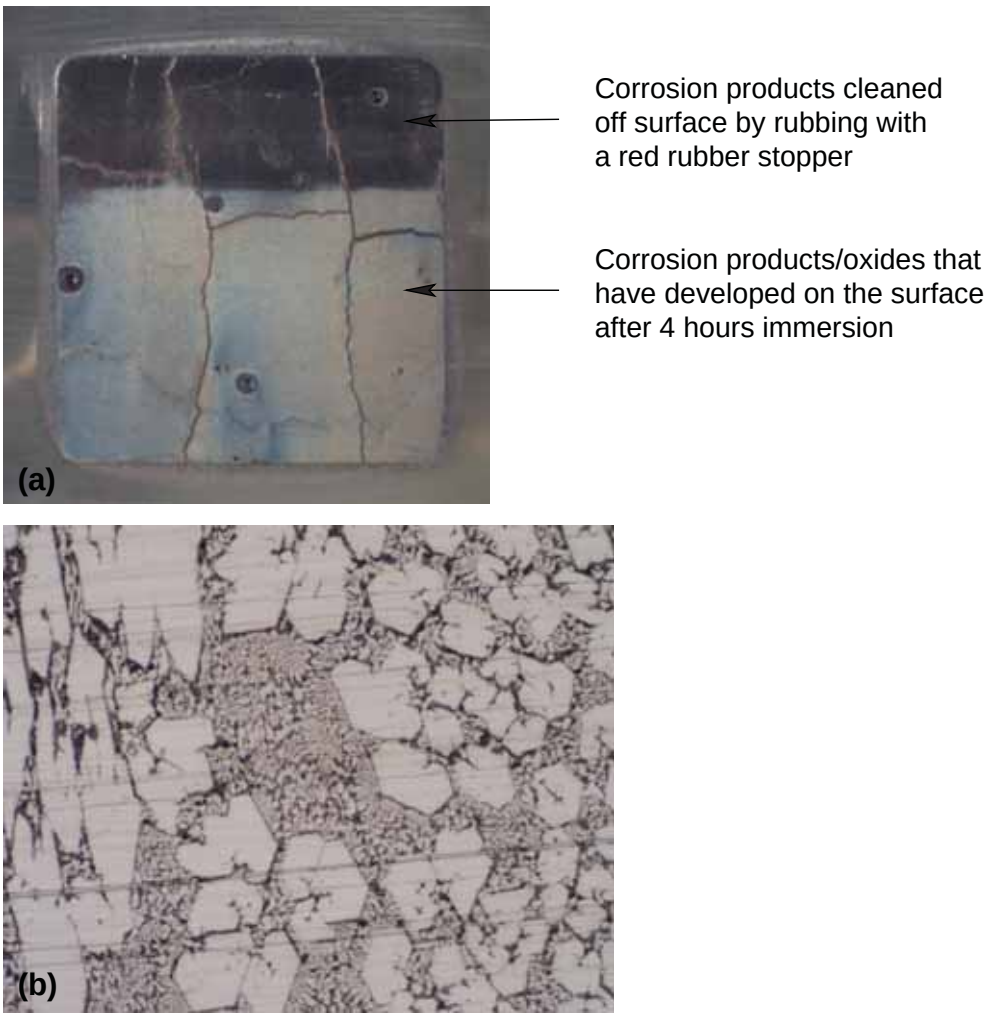

Figure 6.37: WeldoverlayA after immersion at the active dissolution potential of -0.825V_{SHE} for 4 hours. (a) General overview of sample with top section having the corrosion product/oxides removed by rubbing with a red rubber stopper. (b) Light micrograph of the top cleaned section of the immersion test sample, 500x magnification.

Further examination in a FESEM at higher magnification confirmed that the matrix originally surrounding the primary and eutectic M_7C_3 carbides had been removed, Figure 6.38. The images show that the matrix could not readily be seen between the closely spaced eutectic carbide regions, indicating the matrix is significantly recessed with respect to the plane of

the carbides. A small portion of the halo that surrounds the primary carbides can still be seen in isolated regions. The as tested area (the area that had not been cleaned) had traces of the plate like crystals that was seen in Figure 6.36(c). However, the size and quantity of the plate like crystals was not as significant.

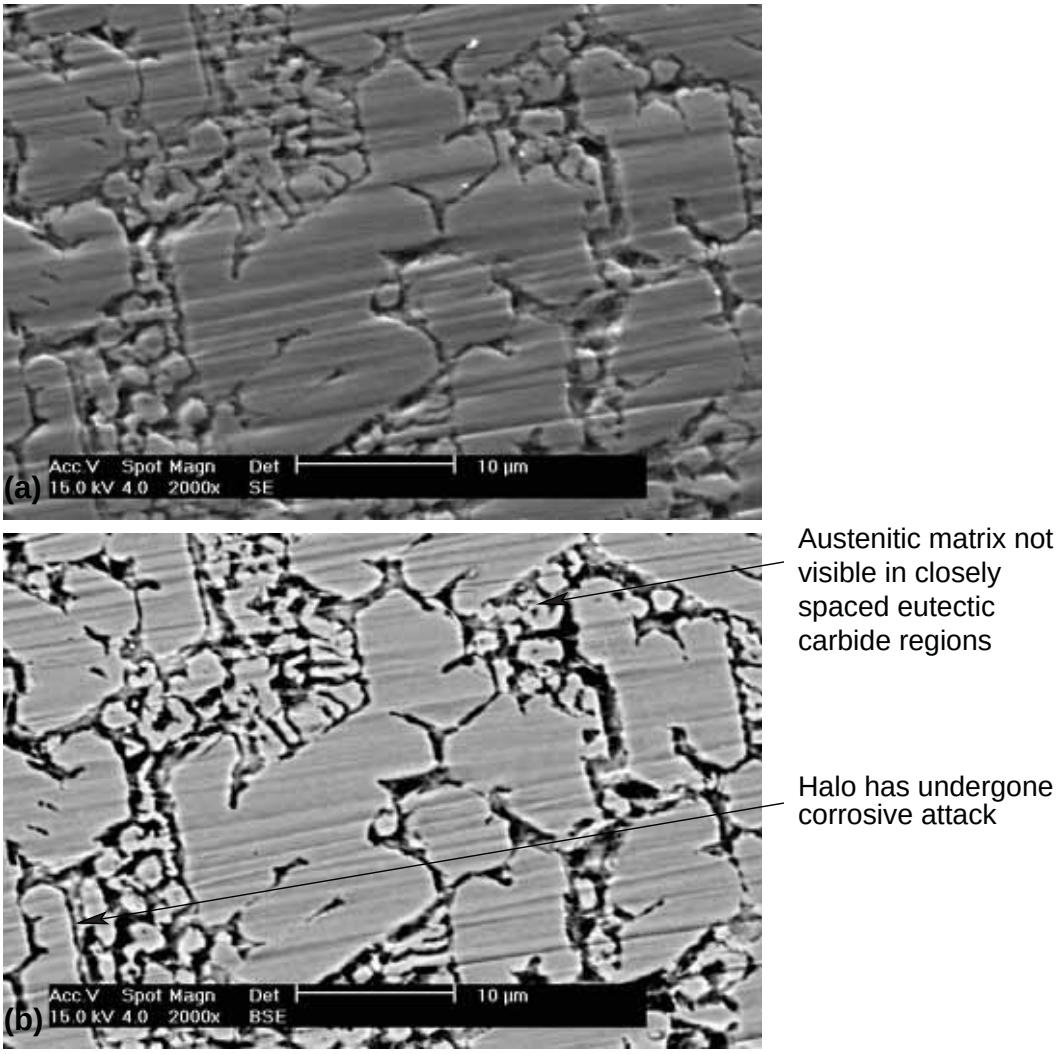

Figure 6.38: WeldoverlayA after immersion at the active dissolution potential of -0.825V_{SHE} for 4 hours. (a) General secondary electron micrograph of the area that has been cleaned. (b) Corresponding back scattered electron micrograph of (a).

Passive Potential

The WeldoverlayA sample after constant potential immersion in the passive potential regime at -0.406 V_{SHE} for 4 hours is shown in Figure 6.39. After the test the sample was covered with black/red corrosion product. The majority of the corrosion product could be removed by gently rubbing with a red rubber stopper. However, traces of the corrosion product could not be removed by rubbing indicting that it was tightly adhered to the alloy. The 1200 grit polishing marks were only slightly distinguishable on the sample surface after cleaning. Figure 6.39(b) shows a light micrograph of the test surface. The optical micrographs show

that the corrosion product could be removed from the carbides but remained adhered to the matrix and is of a red colour. It could not be easily determined whether the matrix had undergone significant amounts of corrosion from these images.

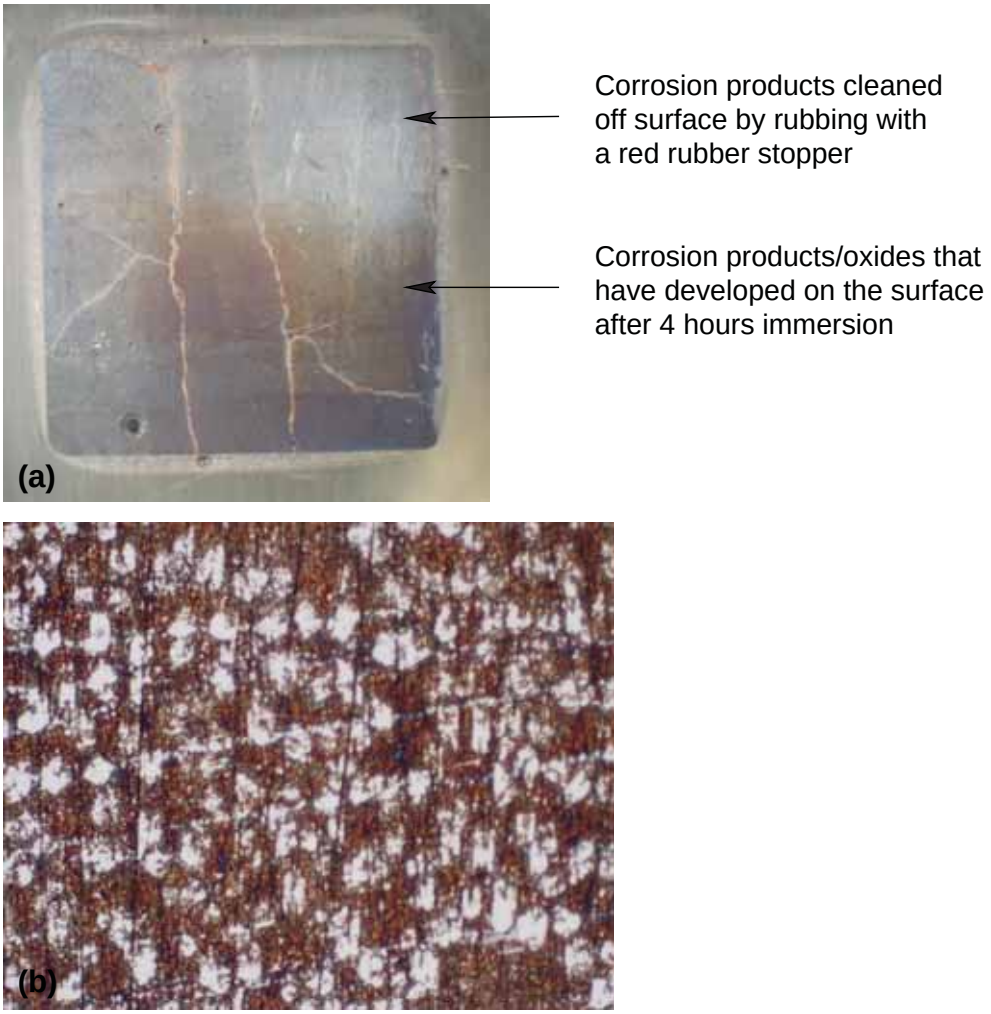

Figure 6.39: WeldoverlayA after immersion in the passive potential regime at -0.406 V_{SHE} for 4 hours. (a) General overview of sample with top section having the corrosion product/oxides removed by rubbing with a red rubber stopper. (b) Light micrograph of the top cleaned section of the immersion test sample, 500x magnification.

Further examination in a FESEM revealed that the matrix surrounding the primary and eutectic carbides did suffer corrosion, Figure 6.40. Figure 6.40(a) is a general secondary electron micrograph of the sample surface and shows that the matrix had been preferentially attacked in comparison with the carbides. The higher magnification back scattered electron micrographs give a better indication of the corrosive attack, Figure 6.40(b) and (c). The austenite halos surrounding the primary carbides remain largely intact but have undergone corrosion at the austenite carbide interface. The eutectic austenite that resides in between the eutectic M_7C_3 carbides is not readily visible, indicating it has undergone significant corrosive attack. The carbides did still show signs of the 1200 grit polishing marks but were, however, not as pronounced as seen in previous samples. This could possibly indicate that the carbides do

undergo a small degree of corrosive attack under these conditions. The test sample surface has a fine dispersion of an unidentified corrosion product covering the surface which could not be removed by rubbing with a red rubber stopper, Figure 6.40(c). No significant traces of the plate like crystals were found on the as tested area (the area that has not been cleaned).

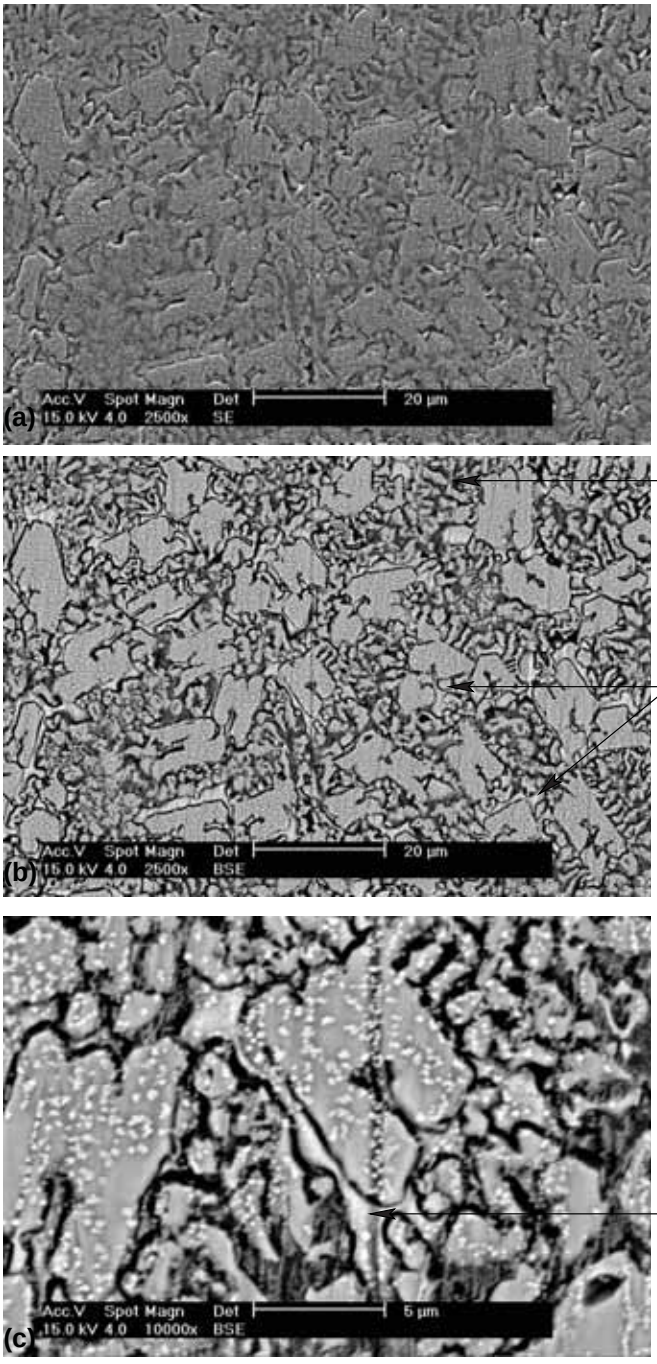

Figure 6.40: WeldoverlayA after immersion in the passive potential regime at -0.406 V_{SHE} for 4 hours.(a) General secondary electron micrograph of area that has been cleaned. (b) Higher magnification back scattered electron micrograph of (a). (c) Higher magnification back scattered electron micrograph of (c).

6.3.3 Summary

Immersion tests in sodium aluminate at 90°C were done for a hypoeutectic casting (HypoA), a hypereutectic casting (HyperA) and a hypereutectic weld overlay (WeldoverlayA). Three different potentials were investigated, these being the open circuit potential, a potential corresponding to the active dissolution regime and a potential corresponding to the passive potential regime. Each immersion test was done for four hours and the surface of the sample was examined using optical and electron microscopy.

For all test conditions the corrosion of the carbides either did not occur, or was negligible, and the matrix corroded preferentially. All three materials were found to corrode during immersion in the hot caustic sodium aluminate solution at the open circuit potential. Holding the materials within the active potential regime clearly increased matrix corrosion for the hypereutectic casting and weld overlay. The corrosion rate of the matrix was reduced for all materials by holding the materials at a passive potential. The castings demonstrated better corrosion resistance that the weld overlay sample with the weld overlay susceptible to severe corrosion of the matrix even in the passive potential regime. Preferential corrosion of the matrix was found to occur at the carbide-matrix interface, which was most clearly seen on the weld overlay sample.

Chapter 7

Erosion-Corrosion Tests

7.1 Introduction

Erosion-corrosion tests involved slurry pot tests and electrochemical erosion-corrosion tests. The slurry pot test apparatus consisted of a rotor with three pairs of test samples that were rotated in an erosive corrosive slurry. The slurry pot tests provided comparative wear rates by means of weight loss. An erosion-corrosion test apparatus was developed as part of this work. It had the capability to measure in-situ electrochemical corrosion data under erosion-corrosion conditions.

7.2 Slurry Pot Tests

Slurry pot testing was undertaken to compare the weight loss of selected high chromium white iron castings and weld overlays in a controlled wear environment. A low carbon steel was used as a reference material. These tests were carried out in the apparatus described in Section 2.5.1.1 and schematically shown in Figure 2.8. The test environment consisted of a liquor phase, which was the sodium aluminate solution used for the corrosion tests, and an abrasive phase. The abrasive phase, or erodent, consisted of various sized quartz particles based on averaged data from from the red side of the alumina refining process. The size and proportion of the quartz particles are given in Table 2.3. The use of a variable sized erodent was chosen to replicate more accurately what is found in industrial process.

7.2.1 Materials Investigated

The alloys investigated were hypereutectic and hypoeutectic high chromium white iron castings, a hypereutectic high chromium white iron weld overlay deposited on a steel substrate

using flux cored arc welding and a hypoeutectic cobalt based Stellite 6 weld overlay deposited on a steel substrate using plasma transferred arc (PTA) welding. The cast samples and the hypereutectic weld overlay samples were sectioned from worn plant components, and the Stellite 6 sample was sectioned from a bead on plate PTA deposit.

The hypereutectic casting, HyperA, was in the as-cast condition and was the same alloy that had previously been used in the corrosion tests. The microstructure of HyperA, Figure 7.1, consisted of large primary M_7C_3 carbides in a matrix of austenite, martensite and secondary carbides.

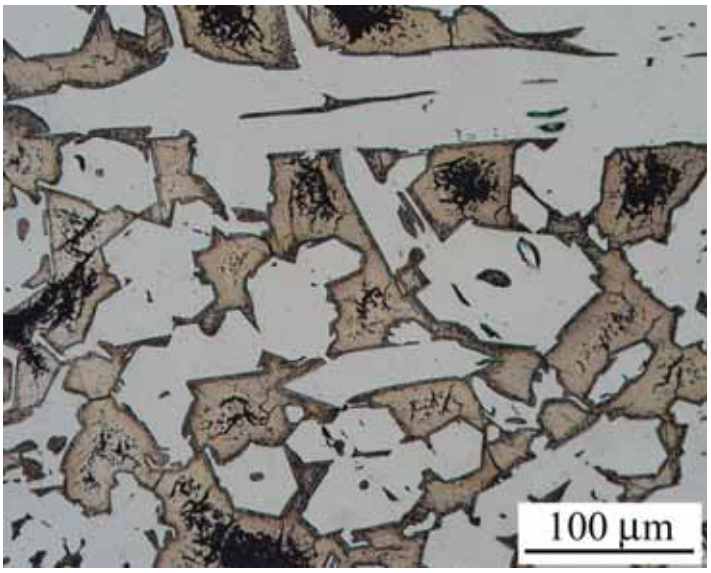

Figure 7.1: Light micrograph of the HyperA casting sample.

The hypoeutectic casting, HypoB shown in Figure 7.2, had undergone a destabilization heat treatment to transform the primary and eutectic austenite to a matrix of martensite and secondary $M_{23}C_6$ carbides. The microstructure consisted of eutectic M_7C_3 carbides in a matrix of martensite and secondary carbides.

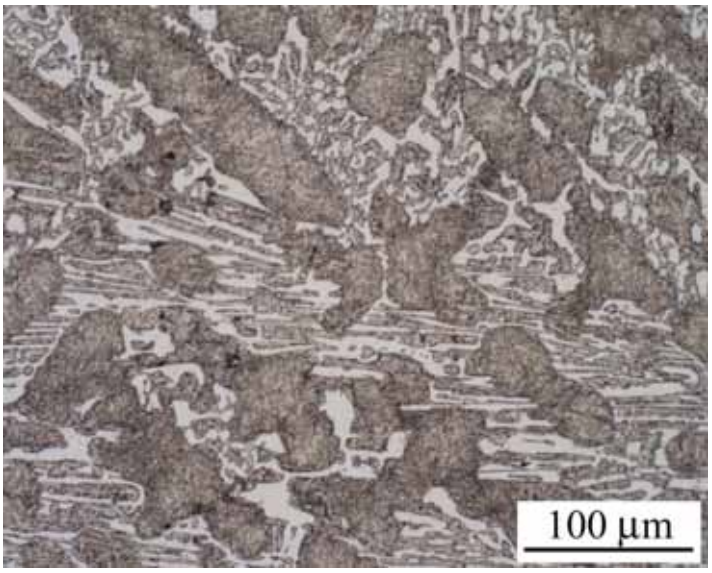

Figure 7.2: Light micrograph of the HypoB casting sample.

The hypereutectic weld overlay, WeldoverlayA, was the same alloy that had previously been used in the corrosion tests and was deposited onto a steel substrate using the flux-cored arc welding process. The microstructure consisted of primary M_7C_3 carbides and a eutectic of austenite and eutectic M_7C_3 carbides, Figure 7.3. It should be noted that the primary and eutectic M_7C_3 carbides of the weld overlay were much finer than those of the hypoeutectic casting due to the faster cooling rate of the weld overlay. The faster cooling rate of the weld overlay also lead to undercooling resulting in the development of the branched primary carbides and the complex regular eutectic.

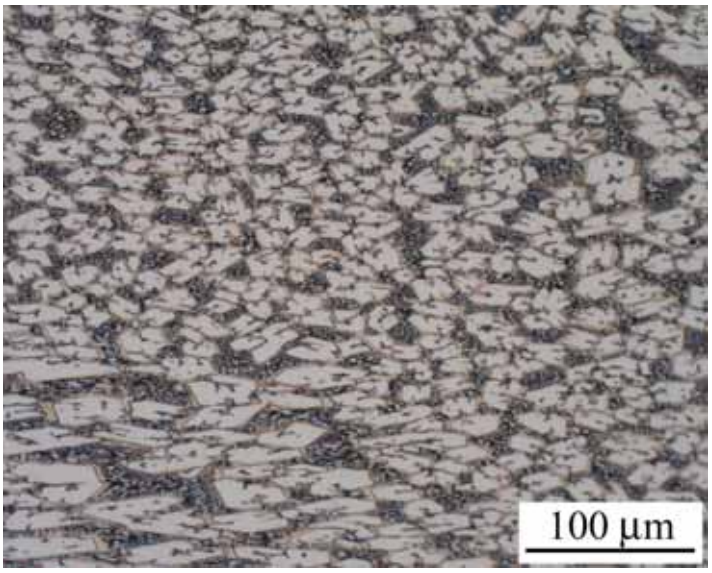

Figure 7.3: Light micrograph of the WeldoverlayA sample.

The Stellite 6 PTA deposit, Figure 7.4, had a hypoeutectic microstructure of primary dendrites of solid solution cobalt and an inter-dendritic eutectic of solid solution cobalt and

eutectic M_7C_3 carbides (the M in this case representing a combination of chromium and cobalt). Unlike the hypereutectic high chromium weld overlays, the PTA deposited Stellite overlays did not contain check cracks.

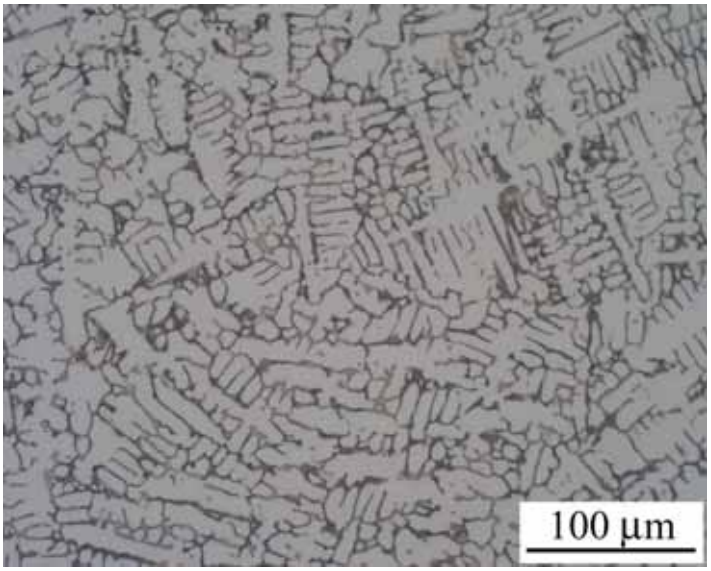

Figure 7.4: Light micrograph of Stellite PTA weld overlay sample.

7.2.2 Experimental Methodology and Test Samples

The experimental methodology is described in detail in Section 2.5.1.2 and is only briefly summarized. The wear face of the test samples was wet ground to a 1200 grit finish in such a manner to align the scratch marks with the long axis of the sample. The samples were degreased in acetone and hot air dried prior to being weighed to an accuracy of 0.1 mg. The samples, tested in pairs, were located in the rotor such that the protrusion was 19.0±0.1 mm. The assembled rotor was placed in the preheated slurry maintained at a temperature of 90±1°C by immersion in a water bath, and coupled to the drive unit. The slurry consisted of the same sodium aluminate solution used for corrosion tests but with the addition of quartz particles (480 g sized quartz in 720 mL solution). The test was started and the rotational speed of the rotor set to 1000 rpm using a digital frequency controller. The duration of the test was 5 hours after which the rotor was removed and cooled in purified water. The test samples were removed and any residual slurry constituents removed by gently rubbing with a red rubber stopper. The samples were further rinsed in acetone and hot air dried prior to weighing. The weight loss of the two test samples was calculated and the results averaged. The tests were repeated to ensure the accuracy of the results.

A commonly encountered problem with hypereutectic high chromium white iron weld overlays is check cracking, Figure 7.5. The check cracking is caused by the relieving of residual stresses produced during the solidification and cooling of the molten weld pool. The check cracks generally extend from the surface of the overlay to the substrate-hard facing interface.

It was necessary to fill the check cracks with an epoxy resin to ensure that the cracks did not fill with quartz particles during testing as this would lead to inconsistencies in results. This was done using standard vacuum techniques.

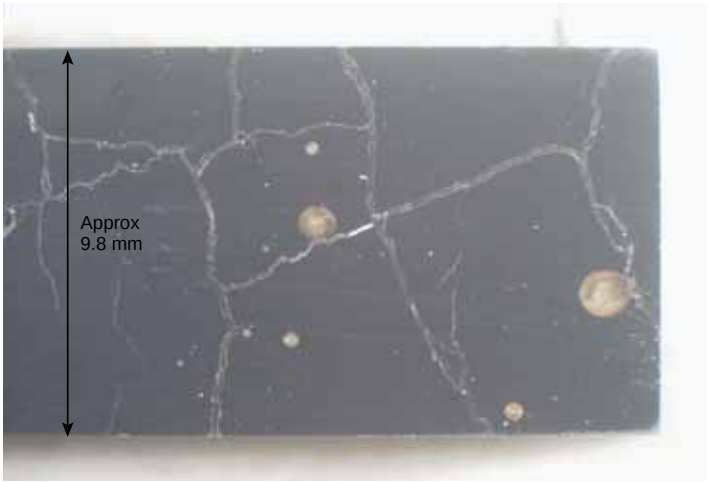

Figure 7.5: WeldoverlayA test sample showing the check cracks that have been filled with epoxy.

7.2.3 Results

The slurry pot weight loss results, in ascending order, are reported as the weight loss relative to low carbon steel, Figure 7.6. The average weight loss of low carbon steel was 14.43 mg. Figure 7.6 also includes a plot of the bulk hardness of the alloys.

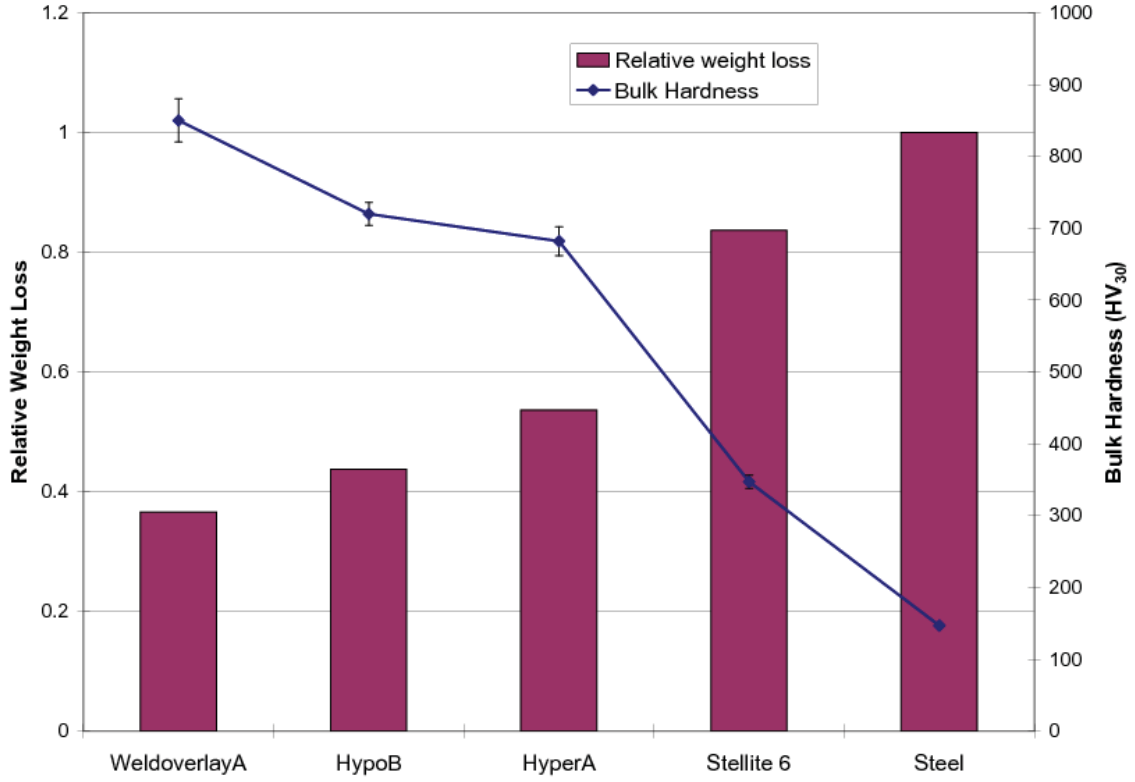

Figure 7.6: Slurry pot weight loss results in sodium aluminate solution with quartz particles (480 g sized quartz in 720 mL solution) compared with low carbon steel.

The wear surfaces of the samples were examined using a field emission scanning electron microscope (FESEM) with EDAX capabilities. The wear surface of AS1163: C350LO low carbon steel is shown in Figure 7.7. The wear surface is microscopically rough and a number of distinct wear tracks are noticeable. It was also common to find non-metallic particles that had become embedded in the material. Arrowed in Figure 7.7(a) is a particle that has gouged a groove in the steel before becoming embedded. Analysis of the particle using EDAX found the particle to consist almost entirely of silicon and oxygen, Figure 7.7(c), which indicates that the particle is the quartz erodent. The higher magnification secondary electron image shown in 7.7(b), shows a region that has been significantly deformed by a particle impact. Material has been deformed to form a protruding ridge.

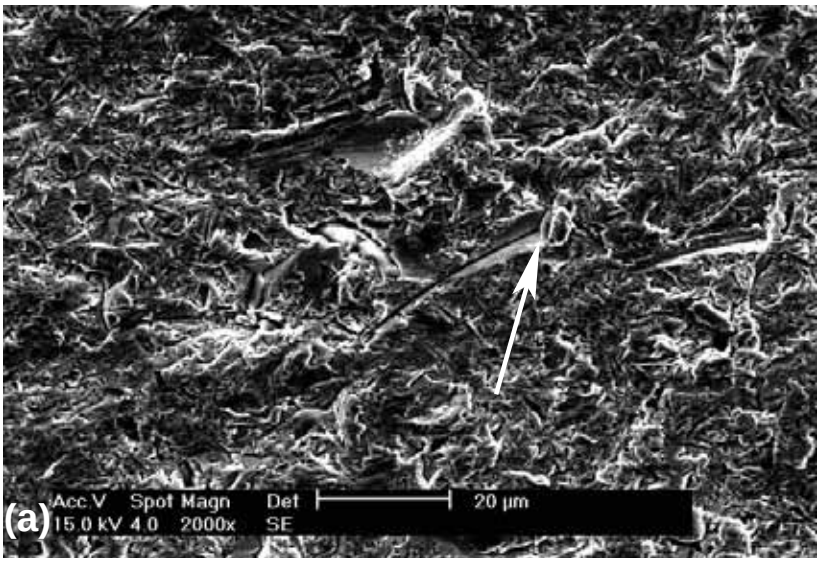

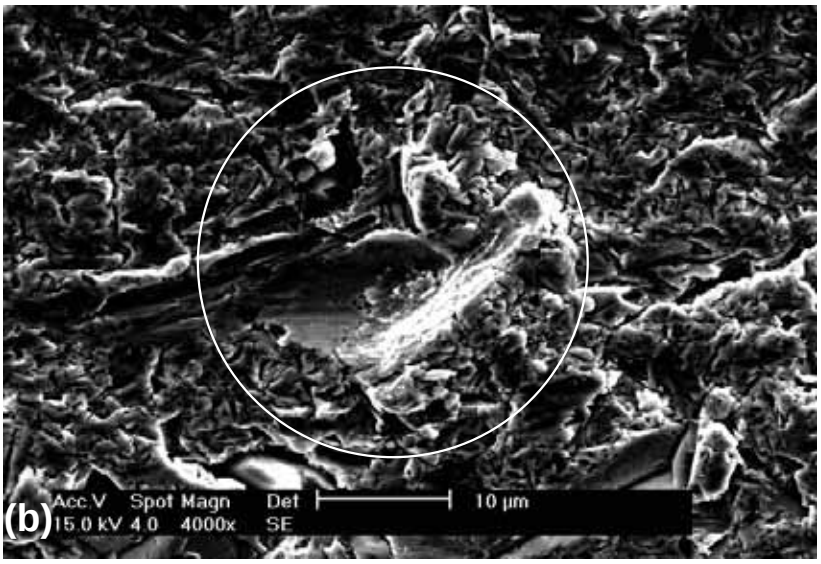

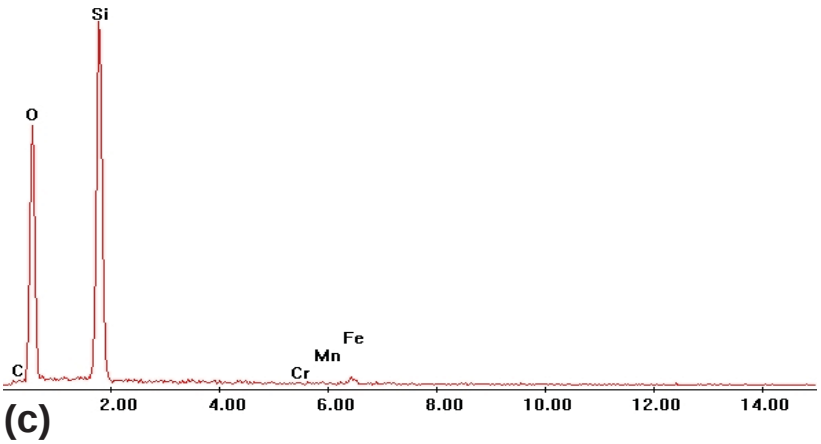

Figure 7.7: Secondary electron images of the steel wear surface. (a) arrow points to embedded particle. (b) circle shows a region of significant deformation due to particle impingement. (c) EDAX analysis of embedded particle arrowed in (a).

The wear surface of Stellite 6 PTA weld overlay is shown in Figure 7.8. In a similar manner to the steel sample, there are a number of particle impact craters where matrix material has been extruded up and out of the impact craters. In many instances, the quartz particles remained embedded in the matrix material as shown in the higher magnification images, Figures 7.8(b) and (c). The embedding of the quartz particles had severely plastically deformed the matrix but had not necessarily removed the matrix. The eutectic M_7C_3 carbides could not be distinguished in the wear surface examination.

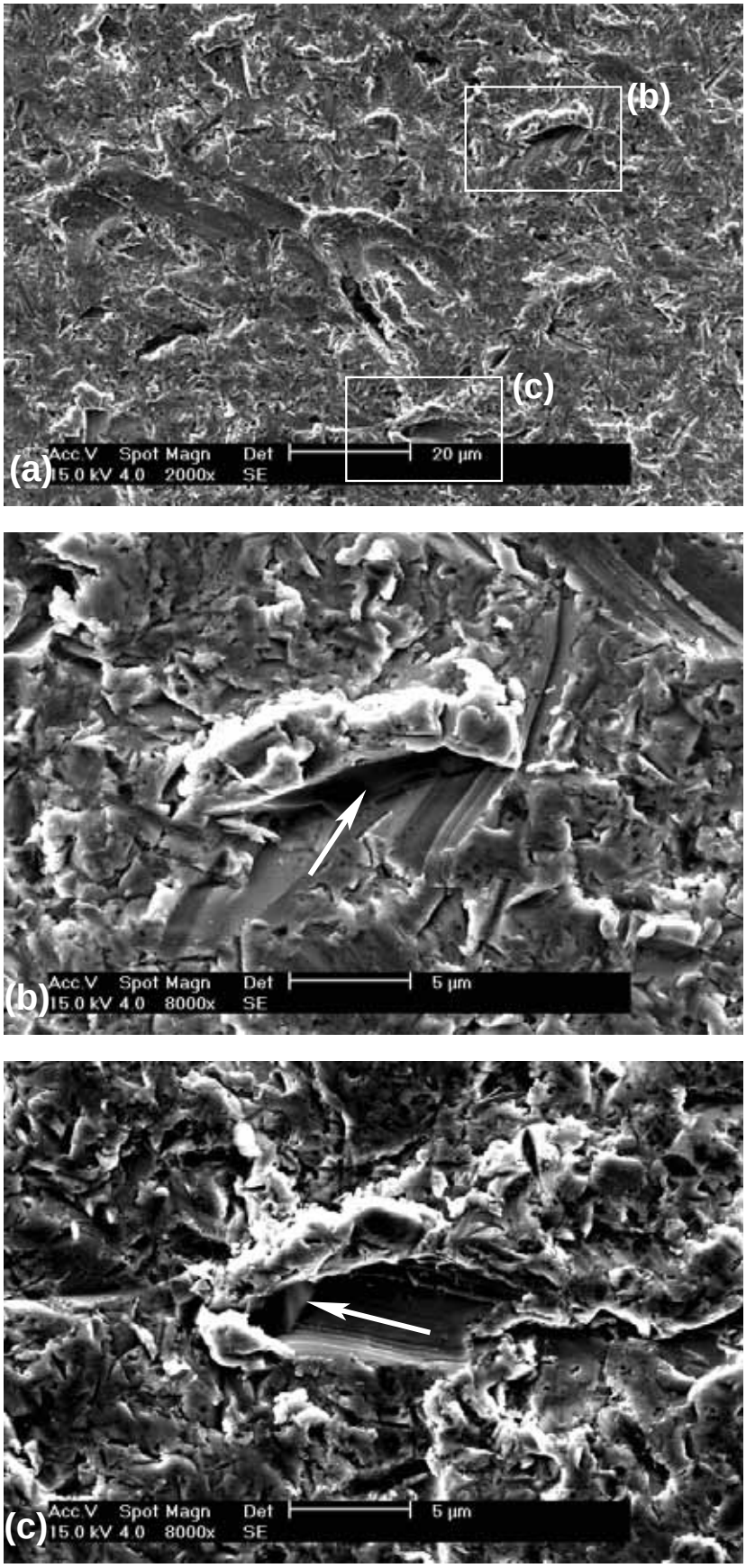

Figure 7.8: Secondary electron images of the Stellite PTA weld overlay wear surface. Boxes labeled in image (a) are expanded in images (b) and (c). Arrow in image (b) and (c) point to embedded quartz particles and associated wear groove.

The wear surface of the hypereutectic casting, HyperA, is shown in Figure 7.9. The large primary M_7C_3 carbides can be seen clearly (darker phase) and are found to be proud of the matrix. Higher magnification images, Figures 7.9(b) and (c), show that the matrix (lighter phase) has undergone more significant wear than the primary carbide. However, the primary M_7C_3 carbides have undergone some wear as shown by their surface appearance and the rounding at their periphery. The matrix is found to have a microscopically rough surface like the previous Stellite 6 and steel samples, and contain a number of particle wear grooves. The arrowed features in Figures 7.9(b) and (c), show where a particle has impinged the surface and plastically deformed and extruded the matrix material ahead of the particle. It was also common to find that the deformation of the matrix material would stop at a carbide, Figures 7.9(c).

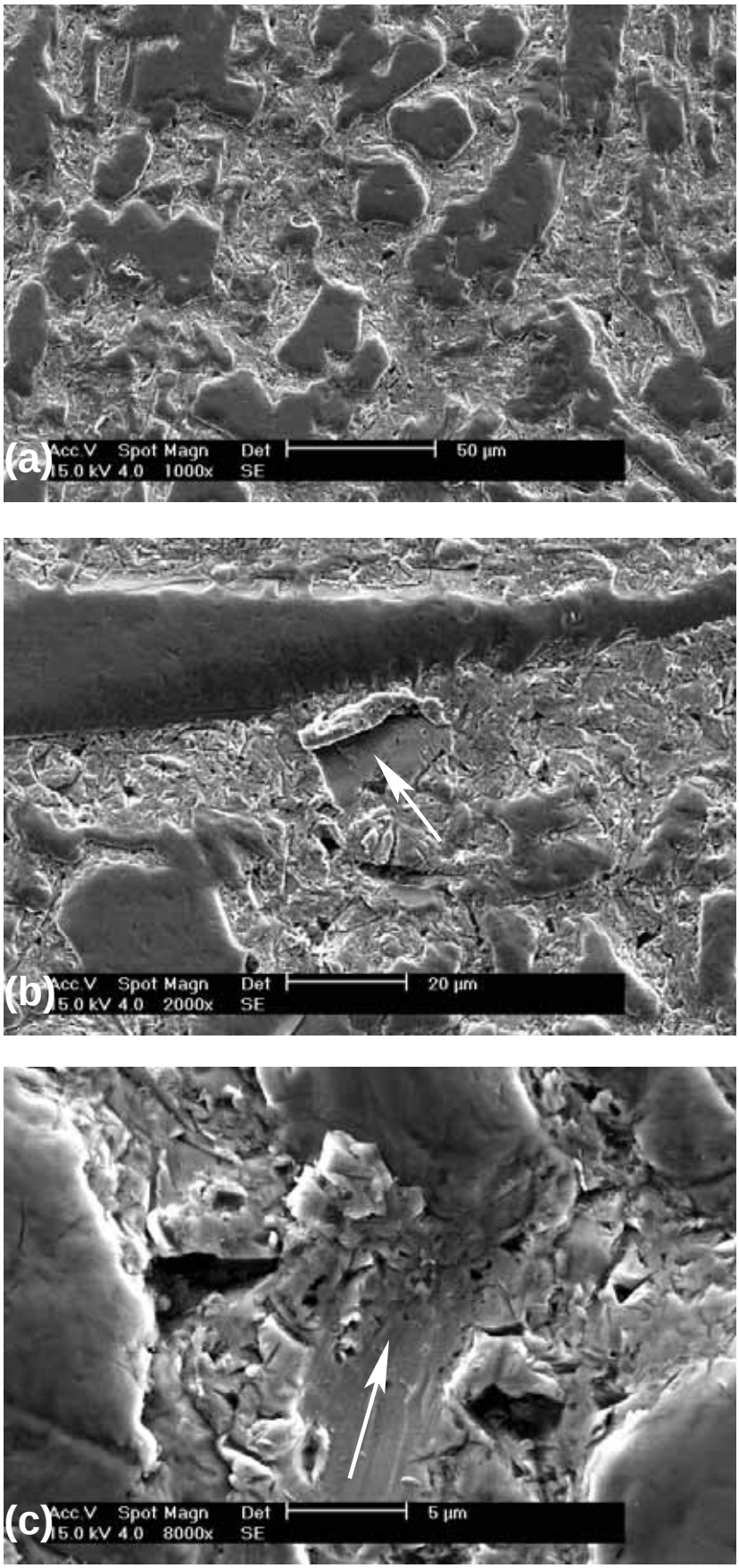

Figure 7.9: Secondary electron images of the HyperA casting wear surface. Arrow in image (b) points to highly deformed section of the matrix. Arrow in image (c) points to wear groove and matrix material that has been extruded against a carbide.

The wear surface of the hypoeutectic heat treated casting, HypoB, is shown in Figure 7.10, which had a distinctly different wear surface to the Stellite 6 and HyperA casting sample. The martensitic matrix of the HypoB casting did not exhibit the degree of deformation caused by particle impingement as was the case for the Stellite 6 deposit and HyperA casting. Figures 7.10(b) and (c) illustrate an embedded quartz particle and the reduced amount of plastic deformation of the matrix due to particle impingement. It was also apparent that the matrix of the hypoeutectic casting was not as recessed with respect to the eutectic M_7C_3 carbides as it was for the HyperA casting in Figure 7.9. It was also evident that the eutectic M_7C_3 carbides were rounded in a similar manner to the HyperA casting. However, due to the smaller size of the eutectic M_7C_3 carbides, the carbides appear more rounded.

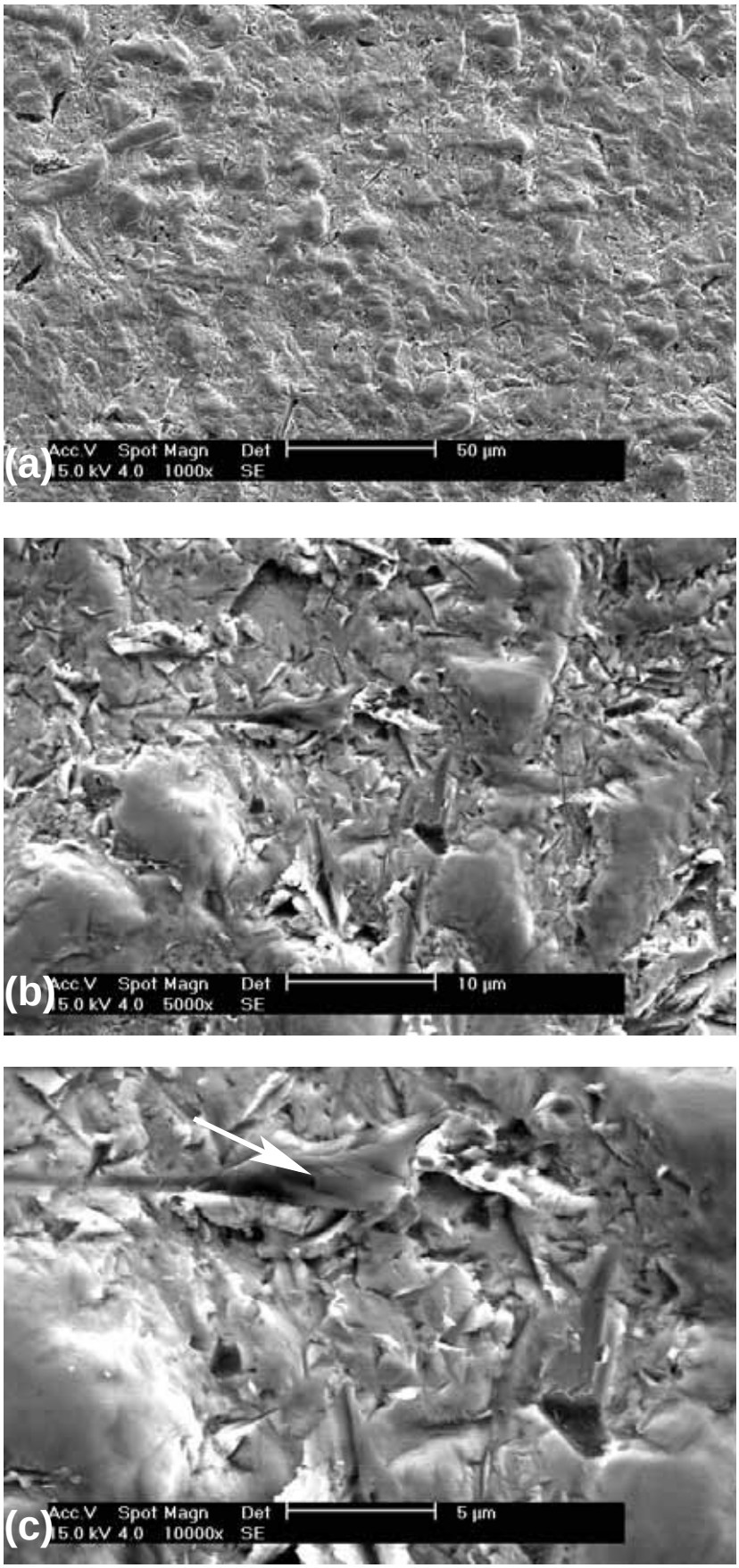

Figure 7.10: Secondary electron images of the HypoB casting wear surface. (c) higher magnification of area in (b). Arrow in image (c) points to embedded quartz particle.

The wear surface of the hypereutectic weld overlay, WeldoverlayA, is shown in Figure 7.11. The primary M_7C_3 carbides have undergone wear, in a similar manner to the HyperA casting as evident by the surface appearance and the rounding at the periphery of the carbides. The carbides are standing in relief due to the removal of the austenitic matrix. It was difficult to resolve the austenitic matrix as it was significantly recessed with respect to the carbides. Due to the close spacing of the primary carbides in the weld overlay, ploughing grooves were not found in the matrix. However, Figure 7.11 shows a quartz particle embedded within the matrix against a primary M_7C_3 carbide.

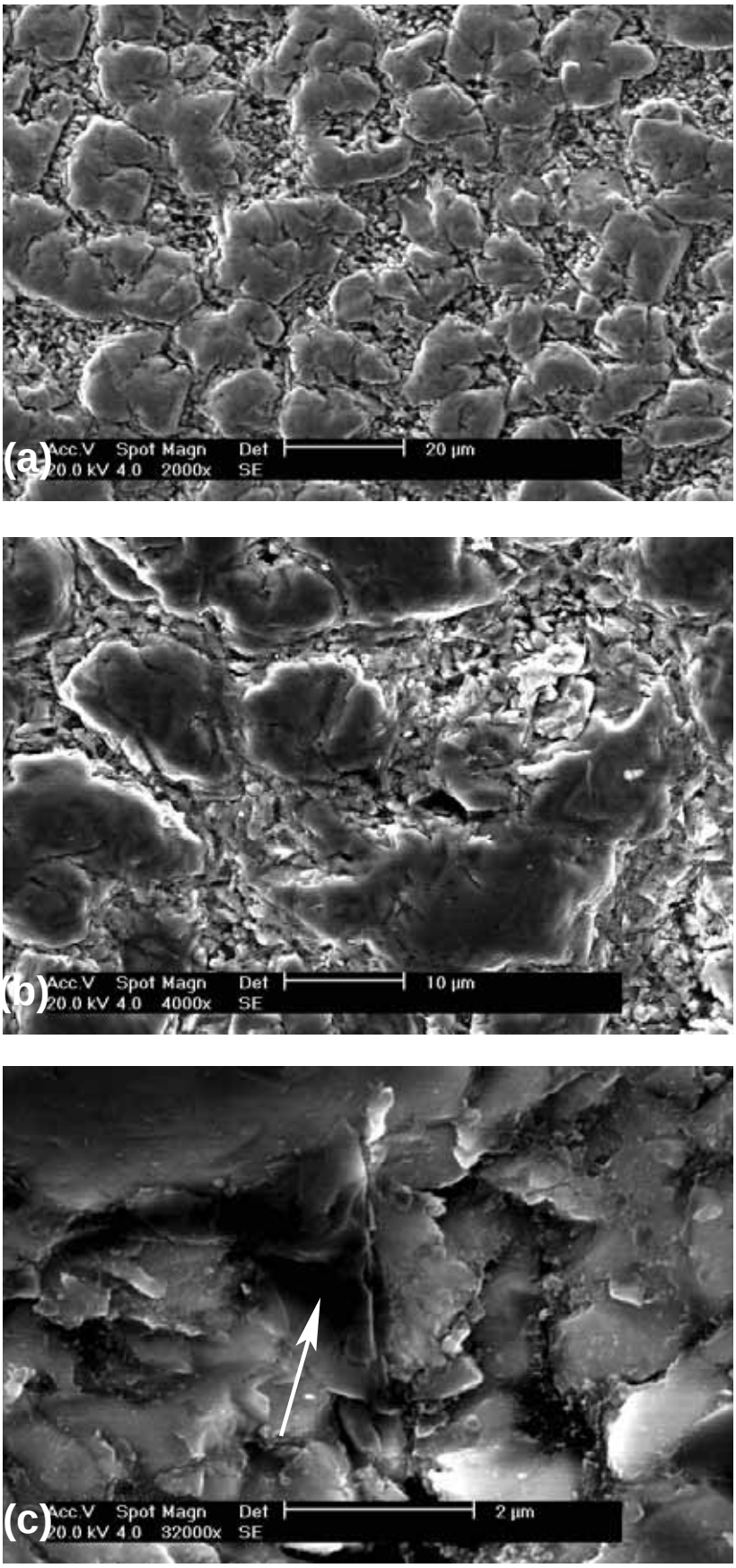

Figure 7.11: Secondary electron images of the WeldoverlayA wear surface. Arrow in image (c) points to embedded quartz particle.

7.2.4 Summary

Three high chromium white iron materials and a cobalt based Stellite plasma transferred arc (PTA) weld overlay were erosion-corrosion wear tested in slurry of various size quartz particles and sodium aluminate solution at 90°C. A low carbon steel test sample was used as a reference for reporting relative weight loss.

The wear rate of the materials was found to be directly related to the bulk hardness of the material. The high chromium white iron weld overlay having the highest bulk hardness had the lowest wear rate. This was followed by a heat treated hypoeutectic high chromium white iron casting which had the second highest bulk hardness.

The wear of the white iron materials was dominated by matrix removal. However, the carbides also wore but at a reduced rate. This was indicated by the rounding at the periphery of the exposed carbides standing proud of the matrix. The wear of steel and the matrix of the white irons was found to occur by a deformation mechanism where impinging particles displaced material either side of a wear groove. For materials with a harder matrix, the amount of displaced material and the size of wear grooves were decreased.

The slurry pot tests have shown that for the high chromium white irons investigated that rate of wear was approximately half that of steel. The wear surface examination found the carbides, although showing wear damage at the periphery of the carbides, to be standing proud of the matrix and therefore beneficial in affording the matrix protection from erosion. These results indicate that high chromium white iron particle-reinforced composites offer superior wear resistance to that of single-phase steels having similar properties to the white iron matrix.

7.3 Electrochemical Erosion-Corrosion Tests

An electrochemical erosion-corrosion test apparatus was designed to obtain in-situ electrochemical corrosion data during erosive-corrosive wear. The test apparatus is described in Section 2.5.2.1 and shown in Figures 2.10 to 2.14. A single tests specimen was positioned on the external wall of the test chamber and an impeller was used to stir the liquid or slurry. Electrochemical data was obtained using a three electrode test cell with the reference electrode housed in an external compartment and the counter electrode (a stainless steel plate) contained within the test cell. The test environment consisted of the sodium aluminate solution used in previous corrosion tests, with either or without the variable sized erodent used for the slurry pot tests.

7.3.1 Materials Investigated

Two high chromium white irons were investigated. These were the hypoeutectic heat treated HypoA casting and the hypereutectic WeldoverlayA. The microstructures were characterized in Section 2.2.

7.3.2 Experimental Methodology

The experimental methodology is described in Section 2.5.2.1. Three tests on each sample were done. The first test was done under static conditions to establish a baseline and for comparison with the test done in the corrosion cell. The second test was done without abrasive particles but stirring the solution. This was to investigate the effect solution velocity alone has on the polarization behaviour. The third test was done in a stirred slurry using the same slurry as used for the slurry pot tests.

7.3.3 Results

HypoA

The anodic polarization curves for the HypoA casting in deaerated sodium aluminate solution under static, stirred with no abrasive and stirred with slurry test environments are shown in Figure 7.12. Potential and current densities for significant features of the polarization curves are summarized in Table 7.1. The reported corrosion current densities are estimated from the polarization curves as Tafel tests were not done.

Comparing the polarization curve under static conditions with the polarization curve previously done in Section 6.2.2, Figure 6.5 using the corrosion test cell, it is found that the curves are similar. There were negligible variations in rest potential and critical potential which varied by 6 and 11 mV respectively. The current density results varied more significantly for the two corrosion test apparatus. This is attributed to the different three-electrode configurations.

When the solution was stirred, without any abrasives, the polarization curve was similar to the static polarization curve. The most noticeable differences were the shift in rest potential of the stirred polarization curve in the anodic direction by 40 mV, the change in cathodic and anodic Tafel slopes and the change in passive behaviour following the critical potential. A significant increase in the corrosion current density and passive current density was found due to stirring of the solution. The corrosion current density increased by over 100 μA/cm^{2}compared with the static conditions.

The erosion-corrosion test using a slurry of sodium aluminate and sized quartz particles resulted in a polarization curve very similar to the stirred polarization curve. Noticeable differences include a small shift in the rest potential in anodic direction by 15 mV, a slight

increase in the critical current density and a more significant increase in current densities in the passive regions. The corrosion current density was found to be similar to the current density under stirred conditions, varying by 15 μA/cm^2.

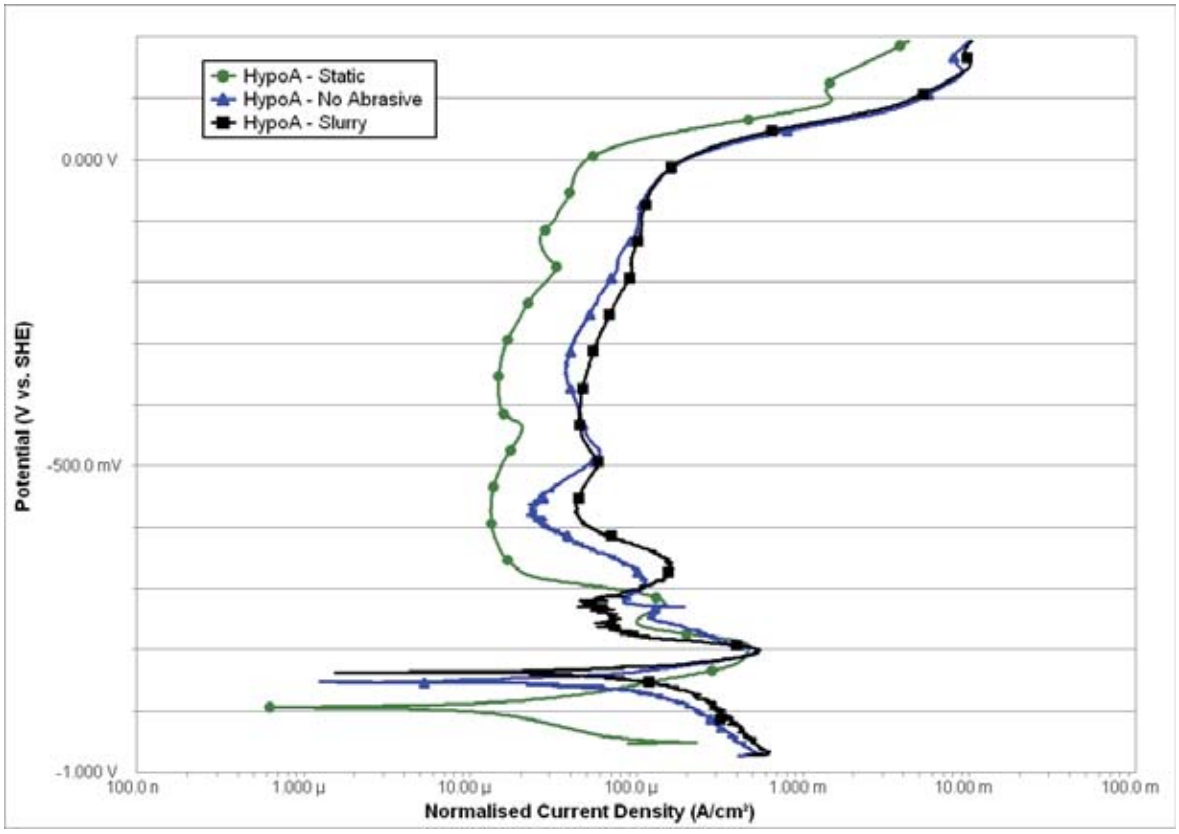

Figure 7.12: Anodic polarization curves for HypoA using the erosion-corrosion test apparatus under static, stirred with no abrasive and with slurry.

Table 7.1: Potential and corrosion test results for HypoA in sodium aluminate solutions under static, stirred and slurry test environments. Results determined from polarization curves.

HypoA	E_{corr} (V_{SHE})	I_{corr} ($\mu A/cm^2$)^	$E_{critical}$ (V_{SHE})	$I_{critical}$ ($\mu A/cm^2$)	$I_{passive}$* ($\mu A/cm^2$)
Static	-0.894	32.2 ± 4.3	-0.793	476.4	16.0
Stirred	-0.852	156.9 ± 33.2	-0.802	537.1	40.3
Slurry	-0.837	172.9 ± 13.6	-0.800	551.7	55.9

*I_{pass} at a potential of -0.306 V_{SHE} (-0.5 $V_{Red\ Rod}$)
^I_{corr} standard deviation determined from multiple Tafel fits

WeldoverlayA

The anodic polarization curves for WeldoverlayA in deaerated sodium aluminate solution under static, stirred with no abrasive and slurry test environments are shown in Figure 7.13. Potential and current densities for significant features of the polarization curves are summarized in Table 7.2. The reported corrosion current densities were estimated from the

polarization curves as Tafel tests were not done.

The polarization curve under static conditions was similar to the polarization curve previously done in Section 6.2.4, Figure 6.21 using the corrosion test cell. There were negligible variations in rest potential and critical potential which varied by 13 and 7 mV respectively. The current density results varied more significantly for the two corrosion test apparatus. This is attributed to the different three-electrode configuration.

When the solution was stirred, without any abrasives, the polarization curve was similar to the static polarization curve. The most noticeable differences were the shift in rest potential of the stirred polarization curve in the anodic direction by 40 mV, the change in cathodic and anodic Tafel slopes and the change in passive behaviour following the critical potential. A significant increase in the corrosion current density and passive current density was found due to stirring of the solution. The corrosion current density increased by over 200 μA/cm^{2}compared with the static conditions.

The erosion-corrosion test using a slurry of sodium aluminate and sized quartz particles resulted in a polarization curve very similar to the stirred polarization curve. Noticeable differences include a slight increase in the critical current density and a more significant increase in current densities in the passive regions. The corrosion current density under erosion-corrosion conditions was found to increase by 50 μA/cm^2 compared with the stirred conditions.

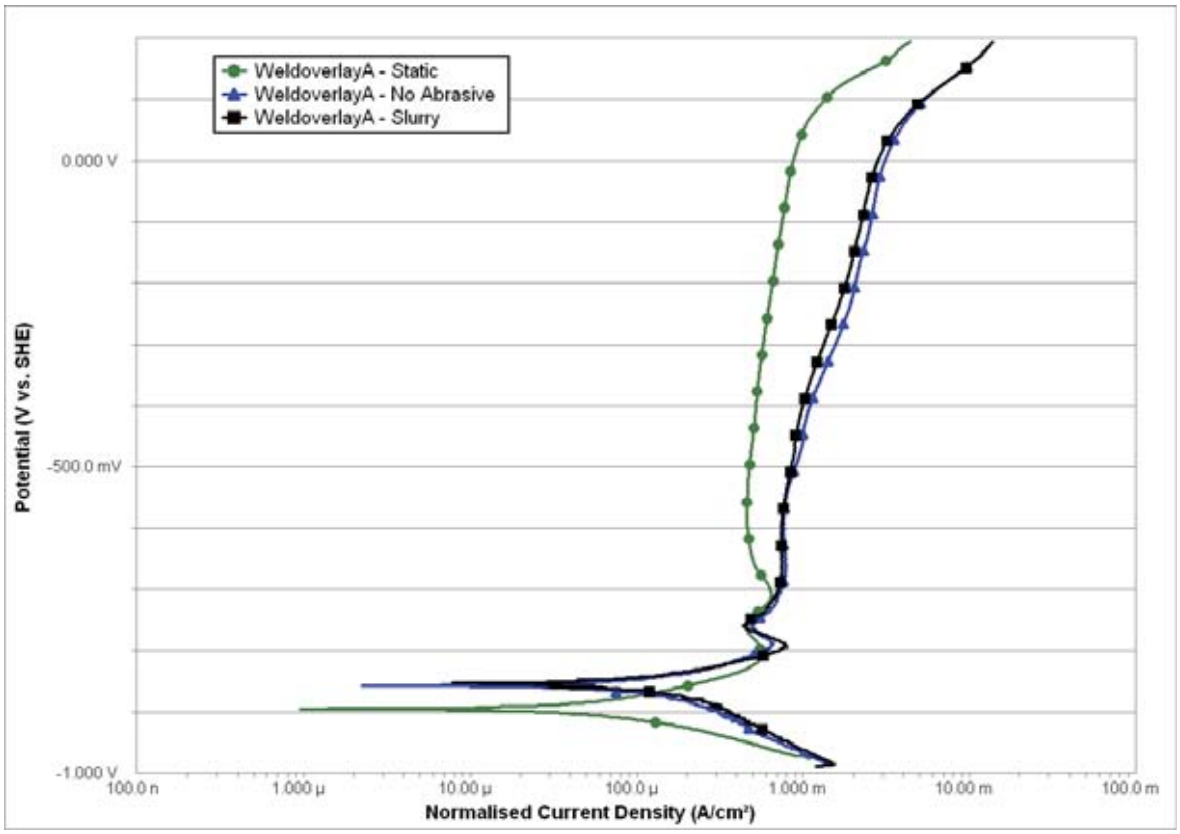

Figure 7.13: Anodic polarization curves for WeldoverlayA using the erosion-corrosion test apparatus under static, stirred with no abrasive and with slurry.

Table 7.2: Potential and corrosion test results for WeldoverlayA in sodium aluminate solutions under static, stirred and slurry test environments. Results determined from polarization curves.

WeldoverlayA	E_{corr} (V_{SHE})	I_{corr} ($\mu A/cm^2$)^	$E_{critical}$ (V_{SHE})	$I_{critical}$ ($\mu A/cm^2$)	$I_{passive}$* ($\mu A/cm^2$)
Static	-0.895	85.4 ± 6.4	-0.807	560.0	571
Stirred	-0.857	226.0 ± 12.8	-0.790	658.3	1533
Slurry	-0.854	277.3 ± 18.2	-0.792	798.2	1305

*I_{pass} at a potential of -0.306 V_{SHE} (-0.5 $V_{Red\ Rod}$)
^I_{corr} standard deviation determined from multiple Tafel fits

7.3.4 Summary

A hypoeutectic high chromium white iron casting that had undergone a destabilization heat treatment and a hypereutectic high chromium white iron weld overlay were tested in a purpose built erosion-corrosion tests apparatus that can measure in-situ electrochemical corrosion data. Three corrosion tests were done for each sample. These were a static corrosion test to establish baseline results and to compare with previous results form the corrosion test cell, corrosion tests where the liquid was stirred to investigate the effect of solution agitation and finally a corrosion test using a stirred slurry to investigate the electrochemical erosion-corrosion behaviour. All tests were done at 90°C under deaerated conditions using the same sodium aluminate solution as used in previous corrosion and slurry pot tests.

The test results under static condition produced similar polarization curves to those found using the corrosion test cell except for variations in current density. These variations were attributed to the different three electrode cell configuration used in the erosion-corrosion test apparatus. The stirring of the solution without any abrasive particles was found to significantly increase the corrosion current density, the critical current density and the passive current density. Polarization curve features for the static and stirred cases occurred at similar potentials. Polarization tests under erosive-corrosive conditions, resulted in a further increase in the free corrosion rate and the critical current density. The passive current density for the casting sample was found to increase under slurry test conditions but was found to decrease for the weld overlay sample.

Part V

Discussion and Conclusions

Chapter 8

Discussion

8.1 Development of Microstructure

The microstructure of four different high chromium white iron castings and two different high chromium white iron weld overlays were examined. Material characterization included optical microscopy, electron microscopy, electron probe microanalysis, macro and micro hardness. All the samples, with the exception of the experimental casting HyperEXP, were commercially produced. The bulk chemical composition along with the chromium to carbon ratio and carbide volume fraction of the investigated alloys are summarized in Table 8.1.

The development of microstructure in high chromium white irons has been extensively reviewed in the literature, with the review of microstructure by Tabrett et al. (1996) and Laird II et al. (2000) being two of the most comprehensive. However, as will be discussed in the following sections, there is still room for expansion of this knowledge particularly relating to the development of microstructure in hypereutectic high chromium white iron castings and weld overlays. Heat treatments of selected high chromium white irons were done to assist in understanding the changes in properties due to variations in microstructure.

The results reported in Chapter 5 are discussed based on the factors outlined in Figure 3.1; "Factors influencing microstructure and hardness of high chromium white irons and their influence on corrosion and wear." This includes solidification, heat treatments after solidification, chemical composition of phases, carbide volume fraction and hardness.

Table 8.1: Summary of bulk chemical compositions, Cr/C ratio and CVF for the high chromium white iron castings and weld overlays investigated.

Material	Bulk Chemical Composition wt%							Cr/C ratio	CVF*
	C	Si	Cr	Mn	Fe	Ni	Mo		
HypoA Casting	2.4	0.97	26.6	0.69	68.9	0.06	0.02	11.1	25.8 ± 1.1
EutecticA Casting	3.6	0.53	17.8	0.65	75.9	0.10	1.35	4.9	38.6 ± 3.1
HyperA Casting	4.5	0.49	34.0	1.9	57.7	0.12	0.95	7.6	51.9 ± 2.5
HyperEXP Casting	4.51	0.45	25.0	4.6	60.2	4.8	0.33	5.5	49.9 ± 4.3
WeldoverlayA	5.5	1.6	24.5	1.1	67.0	0.11	0.03	4.5	58.8 ± 2.4
WeldoverlayB	4.9	0.94	27.3	1.2	65.5	0.06	0.02	5.6	51.2 ± 3.4

*Carbide volume fraction of primary and eutectic M_7C_3 carbides

8.1.1 Solidification

The high chromium white iron castings and weld overlays investigated have been plotted on the Fe-rich corner of the metastable Fe-Cr-C liquidus surface, Figure 8.1. The chemical compositions and resulting microstructures of the alloys investigated was found to correspond with phase fields predicted using the liquidus surface developed by Thorpe and Chicco (1985). Most notably the EutecticA alloy corresponded very closely to the eutectic valley and the resulting microstructure was typical of a eutectic composition. This further validates the use of the liquidus surface developed by Thorpe and Chicco (1985) as an industrial tool to predict the resulting microstructure for a given carbon and chromium composition.

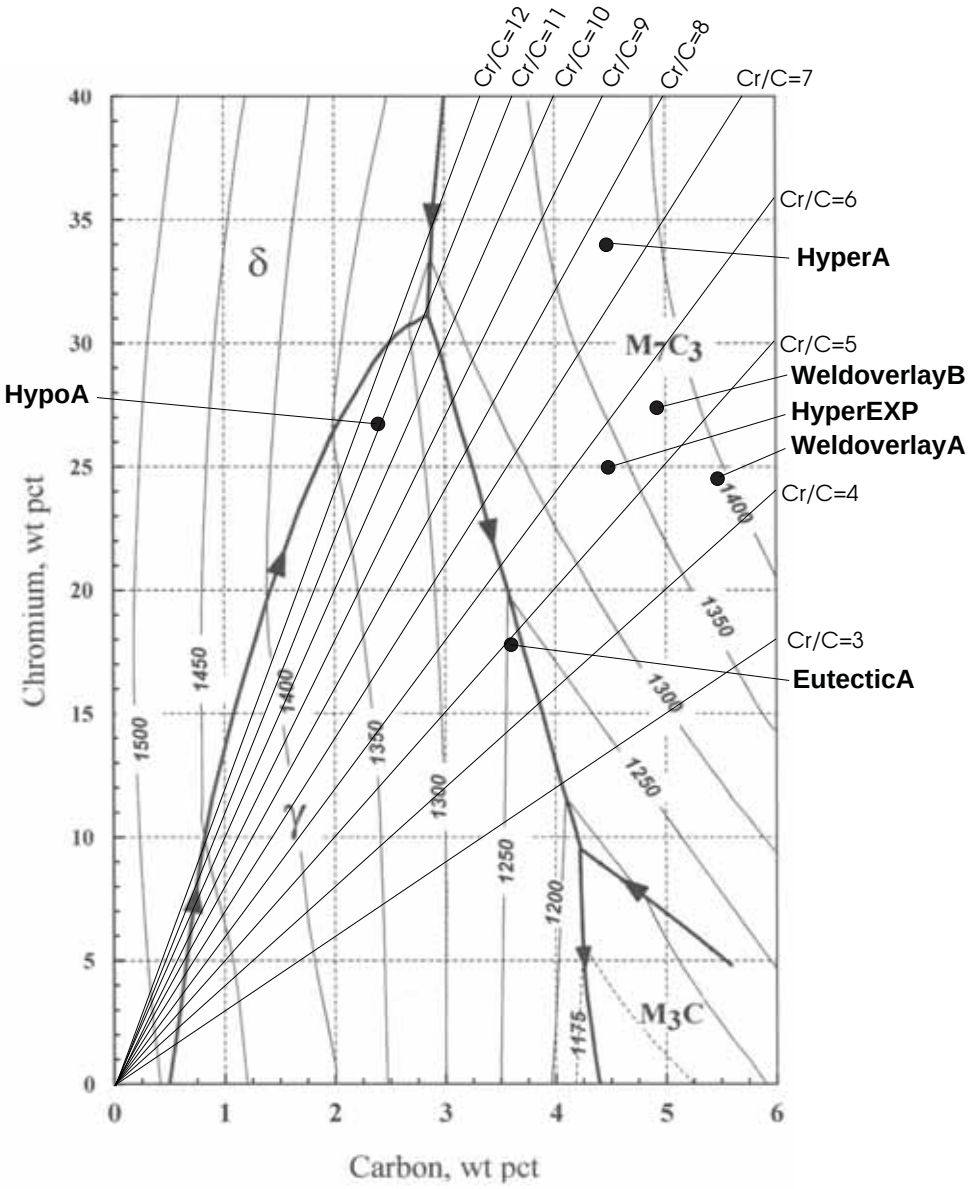

Figure 8.1: The metastable Fe-Cr-C liquidus surface (after Thorpe and Chicco (1985)) with plotted lines of constant chromium to carbon ratio (Cr/C) and the location of the high chromium white iron castings and weld overlays investigated.

The HypoA casting was received in the heat treated condition, therefore, no conclusion can be made as to the as-cast microstructure. However, the outline of the primary austenite dendrites are clearly apparent and the inter-dendritic eutectic carbides, generally not effected by destabilization heat treatments, had a blade like morphology. This microstructure is typical of a high chromium white iron of hypoeutectic composition.

The EutecticA casting was received in the as-cast condition and the microstructure showed no clear evidence of primary austenite or carbides. The microstructure consisted of an even distribution of eutectic carbides having a similar blade like morphology to the HypoA eutectic carbides. The EutecticA matrix consisted of austenite, martensite and regions of pearlite, which is undesirable in high chromium white iron castings as it reduces toughness (Tabrett

et al., 1996). The pearlite would have formed due to the slow cooling rate during solidification and insufficient pearlite suppressing alloying elements. The solidified microstructures for both HypoA and EutecticA are consistent with what is reported in the literature and will not be further discussed.

The commercially produced HyperA casting was reported to be in the as-cast condition. The microstructure comprised large randomly orientated primary M_7C_3 carbides greater than 50 μm in cross section and having the characteristic near hexagonal cross section. The microstructure of the eutectic phase of this alloy was found to differ from that reported in the literature. The eutectic carbides were large and had large inter-carbide spacings compared with other high chromium white iron eutectic M_7C_3 carbides (compare Figure 5.6(a) of HyperA with 5.1(a) HypoA, 5.4(a) EutecticA, 5.8(a) HyperEXP). This carbide arrangement has not been explained in the literature and is not consistent with what is expected under near equilibrium cooling conditions. The matrix was comprised of austenite and martensite, which would typically form a band around the primary and eutectic carbides. Within central matrix regions, a dense precipitation of sub micron carbides was seen. The carbides had a discrete rod like shape and were not characterized as part of this work but are likely to be $M_{23}C_6$ or M_7C_3 carbides. Reasons for the variations in microstructure of the HyperA alloy compared with the other alloys examined could be due to foundry techniques such as control of superheat, inoculation or control of cooling rate.

The HyperEXP casting was in the as-cast condition and was comprised of large randomly orientated primary M_7C_3 carbide rods greater than 50 μm in cross section having the characteristic near hexagonal cross section. The eutectic carbides were much smaller than the primary carbides and were evenly distributed. This microstructure is typical of a hypereutectic casting cooled near equilibrium conditions. The matrix of the HyperEXP alloy consisted entirely of austenite as the alloy showed no attraction to a strong magnet. Within the austenitic matrix regions there was carbide precipitation, but not to the extent seen in the HyperA alloy. The non-magnetic nature of this alloy is attributed to the additions of the austenite stabilizing elements manganese and nickel which would have suppressed transformation of austenite to martensite on cooling.

Both the weld overlay samples, WeldoverlayA and WeldoverlayB, examined showed many similar characteristics and will be discussed together. The microstructure of the high chromium white iron weld overlays was found to be very variable having many different carbide morphologies depending on the section of the deposited weld bead examined (i.e. longitudinal or transverse sections). The regions examined showed halos surrounding the primary carbides, the branched primary carbide morphology and the complex regular carbide morphology. These different microstructures are a result of the faster cooling rates in the weld deposits and the ability of the nonfaceted-faceted high chromium white iron alloys to readily undercool (Powell et al., 2003).

In many sections of the weld overlay the microstructure was more consistent with what is

expected from a near equilibrium cooling rates alloy such as achieved in large casting. The primary M_7C_3 carbides were well defined and had a diameter of approximately 15 to 25 μm and a eutectic of smaller M_7C_3 carbides having a diameter less than 5 μm. The primary carbides were generally aligned perpendicular to the substrate, which is the direction of heat flow. However, even in these regions there is evidence that the alloy has experienced undercooling due to the formation of austenite halos surrounding the primary M_7C_3 carbides. In the eutectic regions, the inter-carbide spacing is approximated by eutectic carbide size, that is, less than 5 μm. In these closely spaced regions the eutectic matrix was generally austenite but martensite laths were often seen extending from the carbides into the matrix (refer Figure 5.13(b)).

Adjacent to the surface of the weld overlay and to the substrate-weld overlay interface, where the cooling rate would be the greatest, the branched primary and complex regular microstructures were seen. The branched primary carbide forms due to greater undercooling than is required for halo formation and results in a grain of primary carbides that are interconnected and monocrystalline (refer Figure 5.10(b)). The complex regular microstructure forms due to even greater undercooling than for branched primary carbides. The complex regular microstructure is characterized as a large number of eutectic carbides that are joined together to form monocrystalline arrays that can be up to millimeters in width. The conventional solidification sequence of primary carbides does not occur as the undercooling is too large. The complex regular grains have a three fold symmetry and therefore appear as equilateral triangles (refer Figures 5.11(a) and 5.16(c)). With both the branched primary and complex regular microstructures, it was often found that check cracks would pass through these regions.

The differences in the microstructures between the castings and weld overlays is significant. The most notable difference between the hypereutectic castings and weld overlays investigated was the size, morphology and distribution of primary and eutectic M_7C_3 carbides. The HyperA and HyperEXP castings had numerous large randomly orientated primary carbides around 50 μm in diameter. WeldoverlayA and WeldoverlayB had primary carbides less than 25μm in diameter (compare Figures 5.6 and 5.8 with Figures 5.10 and 5.15). The weld overlays were also found to form the branched primary and complex regular carbide microstructures as a result of undercooling and these were not seen in any of the castings examined. However, the presence of the complex regular microstructure has been reported in castings deliberately cooled on the surface using chills, which is further verification that the different carbide morphologies found in weld overlays are due to cooling rate effects (Sare, 1979). As the properties and performance of alloys are determined by their microstructure, it is expected that the vast differences seen in microstructures between the castings and weld overlays will give rise to different wear and corrosion performance. What has been highlighted is how the cooling rate, or the control of cooling rate, can give rise to significantly different microstructures. A faster cooling rate produces a finer dispersion of more closely spaced primary and eutectic carbides.

The difference in chemical composition between the casting and weld overlays could be a contributing factor to the variation in carbide size and morphology. Silicon, which is greater by about 0.5% in the weld overlays compared with the castings, has been reported to inhibit carbide growth in eutectic casting alloys and change the carbide morphology in weld overlays to a more equiaxed shape. The increased carbon composition of the weld overlays is another difference. Based on Maratray and Usseglio-Nanot (1970) formula this would lead to the greater carbide fraction in the weld overlays but the effect on carbide morphology has not been reported. While the role of chemical composition on carbide morphology is difficult to determine from the alloys examined as part of this work, it cannot be ruled out as a contributing factor.

8.1.2 Heat Treatments After Solidification

As discussed in the previous section on solidification, high chromium white irons generally solidify with a predominantly austenitic matrix. The austenite is metastable as it is supersaturated with carbon, chromium and other alloying elements. The matrix may also contain a proportion of martensite and pearlite as was the case with the EutecticA alloy.

For castings, it is often desirable to heat treat the as-cast alloys to transform the matrix to martensite to increase bulk hardness and improve wear resistance. This is generally the aim of conventional destabilization heat treatments, commonly done on hypoeutectic and eutectic high chromium white iron castings, which constitute the major use of high chromium white iron castings (Tabrett et al., 1996, Pearce, 2002). More recently, high temperature heat treatments have been used on high chromium white iron castings with the aim of improving toughness (Kootsookos, 1995, Hann, 1998). Heat treatment of hypereutectic high chromium white iron castings or weld overlays is seldom done in practice as the resulting microstructure is generally too brittle for wear applications.

The heat treatment after solidification section will discuss the heat treatments of four of the high chromium white iron casting samples covered in Section 5.3. The purpose for undertaking these heat treatments was to examine the resulting microstructures and to vary the matrix microstructures for corrosion testing purposes. Two heat treatments were done on each alloy, one heat treatment typical of a destabilization heat treatment and the other typical of a high temperature normalizing heat treatment. The laboratory heat treatment methodology is described in Section 2.3.

8.1.2.1 Destabilization Heat Treatments

Conventional heat treatments of high chromium white iron are used to destabilize the austenite by holding at a temperature between 800^0C and 1100^0C to allow the precipitation of secondary chromium carbides (Pearce, 1984, Pearce and Elwell, 1986, Powell and Laird II,

1992, Wiengmoon et al., 2005a). Between these temperatures solid state precipitation of secondary carbides occurs, reducing the carbon and chromium content of the matrix which allows the subsequent transformation of the matrix to martensite on quenching.

There exists an optimum destabilization temperature which will give the maximum hardness for white iron alloys (Maratray and Poulalion, 1982, Sare and Arnold, 1995, Tabrett et al., 1996). This temperature is different for various alloy compositions and represents a balance between retained austenite levels, martensite with a higher carbon content to increase matrix hardness and the extent of secondary carbide precipitation. To determine a suitable heat treatment temperature, a heat treatment study was undertaken on the HyperA casting alloy. The HyperA casting was heat treated for 6 hours at temperatures from 800 to 1150°C in 50°C increments and furnace cooled. A brief discussion of the results is included in Appendix A. The maximum hardness was achieved at a heat treatment temperature of 950°C and the lowest hardness at a temperature of 1150°C. As a result, the 950°C heat treatment temperature was chosen to heat treat the four casting alloys, however, the samples were air cooled after the heat treatment due to the tendency for the lower alloy content alloys (HypoA and EutecticA) to form pearlite on furnace cooling. The alloys were not tempered after heat treatment.

Heat treatment at 950°C for the three castings resulted in the heterogeneous precipitation of secondary carbides within the matrix. The secondary carbides did not nucleate or grow on the primary or eutectic carbides which is consistent with what is reported in the literature. It has been reported that it is possible for the eutectic carbides to undergo an in-situ transformation during destabilization heat treatments to form a shell structure in high chromium content hypoeutectic high chromium white irons (Pearce and Elwell, 1986, Wiengmoon et al., 2005b). The shell type structure was found to be easily distinguished using back scattered electron microscopy. It is also reported that the eutectic M_7C_3 carbides remain unaffected and no change in morphology occurs due to destabilization heat treatments (Pearce and Elwell, 1986, Powell and Laird II, 1992, Wiengmoon et al., 2005a). The destabilization heat treatments done as a part of this work, on HypoA, EutecticA, HyperA and HyperEXP, did not cause any in-situ changes in morphology or composition of the primary or eutectic carbides.

The type of the precipitated secondary carbides was not analytically verified. However, based on the solid state isotherms shown in Figure 1.11, and the previous work reported in the literature (Powell and Laird II, 1992, Powell and Bee, 1996), the secondary carbides are likely to be M_7C_3 or $M_{23}C_6$ or a combination of both carbides. The secondary carbides in the destabilized alloys either had a cubic appearance and were sub micron in size or formed rods having a length of 2 to 3 μm. These carbide morphologies are consistent with what has previously been reported for compositions similar to HypoA and EutecticA (Powell and Laird II, 1992, Powell and Bee, 1996).

Whilst the matrix of the EutecticA and HyperA alloys underwent transformation to martensite, which was indicated by the samples being magnetic and having high hardness, the Hy-

per EXP alloy remained austenitic even though there was secondary carbide precipitation. The conclusion that the HyperEXP alloy was 100% austenitic was due to the alloy being non-magnetic. The austenitic matrix of the HyperEXP sample is undoubtedly due to the austenite stabilizing effect of the nickel, which segregates exclusively to the matrix, and manganese that suppresses the martensite start temperature, Equation 1.9. As a test, not reported in the results section, to determine if the martensite transformation would occur, a sample of the destabilized alloy was immersed in liquid nitrogen. After immersion the alloy did have a slight attraction to a strong magnet indicating that some transformation of the austenite to martensite had occurred.

8.1.2.2 High Temperature Heat Treatments

High temperature heat treatments of high chromium white irons are generally done at temperatures above 1100^0C. Based on the heat treatment study of the HyperA alloy, Appendix A, a heat treatment temperature of 1150^0C for 6 hours followed by air cooling was selected for this investigation as it gave an austenitic matrix almost free of secondary carbides. The HypoA, EutecticA, HyperA and HyperEXP alloys were investigated.

The high temperature heat treatment of the destabilized HypoA alloy resulted in the dissolution of the secondary carbides to form a near homogeneous austenitic matrix with very limited secondary carbide precipitation on austenite grain boundaries. After the heat treatment, the alloy was found to be slightly magnetic, which would indicate the presence of martensite. Similarly, for the EutecticA and HyperA alloy, the high temperature heat treatment resulted in an austenitic matrix together with some martensite. The EutecticA alloy was free of secondary carbides, but the HyperA alloy did have isolated secondary carbide regions that could have precipitated during the heat treatment or did not completely dissolve at the heat treatment temperature. The high temperature heat treatment of the HyperEXP alloy resulted in a microstructure similar to HyperA, i.e. an austenitic matrix and isolated secondary carbide regions. The HyperEXP sample was again nonmagnetic, indicating that the matrix was fully austenitic. The fully austenitic nature of the HyperEXP alloy is due to the nickel and manganese alloying additions discussed previously.

The resulting austenitic microstructure for the alloys investigated is due to the increased solid solubility of carbon and chromium in austenite with increasing temperature as indicated by the solid state isotherms Figure 1.11. At the heat treatment temperature of 1150°C the secondary or precipitated carbides dissolve leading to an increase in the carbon and chromium composition of the austenitic matrix. The increase in chromium content of the austenite has been confirmed by EPMA for the high chromium white iron alloys investigated. This increase in carbon and chromium results in a metastable austenite that is supersaturated with carbon and chromium and does not readily transform to martensite on cooling to room temperature due to a reduction in the M_S temperature.

The morphology and composition of the primary and eutectic M_7C_3 carbides was not altered during heat treatments at temperatures up to 1150°C.

8.1.3 Chemical Composition of Microstructural Phases

The most important alloying elements in high chromium white irons are carbon and chromium. In general, other alloying elements are added to help with casting, deposition characteristics or to improved the heat treatment characteristics of the alloy. In the case of the HyperEXP alloy, above normal alloying additions of Ni and Mn have been added to give a fully austenitic matrix microstructure irrespective of heat treatment. It is often desirable to determine how the alloying elements distribute between microstructural phases to help in the understanding of microstructural development, the ability to heat treat the alloys and to determine corrosion performance. In the case of high chromium white irons, there are two distinct microstructural phases, the carbides and the matrix. By knowing how alloying elements segregate between the carbides and the matrix, alloying composition can be manipulated to improve mechanical properties or wear resistance.

The chemical composition of the carbides and the matrix were determined by electron probe microanalysis (EPMA) for all of the alloys investigated. The as-received, destabilized and normalized heat treated conditions were examined. Relationships between bulk chemical composition, microstructural phases formed and segregation of the phases were examined.

8.1.3.1 Chemical Composition of the Carbides

The chemical composition of the carbides is given in Table 8.2. The chromium content of the carbides is found to increase with increasing Cr/C ratio, irrespective of whether the carbides are primary M_7C_3 or eutectic M_7C_3 carbides. The primary carbides were found to have a higher chromium composition than the eutectic carbides by 8% for the HyperA and 20% for the HyperEXP alloys. The higher chromium content of the primary carbides with respect to the eutectic carbides is expected based on the solidification of hypereutectic alloys. With reference to the phase diagram, Figure 8.1, hypereutectic alloys will solidify by following a path perpendicular to the isotherms until the eutectic valley is reached. As the primary M_7C_3 carbides grow consuming carbon and chromium, the remaining liquid is depleted of carbon and chromium until the eutectic composition is reached. The chromium content of the remaining liquid at the eutectic composition will be less than the original liquid composition and it is therefore expected that the eutectic carbides will have a lower chromium content.

Table 8.2: Summary of carbide chemical composition. Values obtained using EPMA.

Sample	Condition	Carbide Analysed	Chemical Composition wt%						
			C	Si	Cr	Mn	Fe	Ni	Mo
HypoA	As-received	Eutectic M_7C_3 carbides	8.88 ± 0.50	0.00 ± 0.00	62.49 ± 0.35	0.49 ± 0.03	27.65 ± 0.25	0.01 ± 0.01	0.01 ± 0.03
Eutectic A	950°C for 6hrs	Eutectic M_7C_3 carbides	8.38 ± 0.15	0.00 ± 0.00	45.63 ± 1.63	0.72 ± 0.06	44.19 ± 1.14	0.00 ± 0.00	1.39 ± 0.24
HyperA	As-cast	Primary M_7C_3 carbides	8.83 ± 0.27	0.00 ± 0.00	57.36 ± 0.79	1.59 ± 0.06	31.46 ± 0.69	0.05 ± 0.02	0.61 ± 0.04
		Eutectic M_7C_3 carbides	8.69 ± 0.20	0.01 ± 0.01	52.94 ± 1.76	2.31 ± 0.15	33.80 ± 0.97	0.05 ± 0.03	1.14 ± 0.30
HyperEXP	As-cast	Primary M_7C_3 carbides	8.76 ± 0.13	0.01 ± 0.01	54.46 ± 0.83	4.31 ± 0.16	32.77 ± 0.47	0.56 ± 0.07	0.22 ± 0.04
		Eutectic M_7C_3 carbides	8.61 ± 0.09	0.01 ± 0.01	45.13 ± 2.15	6.32 ± 0.56	40.09 ± 1.35	0.67 ± 0.08	0.50 ± 0.10
	1150°C for 6hrs	Primary M_7C_3 carbides	8.59 ± 0.18	0.01 ± 0.01	54.42 ± 0.82	4.34 ± 0.14	32.86 ± 0.70	0.58 ± 0.09	0.31 ± 0.04
		Eutectic M_7C_3 carbides	8.28 ± 0.14	0.01 ± 0.01	45.40 ± 1.21	7.10 ± 0.54	38.34 ± 0.45	0.63 ± 0.14	0.90 ± 0.31
WeldoverlayA	As-deposited	Primary M_7C_3 carbides	9.06 ± 0.14	0.05 ± 0.02	42.19 ± 1.40	1.16 ± 0.05	47.82 ± 1.15	0.03 ± 0.02	0.00 ± 0.01
WeldoverlayB	As-deposited	Primary M_7C_3 carbides	9.09 ± 0.26	0.03 ± 0.01	46.55 ± 0.64	1.25 ± 0.02	43.17 ± 0.58	0.02 ± 0.02	0.01 ± 0.02

Silicon is found to be insoluble in the primary and eutectic M_7C_3 carbides. The silicon values reported in Table 8.2 of 0.01 to 0.05wt% are attributed to stray readings of the electron micro probe analysis machine. Nickel was found to have limited solubility in the primary and eutectic carbides. This was highlighted by the HyperEXP alloy having a bulk nickel content of 4.8 wt%, which resulted in the primary and eutectic M_7C_3 carbides having a nickel content of approximately 0.6wt%. The variations in nickel composition between the primary and eutectic M_7C_3 carbides were not significant but it appears that the eutectic M_7C_3 carbides have a higher nickel content than the primary M_7C_3 carbides by 0.1wt%. Manganese was found in varying quantities in the primary and eutectic M_7C_3 carbides, with the alloys having a higher bulk manganese composition, such as HyperEXP, having a higher manganese content in the carbides. The eutectic carbides were found to have more manganese than the primary carbides. In a similar trend to manganese, molybdenum was found in the primary and eutectic M_7C_3 carbides with the alloys having a higher bulk molybdenum composition, such as HyperA, having a higher molybdenum content in the carbides. The eutectic carbides were found to contain more molybdenum than the primary carbides.

The segregation of the alloying elements is generally consistent with the reported literature, with the exception of the HyperEXP alloy having just over 0.5 wt% Ni within the primary and eutectic M_7C_3 carbides. It is reported that nickel has negligible solubility in the M_7C_3 carbides (Pearce, 2002) but it is believed the higher bulk nickel composition increased the driving force for the segregation of nickel into the carbides for the HyperEXP alloy.

8.1.3.2 Chemical Composition of the Matrix

The matrix of high chromium white irons is generally a mixture of metastable austenite and martensite in varying proportions. It is possible for high chromium white irons to contain pearlite if there are insufficient hardenability alloying elements within the matrix in the as cast condition, or if the quenching rate after heat treatment is not fast enough. EutecticA was found to contain pearlite in the as-cast condition. EutecticA and HypoA were also found

to develop a pearlitic matrix after a destabilization heat treatment and slow furnace cooling. The chemical composition of the matrix phase for the alloys investigated is given in Table 8.3.

Table 8.3: Summary of matrix chemical composition. Values obtained using EPMA.

Sample	Condition	Chemical Composition wt%						
		C	Si	Cr	Mn	Fe	Ni	Mo
HypoA	As-received	0.40 ± 0.10	1.26 ± 0.02	12.57 ± 0.81	0.71 ± 0.01	85.59 ± 1.15	0.19 ± 0.02	0.05 ± 0.04
	1150°C for 6hrs	0.70 ± 0.11	1.27 ± 0.04	13.78 ± 0.24	0.76 ± 0.02	83.20 ± 0.38	0.18 ± 0.03	0.01 ± 0.02
EutecticA	950°C for 6hrs	0.81 ± 0.11	0.79 ± 0.02	7.14 ± 0.30	0.76 ± 0.03	90.81 ± 0.88	0.18 ± 0.02	1.01 ± 0.48
	1150°C for 6hrs	0.63 ± 0.08	0.62 ± 0.02	10.85 ± 0.55	0.75 ± 0.08	85.59 ± 0.83	0.17 ± 0.10	1.41 ± 0.37
HyperA	As-cast	0.78 ± 0.08	0.90 ± 0.02	10.62 ± 0.62	2.23 ± 0.10	83.79 ± 1.08	0.60 ± 0.03	1.37 ± 0.37
	950°C for 6hrs	0.95 ± 0.18	0.91 ± 0.03	9.62 ± 0.73	2.28 ± 0.11	83.30 ± 0.90	0.60 ± 0.02	1.58 ± 0.54
	1150°C for 6hrs	0.91 ± 0.11	0.87 ± 0.01	10.80 ± 0.18	2.20 ± 0.06	83.75 ± 0.42	0.59 ± 0.02	1.78 ± 0.31
HyperEXP	As-cast	1.20 ± 0.10	0.82 ± 0.04	8.66 ± 0.68	5.85 ± 0.56	76.54 ± 0.56	8.41 ± 0.30	0.26 ± 0.12
	950°C for 6hrs	0.76 ± 0.08	0.91 ± 0.03	5.82 ± 0.44	5.87 ± 0.47	79.71 ± 0.52	8.79 ± 0.72	0.26 ± 0.14
	1150°C for 6hrs	0.92 ± 0.08	0.82 ± 0.03	8.62 ± 0.47	5.81 ± 0.44	76.50 ± 0.61	8.43 ± 0.41	0.28 ± 0.10
WeldoverlayA	As-deposited	1.32 ± 0.20	2.94 ± 0.15	8.07 ± 0.76	1.23 ± 0.10	87.56 ± 0.78	0.29 ± 0.02	0.01 ± 0.01
WeldoverlayB	As-deposited	1.62 ± 0.13	1.94 ± 0.17	10.59 ± 1.31	1.44 ± 0.09	84.94 ± 1.54	0.22 ± 0.22	0.02 ± 0.03

The alloying elements that are insoluble or slightly soluble in the carbides such as silicon, manganese and nickel are present in the matrix in greater concentrations. Molybdenum is found to partition between the carbides and the matrix, but no apparent trend was evident.

The chromium composition of the matrix is often of great interest as it is believed to improve corrosion performance at compositions greater than 12% due to the formation of a passive chromium oxide layer on the surface. The matrix chromium composition for the alloys investigated varied from 5.8 wt% up to 13.8 wt% as shown in Table 8.3 and presented graphically in Figure 8.2. It is found that it is difficult to predict the chromium composition of the matrix based on bulk carbon and chromium composition. Maratray and Usseglio-Nanot (1970) formula for predicting matrix chromium composition, based on a linear relationship between bulk carbon and chromium, is plotted in Figure 8.3. The error bars represent a standard deviation of ± 2.11 wt%. As seen from the graph, there is a reasonable degree of in scatter in the calculated and measured matrix chromium compositions. The results for the alloys investigated suggest that matrix chromium composition is not a linear relationship with respect to the chromium to carbon ratio. Quantitative micro chemical analysis methods should be used to determine matrix chromium composition, otherwise variations in excess of 2 to 5% could be expected if the linear Maratray and Usseglio-Nanot (1970) formula for predicting matrix chromium composition based on bulk chemical composition is used.

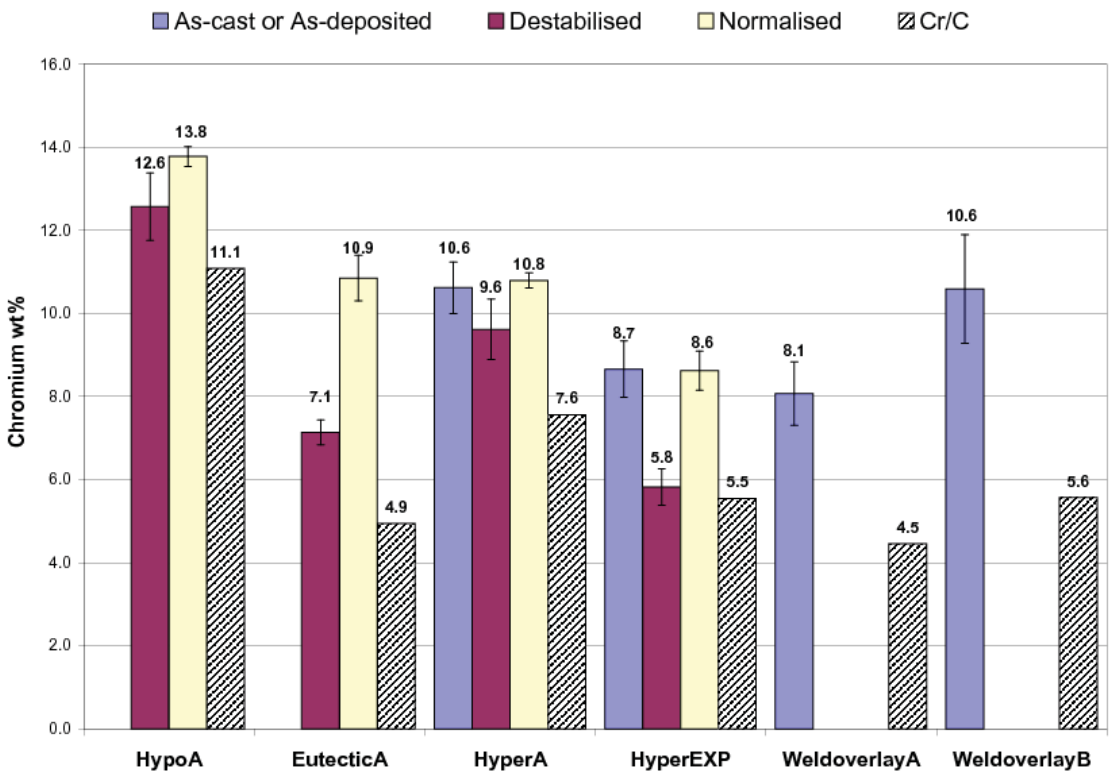

Figure 8.2: Comparison of matrix chromium composition for alloys investigated in the as-cast or as-deposited (weld overlays), destabilized heat treated condition and normalized heat treated condition. The chromium to carbon ration (Cr/C) is also graphically represented.

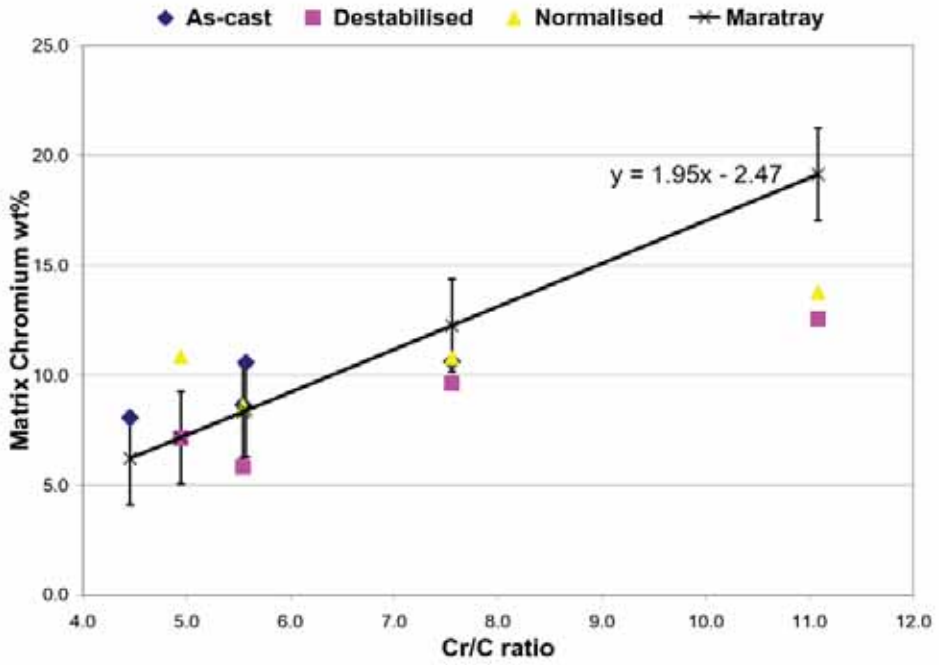

Figure 8.3: Matrix chromium composition of alloys studied verses chromium to carbon ratio compared with the composition predicted using the method of Maratray and Usseglio-Nanot (1970).

The destabilization heat treatment resulted in a reduction in matrix carbon and chromium composition for the four castings samples investigated due to the precipitation of carbon and chromium rich secondary carbides. For the HyperA and HyperEXP alloys, the matrix chromium compositions in the as-cast condition were similar to the matrix chromium compositions in the normalized condition. Variations in chromium compositions between the destabilized and normalized conditions ranged from 1.0 wt% for HyperA and 3.8 wt% for EutecticA.

For the weld overlays, WeldoverlayB had a Cr/C ratio of 5.6 compared with 4.5 for WeldoverlayA. The chromium composition of the austenitic halo region of 10.6 wt% for WeldoverlayB was 2.5% greater than for the WeldoverlayA sample. While the WeldoverlayB alloy did have a higher bulk chromium composition of 2.8 wt% compared with the WeldoverlayA sample, the higher halo chromium composition of WeldoverlayB would be due to the lower bulk carbon composition of 0.6 wt% resulting in a reduced tendency for carbide formation and consumption of matrix chromium. This reduction in carbide formation is reflected in a lower CVF for WeldoverlayB compared with WeldoverlayA, Table 8.1.

8.1.4 Carbide Volume Fraction and Hardness

CVF and hardness are the most common microstructural factors that are used to determine wear resistance. It would be desirable to know if there is any relationship between the bulk chemical composition and CVF and what factors influence carbide size and spacing.

8.1.4.1 CVF and Bulk Carbon and Chromium Composition

As determined by the equilibrium phase diagram for C-Cr-Fe, the carbide volume fraction is a function of bulk carbon and chromium composition. The CVF has been has been plotted along with the bulk carbon and chromium compositions of the alloys, Figure 8.4. The calculated CVF based on bulk carbon and chromium composition using the CVF equation proposed by Maratray and Usseglio-Nanot (1970) (Equation 1.6) was also plotted for comparison. The CVF represents the proportion of primary and or eutectic M_7C_3 carbides. Secondary carbides have been excluded from the CVF analysis due to their finite size. As previously discussed, the carbides are not effected by heat treatment and therefore, the CVF is unchanged.

From the graph, the calculated CVF tends to overestimate the actual CVF by 5 to 8% for the hypereutectic compositions. Clearly, the carbon composition and not the chromium composition has a greater influence in determining the CVF, with a bulk carbon composition of 4.5 wt% giving approximately a 50% CVF. It also appears that other alloying additions other than C and Cr have minimal influence on the CVF.

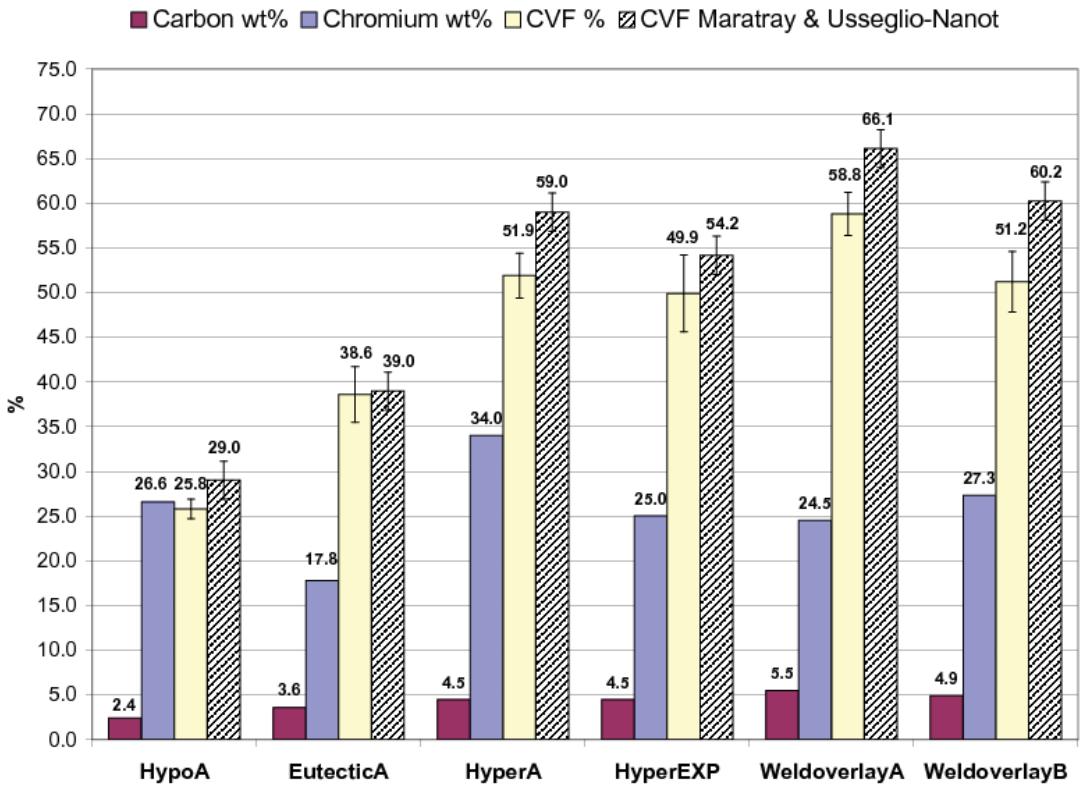

Figure 8.4: Comparison of carbon and chromium composition with measured CVF and calculated CVF based on Maratray and Usseglio-Nanot (1970) formula.

8.1.4.2 CVF and Bulk Hardness

It is often considered that increasing the CVF will increase the bulk hardness and give greater wear resistance. This work has shown that no simple relationship exists between the CVF and bulk hardness. This is clearly illustrated in Figure 8.5 that shows the HyperEXP hypereutectic alloy having a CVF of approximately 50% has the lowest bulk hardness of all of the alloys investigated. Likewise, the EutecticA alloy in the normalized condition has a CVF of 39% and has a similar hardness to the HypoA alloy in the normalized condition with a CVF of 26%.

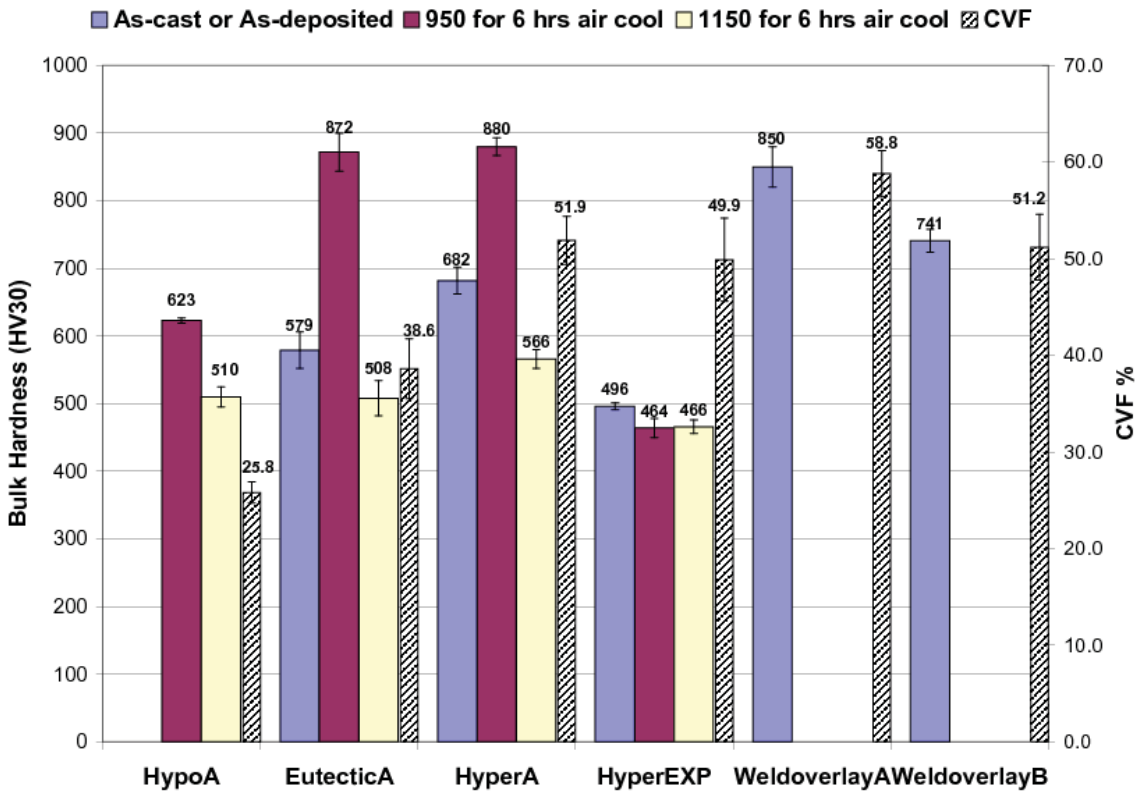

Figure 8.5: Comparison of bulk hardness and CVF for the castings and weld overlays investigated. Note: CVF does not change after destabilization or normalizing heat treatments.

However, the results indicate that the matrix has a significant influence on the bulk hardness. For those alloys where the destabilization heat treatment transforms the matrix to a combination of martensite and retained austenite, the bulk hardness increases considerably. In addition it is apparent that the matrix structure has a greater influence on bulk hardness than the CVF. Comparing the results for HyperA and EutecticA alloys in the destabilized condition it can be seen that the bulk hardness are similar but the carbide fractions are 52% and 39% respectively. The exception to this was the HyperEXP alloy that, irrespective of heat treatment, always had a fully austenitic microstructure and therefore a similar bulk hardness. Even though extensive precipitation of secondary carbides occurred for the HyperEXP alloy after the destabilization heat treatment, the presence of the secondary carbides did not increase the bulk hardness. This indicates that increases in bulk hardness of high chromium white iron alloys due to heat treatments are achieved by the transformation of the matrix to martensite. All of the alloys other than the HyperEXP alloy had varying proportion of martensite in their matrix as they were ferromagnetic. The presence of secondary carbides, sub micron in size at least, does not contribute significantly to bulk hardness.

The reasonably high hardness of the weld overlay samples in the as-deposited condition is attributed to the presence of martensite within the austenitic matrix and the carbide morphology. The weld overlays were found to contain undercooled carbide morphologies such

as complex regular and branched primary. These undercooled carbide morphologies consist of a large number of closely spaced interconnected carbide rods that form hard but brittle clusters.

8.1.4.3 Carbide Size and Inter-Carbide Spacing

Carbide size and inter-carbide spacing is of interest in wear environments. It has previously been discussed that the weld overlay samples had a smaller carbide size and inter-carbide spacing compared with the castings and this difference was attributed to the cooling rate. The carbide size for the primary carbides of the hypereutectic castings samples were greater than 50 μm in cross section compared with the primary carbides of the hypereutectic weld overlays that were less than 25 μm in cross section. While the carbide size and and inter-carbide spacing was not quantitatively examined, it can be seen from the examination of the micrographs that the hypereutectic castings, HyperA and HyperEXP, had larger carbides and larger inter-carbide spacings. Conversely the weld overlay had smaller more numerous carbides and a smaller inter-carbide spacing.

The relationship between carbide size and inter-carbide spacing can be proven mathematically by considering an ideal grid of carbides having a smaller diameter and carbides having a larger diameter but each with the same total carbide volume fraction, Appendix B. It is found that the number of smaller carbides compared with the number of larger carbides is the squared value of the ratio of the large carbide diameter to the small carbide diameter. The inter-carbide spacing of the large carbides is found to be the smaller carbide size multiplied by the ratio of the large carbide diameter to the small carbide diameter.

Hence, by controlling the cooling rate, the carbide size and therefore inter-carbide spacing can be controlled. A faster cooling rate will give smaller but more numerous carbides that will have a smaller inter-carbide spacing (e.g. weld overlays). A slow cooling rate will give larger carbides with a larger inter-carbide spacing (e.g. large castings).

8.2 Corrosion

The corrosion of high chromium white iron castings and weld overlays was investigated in hot sodium hydroxide and sodium aluminate solutions having a minimum pH of 14. A plain low carbon steel and an AISI 420 martensitic stainless steel were also investigated to establish a baseline for comparing with the white irons.

Anodic polarization tests were done using the potentiodynamic polarization method to investigate the corrosion behaviour of the material over a broad range of potentials and to highlight corrosion features for further investigation. Immersion tests were done at the open circuit potential and at two other potentials of interest identified from the polarization tests

to qualitatively examine the effect potential has on corrosion rate. The Tafel technique was used to quantify the corrosion rate of the materials when immersed in the solution. Corrosion and immersion tests were done at 90^{o}C under deaerated conditions using the methodology outlined in Section 2.4.

The discussion of the corrosion results presented in Section 6 is divided into two broad categories that discuss the influence of environment on corrosion and the influence of microstructure on corrosion.

8.2.1 Influence of Environment on corrosion

This section discusses the corrosion behaviour of three high chromium white irons in sodium aluminate solution and sodium hydroxide solutions of 2.5M and 5.0M concentrations. The significance of the standard 2.5M and 5.0M sodium hydroxide solutions is that these concentrations approximate the free (not combined with aluminium) and total caustic of sodium aluminate solution, which is 2.7M and 4.9M respectively. The corrosion response of the white irons is compared with a low carbon steel, the anodic polarization response of which is well characterized in the literature, and an AISI 420 martensitic stainless. The significance of the 420 martensitic stainless steel is that the chemical composition and microstructure is very similar to that expected for the matrix of heat treated high chromium white irons.

The corrosion of low carbon steel and AISI 420 martensitic stainless steel is discussed first to validate the test procedure and introduce the likely corrosion mechanisms for the matrix of high chromium white irons. This background will enable the corrosion mechanism of high chromium white irons, based on the data from the polarization curves, to be determined and discussed in more detail. The immersion tests of the three different high chromium white irons at different potentials will be used and discussed to validate the polarization test results.

8.2.1.1 Corrosion of Low Carbon Steel and AISI 420 Martensitic Stainless Steel

The polarization response of AS1163: C350LO low carbon steel in 2.5M and 5.0M sodium hydroxide solution tested as part of this work, Figure 6.3, is consistent with the results reported in the literature (Zou and Chin, 1987, 1988). The polarization curves show active-passive behaviour with well defined Tafel slopes followed by a final transpassive regime, Figure 6.3. The consistent results verifies the validity of the corrosion test apparatus, the methods used and, the experimental polarization results.

The corrosion behaviour of low carbon steel in deaerated sodium hydroxide solutions, of various concentrations and temperatures, has been comprehensively explained by Zou and Chin (1987) and is briefly summarized. Their work indicated that an increase in solution concentration from 2.5M to 5.0M NaOH, shifted the open circuit potential (Figure 8.6), the critical potential (Figure 8.8), the potential of the second current peak, and the passive-transpassive

transition potential in the negative direction. The increase in solution concentration increased the corrosion current density (Figure 8.7), the critical current density (Figure 8.9) and greatly enhanced the dissolution current density in the passive or hump potential regime. Based on the measured corrosion current densities, the expected corrosion rate using Faraday's Law is 0.48 mm/yr and 0.84 mm/yr for the 2.5M and 5.0M NaOH cases respectively. However, the increase in solution concentration decreased the size of the second current peak in the active to passive transition.

When steel is immersed in deaerated caustic solution, the steel will corrode by the evolution of hydrogen at cathodic sites and the active dissolution of iron at anodic sites, which is consistent with the potential-pH diagram for iron, Figure 8.10. The active dissolution of the steel between -0.9 V_{SHE} and -0.75 V_{SHE} is due to the formation of the $HFeO_2^-$ ion (the dihypoferrite ion), which forms by a rate limiting two electron transfer reaction involving adsorbed $FeOH_{ads}$ species. The reactions around the the critical current peak between -0.75 V_{SHE} and -0.8 V_{SHE} is the result of a number of complex reactions before the eventual passivation of the steel surface due to the formation of an Fe_3O_4 film. The small current peak in the active to passive transition between -0.8 V_{SHE} and -0.5 V_{SHE}, Figure 6.3, is caused by the oxidation of Fe_3O_4 to Fe_2O_3 and FeO_2^- . The passive regime, or the current hump regime between -0.6 V_{SHE} to 0.6 V_{SHE}, represents the formation of a passive film of Fe_2O_3. The humped shape of the polarization curves is caused by the dissolution of the passive film which was found to occur at a higher rate in the 5.0M NaOH solution. The transpassive regime greater than 0.6 V_{SHE} is associated with oxygen evolution due to the molecular break down of water and is consistent with aqueous equilibria (Sriram and Tromans, 1985). Plotting the potential values on the potential-pH diagram, Figure 8.10, shows reasonable agreement with the polarization results and the predicted oxide formation.

The polarization behaviour of low carbon steel in sodium aluminate solution showed many of the same polarization characteristics as the polarization curves in sodium hydroxide solution, Figure 6.3. The open circuit potential was between the open circuit potential for the 2.5M and 5.0M NaOH solutions, Figure 8.6. The critical potential was similar to the 5.0M NaOH solution and an additional current hump was seen at a potential of -0.4 V_{SHE}, Figure 8.8. The most significant difference in the polarization response of low carbon steel in sodium aluminate solution compared with sodium hydroxide solutions is the reduction in corrosion current density, Figure 8.7, the active dissolution regime and critical current density, Figure 8.9, between potentials of -0.9 V_{SHE} and -0.8 V_{SHE}. The reduction in the corrosion current density in the sodium aluminate solution compared with the sodium hydroxide solution was 85.2% and 74% for the 5.0M and 2.5M NaOH solution respectively. This reduces the corrosion rate to approximately 0.12 mm/yr. Likewise the reduction in the critical current density was 81.3% and 74.7% for the 5.0M and 2.5M NaOH solution respectively. The current density in the passive region was similar to the 2.5M NaOH solution and due to a similar concentration of the free caustic in the solution.

The polarization tests have shown that the current density is significantly reduced in sodium aluminate solutions while the potentials for particular corrosion events are similar irrespective of the solution. The reduction in the active dissolution and critical current density in sodium aluminate solutions is due to the inhibiting effect aluminate ions (AlO_2^-) have on the active dissolution of the iron (Gavril et al., 2003, Sriram and Tromans, 1985). The proposed mechanism by which the aluminate ions inhibit active dissolution is by their adsorption onto the metal surface and subsequent incorporation into the iron oxide film, thus inhibiting the intermediate, rate determining, formation of the $FeOH_{ads}$ species that eventually form the dissolved $HFeO_2^-$ species. It was also found that the aluminate species can be incorporated into an amorphous oxide film of the form $Fe_{3-x}Al_xO_4$, which is believed to account for the reduction in the critical current around the active to passive transition.

Corrosion of AISI 420 Martensitic Stainless Steel

The immersion of the AISI 420 martensitic stainless steel, which has had the surface oxides removed, in deaerated sodium hydroxide and sodium aluminate solution results in the active dissolution of the material. Although the corrosion of stainless steel has not been extensively covered in the literature, the mechanism of corrosion is similar to that of steel given the similarities in the polarization curves, Figures 8.12, 8.13 and 8.14. Dissolution occurs due to the formation of dissolved species which are likely to be chromite ions, dihypoferrite ions or a combination via a number of intermediate steps. As the anodic potential is increased to the critical potential, passivation occurs. The passivating action is either due to the formation of hydrated Fe_2O_3 or Cr_2O_3 films or a mixture of both (Pourbaix, 1966). As the material is further polarized in the anodic direction, a transpassive region corresponding to the break down of the passive film is seen, and based on the E-pH diagrams for chromium and iron, is due to the formation of chromate ions (CrO_4^{2-}) (Pourbaix, 1966, Wang and Stack, 2000). With a further increase in potential the transpassive region is followed by a region of secondary passivity, likely due to the passivation of the surface by hydrated iron oxide (i.e. Fe_2O_3). The secondary transpassive region is due to the electrochemical break down of water as was the case for steel.

Comparing the corrosion current densities of AISI 420 martensitic stainless steel and AS1163: C350LO low carbon steel, Figure 8.7, the current density for the martensitic stainless steel is greater than the low carbon steel in 2.5M sodium hydroxide but similar in the 5.0M solution. This suggests the benefits of a chromium bearing steel are negated in sodium hydroxide solutions under freely corroding conditions.The corrosion current density in sodium aluminate solution is similar for the two alloys, and is significantly reduced compared with sodium hydroxide solutions. It has been discussed previously that the presence of aluminate ions in sodium aluminate solutions has an inhibiting effect on the active dissolution of steel by acting as an anodic inhibitor. A similar mechanism appears to occur for the martensitic stainless steel.

The previous paragraph has highlighted that the chromium in the martensitic stainless steel does not provide significant improvements in corrosion performance over ordinary low carbon steel under freely corroding conditions. However, in the sodium hydroxide solutions, the critical current density before passivation is significantly less than steel, which is likely due to the formation of chromium bearing oxides, Figure 8.9. In sodium aluminate solutions, the critical current density is very similar for both martensitic stainless steel and low carbon steel, Figure 8.9. The significant reduction in the critical current density for the chromium bearing martensitic stainless steel compared with the low carbon steel indicates an increase ability of the material to passivate in plain caustic solutions.

The passive current densities in the sodium hydroxide and sodium aluminate solutions investigated, Figures 8.12, 8.13 and 8.14 for the martensitic stainless steel and the low carbon steel are similar. The martensitic stainless steel had a marginally better passive corrosion performance up to a potential of 0 V_{SHE}. The improved performance of the AISI 420 martensitic stainless steel, particularly in the 5.0M sodium hydroxide solution, is attributed to the better passive film characteristics due to the presence of chromium.

By comparing the polarization behaviour of AISI 420 martensitic stainless steel with AS1163: C350LO low carbon steel in sodium hydroxide solution it was found that under freely corroding conditions that the martensitic stainless steel with a chromium content of 13 wt% did not lead to improvements in corrosion performance. However, the martensitic stainless steel did have a much lower critical current density, indicating its ability to better passivate and more quickly form a protective oxide layer. In the sodium aluminate solutions, the corrosion behaviours of the martensitic stainless steel and the low carbon steel are very similar and the polarization curves almost overlap up to 0 V_{SHE}, Figure 8.14. The similar corrosion performance for the two materials in sodium aluminate solution is due to the anodic inhibiting effect the aluminate ions have on steel. The increased chromium of the martensitic stainless steel can lead to improvements in corrosion performance in sodium hydroxide solutions, however, the improvements in corrosion performance in sodium aluminate solutions are limited.

8.2.1.2 Corrosion of High Chromium White Iron Castings

The corrosion behaviour of three high chromium white iron castings with different compositions and microstructures has been investigated in deaerated sodium aluminate, 2.5M sodium hydroxide and 5.0M sodium hydroxide solutions. All tests were conducted at 90°C. Two of the white irons investigated are commonly used for slurry pump impellers in alumina refineries. They were a hypoeutectic heat treated 27% Cr type, designated HypoA, and a hypereutectic high chromium white iron in the as-cast condition having 34% Cr, designated HyperA. The third high chromium white iron was an experimental hypereutectic white iron, designated HyperEXP, having 25% Cr and above normal additions of manganese and nickel.

Sodium Hydroxide Solution

The polarization curves for the high chromium white iron castings tested were similar to those reported for low carbon steel and AISI 420 martensitic stainless steel, Figure 8.12 and 8.13. The polarization behaviour of all the white irons tested showed an active region from the corrosion potential ranging from -0.93 V_{SHE} to -0.875 V_{SHE} up to the critical potential of -0.84 V_{SHE} to -0.75 V_{SHE}. Following the active dissolution regime was the transition from active to passive behaviour and a drop in current density. For the HypoA and HyperA castings the passive behaviour consisted of a well defined humped potential regime up to -0.25 V_{SHE} to -0.2 V_{SHE} where the materials showed a current peak followed by pseudo passive behaviour. The HyperEXP material demonstrated a different polarization behaviour following the active to passive transition such that at -0.30 V_{SHE} to -0.25 V_{SHE}, the current increased and and peaked before the passive humped regime. At potentials from -0.10 V_{SHE} to 0.0 V_{SHE} all of the white iron materials demonstrated transpassive behaviour and the onset of carbide corrosion with increasing potential.

In a similar manner to that found for the AS1163: C350LO steel and AISI 420 martensitic stainless steel, an increase in the sodium hydroxide solution concentration, hence an increase in the hydroxide activity, shifted the corrosion potential and the critical potential in the negative direction, Figure 8.6 and 8.8. However, irrespective of the material and variations in chemical composition and microstructure, the variations in potentials were between 30 mV and 90 mV for the open circuit and critical potentials respectively. The typical open circuit potentials of the white irons were 10 to 30 mV more negative than the values for the steel and stainless steel in both the 2.5M and 5.0M NaOH solutions. Similarly, the critical potential was also in the range of 20 to 40 mV, Figure 8.8. The variations of 20 mV to 90 mV for the potential readings indicates that the steel, stainless steel and high chromium white iron castings are located in similar regions of the potential-pH diagram, Figure 8.10 and 8.11. Based on the potential-pH diagrams and the similarities in potential for corrosion events as shown by the polarization curves (Figures 8.12 and 8.13), the dissolution and passivation mechanisms are similar.

The corrosion current densities were found to increase with increasing sodium hydroxide concentration by 3 to 4 $\mu A/cm^2$ for the three different high chromium white iron alloys investigated. Likewise, the critical current density and the passive current densities were found to increase with increasing solution concentration. Comparing the quantitative corrosion values obtained from the corrosion tests reveals some interesting comparisons between the low carbon steel and AISI 420 martensitic stainless steel. In the 2.5M and 5.0M sodium hydroxide solutions, the corrosion current densities for steel and AISI 420 are significantly greater than the three different white irons, by 20 and 50 $\mu A/cm^2$ for the 2.5M and 5.0M NaOH solutions respectively, Figure 8.7. These results indicate that the corrosion performance of high chromium white iron alloys, with prior oxide layers removed, when immersed in sodium hydroxide solution is superior to the corrosion performance of AS1163: C350LO low carbon

steel and AISI 420 martensitic stainless steel. This is an interesting finding as the consensus in the literature is that the presence of the primary and or eutectic carbides significantly degrades the corrosion performance due to galvanic interaction between the carbides and the matrix (Kumar and Patwardhan, 1993, Tu et al., 2004).

Comparing the corrosion current values for the three white irons reveals some interesting relationships, Figure 8.7. The ranking of the materials in order of corrosion performance from lowest corrosion rate to highest corrosion rate was HyperA, HypoA and HyperEXP. The difference in corrosion current values between any of the three different materials did not exceed 10 μA/cm^2. However, the carbide volume fraction and matrix phase of the materials did vary. HyperA, which had the lowest corrosion current density had a hypereutectic microstructure with a carbide volume fraction greater than HypoA and similar to HyperEXP. The chromium content of the matrix of HyperA was 10.7%, which was also between the the matrix chromium content of 13.3% and 8.7% for HypoA and HyperEXP respectively. These findings indicate that carbide volume fraction alone is not a good indicator of corrosion performance. The corrosion performance of high chromium white iron alloys in sodium hydroxide solutions is believed to be a complex interaction between carbide volume fraction, inter-carbide spacing, matrix chemical composition, matrix phase and the presence of secondary carbides within the matrix.

The critical current density of the three high chromium white irons was also found to increase with increasing solution concentration, Figure 8.9. The critical current density was found to be the lowest for the HyperEXP alloy, followed by HyperA and HypoA for both the 2.5M and 5.0M NaOH solution. This ranking is opposite to the ranking for the corrosion current density. The difference between the critical current densities was approximately 100 μA/cm^2 for each of the alloys.

Given the similarities in polarization behaviour of the high chromium white iron castings, the AS1163: C350LO steel and AISI 420 martensitic stainless steel, it is likely that the corrosion mechanism in highly caustic sodium hydroxide solutions occurs by a similar mechanism in all cases. However, the rate of corrosion, as indicated by the current density, varies depending on the material. Based on the potential-pH diagrams for iron and chromium (Figures 8.10 and 8.11 respectively) and the literature, the corrosion mechanism in the active dissolution regime would be the dissolution of the matrix due to the formation of the $HFeO_2^-$ or $Cr(OH)_4^-$ ions via multiple reaction steps. The reaction at the active to passive transition would be iron dominated as chromium is unlikely to form an oxide. The passivation of the sample surface at the active to passive transition is most likely due to the formation of an Fe_3O_4 film. As the potential increases in the passive hump regime, further oxidation of the Fe_3O_4 film to Fe_2O_3 takes place resulting in a mixed oxide layer. When transpassive potentials greater than 0.0 V_{SHE} are reached, the rapid dissolution of the carbides occurs due to the dissolution of chromium to form CrO_4^{2-}. The dissolution of high chromium white iron in the transpassive regime being chromium dominated is verified by comparing the steel and AISI 420 stainless

steel polarization curves, Figures 8.12 and 8.13. Theses polarization curves show the passive behaviour of steel around 0.0 V_{SHE} is not affected while the AISI 420 stainless steel is.

Sodium Aluminate Solution

The anodic polarization curves for all of the materials investigated in the sodium aluminate solution at 90°C are shown in Figure 8.14. All of the materials showed an active dissolution regime with an approximately linear Tafel behaviour followed by active to passive transition at the critical potential in the potential range of -0.9 V_{SHE} to -0.8 V_{SHE}. The critical current densities for the three white irons were similar, but were significantly greater than the current densities for the low carbon steel and AISI 420 stainless steel. HyperA and HypoA showed very similar anodic polarization curve characteristics up to -0.3 V_{SHE}, with HypoA having a lower passive current density. HyperEXP did not follow a similar trend to HyperA or HypoA in the potential region above -0.7 V_{SHE}. After a region of active to passive behaviour, the current density increased with increasing potential, with a secondary current peak at -0.4 V_{SHE}. The current densities for HyperEXP in the passive region were also greater than those of HyperA and HypoA.

When the open circuit potential of the three different high chromium white irons in sodium aluminate solution are compared with the open circuit potential in the sodium hydroxide solutions (Figure 8.6) it was found that the open circuit potential in sodium aluminate solution is between those in 2.5M and 5.0M NaOH solutions. This result is attributed to the sodium aluminate solution having a free caustic concentration between the two sodium hydroxide solutions equivalent to a 2.7 M NaOH solution. The critical potential for the high chromium white iron castings investigated did not follow a uniform trend, Figure 8.8. The critical potentials for the HypoA and HyperEXP casting were between the potential for the 2.5 and 5.0M NaOH solutions in a similar manner to the open circuit potential results. However, the critical potential for the HyperA casting was less than the 2.5M NaOH solution critical potential by 0.40 mV. This result indicates the onset of passivation occurs at lower potentials in sodium aluminate solution for the HyperA alloy.

The corrosion current densities of the high chromium white iron castings in sodium aluminate solution were all found to be less than the 5.0M NaOH solution corrosion current density, Figure 8.7. Typical variations were 2 to 11 $\mu A/cm^2$ in the corrosion current density with the HyperEXP casting having the largest variation. With the exception of the HyperEXP casting, the corrosion current densities for the HypoA and HyperA castings were found to be 0.5 to 1.5 $\mu A/cm^2$ greater than the 2.5M NaOH solution corrosion current density. Comparing the corrosion current density results for all the materials investigated (Figure 8.7), it is found that the significant drop in current density in the sodium aluminate solution compared with the NaOH solutions seen for the low carbon steel and AISI 420 stainless steel does not occur for the high chromium white iron casting alloys. It is also found that the corrosion cur-

rent density for the low carbon steel and AISI420 stainless steel are less than the white iron castings in sodium aluminate solution but significantly greater in sodium hydroxide solution. It has been previously discussed that the sodium aluminate solution has an inhibiting effect on the active dissolution behaviour of steel and AISI 420 stainless steel due to the presence of the aluminate ions which adsorb on the surface and inhibits the rate of corrosion. However, these results indicate that the aluminate ions have no noticeable inhibiting effect on the corrosion rate for the high chromium white iron castings investigated under freely corroding conditions.

The critical current densities for the high chromium white irons (Figure 8.9) show that the active dissolution up to the critical potential was significantly higher in the sodium aluminate solution compared with the 2.5 and 5.0M NaOH solutions. The increase in critical current densities ranged 550 to 750 μA/cm^2 compared with the 5.0M NaOH solution critical current density. These results demonstrate that the presence of aluminate ions significantly enhance the active dissolution of high chromium white ions compared with aluminate free NaOH solutions of similar caustic concentration. While a reduction in the critical current density in sodium aluminate solution compared with the 5.0M NaOH solution was seen for steel and a negligible increase for AISI 420 stainless steel, the results for the high chromium white irons must be influenced by their microstructure.

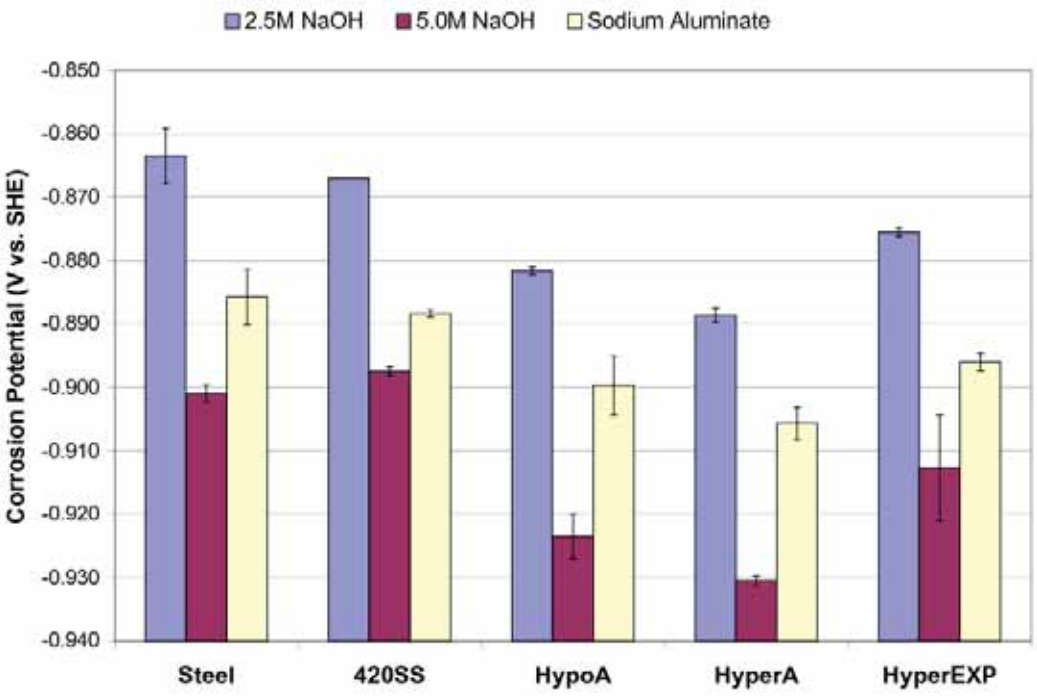

Figure 8.6: Variation in the corrosion potential for the 2.5M, 5.0M NaOH and sodium aluminate solution for the alloys investigated.

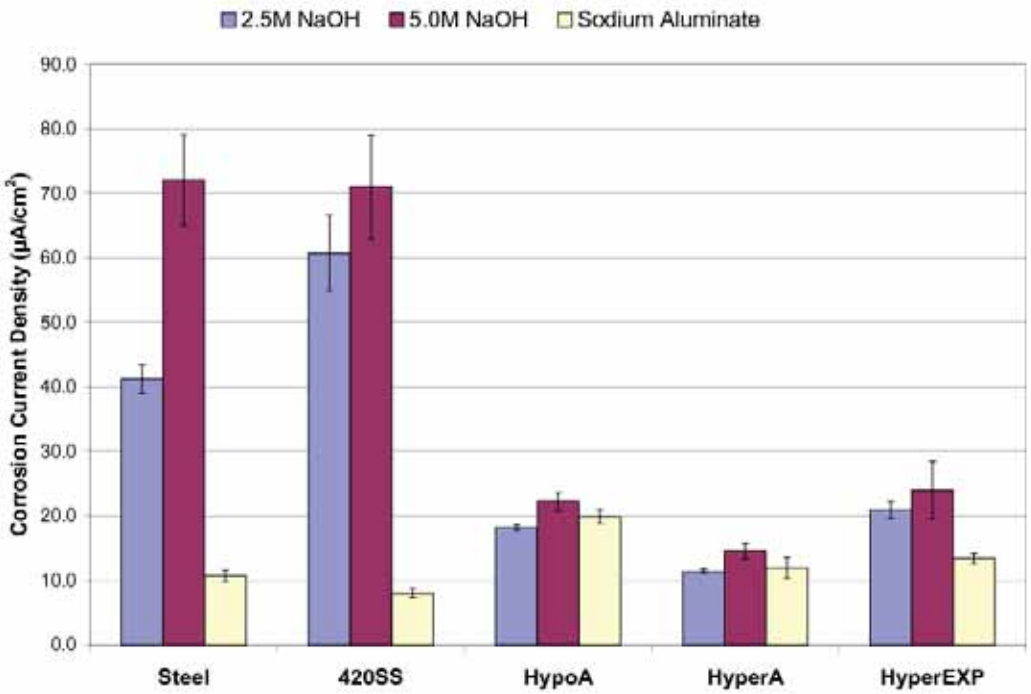

Figure 8.7: Variation in the corrosion current density for 2.5M and 5.0M sodium hydroxide solutions and sodium aluminate solution for the alloys investigated.

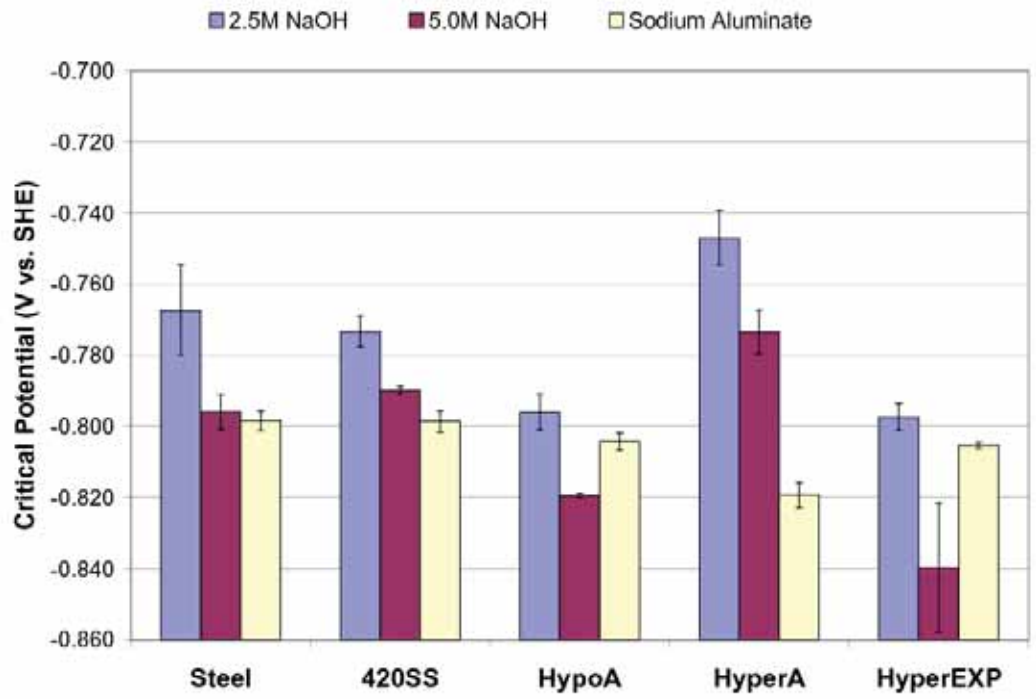

Figure 8.8: Variation in the critical potential for the 2.5M, 5.0M NaOH and sodium aluminate solution for the alloys investigated.

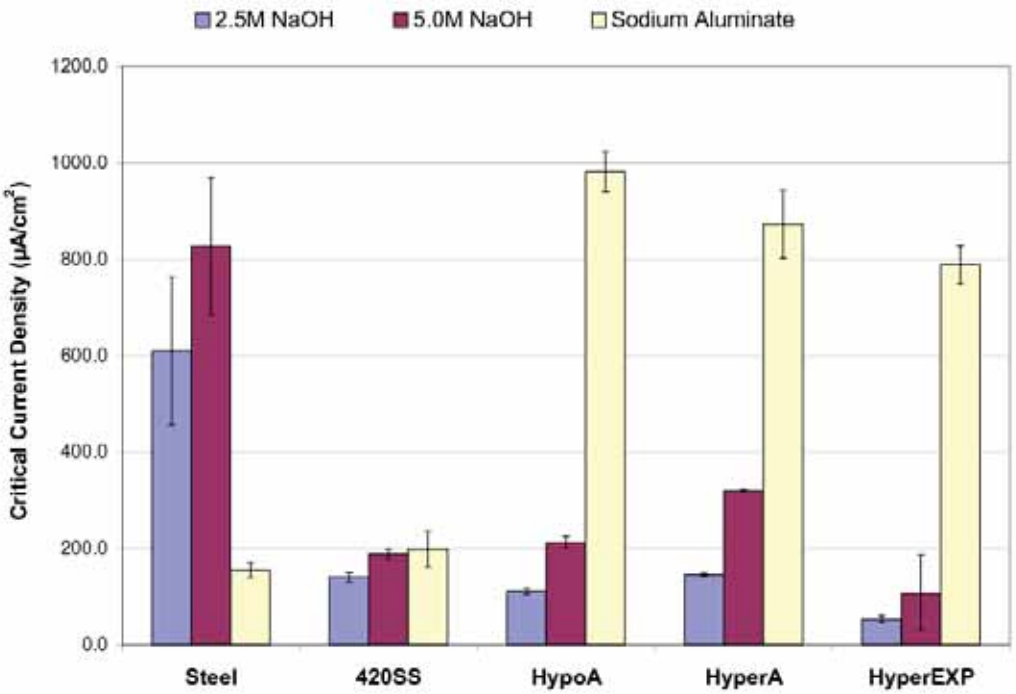

Figure 8.9: Variation in the dissolution current density for all of the materials investigated in deaerated 2.5M, 5.0M NaOH and sodium aluminate solution for the alloys investigated.

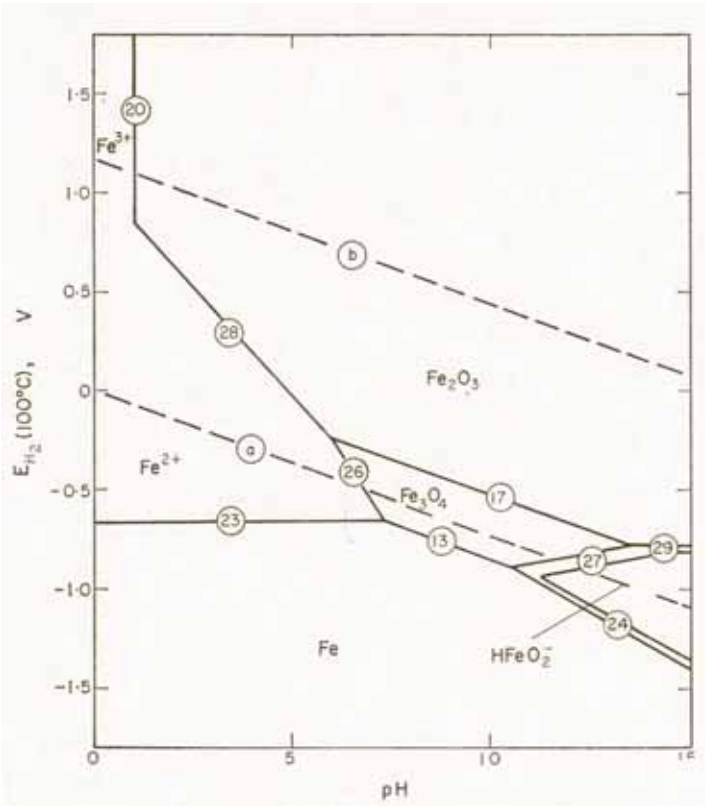

Figure 8.10: Potential pH diagram for iron at 100°C (Townsend Jr, 1970).

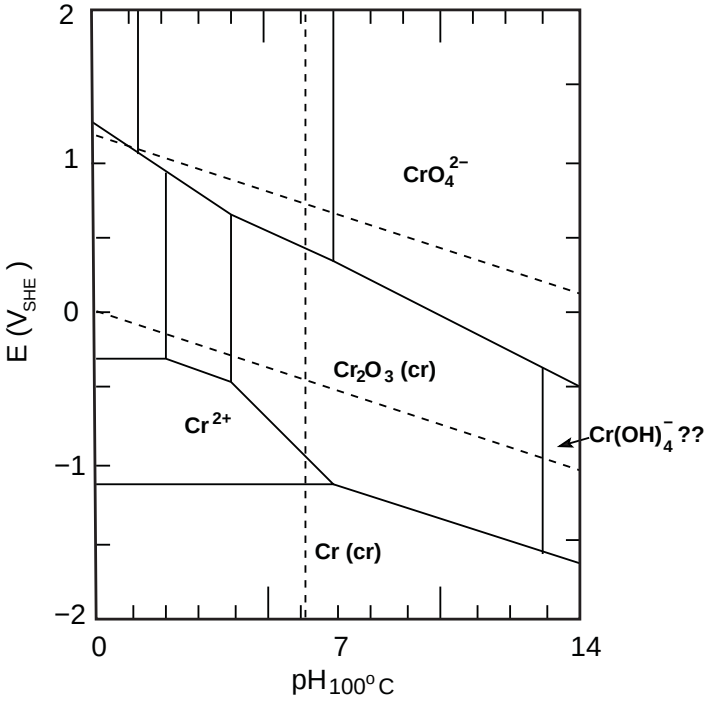

Figure 8.11: Potential pH diagram for chromium at 100°C (Beverskog and Puigdomenech, 1997).

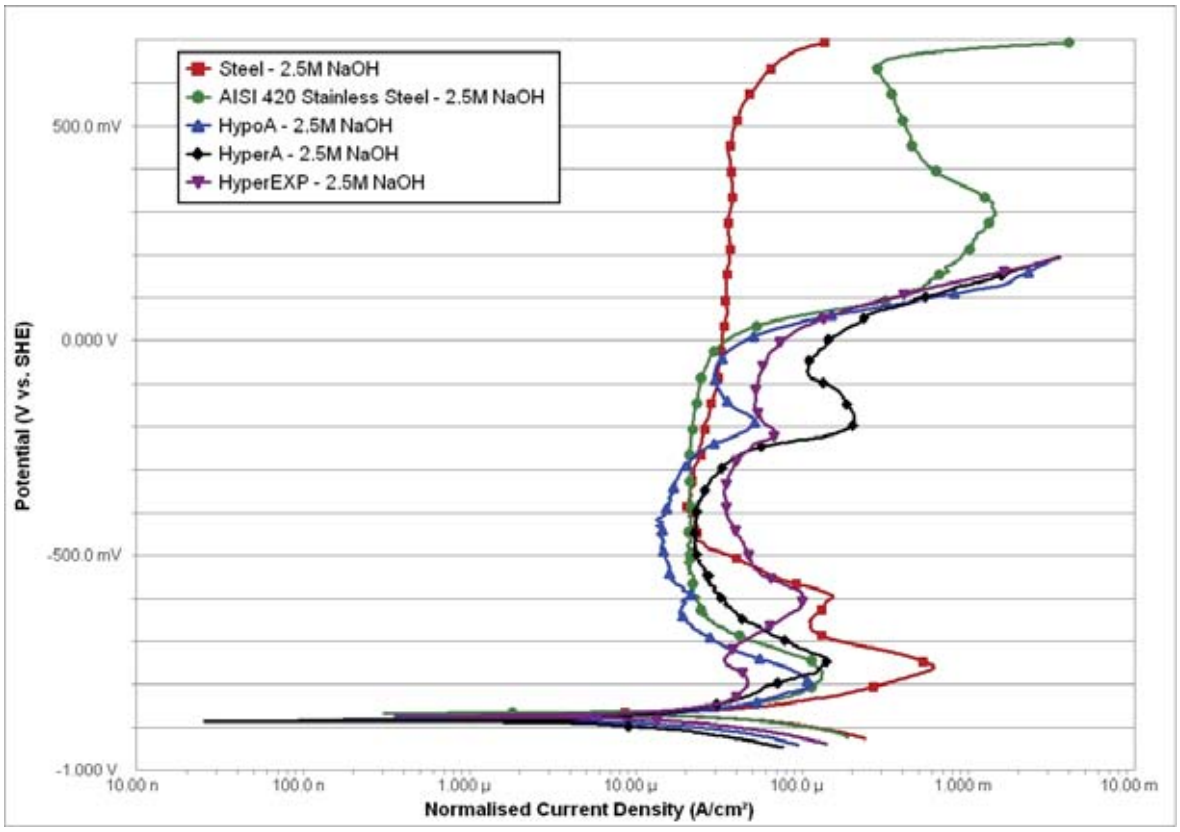

Figure 8.12: Anodic polarization curves for all of the samples investigated in deaerated 2.5M NaOH solution at 90°C and at a scan rate of 1 mV/s.

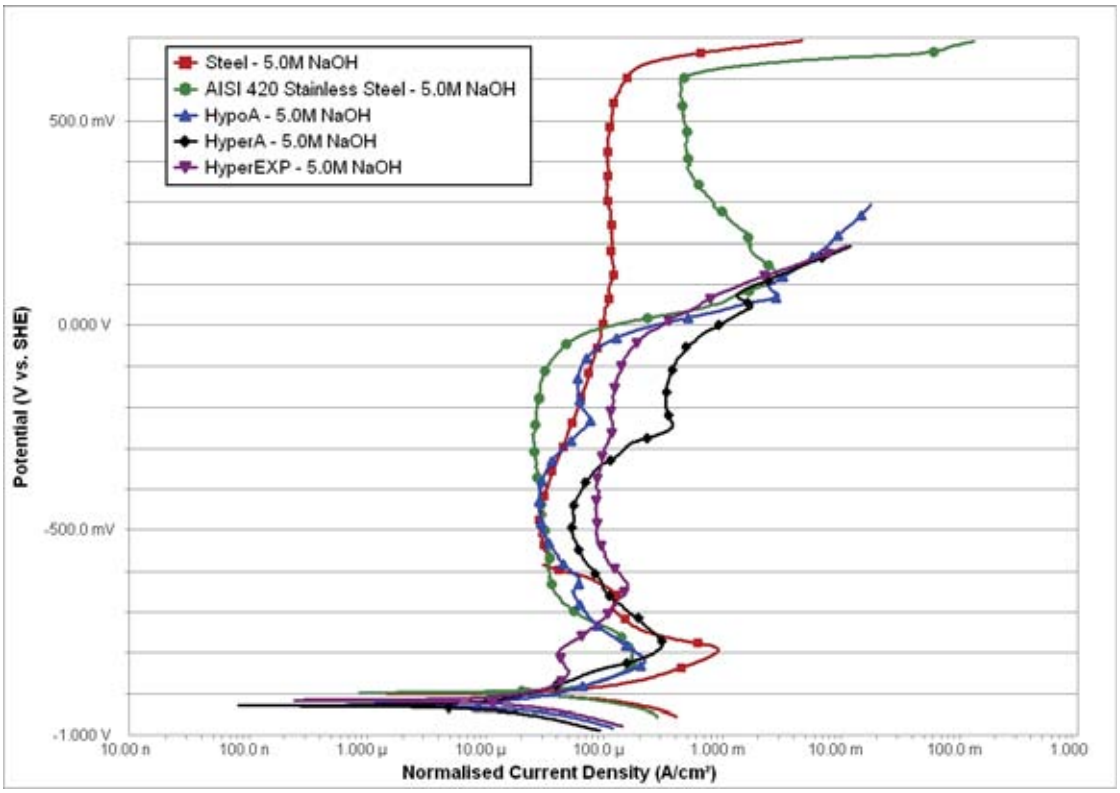

Figure 8.13: Anodic polarization curves for all of the samples investigated in deaerated 5.0M NaOH solution at 90°C and at a scan rate of 1 mV/s.

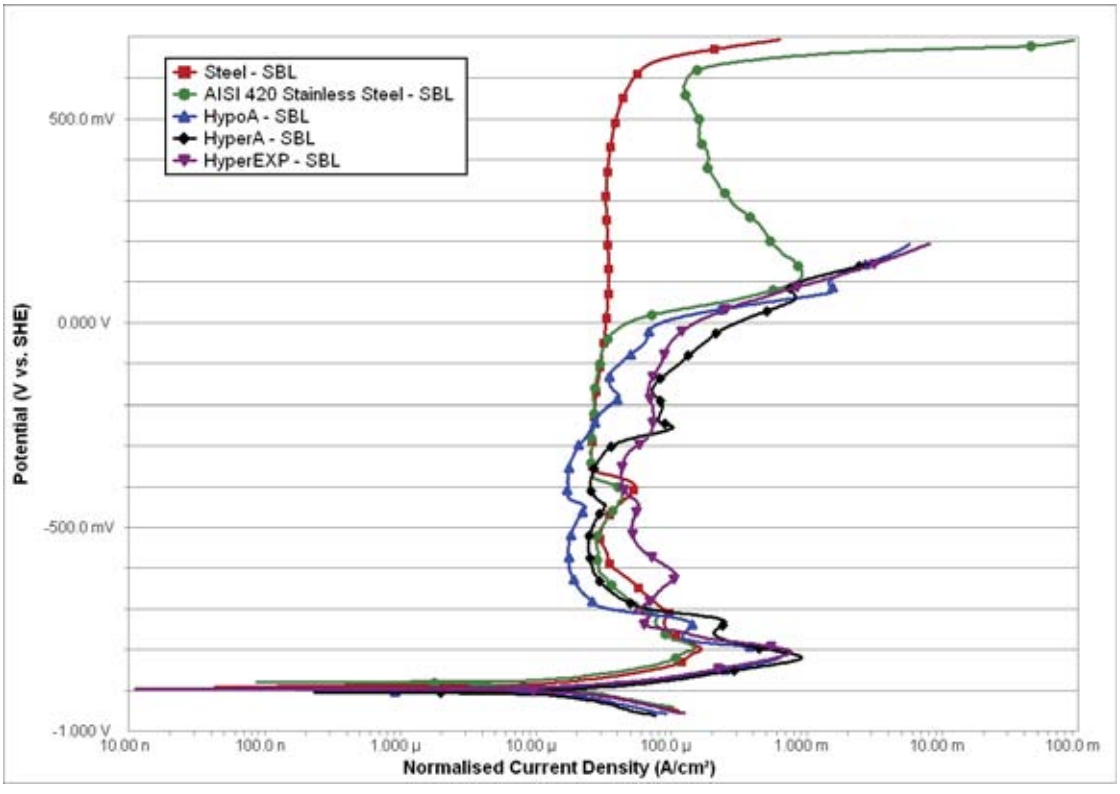

Figure 8.14: Anodic polarization curves for all of the samples investigated in deaerated sodium aluminate solution at 90°C and at a scan rate of 1 mV/s.

8.2.2 Corrosion of Weld overlays In Sodium Aluminate Solutions

The corrosion of two commercially deposited hypereutectic high chromium white iron weld overlays of slightly different chemical composition was investigated in 90°C deaerated sodium aluminate solution. The corrosion testing of the weld overlays was found to give variable results when different sections of the same alloy were tested or a test was duplicated on the same sample. Figure 6.21, shows two different polarization curves for the same sample and the variation in current density values. This difficulty in corrosion testing was attributed to large variations seen in microstructures and that the samples contained check cracks. For the corrosion tests samples, it was attempted to fill the check cracks with epoxy resin, however, the integrity of the epoxy and its ability to eliminate the environment from the cracks was questionable in the 90°C pH 14 solution due to the epoxy softening.

The polarization response of the two materials generally showed similar characteristics, Figure 6.21. An active dissolution regime was seen from -0.91 V_{SHE} to -0.8 V_{SHE} with approximately linear Tafel regions. Following the active dissolution, the WeldoverlayB sample showed passive behaviour characterized by a hump potential regime with a decrease in current density compared with the critical current density. The WeldoverlayA sample showed a slight decrease in current density above the critical potential to -0.78 V_{SHE} before increasing again and peaking at -0.7 V_{SHE}. Following this slight peak was a passive hump regime. Above 0.0 V_{SHE} both materials demonstrated transpassive behaviour and carbide corrosion.

When the polarization results for the weld overlays are compared with the castings samples, Figure 8.16, it is seen that the the potential at which corrosion features occur are similar indicating that similar corrosion mechanisms are occurring. However, significant differences are seen in the current density results, particularly in the passive potential regime which indicate an increase in corrosion rate. Comparing the corrosion currents, Figure 8.15, it is found that the corrosion current is approximately an order of magnitude greater than the corrosion current for the cast samples. However, the critical current density is similar for the weld overlay and castings with the WeldoverlayA sample having the lowest average of all high chromium white irons tested. These large difference in corrosion current density are attributed to the presence of check cracks and the variations in microstructure compared with the cast samples.

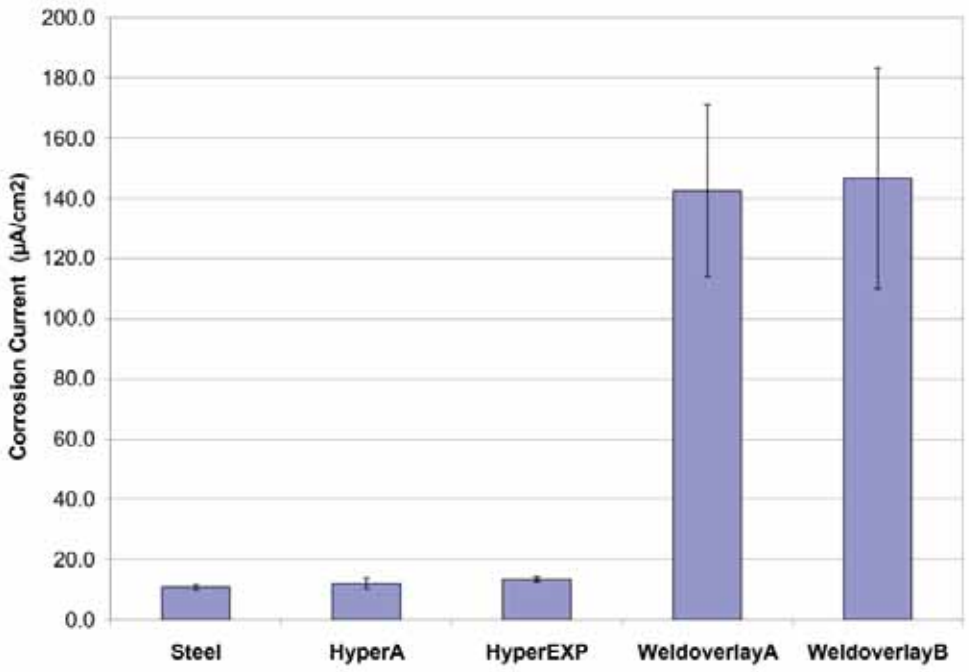

Figure 8.15: Variations in the corrosion current density for the weld overlays compared with the hypereutectic castings and steel in deaerated sodium aluminate solution at 90°C.

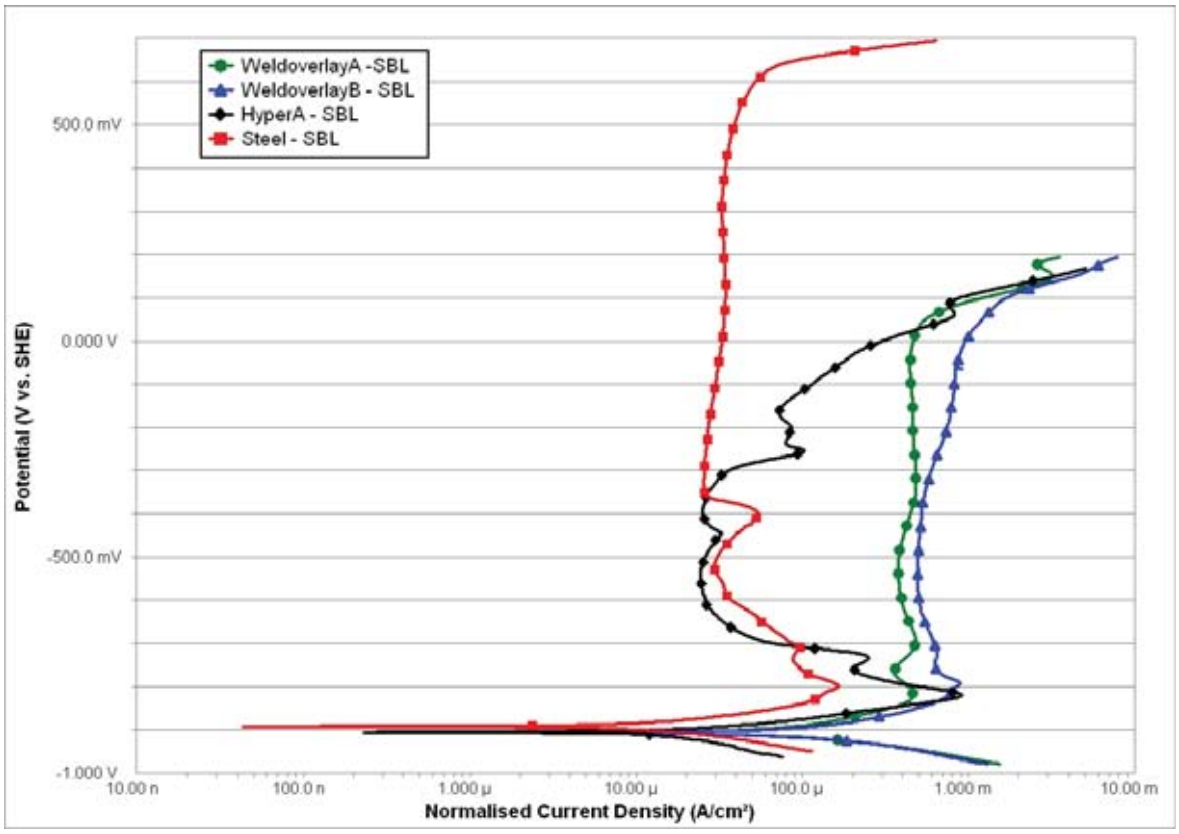

Figure 8.16: Comparison of the typical anodic polarization curves for AS1163: C350LO low carbon steel, HyperA, WeldoverlayA and WeldoverlayB in deaerated sodium aluminate solution at 90°C and a potential scan rate of 1 mV/s.

8.2.3 Immersion Tests In Sodium Aluminate Solution

The immersion tests done at the open circuit potential, active dissolution potential and the passive potential revealed that the matrix corrodes while the carbides undergo little or no corrosion. This is consistent with what is reported in the literature, in that the corrosion of high chromium white irons occurs by the dissolution of the matrix (Neville et al., 2006, Meulendyke et al., 1987, Ma et al., 1990, Zhang et al., 2004, Day, 1982).

Open Circuit Potential

The immersion tests done in hot sodium aluminate solution for four hours at open circuit potential, showed that the matrix corrodes and the carbides undergo little or no corrosion. This was evident by the 1200 grit polishing marks still seen running through the carbides after the immersion test. After the immersion test, the two cast samples and weld overlay sample were covered with a grey/black corrosion product, or a tarnish, that was easily removed by gently rubbing with a red rubber stopper. The corrosion product covering the surface on the two casting samples was not identified but it is believed to be a non protective and non equilibrium film of $Fe(OH)_2$ (Singbeil and Tromans, 1982). For the weld overlay sample the corrosion product covering the surface was similar to the castings but in addition had plate like crystals in the region between the carbides once occupied by the matrix. These plate like crystals were identified to be rich in aluminium and oxygen which would imply they are crystals of alumina hydrate. It is possible that the presence of the alumina hydrate crystals could affect the rate of corrosion.

For the HypoA and HyperA casting samples it appeared that one matrix phase was preferentially attacked. Both of the cast samples had a heterogeneous matrix of retained austenite and martensite (refer Figures 5.2 and 5.6 for the microstructures of HypoA and HyperA respectively). The electron micrographs of the immersion test sample surface for HypoA (Figure 6.23) show that the phase that was preferentially attacked occurred uniformly throughout the matrix. For the HyperA sample (Figure 6.30) the phase that was preferentially attacked was readily seen to occur around the large carbides and precipitated carbides (also refer Figure 6.32 for the HyperA casting at the active dissolution potential for a similar matrix appearance). From the microstructural examination and the location of the preferential corrosion from the immersion tests, it is likely that the phase that is preferentially attacked is the martensitic phase. It is likely that the martensitic phase was anodic with respect to the austenitic phase or there was a greater infinity for corrosion of the martensitic phase. It is common for heterogeneous materials to experience greater corrosion rates (Fontana, 1986).

Qualitatively, it was seen that the weld overlay suffered the most corrosion, followed by the HypoA casting and HyperA casting underwent the least. This is consistent with the corrosion current results shown in Figure 8.15. The rate of matrix corrosion in the weld overlay sample was so significant that the majority of the matrix could not be seen between the closely spaced

primary and eutectic carbides. Traces of the matrix were only seen in regions where there were large austenite halos surrounding the primary carbides. Even then, the halo showed evidence of corrosive attack that was greater adjacent to the carbides, Figure 6.36. It was also seen in the case of the HyperA casting sample that matrix regions surrounding the precipitated carbides would undergo greater corrosion, Figure 6.30.

The presence of manganese sulphide inclusions was found to create the appearance of pitting on the test surface. FESEM examination of the surface found that the inclusion were subjected to accelerated corrosion attack as well as the surrounding matrix areas, Figures 6.23, 6.25, 6.32.

Active Dissolution

Immersion of the two cast samples and weld overlay sample in the active dissolution regime showed similar results to the open circuit potential response discussed above. However, qualitatively comparing the corrosion surface, it would appears that the matrix has undergone greater corrosion than at the open circuit potential. This is consistent with the polarization test results as an increase in anodic potential results in a large increase in current in the active dissolution regime. As the mechanism by which corrosion occurs is due to the formation of dissolved iron or chromium ions, the increase in matrix corrosion is as expected.

It is again found that the matrix preferentially corrodes adjacent to the carbides, the clearest evidence being the remaining halo regions of the weld overlay sample, Figure 6.38, and the corrosion around the secondary carbides in the HyperA alloy, Figure 6.32.

The corrosion product covering the HyperA alloy also contained alumina hydrate crystals similar to the weld overlay at the open circuit potential. Likewise, the weld overlay had traces of alumina hydrate that covered the surface.

Passive Potential

Immersion in the passive potential regime resulted in less corrosion of the matrix for all of the samples compared with the open circuit potential immersion tests. The sample surface was still covered with a corrosion product layer, the bulk of which could easily be removed. However, examination at higher magnification found that the matrix was covered with an oxide layer that was not removed by gently rubbing the surface with a red rubber stopper (e.g. Figure 6.39).

For the two casting samples that matrix was readily visible, still containing the 1200 grit polishing marks. It is apparent that the HypoA sample has undergone very little matrix carbide interaction. The HyperA casting on the other hand shows that corrosion of the matrix was generally associated with the precipitated carbides and in a region adjacent to the primary carbides, Figure 6.34. The region adjacent to the primary carbides has a band of martensite

(see Figure 5.6) and the accelerated corrosion in this region could be due to variations in chemical composition or due to increased galvanic interaction. The higher corrosion rate of the HyperA alloy compared with the HypoA alloy is reflected in the passive corrosion current densities from the polarization results, with HyperA having the higher current density.

The matrix corrosion of the weld overlay in the passive potential regime was more significant than for the hypoeutectic and hypereutectic castings investigated, Figure 6.40. As per the open circuit and active potential regime immersion tests, the matrix in closely spaced eutectic carbide regions could not be seen indicating that the matrix is significantly recessed with respect to the carbides. However, the austenite halos surrounding the primary carbide were found to undergo less corrosion compared with the active dissolution regime. The preferential corrosion of the austenitic halos adjacent to the carbide-matrix interface was clearly seen from these tests. From the microstructural examination undertaken as part of this thesis and the reported literature (Powell and Bee, 1996), it is common to find a thin band of martensite surrounding the carbides. This martensitic layer is a result of the depletion of carbon and chromium in the matrix adjacent to the carbide due to the solidification and subsequent solid state growth of the carbides.

8.2.4 Influence of Microstructure on Corrosion

The previous section on the influence of environment on corrosion has investigated the polarization response of five different high chromium white iron alloys and compared them with AS1163: C350LO steel and AISI 420 martensitic stainless steel. The polarization and immersion tests done at potentials of interest have identified that the matrix of the high chromium white iron alloys corrodes and the carbides remain uneffected. Due to the similarities in polarization curves with respect to corrosion events occurring at a particular potential for all of the alloys investigated, it was deduced that the corrosion mechanism of the matrix is also similar for all of the alloys. However, the rate of corrosion, as indicated by the different current densities of the polarization curves, was dependent on the composition and whether it was cast or a weld overlay. From the set of tests in the sodium hydroxide solutions and the sodium aluminate solution, it was only possible to draw general conclusion as to the the role of microstructure and its influence on corrosion.

The set of tests reported in Section 6.2.3 that investigates the effect of microstructure on corrosion was done to more rigorously examine the role matrix microstructure has on corrosion. Heat treatments of four different high chromium white iron castings were used to alter the matrix phases while leaving the primary and eutectic carbides unchanged. Thus any variations in polarization curve response would be attributed to variations in matrix microstructure.

8.2.4.1 Comparison of Microstructures

The materials investigated included HypoA, EutecticA, HyperA and HyperEXP castings in the destabilized heat treated condition and normalized heat treated condition. The microstructures of these four high chromium white iron castings have been well characterized and previously discussed. The CVF along with the bulk chromium and carbon composition are compared in Figure 8.4.

8.2.4.2 Influence of Matrix on Corrosion

The polarization tests on the four high chromium white iron castings in various conditions, i.e. as-cast, destabilized and normalized, has indicated that the matrix microstructure has an influence on the corrosion response of the alloy, Figures 6.9, 6.11, 6.13 and 6.15. For a particular alloy the variations in potentials of the corrosion phenomena for the different matrix conditions was small. Variations in the open circuit potential ranged from 1 to 14 mV and variations in the critical potential ranged from 0 to 14 mV. However, the corrosion rate as indicated by the corrosion current density varied more significantly with changes in the matrix microstructure, Figure 8.17 and 8.18.

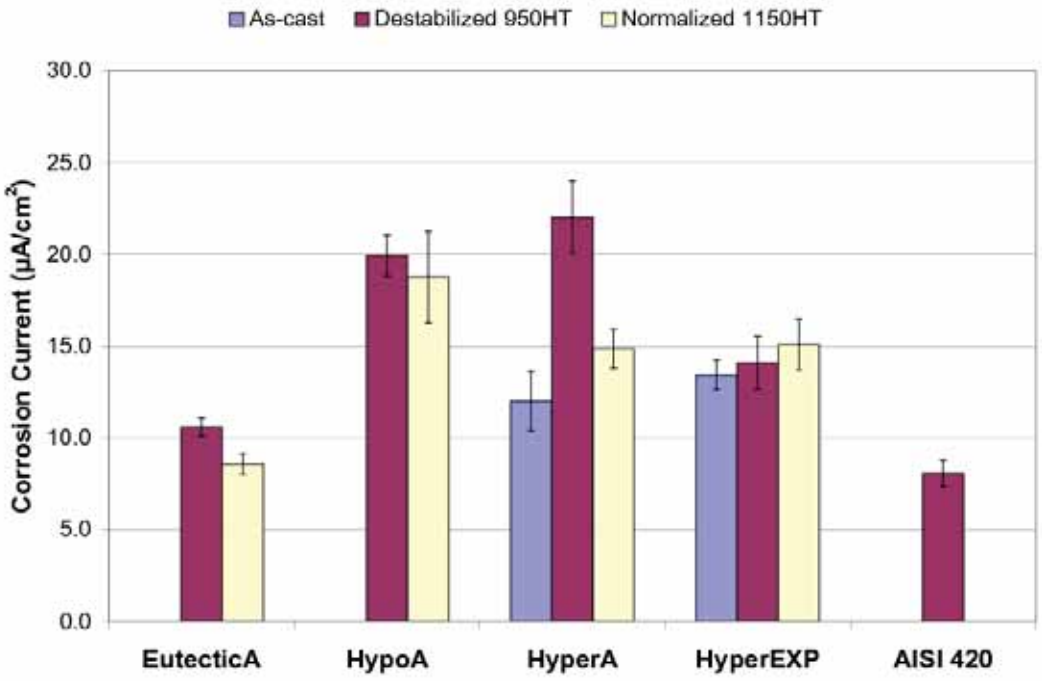

Figure 8.17: Comparison of the corrosion current densities in sodium aluminate solution at 90°C for the investigated alloys in the as-cast, destabilized and normalized condition.

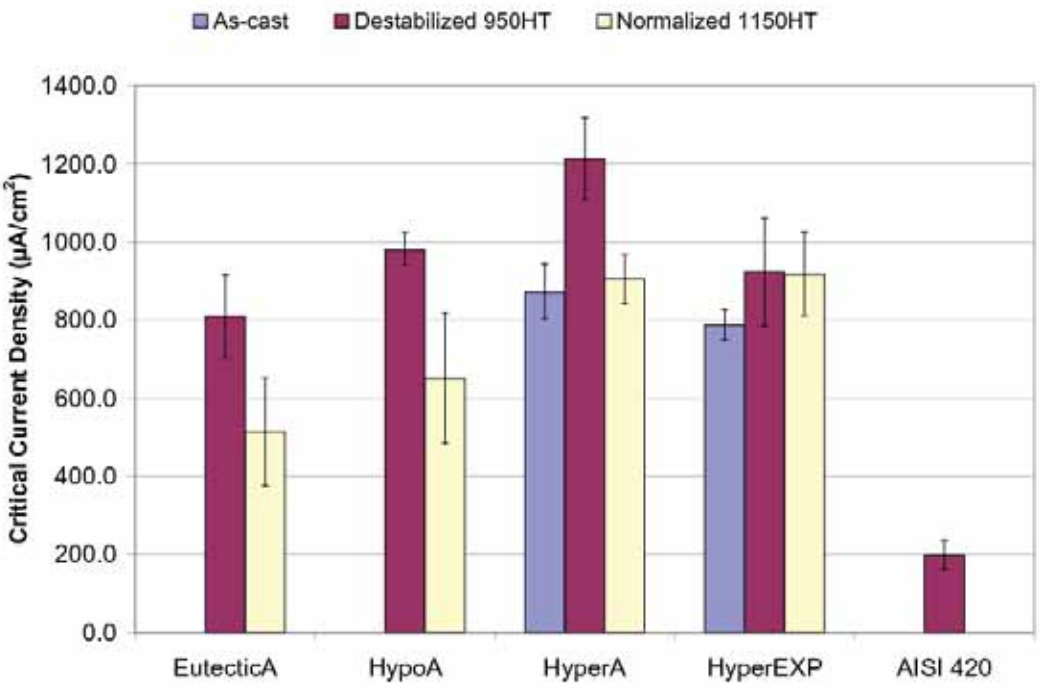

Figure 8.18: Comparison of the critical current densities in sodium aluminate solution at 90°C for the investigated alloys in the as-cast, destabilized and normalized condition..

With the exception of the HyperEXP alloy, a reduction in the corrosion current density and critical current density, Figure 8.17 and 8.18 respectively, was noticed for the normalized condition compared with the destabilized condition. Similarly, the current density in the passive hump regime was generally less for the normalized condition than the destabilized condition. For the HyperEXP alloy, the corrosion current density and critical current density were found to be similar for the destabilized and normalized conditions. The current density in the passive regime for the HyperEXP sample was found to be nearly identical for the destabilized and normalized condition, Figure 6.15.

The nearly identical polarization behavior of the HyperEXP alloy in the two heat treated conditions is interesting given that the matrix microstructures are distinctly different, Figure 6.14, and that the chemical composition of the matrix is also different. In the destabilized condition the matrix of the HyperEXP casting has extensive precipitation of small secondary carbides and a subsequent reduction in matrix chromium composition of about 2.8% compared with the normalized condition. In the normalized condition, there are fewer but larger secondary carbides and the matrix chromium composition is higher. However, for both the destabilized and normalized conditions, the matrix remains fully austenitic (shows no attraction to a strong magnet). For the HypoA and HyperA casting alloys, the presence of precipitated carbides have been shown to cause accelerated corrosion of the matrix in areas immediately surrounding the small carbides as highlighted in the immersion tests. These results for the HyperEXP casting in the destabilized and normalized condition suggest that

the presence of small precipitated carbides has negligible influence on the rate of corrosion, or that the reduced matrix chromium content leads to an improvement in corrosion performance.

The matrix microstructures of the destabilized and heat treated HypoA, EutecticA and HyperA castings were comprised of secondary carbides in a transformed matrix of martensite and retained austenite. The normalized matrix is generally precipitated carbide free and dominantly austenitic with some martensite (alloys show reasonable attraction to a magnet). The chromium composition of the destabilized matrix is also less than the normalized condition, with the HypoA alloy being the only alloy to have greater than 12% matrix chromium in the destabilized and normalized condition.

The superior corrosion performance of the HypoA, EutecticA and HyperA castings in the normalized condition is attributed to the matrix being dominantly austenite and more homogeneous. The reduction in corrosion performance of the same alloys in the destabilized condition is attributed to the matrix being heterogeneous due to the presence of multiple matrix phases (martensite and retained austenite) and the presence of precipitated secondary carbides. The immersion tests have shown that a matrix phase is preferentially attacked. The evidence suggests that it is the martensitic phase which corrodes at an accelerated rate and the austenite phase at a lesser rate. The increased corrosion rate of the martensitic phase may be due to a reduction in alloy composition or the martensitic phase is anodic with respect to the austenite. The immersion tests also showed that the presence of precipitated carbides cause accelerated corrosion in the areas surrounding the carbides. This would also account for the increased corrosion rate in the destabilized condition.

The variations in matrix chromium composition between the normalized and destabilized condition were quantitatively measured to be different, Figure 8.2, however, the influence of increasing chromium composition to improve corrosion performance in highly alkaline sodium aluminate solutions was questionable. It was found that the HypoA alloy having the highest matrix chromium composition of approximately 14 wt% and the lowest CVF of 26% in the normalized condition did not have the lowest corrosion current density or critical current density, Figures 8.17 and 8.18 respectively. The high chromium white iron found to have the best overall open circuit and active dissolution corrosion performance was the EutecticA alloy which had a matrix chromium composition of approximately 11 wt% and a CVF of 39%. However, the current density in the passive potential regime for the HypoA casting in the destabilized or normalized condition was lower than all of the other castings investigated, Figures 8.19 and 8.20 respectively. These findings suggest that increasing matrix chromium alone will not lead to improved corrosion performance at the corrosion potential or in the active dissolution regime (i.e. under freely corroding conditions) but may contribute to improve the corrosion performance in the passive potential regime. However, in an erosive corrosive environment it is unlikely that a passive film will form and the material will remain in the active dissolution regime, thus, a low alloy white iron such as EutecticA is likely to

give better corrosion performance.

The finding that increased matrix chromium composition does not lead to improved corrosion resistance under freely corroding conditions in highly alkaline sodium aluminate environments is similar to the finding reported by Tu et al. (2004). Tu et al. (2004) reported the static corrosion in concentrated caustic for a hypoeutectic alloy of 3C, 27Cr and matrix chromium of about 16 wt% was greater than a 1.9C, 14Cr alloy with a matrix chromium composition of about 12 wt%. It was believed that increasing matrix chromium resulted in the increased dissolution, however, it should be noted that CVF of the alloy having the lower corrosion rate was also significantly lower. This work has shown that the increasing corrosion rate with increasing matrix chromium composition under freely corroding conditions is independent of CVF. These findings are contrary to the consensus reported in the literature that increasing matrix chromium composition will improve corrosion performance. However, the basis for these findings reported in the literature is in solutions having pH values typically less than 11 that have been extrapolated to include the higher pH environments. The potential-pH diagram for chromium, Figure 8.11, indicates that chromium will not form any protective oxide layers in a solution with a pH greater than 13 at elevated temperatures. This provides further verification that matrix chromium composition is likely to have negligible influence on corrosion performance in highly caustic pH 14 solutions.

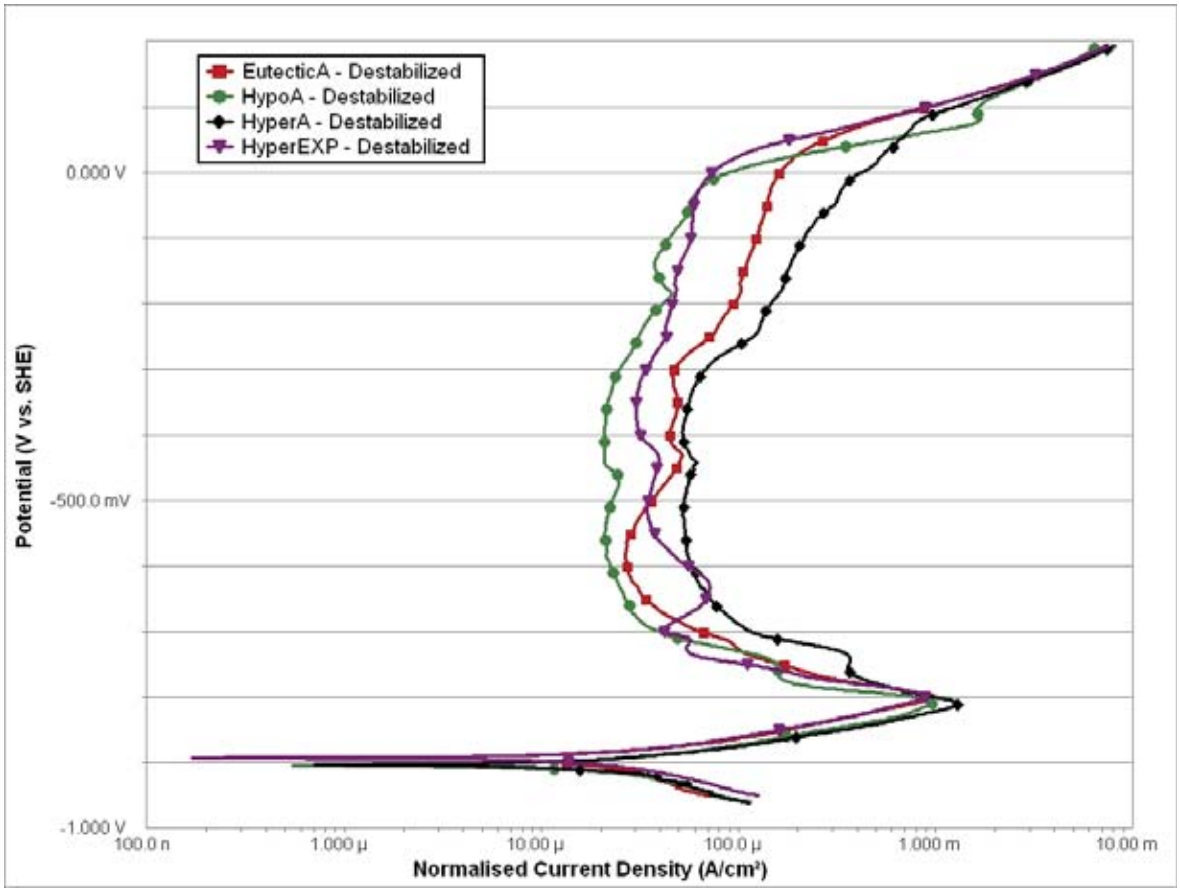

Figure 8.19: Polarization curves all materials heat treated or hardened at 950°C for 6 hours and air cooled.

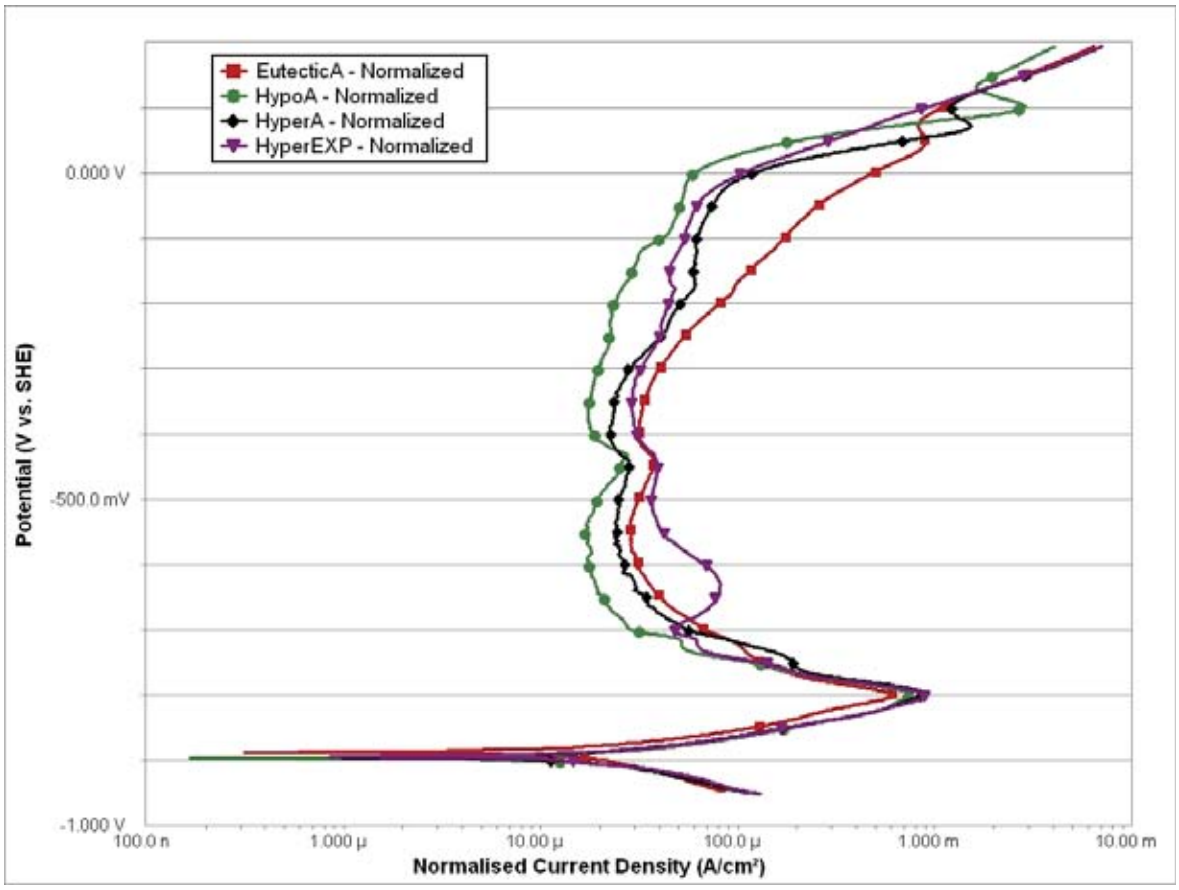

Figure 8.20: Polarization curves for all materials heat treated at 1150°C for 6 hours and air cooled.

8.2.4.3 Influence of Carbides on Corrosion

The finding of the experimental work was that the carbides of high chromium white irons remain inert, or the corrosion of the carbides is negligible while the matrix corrodes. Observations from the immersion tests found that the matrix generally corrodes at the carbide matrix interface. This suggests that there may be a galvanic interaction between the carbides and the matrix, that there are variations in the matrix phase adjacent to the carbides, or there is a variation in composition of the matrix phase adjacent to the carbides that leads to an increase in interface corrosion.

The chemical compositions of the carbides were found to vary slightly in chromium and other minor alloying elements depending on the bulk chromium to carbon ratio. These slight variations in chemical composition could change the open circuit potential of the carbides, possibly increasing the galvanic interaction between the carbides and the matrix. Zhang et al. (2004) has reported that the difference in the potential between the eutectic M_7C_3 carbides in a 2.5C, 14Cr and 2.6C, 23Cr alloy varied by 11 mV in an acidic pH 1.5 solution. The carbides in the 23Cr alloy contained more chromium and had a more noble potential. Based on Zhang et al. (2004) findings, it is expected that the slight variations in chemical composition of the carbides in high chromium white irons in highly alkaline sodium aluminate solutions would

also vary their open circuit potential. However, this has not been verified in the current work and no further indication can be given of the magnitude of the shift in potential or if it is in the noble or active direction for an increase in carbide chromium composition.

The galvanic couple between the carbides and the matrix can be examined by application of mixed potential theory for two corroding metals, Figure 8.21 (Fontana, 1986). The carbides, labeled M, are considered to be the more noble material, hence the cathode, and have a low corrosion rate. The corrosion reactions of the carbides in caustic solutions are not known but at cathodic sites are probably the evolution of hydrogen and the dissolution of the carbide as metal cations having a corrosion rate icorr(M). The matrix, labeled N, is considered the more active metal, hence the anode, and would have a higher corrosion rate. It has been shown that the cathodic reaction of the matrix is the evolution of hydrogen and the anodic reaction is the dissolution of iron or chromium having a corrosion rate icorr(N). When the carbides and matrix are in electrochemical contact, the cathodic reaction will increase as the vector sum of the respective cathode reactions for the individual metals to the dashed total reduction rate line (note the log scale). Likewise the anodic reaction will increase to the total oxidation rate line. The coupled corrosion rate occurs where the total oxidation rate at the anode equals the total reduction rate at the cathode. This occurs at a potential between the two materials, Ecouple. The new corrosion rate of the anode, or the matrix, is increased to icorr M-N* and the corrosion rate of the cathode, or the carbides, is reduced to icorr M*-N. Therefore, the corrosion rate of the matrix increases while the corrosion rate of the carbides is reduced due to the couple. As can be seen from Figure 8.21, galvanic corrosion is determined by the the reversible electrode potentials of the actual process involved (i.e. $E_{H+/H2}$ and $E_{M/M+}$), their exchange current densities (i.e. $i_{0H2(M)}$ and i_{0M}), and Tafel slopes.

Figure 8.21: Galvanic couple between two corroding metals (Fontana, 1986).

One of the driving forces for galvanic corrosion is the potential difference between the coupled metals. Minimizing the potential difference between the carbides and matrix would lead to a reduction in corrosion rate of the matrix. This applies to the primary and eutectic M_7C_3 carbides and the secondary carbides. It is difficult to conclusively determine from the experimental results what factors would influence the rest potential of the matrix or the carbides. Factors are likely to be chemical composition and whether the matrix is homogeneous or heterogeneous.

Another driving force for galvanic corrosion is the relative area between the cathode and anode which has a significant influence on the galvanic corrosion rate (Fontana, 1986). As the relative size of the cathode in a galvanic couple is increased, the corrosion rate of the anode increases. The anode to cathode ratio of high chromium white irons is determined by the CVF. Increasing the cathode area by increasing the CVF, increases the exchange current, effectively moving the cathodic reaction line ($io_{H2(M)}$) to the right in Figure 8.21. The total vector sum of the cathodic reduction reactions are greater and the intersection of the total reduction rate and the total oxidation rate lines will occur at a higher potential that is closer to the rest potential of the cathode resulting in the higher corrosion rate of the anode.

As high chromium white irons consist of carbide rods, the corrosion of the matrix would expose the sides of the carbide rods. This leads to a greater cathode to anode area and would increase the rate of matrix corrosion. From the earlier discussion on CVF versus carbide size, a white iron having more numerous carbides that are more closely spaced would have a greater cathode to anode area than a white iron having the same CVF but with larger carbides that are spaced at a greater distance (refer Appendix B). Also, accelerated corrosion due to the galvanic effects is usually greatest near the junction between the cathode and anode, with attack decreasing with increasing distance from the junction. Therefore, a smaller inter-carbide spacing is likely to further enhance the corrosion rate of the matrix. The increases in matrix corrosion rate due to a large number of carbides with a small inter-carbide spacing was typical of what was seen for the hypereutectic weld overlay (WeldoverlayA) in the immersion tests. The matrix of the weld overlay had corroded so much in the closely spaced carbide regions that it was unresolvable during FESEM examination. This result is compared with the immersion test for a hypereutectic casting (HyperA) which has larger carbides spaced further apart and showed significantly less corrosion of the matrix but a greater corrosion rate adjacent to the carbides.

Based on the mixed potential theory, if the corrosion of the carbide rods is negligible, as the experimental results have indicated, then the measured current density would be attributed to the dissolution of the matrix. As the matrix only represents 75 to 50% of the material, the actual current density would be 33 and 100% greater than the actual current densities measured. This would represent a significant increase in the penetration rate of the matrix.

The experimental results have shown that CVF alone is not a good indicator of corrosion performance, Figure 8.17. The EutecticA alloy having a CVF of approximately 39% had a

lower corrosion rate than the HypoA alloy having a CVF of approximately 26% in both the destabilized and normalized condition. It was also found that the HyperA and HyperEXP alloys having a CVF of around 50% had a lower corrosion rate than the HypoA alloy in the normalized condition. It is reiterated that the galvanic interaction does not solely depend on the cathode to anode ratio (i.e. CVF). The materials investigated had varying chemical compositions of the carbides and matrix, varying carbide sizes and inter carbide spacing. All of these factors influence the galvanic corrosion interaction.

8.3 Erosion-Corrosion of High Chromium White Irons in Sodium Aluminate Solutions

8.3.1 Slurry Pot Tests

The alloys investigated were hypereutectic and hypoeutectic high chromium white iron castings, a hypereutectic high chromium white iron weld overlay deposited on a steel substrate using flux cored arc welding and a hypoeutectic cobalt based Stellite 6 deposited on a steel substrate using plasma transferred arc (PTA) welding. The cast samples and the hypereutectic weld overlay samples were sectioned from worn plant components, and the Stellite 6 sample was sectioned from a bead on plate PTA deposit.

The slurry pot testing device used in this work was similar to that used by Lathabai and Pender (1995). Six test samples in the form of square bars ($9.8\pm0.1 \times 9.8\pm0.1 \times 40.0\pm0.1$ mm) were mounted radially in a circular spindle. The rotational speed was set at 1000 rpm, which corresponds to a wear velocity at the tip of the sample of approximately 5.6 m/s. The test solution was the sodium aluminate solution used for previous corrosion and immersion tests but was not deaerated. The erodent consisted of various sized quartz particles and was based on average particle size data from the red side of alumina refinery operations which use slurries as the transfer mechanism between stages. Tests were done at a temperature of 90^{o}C for 5 hours.

8.3.1.1 Erosion-Corrosion

As highlighted in the literature review, erosion-corrosion wear can be considered the wear due to the contribution of pure erosion, pure corrosion, the effect of erosion on corrosion (additive effect) and the effect of corrosion on erosion (synergistic effect), equation 1.13. The slurry pot test results represent the total weight loss due to erosion-corrosion that encompasses all the aforementioned erosion and corrosion factors. The erosion-corrosion of high chromium white irons is due to the removal of the matrix and the carbides.

The matrix wear rate was found to be greater than that of the carbide wear rate as the carbides were found to stand proud of the the matrix after testing. The carbide rods developed a rounded appearance at the exposed surface. The matrix had a roughened appearance characteristic of a material that has undergone erosive wear.

For the materials investigated the erosion-corrosion wear resistance in sodium aluminate solution at 90°C using variable sized quartz particles was found to be dependent on the bulk hardness of the material. The high chromium white iron weld overlay, WeldoverlayA, which had the highest hardness had the lowest material weight loss over the 5 hour test period. The Stellite weld overlay, having the lowest bulk hardness, had the highest material weight loss. The HypoB sample was of the hypoeutectic composition but had been heat treated such that it had a higher hardness than the hypereutectic HyperA sample. The wear resistance of the HypoB sample was better than that of the HyperA sample. These results of increasing weight loss with decreasing hardness are typically what can be expected under pure erosion conditions. An interesting factor from the results is the improvements that can be gained by undertaking a destabilization heat treatment to increase hardness. This is the reason why the lower CVF HypoB sample outperformed the HyperA sample. The corrosion experiments found that the WeldoverlayA sample had the worst corrosion performance but the erosion-corrosion tests found that the weld overlay had the best erosion-corrosion performance. Therefore, erosion-corrosion wear in highly caustic sodium aluminate solution is dominated by erosive wear.

8.3.1.2 Erosion

Microscopic examination of the wear surfaces of all of the alloys found that both the matrix and carbides showed signs of erosive wear damage. The carbides, irrespective of whether they were primary or eutectic M_7C_3, large or small, developed a rounded appearance on the surface of the carbide rod. The carbides were found to stand proud of the matrix, with the exception of the Stellite weld overlay where the carbides could not be distinguished on the wear surface, due to their fine nature. The carbides standing proud of the matrix indicated that they had superior wear resistance to the matrix and provide the matrix with protection from erosion.

The hardness of the M_7C_3 carbides is greater than that of the erodent quartz particles (carbides varied from approximately 1500 to 1800 HV and quartz is estimated to vary between 900 and 1280 HV) (Tabrett et al., 1996). The difference in hardness between the carbides and the eroding quartz particles eliminates the possibility that the carbides can be damaged due to scratching or scouring by the quartz particles. Therefore, the damage to the carbides has to occur by a chipping mechanism where small sections at the surface of the carbide are removed by microfracture due to particle impingement. This wear mechanism is consistent with other work reported in the literature (Sapate and Rama Rao, 2004).

The wear of the matrix is believed to be the rate controlling factor in the erosive wear of the materials investigated. The matrix, whether soft austenite or hard martensite, showed evidence of deformation due to particle impingement. This was most pronounced in the Stellite and HyperA casting samples which have a matrix hardness nearly half that of the quartz particles. The matrices of these two materials had regions of material that had been deformed by successive particle impacts or forced against a carbide by a ploughing wear mechanism to form thin highly stressed regions of matrix material. These highly stressed regions of matrix material were then susceptible to fracture from further particle impact. This mechanism of erosion is consistent with the platelet mechanism of erosion reported elsewhere (Levy, 1995).

The influence of an erodent of varying sized particles and quantities on the wear rate of the alloys can not be determined conclusively from the initial slurry pot results. It is hypothesized that the presence of the larger abrasive particles would cause greater deformation of the matrix and wear due to the greater kinetic energy transfer.

8.3.1.3 Corrosion

From the examination of the wear surfaces the contribution of corrosion to the total wear loss was difficult to determine. However, the corrosion tests undertaken as part of this thesis have indicated that the matrix corrodes while the corrosion of the carbides is negligible. This is further verification that the damage to the carbides during erosion-corrosion is due to erosion mechanisms.

The corrosion tests have shown that high chromium white iron alloys, cleaned of oxide layers, when immersed in sodium aluminate solution will freely corrode. The surface of the freely corroding sample will be covered with a loosely adherent layer of corrosion product and if an anodic potential is applied it is possible that a more adherent oxide layer can protect the matrix. The stirring of the solution, free of erosive particles, increases the corrosion rate due to the increased mobility of ions to and from the surface.

The erosion-corrosion test results have shown that the wear of the matrix is not due to corrosion alone as the wear tracks of erosive particles and associated deformation are clearly evident. The roughening of the surface which intensifies local electric fields, deformation of the surface that introduces highly localized stresses and the removal of any protective or non-protective oxide layer exposing fresh metal have all been found to cause higher corrosion rates in steel and stainless steel (Wang and Stack, 2000). The impact of erosive particles has been shown to be severe enough to cause deformation of the matrix in high chromium white iron castings and weld overlays and would therefore be capable of disturbing any corrosion product or oxides layers that would otherwise afford protection to the matrix. This would result in an increased corrosion rate of the matrix.

8.3.2 Electrochemical Erosion-Corrosion Tests

The slurry pot tests together with the previous discussion have shown that the matrix of high chromium white irons in erosive-corrosive environments is due to both the removal of the matrix by erosive wear mechanisms and by corrosion. However, the rate of matrix erosion and matrix corrosion could not be separated. A test apparatus that can monitor the in-situ corrosion response of alloys under erosion-corrosion conditions was required to investigate the role corrosion plays in erosion-corrosion wear. A trial test apparatus was developed specifically for this purpose. Due to time and resource constraints, the preliminary electrochemical erosion-corrosion tests were only done on the HypoA hypoeutectic casting and WeldoverlayA hypereutectic weld overlay.

The polarization curves showed similar characteristics at similar potentials for the static, stirred and erosion-corrosion cases Figure 7.12 and 7.13. This indicates that similar corrosion mechanisms are occurring. However, the current density for the different test scenarios varied, indicating the rate of corrosion varied. Results of the testing found that for both the HypoA and WeldoverlayA samples tested the corrosion rate increased by approximately 125 and 140 μA/cm^2 respectively when the solution was stirred without the addition of any abrasive particles. This was particularly evident by the changes in cathodic Tafel slopes for the static and stirred tests Figure 7.12 and 7.13. When abrasive particles were added to the solution to provide erosion-corrosion conditions, the corrosion rate further increased by approximately 16 and 51 μA/cm^2 for the HypoA and WeldoverlayA respectively. Thus under freely corroding conditions, the impinging abrasive particles further enhanced the dissolution reaction on the sample surface but the largest increase in corrosion rate was due to the stirring of the solution.

The dissolution current densities were similar for the HypoA sample for all test conditions, but were only found to increase from the static test condition to the erosion-corrosion test condition for the WeldoverlayA sample. In the passive potential regime the corrosion current density was found to be greater under the stirred and erosion-corrosion conditions for both samples. These variations in corrosion current density are attributed to the increased solution velocity, the mobility of ions, and the reduction in the width of the electrochemical double layer. It was found that the HypoA alloy still passivated under the stirred and erosion-corrosion test conditions. The passive current density was greater under the erosion-corrosion conditions than the stirred which is due to the ability of the abrasive particles to remove the oxide layers. For the WeldoverlayA sample it was found that the passive current density was similar for both the stirred and erosion-corrosion test conditions. This result indicates that the abrasive particles do not enhance corrosion, which is likely considering that the abrasive particles had difficulty removing the matrix by erosive wear mechanisms because of the small inter-carbide spacing.

8.3.3 Influence of Microstructure on Erosion-Corrosion

8.3.3.1 Bulk Hardness

The slurry pot tests showed that the bulk hardness was the main indicator of erosion-corrosion wear performance, with the hardest material having the best wear performance. While it is still debatable that bulk hardness is a suitable indicator of wear performance, particularly in erosion-corrosion environments, these results indicate that bulk hardness can be used to rank wear performance for the set of test conditions used. The test conditions were a sample tip velocity of 5.6 m/s and a turbulent particle environment that would have given a range of particle impingement angles. While the tests were limited to the single velocity and constant particle size distribution, it is possible that changes in the test environment, such as velocity and test duration could change the ranking of the materials and relationship between erosion-corrosion wear resistance and hardness. For example, an increased velocity may make smaller carbides more susceptible to fracture due to increased energy transfer or an increased test duration may lead to more matrix corrosion and subsequent fracture of the carbides. It should also be considered that other microstructural factors other than bulk hardness may have influenced the erosion-corrosion performance but were not readily identified from the limited number of tests.

Previously it has been found that the bulk hardness of high chromium white iron is more strongly influenced by the matrix microstructure rather than the CVF. This is clearly evident by the the HypoB sample having a higher bulk hardness than HyperA but having a lower CVF. By undertaking destabilization heat treatment of the high chromium white iron alloys to transform the matrix to a proportion of martensite, it is likely that the erosion-corrosion wear resistance of high chromium white irons in alumina processing environments can be improved. It is also found that comparable bulk hardness can be achieved with low alloyed irons such as the EutecticA alloy which has a hardness comparable with the HyperA alloy but a CVF of 39 and 52% respectively. However, it should also be taken into consideration that increasing bulk hardness will reduce the ductility and toughness of a white iron.

8.3.3.2 Matrix

The matrix is found to undergo the majority of the wear during erosion-corrosion tests. When the inter-carbide spacing is large compared with the erosive particles, the matrix removal is dominated by the erosion processes that occurs by the repeated deformation of the material and eventual fracture of small fragments. The erosive wear pattern seen on the matrix is characteristic of particles impacting the surface at oblique angles and displacing material by a ploughing mechanism. At low particle impingement angles, increasing matrix hardness will decrease the wear rate (Zum Gahr, 1998). This was clearly demonstrated by the amount of deformation seen on the wear surfaces of the alloys investigated, with the softer matrix of

the Stellite sample showing more significant deformation than the HypoB sample which had a matrix hardness approximately 73% greater .

The hardness of the matrix in high chromium white irons can be increased by undertaking a destabilization heat treatment to transform the dominantly austenitic (or austenitic and pearlitic) as cast matrix structures to martensite. As highlighted in the heat treatment study, each high chromium white iron will have an optimum destabilization heat treatment temperature that will maximize the matrix hardness. The maximum matrix hardness represents a balance between martensite that has sufficient carbon content to increase hardness and retained austenite levels. For the HyperA alloy this was found to occur at about 950^{o}C.

The matrix is also susceptible to corrosion. From the potentiodynamic polarization tests, the rate of corrosion of the castings alloys was found to be an order of magnitude less than that of the weld overlay. The matrix removal of the weld overlay in erosion-corrosion environments due to corrosion is reinforced by the slurry pot tests that showed the small inter-carbide spacing prevented erosive particles from removing a reasonable proportions of the matrix. The high matrix corrosion rate of the weld overly sample was attributed to the increased galvanic interaction between the carbides and matrix due to a small inter-carbide spacing. However, as the erosion-corrosion tests have demonstrated, the overall erosion-corrosion wear in the sodium aluminate solution over a test period of 5 hours is erosion dominated as the material with the greatest wear resistance had the highest matrix corrosion rate. Therefore, preference should be given to increasing matrix hardness rather than corrosion resistance of high chromium white irons to increase erosion-corrosion wear resistance in sodium aluminate environments.

8.3.3.3 Carbides

The carbides have been found to be responsible for the wear resistance of high chromium white irons, however, they were found to undergo wear in erosive-corrosive environments. The wear of the carbides in erosive-corrosive environments is due to erosive wear mechanisms, as the corrosion tests have indicated the corrosion of the carbides is negligible. The wear mechanism of the carbides is due to chipping of the edges of the carbide by impacting particles.

The spacing of the carbides has an influence on erosive-corrosive wear performance with a small inter-carbide spacing being preferable to a larger spacing. This is most clearly evident when the erosion-corrosion wear results of the WeldoverlayA sample, having a small inter-carbide spacing and better wear resistance, is compared with the HyperA sample, having a larger inter-carbide spacing and poorer wear resistance, but both samples having similar CVF. The smaller inter-carbide spacing prevents larger particles from impacting the matrix and removing it due to erosive wear. It has previously been discussed that cooling rate effects carbide size, with a higher cooling rate leading to a smaller carbide size and inter-carbide

spacing.

The extent to which carbide size affects the wear mechanism and the wear rate of the carbides can not be conclusively determined from these test results but it is believed larger carbides will be less susceptible to wear.

8.4 Review of Plant Samples

The examination of a number of ex-service plant samples was done to gain an insight into the wear mechanisms in alumina plant environments and to determine if controlled laboratory based experiments could be used to reproduce the wear surfaces. High chromium white iron centrifugal pump impeller castings and FCAW weld overlays were examined. The examination consisted of a macroscopic and a microscopic wear surface examination.

8.4.1 General Review of Plant Samples

The macroscopic wear surface appearance of the two impeller castings was different. The HypoA casting had a scalloped wear surface appearance (Figure 4.1) and the HyperA casting had a smooth wear surface appearance (Figure 4.2). The wear environments and operational parameters such as solid particle loading, location within the plant and rotational velocity would have influenced the wear surface appearance. Both of the impeller castings showed more significant wear on the trailing edges of raised features and at the periphery of the impeller which can be attributed to localized flow conditions and the increase in the relative slurry velocity.

The microscopic examination of the two impeller castings, HypoA and HyperA, showed a number of similar wear surfaces features. For both of the samples, the carbides were clearly distinguishable and found to protruded above the level of the matrix, with this being more apparent for the HyperA sample than the lower CVF HypoA sample. The amount that the carbides protrude above the matrix would have depended on the wear rate of the carbides themselves and the wear rate of the matrix. Clearly in the cases of the castings examined, the matrix had been wearing at a greater rate than the carbides to allow the carbides to protrude.

The matrix of the castings showed a number of wear features characteristic of erosive wear. These ranged from small sub-micrometer gouges and wear tracks in the matrix of the HypoA sample to larger 10 μm gouges and wear tracks in the HyperA sample. In the matrix of the HyperA quartz (silica sand) particles were found embedded in the matrix. The HypoA casting had a martensitic matrix while the HyperA sample had a predominantly austenitic matrix with regions of martensite surrounding the carbides. The differences in matrix wear surface appearance can largely be attributed to the differences in hardness of the martensitic matrix of the HypoA sample compared with the softer austenitic matrix of the HyperA sample. The

softer austenitic matrix showed significantly more erosive wear damage and is likely to have worn at a greater rate than the martensitic matrix. The erosive material removal mechanism is consistent with the platelet mechanism of erosion consisting of continuous plastic deformation and the eventual fracture of small fragments of material as indicated by the matrix wear surface appearance. The platelet mechanism of erosion occurs more readily in ductile materials. The increased erosive wear of the matrix of the HyperA sample is consistent with the carbides protruding above the surface to a greater degree.

It has been demonstrated that the matrix of high chromium white iron castings corrode. The appearance of the matrix as a result of corrosion, evident from immersion tests, is smooth with preferential attack adjacent to primary or eutectic carbides and secondary carbides. While limited corrosion adjacent to the carbides is evident from the microscopic examination of the plant samples, possibly masked by extensive erosive wear damage. The dominant matrix wear mechanism of the matrix is as a result of erosion.

The wear damage to the carbides is a result of erosion as it has been demonstrated that the corrosion of the carbides is negligible. The wear damage is characterized by a rounding or chipping at the periphery of the exposed carbide due to particle impact. It is probable that the size of the carbides influences the amount of wear and the degree of protrusion above the matrix. The HypoA sample had smaller average diameter eutectic M_7C_3 carbides compared with the large primary M_7C_3 carbides of the HyperA sample. The carbides of the HypoA sample may have worn at a greater rate than the HyperA sample due to their smaller size making them more susceptible to chipping at the edges and fracture which could account for the differences in the amount of protrusion of the carbides between the two samples. A more aggressive wear environment or less protection afforded to the matrix by the carbides as a consequence of their morphology and differences such as inter-carbide spacing can not be discounted for the difference in the amount of protrusion of the carbides between the two samples. It can be concluded that the matrix wears at a faster rate than the carbides, or is preferentially removed while the carbide remain inert, leaving the carbides to protrude above the surface of the matrix.

The macroscopic wear surface appearance of the weld overlays showed many more wear surface features (Figure 4.5 and 4.6) which is largely due to the deposition of the overlay as a number of parallel, overlapping weld beads. The wear surface showed grooves that ran parallel to the longitudinal direction of the spool and the weld beads, creating raised and lowered sections of the overlay. Microscopic examination of transverse sections of lightly etched samples found that the grooves corresponded to areas that had a slightly lower CVF or a slightly different primary carbide orientation. These differences are due to the deposition parameters and variations in weld overlay dilution between adjacent weld beads in different regions of the spool. The reduced wear rate in the overlapped areas with reduced dillution supports the view that an increasing CVF will lead to a reduction in wear rate in these wear environments.

One of the pipe spools provided for examination, WeldoverlayB, was a trumpet spool used to expand the flow downstream of a control valve. The spool showed significant wear adjacent to the flange connection with undermining of the overlay and wear of the substrate. This severe accelerated wear adjacent the flange would be due to the flow regime. It is commonly reported that spools adjacent to pump and control valves experience turbulent flow. As with the accelerated wear at the periphery of the pump impeller casting or adjacent to protruding surface features such as pump vanes, the turbulent flow and the increase in relative velocity of the slurry causes significantly accelerated wear. The wear associated with the turbulent environments, highlighted by the trumpet spool, can lead to reduced operational efficiency or premature failure.

Both WeldoverlayA and WeldoverlayB samples had check cracks (or relief-check cracks) in a 5 to 10 mm mesh over the entire weld overlayed surface. The check cracks were often found to extend to the substrate-overlay interface and sometimes continued along the interface. The check cracks exposed to the surface contained traces of plant residue and preferential wear of the crack edges at the wear surface. It is well established that check cracking is a common occurrence in high chromium white iron weld overlays due to the difference in thermal expansion of the steel substrate and the deposited high chromium white iron with a low toughness (AS 2576: 1996, Francis and Jones 1997). Traces of plant residue within the check cracks indicate that there is an access path for the plant liquor to reach the substrate-overlay interface and the potential for corrosion by crevice corrosion mechanisms or galvanic corrosion mechanisms between the substrate and overlay material. It would be of great benefit to at least minimize the extent of check cracking to minimize the potential for additional corrosion or wear mechanisms to occur, particularly at the overlay-substrate interface.

The examination of the high chromium white iron weld overlay cross-sections indicated that the presence of a number of spherical subsurface pores that were often intersected by check cracks. The pores had smooth non-oxidized surfaces and were most likely hydrogen pores that formed during the solidification of the weld. It has been reported that a number of applicators of high chromium white iron weld overlays often use water cooling, or a form of forced cooling, on the outside of pipe spools during weld deposition. The use of water cooling is to reduce the likelihood of burn through whilst maintaining high average heat input levels to increase or maintain productivity. The presence of a humid welding environment is one of the likely sources for hydrogen to enter the weld deposits. It was also found that the wear surface of the weld overlayed samples contained a number of circular depressions that are likely to be due to progressive wear of the surface which exposes the subsurface hydrogen pores.

Of particular interest found from the microscopic examination of the weld overlays was that the matrix was virtually undetectable as it had been removed, leaving both the primary and eutectic carbides standing in relief. There was only one isolated instance where the matrix

was detectable in WeldoverlayA, Figure 4.17(c). While the cleaning process may have been responsible for some of the corrosion to the matrix, the smooth nature and the preferential corrosion of the matrix adjacent to the carbides is undoubtedly due to in service corrosion and not erosion. This finding is consistent with the finding of the laboratory immersion test (refer Figures 6.36, 6.38 and 6.40).

The microscopic examination of the weld overlays found that the primary carbides would protrude above the eutectic carbides. This was more noticeable in the WeldoverlayB sample, Figure 4.16, compared with the WeldoverlayA sample, 4.17. As the corrosion and immersion tests have demonstrated that neither the primary or eutectic carbides are susceptible to corrosion, the difference in carbide levels has to be due to erosive wear. The primary carbides did show signs of rounding at the exposed periphery, but not as significant as seen in the casting samples. Close examination of the eutectic carbides found that it was common to see irregular exposed surfaces that would be expected if the carbide were to be fractured, Figure4.14(c). This reinforces what was found with the erosive wear of the carbides in the castings samples that larger carbides will wear at a slower rate.

8.4.2 Comparison With Laboratory Based Tests

Comparing the wear surfaces from laboratory based erosion-corrosion slurry pot tests with the ex-service alumina plant samples, it was found that the laboratory wear environment was more aggressive than the alumina plant wear environment as both the casting and weld overlay laboratory test samples had more wear related damage, Figure 8.22. For the casting samples, the matrix had more gouges and plastic deformation than the ex-service plant samples. The carbides of the castings were found to have undergone more chipping at the periphery of the carbide giving a more rounded appearance, but were still found to protrude above the level of the matrix as found with the plant samples. For the weld overlay, the matrix was found to be removed leaving the primary and eutectic carbides standing in relief in a similar fashion to the plant sample. The primary carbides had undergone significantly more damage compared to the plant sample but were still found to protrude above the eutectic carbides. The increased damage seen on the casting and weld overlay samples is consistent with a more aggressive erosive environment as the carbides are not susceptible to corrosion.

The more aggressive erosive environment of the the laboratory slurry pot test apparatus is attributed to the flow environment being turbulent in nature and having higher particle impact velocities than found in the plant. The turbulent slurry pot environment produces a mix of erosive particle impingement angles up to 90 degrees compared with the plant environment which is expected to be less turbulent and particle flow close to parallel with the wear surface. It is known that at increasing particle impingement angles up to 90 degrees, carbide fracture is found to occur more readily. This is consistent with the flow environment of the slurry pot test apparatus and the more significant damage seen on the wear surface of the laboratory

test samples compared with the plant samples.

Although the laboratory wear environment was a more aggressive erosive environment than the plant environment, the wear mechanisms for both the castings and the weld overlay were still similar to the plant samples. Thus, the slurry pot test apparatus is suitable for identifying the likely wear mechanisms and can be used for the ranking of wear resistant materials. Combining this information with the findings from the potentiodynamic corrosion tests, immersion tests and electrochemical erosion-corrosion tests provides a better indication of the wear mechanisms of high chromium white irons in alumina plant environments.

For the casting samples, the immersion tests have shown that the carbides are not susceptible to corrosion and that the matrix corrodes over the potential range found in an alumina plant. As evident from the immersion tests and potentiodynamic corrosion tests, the matrix corrosion rate is significantly reduced when in the material's passive region. The electrochemical erosion-corrosion tests have shown that the corrosion of the matrix is increased by fluid movement over the wear surface for all potentials. The corrosion rate is further enhanced when the moving fluid contains erosive particles. Thus, the wear of high chromium white iron castings in alumina plant environments occurs by the wear of the matrix due to erosion and corrosion, with the wear rate being enhanced due to the combined effects of erosion-corrosion. Erosion of the matrix occurs at a greater rate for the softer austenitic matrix microstructures compared with harder martensitic matrix microstructures as a result of the platelet mechanism of erosion. The carbides, both primary and eutectic, wear due to a chipping mechanism at the periphery of the carbide which is enhanced in turbulent environments and is attributed to the higher proportion of erosive particles impacting the carbide at close to normal incidence.

For the weld overlay sample, the immersion tests and potentiodynamic corrosion tests have shown that the matrix is highly susceptible to corrosion over the potential range found in an alumina plant. Corrosion current densities were typically an order of magnitude greater for the weld overlays compared with the hypereutectic castings investigated. Even when the weld overlay are in the passive potential regime, significant corrosion of the matrix still occurred, Figure 6.40. Due to the high proportion of closely spaced primary and eutectic carbides, it is unlikely that erosion of the matrix could occur. This is reinforced by the erosion-corrosion test results which showed no increase in corrosion current density in the passive potential regime when erosive particles were used to form a slurry compared with the test solution with no abrasive particles, Figure 7.13. This indicated that, unlike the increase in corrosion rate in the passive region due to removal of matrix corrosion products for the castings under erosion-corrosion conditions, that the matrix of the weld overlay does not undergo any significant erosion-corrosion. Thus, the removal of the matrix of hypereutectic weld overlays in alumina plant environment occurs by corrosion with negligible contribution from erosion.

The matrix corrosion rate of the hypereutectic weld overlays is believed to be influenced

by the close eutectic carbide spacing leading to galvanic corrosion effects. This removes the support for the primary and eutectic carbides. As the carbides are not susceptible to corrosion, the damage seen to the carbides in both the plant and laboratory samples is a result erosion. It is interesting to note that although the weld overlays are highly susceptible to matrix corrosion, the slurry pot tests indicated that the weld overlay had the best erosion-corrosion wear performance.

The variation in height between the primary and eutectic carbides seen with the laboratory test samples and plant samples is attributed to the higher susceptibility of the smaller eutectic carbides to wear at a greater rate than the larger primary carbides. The wear mechanism is again due to a chipping mechanism at the periphery of the carbides, but for the smaller carbides, this mechanism appears to more effective leading to a higher carbide erosion rate. This is also supported by the reduced wear of the larger primary carbides of the hypereutectic casting compared with the increased wear of the smaller eutectic carbides of the hypoeutectic casting. Any variation in carbide microhardness between the primary and eutectic carbides is expected to have negligible influence on the erosive wear rate as the typical carbide hardness is greater than the erosive quartz particles.

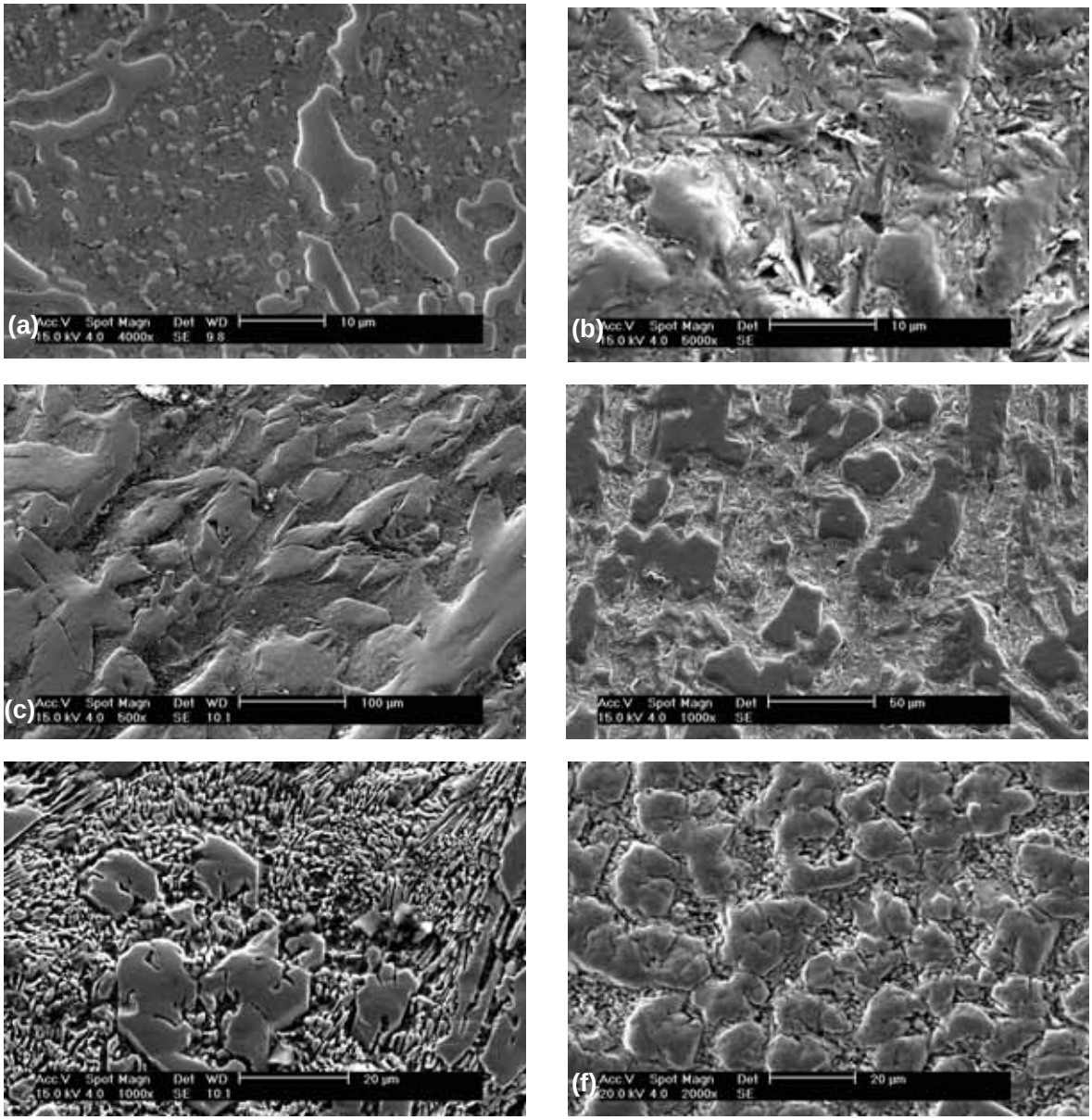

Figure 8.22: Wear surface of ex-service plant samples and laboratory plant samples (a) HypoA plant sample, (b) HypoB laboratory sample, (c) HyperA plant sample, (d) HyperA laboratory sample, (e) WeldoverlayA plant sample and (f) WeldoverlayA laboratory sample.

Chapter 9

Conclusions

This thesis investigated the relationships between microstructure and wear of high chromium white irons used in the Australian Alumina Industry. The influence of variables such as the chemical composition, cooling rate and heat treatment on the microstructure were assessed. Microstructural characteristics that influence wear and corrosion were investigated by undertaking corrosion and erosion-corrosion wear tests to identify microstructural features that have the most significant influence on erosion-corrosion in a sodium aluminate solution representative of what is found in the alumina processing industry. The corrosion of high chromium white irons in sodium hydroxide solution was compared with sodium aluminate solution to investigate the role the aluminate ions have on corrosion.

A range of high chromium white irons castings and weld overlays that are commonly used in alumina processing plants were investigated and compared with an experimental high chromium white iron casting, a low carbon steel and a martensitic stainless steel. All corrosion and erosion-corrosion tests were done at 90^{o}C with the corrosion tests being deaerated.

The conclusions from this work are discussed in terms of the development of microstructure in high chromium white irons and what microstructural characteristics influence corrosion and wear. The influence of the corrosive environment being sodium hydroxide or sodium aluminate is discussed and finally, the wear of high chromium white irons in alumina plant environments.

9.1 Development of Microstructure

The development of microstructure in high chromium white irons is related to the bulk chemical composition, the cooling rate during solidification and whether any heat treatments have been done post solidification. The bulk carbon composition of high chromium white iron castings and weld overlays was found to have more influence on the CVF than the bulk chromium composition irrespective of cooling rate during solidification. As the bulk

chromium composition and chromium to carbon ratio increased, the chromium composition of the carbides and matrix was found to increase for both castings and weld overlays. For casting alloys having primary and eutectic carbides, the chromium composition of the primary carbides was found to be greater than the eutectic carbides. No simple trends based on the bulk chemical composition that can accurately predict the CVF and the chemical composition of microstructural phases for a broad range of high chromium white iron compositions varying from hypoeutectic to hypereutectic could be determined.

The microstructure of the high chromium white iron castings and weld overlays investigated consisted of M_7C_3 carbides and a limited proportion of secondary carbides. The morphology of the carbides were rods of hexagonal cross section or blade like. The size of the carbides was influenced by the cooling rate, with a higher cooling rate leading to a greater number of smaller closely spaced carbides. At the high cooling rates associated with the deposition of weld overlays, the development of undercooled carbide morphologies such as branched primary and complex regular were found to occur.

The destabilization heat treatment of high chromium white irons done at 950°C for 6 hours followed by air cooling resulted in the precipitation of secondary carbides and the transformation of the matrix to martensite, provided the matrix was not over stabilized with elements such as Ni and Mn. Transformation to martensite occurred as the precipitation of secondary carbides reduced the carbon and chromium composition of the matrix raising the M_s temperature. If the matrix contained greater than 5.5 wt% Mn and 8.0 wt% Ni, it will not transform to martensite using conventional destabilization heat treatments and remains fully austenitic. Normalizing heat treatments done at 1150°C for 6 hours followed by air cooling resulted in a matrix composed almost entirely of austenite and a limited proportion of secondary carbides. This is a result of the increased solid solubility of carbon and chromium in austenite at 1150°C which reduced the driving force for secondary carbide precipitation. Upon cooling, the austenite is supersaturated with carbon and chromium reducing the M_s to below room temperature, however, some transformation to martensite was found to occur for alloys that were not over stabilized with manganese or nickel. No changes in carbide type, morphology or the development of a shell structure were found to have occurred as a result of the heat treatments.

The bulk hardness of the high chromium white irons was found to be more strongly influenced by the matrix phase rather than CVF such that low alloyed eutectic compositions can have a higher hardness than highly alloyed hypereutectic compositions in the destabilized condition. Increases in bulk hardness after heat treatments are a result of increasing the proportion of martensite within the matrix. Each high chromium white iron will have a different destabilization temperature that will yield the maximum hardness. Higher bulk hardness can be achieved with compositions that are not as highly alloyed with chromium and carbon (e.g. chromium to carbon ratio of 4.9 compared with 7.6) due to more complete transformation of the matrix to harder martensite.

The deposition of hypereutectic high chromium white iron weld overlays using the FCAW process on steel substrates and forced water cooling on the underside of the substrate leads to the development of undercooled non-equilibrium microstructures, such as branched primary and complex regular. These microstructures can also be formed adjacent to the surface of hypereutectic castings if the cooling rate is high enough. The matrix of the weld overlays is generally austenitic but a layer of martensite has been found to surround the carbides and martensite laths have been found to extend into the matrix, which is expected to be the preferred path for check cracking.

9.2 Influence of Microstructure on Corrosion

The corrosion of high chromium white iron castings and weld overlays in highly caustic pH 14 sodium hydroxide or sodium aluminate solution at 90^{o}C sufficiently free of oxygen is dominated by the dissolution of the matrix. The dissolution of the matrix is due to the formation of dissolved iron species, chromium species or a combination of both. The corrosion characteristics at the open circuit potential and at anodic potentials demonstrated good agreement with the potential pH diagram for iron and chromium at 100^{o}C, validating their use as a first order approximation of corrosion behaviour for a wide potential range. It was found that corrosion behaviour is dominated by iron reactions close to the corrosion potential and the onset of passivation is more likely due to iron oxides rather than chromium oxides as indicated by the potential-pH diagrams. The benefits of having a matrix chromium composition greater than 12% to improve corrosion performance in highly caustic solution are questionable with superior corrosion performance being achieved with alloys having a lower matrix chromium composition but higher CVF.

The primary and eutectic M_7C_3 and secondary carbides did not undergo any detectable corrosion in the caustic solutions. By applying mixed potential theory for a galvanic couple with the carbides forming the cathode and the matrix the anode, the enhanced corrosion of the matrix and reduction in corrosion of the carbides to negligible rates was explained. As the corrosion of the matrix exposes the carbide rods, which will in turn increase the cathode to anode area, the corrosion rate of the matrix will be further enhanced as corrosion of the matrix continues.

CVF cannot be used as an indicator of corrosion behaviour in highly caustic solutions. An alloy having an intermediate CVF had the best overall corrosion performance and high CVF alloys had better corrosion performance than a low CVF alloy. No simplistic explanation could be given for this result except that the factors that determine the galvanic interaction between the carbides and matrix is a complex combination of the respective phase compositions and carbide morphology.

Accelerated corrosion of the matrix occurred adjacent to the carbide-matrix interface with

the corrosion rate decreasing with increasing distance from the interface. This was explained in term of the increased galvanic interaction between the carbides and matrix, intensifying the local electric field at the interface which then reduces with increasing distance from the carbides. As a result of this, castings with larger inter-carbide spacing had superior corrosion performance to weld overlays with smaller inter-carbide spacings by an order of magnitude.

Castings were found to give better overall corrosion performance compared to weld overlays, with a casting alloy having a CVF corresponding to the eutectic composition having the lowest corrosion rate. Weld overlays demonstrated the worst corrosion behaviour, with corrosion rates being an order of magnitude greater than castings of comparable CVF. The increase in corrosion rate of the weld overlays is largely attributed to the galvanic interaction between the carbides and the matrix due to the numerous small carbides with a small inter-carbide spacing.

A high chromium white iron having a homogeneous matrix of austenite will have superior corrosion performance compared to the same alloy having a heterogeneous matrix comprised of martensite and retained austenite. It could not be determined if the degradation in corrosion performance of the heterogeneous matrix was due to the increased galvanic interaction between phases or due to changes in chemical composition. It was found that the martensitic phase is preferentially attacked by corrosion.

9.3 Influence of Microstructure on Erosion

The erosion of high chromium white iron castings involved the erosive wear of the matrix and carbides. The erosion of high chromium white iron weld overlays involved the erosive wear of the carbides and negligible erosion of the matrix. The erosive wear of the matrix occurred by the platelet mechanism of erosion where particle impingement would displace matrix material and successive impacts continuously work harden the displaced material until its eventual fracture as small fragments. This mechanism of erosion occurred irrespective of whether the matrix was hard (martensitic) or soft (austenite). The erosive wear of the carbides for both castings and weld overlays occurred due to chipping of the exposed carbide at its periphery. The erosive wear of the carbides was less than the matrix such that the carbides would afford protection to the matrix. Larger carbides (e.g. the larger primary carbides compared with the smaller eutectic carbides of hypereutectic weld overlays) were found to result in less erosive wear.

The CVF alone cannot be used as an indicator of erosive wear performance. The wear performance depends on the carbide morphology and matrix phase. A predominantly martensitic matrix microstructure, resulting from a destabilization heat treatment, will result in less erosion than an austenitic matrix microstructure. This is due to the reduced ability of the erosive particles to plastically deform the harder martensitic matrix. A small inter-carbide spacing

was found to prevent the larger more damaging erosive particles from removing the matrix and is a desirable feature to improve erosive wear resistance.

Improved low stress erosion performance can be achieved by having numerous closely spaced carbides and a predominantly martensitic matrix.

9.4 Influence of Microstructure on Erosion-Corrosion

The erosion-corrosion of high chromium white irons is dominated by the wear of the matrix which is susceptible to erosive wear and dissolution corrosion in castings, and to dissolution corrosion in hypereutectic weld overlays. To a lesser extent, the carbides are susceptible to wear which occurs by a chipping mechanism when quartz particles are the erodent. In erosive-corrosive environments, the erosive wear is greater than the corrosive wear and erosion is therefore the dominate wear mechanism.

The movement of the solution leads to an increased corrosion rate for the castings and weld overlays. The increase in corrosion rate due to the movement of the fluid, without any erosive particles, is attributed to the increased mobility of ions reducing the electrochemical double layer and a reduction in the thickness of corrosion products that would otherwise reduce the corrosion rate due to viscous shear forces.

Where erosion of the matrix due to impinging particles occurred, a further increase in the erosion-corrosion rate under freely corroding conditions occurred and is attributed to the increased texture of the matrix due to deformation. Erosive particles were found to be effective in removing passive oxide layers.

9.5 Influence of Environment on Corrosion

An increase in sodium hydroxide concentration from 2.5M to 5.0M increases the corrosion rate at the open circuit potential, the active dissolution behaviour and the critical current density for high chromium white iron castings. The rest potential and critical potential were also shifted in the negative direction with an increase in solution concentration. The increase in hydroxyl activity was responsible for these results. In the sodium hydroxide solutions, the high chromium white irons demonstrated superior corrosion performance at the open circuit potential compared with AS1163: C350LO low carbon steel and AISI 420 martensitic stainless steel.

The aluminate ions had a significant effect on inhibiting the corrosion of AS1163: C350LO low carbon steel and AISI 420 martensitic steel at the open circuit potential compared with a negligible effect on inhibiting the corrosion of high chromium white irons. The active dissolution behaviour of high chromium white iron castings is significantly enhanced due

to the presence of the aluminate ions while the active dissolution behaviour of AS1163: C350LO low carbon steel and AISI 420 martensitic stainless steel is inhibited.

The primary and eutectic M_7C_3 carbides do not undergo any detectable corrosion attack in sodium hydroxide or sodium aluminate solution at 90°C up to potentials of approximately 0 V_{SHE}. Above potentials of approximately 0 V_{SHE}, the primary and eutectic M_7C_3 carbides are susceptible to rapid dissolution due to the formation of chromate ions (CrO_4^{2-}). The potential for carbide corrosion is well above the potential an alumina plant would operate at.

9.6 Wear of High Chromium White Irons in Alumina Plant Environments

The wear surfaces from the laboratory slurry pot erosion-corrosion tests resulted in more damage to the carbides than was found from the examination of the ex-service alumina plant samples for both the castings and weld overlays investigated. The wear of the matrix in casting samples showed similar wear characteristics to the ex-service alumina plant samples, but was more significant. The sodium aluminate solution for all the tests was representative of what could be found on the red side of the alumina refining process. Although the laboratory slurry pot test apparatus resulted in a more aggressive wear environment than what may be found in an alumina plant, given the similarities between the wear mechanism of the laboratory and plant samples, the slurry pot test apparatus is suitable to investigate the microstructural characteristics that affected the erosion-corrosion in an alumina plant environments.

The use of castings in alumina plant environments gives improved corrosion performance compared with weld overlays. High chromium to carbon ratio castings do not necessarily lead to improved corrosion performance with low alloy white irons giving superior corrosion performance. The corrosion performance is not related to CVF, however, white irons that have numerous closely spaced carbides such as the weld overlays will lead to a higher matrix corrosion rate.

The wear of high chromium white irons castings and weld overlays in alumina plant environments is erosion dominated and alloys that give better erosion performance should be used in preference to alloys that give better corrosion performance. Alloys that have a high bulk hardness will give better erosion-corrosion performance. The bulk hardness was influenced more by matrix phase than CVF. A destabilization heat treatment is required to transform the matrix to martensite and increase the bulk hardness of the alloy. The inter-carbide spacing is also important with a smaller inter-carbide spacing leading to improved erosion performance.

9.7 Characteristics of High Chromium White Irons for Improved Alumina Plant Service

The principal characteristic of a high chromium white iron for alumina plant service is one that has good erosive wear resistance. This is provided by a hypereutectic alloy with small inter-carbide spacing and a hard matrix. The secondary characteristic is good corrosion resistance in sodium aluminate solution. Of necessity the alloy must be sufficiently tough to avoid cracking during casting and heat treatment of large and intricate shapes or during surface overlaying.

No one high chromium white iron alloy investigated has all these properties. The hypereutectic weld overlays had the best erosion wear resistance due to their small inter-carbide spacing but do not have a fully martensitic matrix, have poor corrosion resistance and check crack which leads to spalling. All of the casting alloys, while having a detectable difference in corrosion behaviour, the overall difference in corrosion rate is not significant although superior to weld overlays. The hypoeutectic and eutectic casting alloys are used in the destabilized heat treated condition and have a hard martensitic matrix but do not have a high carbide volume fraction or small inter-carbide spacing. The commercial hypereutectic casting alloy is used in the as-cast condition with a soft, predominantly austenitic matrix and had large widely spaced carbides. The experimental hypereutectic casting alloy had smaller, more closely spaced carbides and good toughness but has a soft austenitic matrix that did not respond to a destabilization heat treatment.

The two hypereutectic casting alloys have the greatest potential for achieving the desirable characteristics if their matrices could be transformed to martensite. Of these it is highly likely that the commercial alloy would be susceptible to cracking during heat treatment because even in the as-cast condition it contains embrittling high carbon martensite at the interface between the carbides and the matrix. The experimental alloy has the greatest potential because the embrittling martensite at the interface has been eliminated and if the composition was modified to allow the transformation of the matrix to martensite after heat treatment, superior wear performance in alumina plant environments would be expected.

Chapter 10

Recommendations for Further Work

This thesis investigated a range of commercially produced castings and weld overlays that were commonly used in the alumina industry. The range of chemical compositions and microstructures varied significantly. It would be of great benefit to investigate model alloys where the chemical composition and cooling rate can be controlled. For example, compare the equilibrium, slightly undercooled and highly undercooled microstructures of a hypereutectic high chromium white iron for the same chemical composition. Not only would this help in the understanding of microstructural development, but by undertaking corrosion and wear tests on these model alloys would further allow the specific microstructural features that influence corrosion and wear to be investigated.

The corrosion investigation found that higher chromium composition white irons did not necessarily lead to better corrosion performance. The benefit of having a matrix with a chromium composition greater than 12 wt% to improve corrosion performance in highly caustic pH 14+ solutions was questionable and requires further investigation.

The active dissolution of high chromium white irons was found to be enhanced due to the presence of aluminate ions compared with sodium hydroxide solutions. The corrosion mechanism for this phenomena could not be explained and would be of interest to determine the effect aluminate concentration has on increasing the active dissolution of white irons.

Further erosion-corrosion wear tests, both slurry pot and electrochemical, using different velocities, particles size and loading are required to further develop the understanding of the influence of microstructure on erosion-corrosion.

The experimental HyperEXP alloy investigated as part of this thesis had a number of unique features, the most interesting of which was its inability to be destabilized and the matrix transformed to martensite. The application of this alloy with a hypereutectic microstructure and a CVF of approximately 50% may well be suited to service in the alumina industry but is also expected to have many more applications due to its high temperature stability and is worthwhile investigating.